Magmatic volatiles as tracers of volcanic activity at the surface and at depth

Gregor Lucic

Department of Earth and Planetary Sciences
McGill University
Montréal, Québec, Canada

August 2015

A thesis submitted to McGill University in partial fulfillment of the requirements of the degree of Doctor of Philosophy

"An understanding of the natural world and what's in it
is a source of not only a great curiosity but great fulfillment."

David Attenborough

Abstract

Studies of magmatic volatiles in volcanic systems have improved our understanding of magmatic evolution at depth, hydrothermal processes in the crust and degassing at the surface. In this thesis, I present three studies that investigate magmatic volatiles at three volcanic centers that range in size and style of activity. Stable carbon isotopes of soil gases collected at Long Valley caldera, California, reveal that CO_2 gas emitted at the surface represents a mixture of atmospheric, biogenic and magmatic-hydrothermal sources of carbon. Magmatic-hydrothermal gases reach the surface along permeable fractures and faults that have formed due to an interplay between regional deformation and caldera resurgence. Carbon, oxygen, hydrogen and helium stable isotopes from fumarole samples at Cerro Negro volcano, Nicaragua, reveal that such faults, under the influence of regional extension, may provide conduits for ascent of gas from the mantle with minimal crustal interaction. Because of these efficient transport networks, changes in the stable isotope compositions of volcanic gases, in both space and time, may be used to monitor the degassing state of magmas at depth and detect potential recharge events. I have developed a methodology for a portable cavity ring-down spectrometer that can be used to characterize surface degassing, monitor changes in the isotopic composition of the gas in near-real time and increase warning times prior to an eruption at volcanic systems with very calm repose periods. These instruments are of great benefit at systems such as Cerro Negro and Hekla in Iceland, where high volatile contents in magmas drive explosive activity with little to no warning time prior to eruption. At Hekla volcano, I show that longer repose intervals lead to more evolved magmas with higher dissolved volatile contents. The magma chamber at depth may be stratified in composition and volatile content, with the most evolved and most volatile-rich material located at or near the top of the magma chamber. As a result, the initial eruptive phase of explosive eruptions at Hekla is dominated by explosive ejection of tephra. Due to a wide range in water contents and low carbon dioxide concentrations in the melt, only a single magma chamber at ~7 km depth can be proposed. Nevertheless, movement and storage of magmas at greater depths are likely; however, such magma plumbing is not recorded in the melt inclusions due to various degrees of volatile undersaturation.

Résumé

L’étude des éléments volatils dans les systèmes volcaniques contribue à une meilleure compréhension de l’évolution des magmas en profondeur, des procédés hydrothermaux dans la croûte et du dégazage en surface. Dans cette thèse, je présente trois études se penchant sur les éléments volatils à trois centres volcaniques de différentes tailles et différents styles d’activité. Les isotopes stables du carbone mesurés dans des échantillons de gaz du sol à la caldeira de Long Valley, en Californie, révèlent que le CO_2 émis à la surface représente un mélange de carbone atmosphérique, biogénique et magmatique-hydrothermal. Les gaz magmatiques-hydrothermaux atteignent la surface le long de fractures et failles perméables qui sont issues de l’interaction entre la déformation régionale et la résurgence de la caldeira. Les isotopes de carbone, oxygène, deutérium et hélium d’échantillons de fumeroles au volcan Cerro Negro, au Nicaragua, démontrent que de telles failles, sous l’influence d’une extension régionale, peuvent servir de conduits pour le transport de gaz depuis le manteau, et ce, avec peu d’interaction avec la croûte. Grâce à ces réseaux de transport efficaces, les changements de compositions isotopiques des gaz volcaniques, dans l’espace et le temps, peuvent être utilisés pour surveiller le dégazage magmatique profond et détecter d’éventuelles réalimentations du système. J’ai développé une méthodologie pour l’application de terrain d’un spectromètre de cavité résonante pour surveiller le dégazage superficiel et les changements de composition isotopique des gaz en temps quasi-réel afin d’augmenter le délai d’avertissement avant les éruptions aux systèmes volcaniques caractérisés par des périodes de repos très calmes. De tels instruments offrent de grands avantages pour la surveillance de volcans tels que le Cerro Negro ou l’Hekla, en Islande, où des concentrations magmatiques élevées en volatils propulsent une activité explosive laissant

que très peu de délai d’avertissement. À l’Hekla, je démontre que de plus longues périodes d’accalmie mènent à l’éruption de magmas plus évolués, plus riches en volatils dissouts. La chambre magmatique en profondeur est stratifiée, de sorte que le matériel plus évolué et plus riche en volatil est situé près du toit de la chambre. En conséquence, la phase initiale des éruptions explosives de l’Hekla produit d’abondants dépôts de tephra. Étant donné une grande variation de la teneur en eau et une faible concentration de CO_2 dans le liquide magmatique, l’existence d’une chambre magmatique située à ~7 km de profondeur est proposée. Néanmoins, le transport et le stockage de magmas à de plus grandes profondeurs sont probables, bien que cette partie de l’architecture magmatique ne soit pas préservée par les inclusions vitreuses dû à des concentrations en volatils sous le niveau de saturation.

Contribution of authors

This manuscript based thesis is composed of three chapters. Chapter 1 was published by the Journal of Geophysical Research: Solid Earth in 2015. I am the main author on this chapter along with two co-authors: my supervisor John Stix and my co-supervisor Boswell Wing. Chapter 2 was published by the Bulletin of Volcanology in 2014. I am the main author of this manuscript along with five co-authors: John Stix, Barbara Sherwood Lollar and Georges Lacrampe-Couloume from the University of Toronto, and Angélica Muñoz and Martha Ibarra Carache from the Instituto Nicaragüense de Estudios Territoriales in Nicaragua. GLC and BSL carried out stable isotope analyses on samples of soil gases, provide advice on sampling techniques, assisted with data interpretation and provided edits on the manuscript. AM was instrumental in providing logistical support and access to sampling localities in Nicaragua. MIB assisted JS and myself in the field and provided support with gas sampling and temperature measurements. I am planning to submit Chapter 3 to the Earth and Planetary Science Letters journal. I am the main author of this manuscript along with two co-authors: Anne-Sophie Berg and John Stix. ASB provided significant support during the sample preparation stage.

All three chapters were written by me. In addition, I developed ideas, designed figures and tables, and carried out the bulk of the fieldwork. JS provided assistance in the field, helped with the development of ideas, helped design sampling methods and strategies, and provided edits on the manuscript. BW helped with the development of ideas in Chapter 1 and 2, suggested designs for figures and provided edits on the manuscript of Chapter 1.

Acknowledgements

First and foremost, I would like to thank my supervisor, John Stix. He has supported me and guided me through my time at McGill and he has taught me many things beyond the scope of this thesis. I would also like to thank his family for their support during my first days in Montreal and for hosting many wonderful "volcano parties".

I am grateful for the support I have received from my co-supervisor Boswell Wing. Working with him has been an absolute blast and I'm going to miss his thoughtful insights, fascinating metaphors and refreshing advice. I would also like to thank Eric Galbraith for being part of my advisory committee.

My time at the department of Earth and Planetary Sciences was made memorable by the support of all the people that make it special. I must begin with the dynamic trio that embodies the heart and soul of our department - Kristy, Angela and Anne. I am going to miss them and I believe that many people around the world could learn a lot from their kindness. I am grateful for all the interactions with numerous professors in our department over the years. They represent some of the smartest people I know and I look forward to reading their research in the future. Special mention goes out to all the support staff that have helped me with instrumentation, laboratory work, IT and anything I needed help with really. Brigitte, Lang, Anna and Isabelle, I wish them all the best!

I am not really sure what to say about the amazing group of people in our research group. To everyone in the volcanology "gang" that I've met throughout the years – Ben, Cristal, Jack, Olivier, Erica, Melissa, Jason, Marc-Antoine, Kalina, Charlie and Brandon. The many adventures and experiences we shared are ours and I will cherish them for many years to come. May you all find fortune wherever you are and whatever you do.

In the end, I want to acknowledge the support of my partner and my family. Despite being an ocean apart they were always there and always supportive. They are the reason I am here and they are the reason this work exists. Thank you.

Last but not least, I want to thank my dad. You might not know it, but you taught me that knowledge is something to be proud of, and I am.

Table of contents

List of tables

Chapter 2

Chapter 3

List of figures

Chapter 1

Chapter 2

Chapter 3

List of appendices

Chapter 1

Chapter 3

General introduction

1. Introduction

The 2010 eruption of Eyjafjallajökull in Iceland demonstrated that even communities far removed from active volcanic centers are affected by them. As the population of this planet grows, an increasing number of people will be at risk from volcanic eruptions. Our ability to forecast volcanic activity and improve our preparedness depends on our understanding of two key aspects: the behavior and evolution of magmas at depth, and the signals measured by monitoring systems.

Below the surface, we turn to geochemical, geophysical and geological investigations to give us insight into the source, evolution and movement of magmas in the crust. Of particular interest are magmatic volatiles such as water and carbon dioxide preserved in melt inclusions, which are isolated pockets of primary melt trapped within a mineral host at depth (Lowenstern, 2001; Wallace, 2005). Volatile concentrations are strongly influenced by the composition of the magma, the pressure and temperature conditions at which they reside and the degassing nature of the magmatic system (Cashman, 2004). When volatiles accumulate within the magma at high concentrations, they hold the potential for driving explosive eruptions (Wallace et al., 1995).

Near the surface, magma degassing provides a window into magmatic changes currently occurring within the crust and sometimes even in the mantle (Sano and Williams, 1996; Hilton et al., 2010). These changes may be related to a reconfiguration of degassing pathways associated with tectonic events (La Femina et al., 2004), movement of magma within the crust (Poland et al., 2009) and injections of new magma into pre-existing reservoirs (Troll et al., 2012), all of which are potentially important precursors before an eruption. Monitoring of degassing in the past has been restricted to distributions and concentrations of gas species; however, advances in isotope geochemistry have fueled the application of stable isotopes of carbon, nitrogen, oxygen, hydrogen and noble gases to provide further insight (Chiodini et al., 1998; Sano and Marty 1995; Shaw et al., 2003; Fischer, 2008). The development of smaller and more portable instrumentation is opening new avenues of research and monitoring.

2. Thesis rationale

This thesis is divided into three chapters that investigate magmatic volatiles at three different stages. In the first I demonstrate an innovative, field-portable method that helps identify zones of diffuse degassing and characterize the isotopic composition of soil gases and magmatic volatiles. In the second chapter I principally use carbon dioxide to shed light on the degassing state of the magma and explore the nature of conduits along which gases and magmas travel to the surface. In the third and final chapter I explore the evolution of volatiles within a magmatic system and the role they play in controlling explosivity. Long Valley caldera in California was selected to explore the first aspect, Cerro Negro volcano in Nicaragua was selected to explore the second and Hekla volcano in Iceland for the last. Each of these volcanic centers provides a unique opportunity to explore a part of the magmatic volatile cycle.

Long Valley caldera, California - The role of caldera and regional faults upon diffuse degassing

The flux of volatiles from the mantle to the atmosphere is a fundamental question of planetary evolution (Oppenheimer, 2003; Burton et al., 2013). Researchers have begun to recognize that the contributions of diffuse degassing from the periphery of volcanoes and along fault zones are much greater that previously estimated (Burton et al., 2013). It is important that we recognize these zones of diffuse degassing, characterize the sources of these gases and estimate their volumes. I developed a new technique utilizing a portable cavity ring-down spectrometer (CRDS) that enabled me to conduct same-day stable isotopic analysis of soil gases and fumarolic gases. The first deployment of this instrument and technique was conducted at Long Valley caldera, California, where the interplay between regional and caldera structures has created an intricate network of degassing pathways. Using this technique, I was able to identify zones where magmatic CO_2 was reaching the surface, and by doing so highlight important targets for future gas studies at other volcanic centers and fault systems around the world.

Cerro Negro volcano, Nicaragua - Magmatic and degassing conduits and their tectonic links

Magmatic degassing enables us to investigate changes happening deep within the plumbing network of a volcano by looking at emissions at the surface (Chiodini et al., 2008). Cerro Negro volcano in Nicaragua is a small basaltic cinder cone capable of producing sub-plinian eruptions in addition to strombolian activity and lava flows. Water-rich magmas rise rapidly to the surface with only minutes of warning time prior to an eruption (Roggensack et al., 1997). Due to the lack of geophysical signals prior to an eruption, I decided to study the isotopic composition of the emitted gases as a potential eruption precursor. My aim was to characterize the sources of soil gases, assess the influence of the hydrothermal system on the degassing regime and identify how magmatic CO_2 input into the system varies in space and time. My four-year sampling campaign helped me to identify degassing conduits near the surface and provided a method by which magma replenishments might be detected in the future, potentially improving warning times. The complementary dataset of carbon ($\delta^{13}C$), helium ($^{3}He/^{4}He$), oxygen ($\delta^{18}O$) and hydrogen (δD) isotopes and CO_2 flux highlighted how a small volcanic center can provide important clues for the release of magmatic and mantle gases.

Hekla volcano, Iceland - The role of volatiles in explosive eruptions

High volatile contents of magmas can influence and even control the style of eruptive activity (Roggensack et al., 1997). It is essential that we understand where these volatile-rich magmas are sourced from, how their concentrations differ for a range of magma compositions and how their contents relate to explosive eruptions. Hekla volcano in Iceland shows a clear link between repose period and magma evolution (Thorarinsson, 1967). Longer repose periods lead to larger, more silicic magmas with more explosive eruptions. This remarkable correlation makes Hekla the perfect natural laboratory to investigate volatile contents in a range of magmatic compositions. I apply a Fourier transform infrared spectrometer (FTIR) to directly measure H_2O and CO_2 contents in four of Hekla's eruptive products. The results from olivine-hosted melt inclusions are used to compare the volatile contents between less evolved and more evolved magma compositions, to determine the storage depths of these magmas and to examine how the volatile contents may affect the range of explosivity seen at Hekla.

The final chapter of my thesis serves as a summary of key conclusions and findings presented in each of the three main chapters, and ties together my study of volatiles from deep levels to the surface. By understanding the behavior of a system in the past using erupted material and complementing this with real-time observations of degassing, we are better equipped to forecast eruptions and understand the subterranean behavior of magma.

References

Burton, M. R., G. M. Sawyer, and D. Granieri (2013), Deep carbon emissions from volcanoes, *Rev. Mineral. Geochem.*, *75*(1), 323-354, doi:10.2138/rmg.2013.75.11

Cashman, K. V. (2004), Volatile controls on magma ascent and eruption, in *Gas is the active agent, and the magma is its vehicle*, edited by F. A. Perret, p. 16, American Geophysical Union, Washington D.C.

Chiodini, G., S. Caliro, C. Cardellini, R. Avino, D. Granieri, and A. Schmidt (2008), Carbon isotopic composition of soil CO_2 efflux, a powerful method to discriminate different sources feeding soil CO_2 degassing in volcanic-hydrothermal areas, *Earth Planet. Sci. Lett.*, *274*(3-4), 372-379, doi:10.1016/j.epsl.2008.07.051

Chiodini, G., R. Cioni, M. Guidi, B. Raco, and L. Marini (1998), Soil CO_2 flux measurements in volcanic and geothermal areas, *Appl. Geochem.*, *13*(5), 543-552, doi:10.1016/S0883-2927(97)00076-0

Fischer, T. P. (2008), Fluxes of volatiles (H_2O, CO_2, N_2, Cl, F) from arc volcanoes, *Geochem. J.*, *42*(1), 21-38, doi:10.2343/geochemj.42.21

Hilton, D. R., C. J. Ramirez, R. Mora-Amador, T. P. Fischer, E. Fueri, P. H. Barry, and A. M. Shaw (2010), Monitoring of temporal and spatial variations in fumarole helium and carbon dioxide characteristics at Poas and Turrialba volcanoes, Costa Rica (2001-2009), *Geochem. J.*, *44*(5), 431-440

LaFemina, P. C., C. B. Connor, B. E. Hill, and W. Strauch (2004), Magma–tectonic interactions in Nicaragua: the 1999 seismic swarm and eruption of Cerro Negro volcano, *J. Volcanol. Geotherm. Res.*, *137*, 187-199, doi:10.1016/j.jvolgeores.2004.05.006

Lowenstern, J. (2001), Carbon dioxide in magmas and implications for hydrothermal systems, *Mineral. Deposita*, *36*(6), 490-502, doi:10.1007/s001260100185

Oppenheimer, C. (2003), Volcanic degassing, in *Treatise on geochemistry*, edited by H. D. Holland and K. K. Turekian, pp. 123-166, Pergamon, Oxford.

Poland, M. P., A. J. Sutton, and T. M. Gerlach (2009), Magma degassing triggered by static decompression at Kīlauea Volcano, Hawai‘i, *Geophys. Res. Lett.*, *36*(16), n/a-n/a, doi:10.1029/2009GL039214

Roggensack, K., R. L. Hervig, S. B. McKnight, and S. N. Williams (1997), Explosive basaltic volcanism from Cerro Negro volcano: influence of volatiles on eruptive style, *Science*, *277*, 1639-1642, doi:10.1126/science.277.5332.1639

Sano, Y., and B. Marty (1995), Origin of carbon in fumarolic gas from island arcs, *Chem. Geol.*, *119*(1-4), 265-274, doi:10.1016/0009-2541(94)00097-R

Sano, Y., and S. N. Williams (1996), Fluxes of mantle and subducted carbon along convergent plate boundaries, *Geophys. Res. Lett.*, *23*(20), 2749-2752, doi:10.1029/96GL02260

Shaw, A. M., D. R. Hilton, T. P. Fischer, and J. A. Walker (2003), Contrasting He–C relationships in Nicaragua and Costa Rica: insights into C cycling through subduction zones, *Earth Planet. Sci. Lett.*, *214*, 499-513, doi:10.1016/S0012-821X(03)00401-1

Thorarinsson, T. (1967), The eruption of Mt. Hekla 1947-1948. 1 - The eruptions of Hekla in historical times, a tephrachronological study. , *Soc. Sci. Isl.*, 170

Troll, V. R., D. R. Hilton, E. M. Jolis, J. P. Chadwick, L. S. Blythe, F. M. Deegan, L. M. Schwarzkopf, and M. Zimmer (2012), Crustal CO_2 liberation during the 2006 eruption and earthquake events at Merapi volcano, Indonesia, *Geophys. Res. Lett.*, *39*, L11302, doi:10.1029/2012GL051307

Wallace, P. J. (2005), Volatiles in subduction zone magmas: concentrations and fluxes based on melt inclusion and volcanic gas data, *J. Volcanol. Geotherm. Res.*, *140*(1-3), 217-240, doi:10.1016/j.jvolgeores.2004.07.023

Wallace, P. J., A. T. Anderson, and A. M. Davis (1995), Quantification of pre-eruptive exsolved gas contents in silicic magmas, *Nature*, *377*(6550), 612-616, doi:10.1038/377612a0

Link to Chapter 1

In the general introduction, I highlight the potential application of stable carbon isotopes as tracers of magmatic activity. In order for this isotopic system to be a reliable indicator of changes at depth, we must improve our understanding of (a) where these gases are reaching the surface and (b) what processes affect their isotopic signature en route to the surface. These are key questions if we are to quantify the flux of carbon from the mantle and utilize stable carbon isotopes as tools in volcano monitoring.

In the following chapter I aim to resolve these questions with a comprehensive carbon isotopic characterization of soil gases emitted at Long Valley caldera in California. An intricate network of regional and caldera faults has altered the permeability of the caldera, enabling the ascent of magmatic gas to the surface at various localities. I deployed a portable cavity ring-down spectrometer to help me characterize contributions from atmospheric, biogenic and magmatic sources of carbon. I used this instrument and the isotopic dataset it provided me to identify which faults and fractures are efficient conduits for magmatic gases. This study can be used as a guide to help identify degassing conduits at other volcanic centers and in areas where active degassing maybe less prominent.

Chapter 1

Structural controls on the emission of magmatic carbon dioxide gas, Long Valley Caldera, USA

Gregor Lucic[1], John Stix[1], Boswell Wing[1]

[1]Department of Earth and Planetary Sciences and GEOTOP, McGill University, Montreal, Quebec, Canada

---

Manuscript I – published as:

Lucic, G., J. Stix, and B. Wing (2015), Structural controls on the emission of magmatic carbon dioxide gas, Long Valley Caldera, USA, *Journal of Geophysical Research: Solid Earth*, *120*(4), 2014JB011760, doi:10.1002/2014JB011760

Abstract

We present a degassing study of Long Valley Caldera that explores the structural controls upon emissions of magmatic carbon dioxide gas. A total of 223 soil gas samples were collected and analyzed for stable carbon isotopes using a field-portable cavity ring-down spectrometer. This novel technique is flexible, accurate, and provides sampling feedback on a daily basis. Sampling sites included major and minor volcanic centers, regional throughgoing faults, caldera related structures, zones of elevated seismicity, and zones of past and present hydrothermal activity. The classification of soil gases based on their $\delta^{13}C$ and CO_2 values reveals a mixing relationship among three end-members: atmospheric, biogenic, and magmatic. Signatures dominated by biogenic contributions (~ 4 vol. %, -24‰) are found on the caldera floor, the interior of the resurgent dome and areas associated with the Hilton Creek and Hartley Springs fault systems. With the introduction of the magmatic component (~100 vol. %, -4.5‰), samples acquire mixing and hydrothermal signatures and are spatially associated with the central caldera and Mammoth Mountain. In particular, they are concentrated along the southern margin of the resurgent dome where the interplay between resurgence-related reverse faulting and a bend in the regional fault system has created a highly permeable fracture network, suitable for the formation of shallow hydrothermal systems. This contrasts with the south moat, where despite elevated seismicity, a thick sedimentary cover has formed an impermeable cap, inhibiting the ascent of fluids and gases to the surface.

1. Introduction

Carbon dioxide is a key magmatic volatile that plays an important role in the evolution of magmatic bodies. It has the potential to affect eruptive dynamics (Roggensack et al., 1997) and represents a major phase in volcanic degassing (Oppenheimer, 2003). Changes in the concentration of CO_2 and its stable isotope ratio ($\delta^{13}C$) are used as proxies for change within magma chambers and hydrothermal systems (Fischer et al., 1996; Werner and Cardellini, 2006; Chiodini et al., 2008; Hilton et al., 2010; Rissmann et al., 2012; Troll et al., 2012). Remote and in situ measurements of volcanic plumes and fumarolic areas are effective methods for detecting such changes; research has shown that zones of diffuse degassing on the periphery of volcanic centers are also important and have the potential of releasing large quantities of CO_2 (Allard et al., 1991; Chiodini et al., 1998). Such zones commonly have important structural controls and are found at volcanic centers that range in size from large calderas (Werner and Brantley, 2003; Chiodini et al., 2007) to small basaltic cinder cones (Lucic et al., 2014). Emissions from these zones have important implications for the total volatile budget of a volcanos magmatic-hydrothermal system (Burton et al., 2013). Given the potential hazards of diffuse CO_2 emissions, e.g., at Mammoth Mountain (Geis, 2006), Vulcano (Granieri et al., 2006) and Solfatara, Italy (Chiodini et al., 2001), it is important that we understand the volcanic and structural controls upon the occurrence of such zones.

In this paper we present the results of a survey of diffuse and active soil gas emissions at Long Valley Caldera made possible by the first use of a portable cavity ring-down spectrometer in a volcanic area. The aim of our project is to establish the role of regional structures such as the Hilton Creek fault and volcanic structures such as the caldera ring faults and resurgent dome faults upon the distribution of magmatic CO_2. Our approach was to sample gas emissions from a dense network of sites and to analyze the emissions on a daily basis with a field-portable spectrometer. We characterized the gases in terms of CO_2 (vol. %) and $\delta^{13}C$, providing a snapshot that allows us to address long-standing questions regarding the presence of caldera-wide CO_2 emissions at Long Valley. Because a substantial body of data already exist for Mammoth Mountain, we focus here on intracaldera degassing and its associated structural controls.

2. Long Valley caldera

2.1 Study Area

The western margin of the Basin and Range Province is home to one of North Americas largest volcanic centers, Long Valley Caldera (Figure 1). Its volcanic history spans ~4 Ma and is highlighted by the caldera-forming Bishop Tuff eruption which occurred at 0.76 Ma. Following the caldera-forming event, smaller-scale eruptive activity formed the Mammoth Mountain dome complex, the Mono-Inyo chain and other smaller domes and lava flows (Bailey, 2004). In the ~100,000 years following the Bishop Tuff eruption, eruptions of early rhyolite were coeval with the development of the resurgent dome, situated in the heart of Long Valley Caldera (Hill, 2006).

Seismic unrest within the caldera beginning in 1978 (Hill, 2006), increased gas emissions (Sorey et al., 1993) and uplift on the resurgent dome (Savage and Cockerham, 1984; Prejean, 2002; Tizzani et al., 2009) have been attributed to a short-term revival of the magmatic system due to basaltic injections at middle to shallow crustal levels beneath the resurgent dome

(Battaglia et al., 2003). There is uncertainty whether or not the caldera will produce another eruption. Historic activity along the Mono-Inyo chain suggests that a future eruption is perhaps more likely to occur in the vicinity of Mono Lake (Bray, 2014).

2.2 Previous work

Studies of degassing at Long Valley Caldera may be separated into research on Mammoth Mountain (Farrar et al., 1995; 1999; Gerlach et al., 1998; 2001; Rogie et al., 2001) and the interior of the caldera (Farrar et al., 1989; 2003). Present-day degassing at Mammoth Mountain is confined to a series of tree-kill zones, supplied by a gas reservoir at upper crustal depths (Sorey et al., 1998). The $\delta^{13}C$ (-4.5‰) and $^{3}He/^{4}He$ ($\sim 6.5R_A$) values of these gases suggest that they originate from a magmatic source. Episodic rupture of a low-permeability seal leads to pulses of gas high in $^{3}He/^{4}He$, implying that fresh basaltic magma is infusing the reservoir at depth with fresh volatiles (Hill and Prejean, 2005). Increases in CO_2 flux have been linked to such periods of reinjection; they typically occur 2-3 years after the onset of increased seismicity (Werner et al., 2014).

Compared to Mammoth Mountain, the CO_2 flux from tree-kill zones on the resurgent dome is much lower (100 t d^{-1} versus 8.7 t d^{-1}, respectively) (Bergfeld and Evans, 2011; Werner et al., 2014). There is an ongoing debate whether the source of these volatiles is related to fresh intrusions beneath the resurgent dome or if they are sourced from the west moat of the caldera (Bergfeld et al., 2006). It is also unclear whether this west moat source is distinct from the source of volatiles that supplies Mammoth Mountain as $^{3}He/^{4}He$ ratios of $\sim 6R_A$ (Hilton, 1996) in thermal fluids from the resurgent dome support a possible second source of volatiles. However, data from the Long Valley Exploratory Well (Sorey et al., 2003) suggest that the thermal structure 6 km beneath the resurgent dome is not consistent with the presence of a fresh intrusion but rather a long-lived hydrothermal system (Pribnow et al., 2003).

In more general terms, the seismic unrest in the caldera raises a series of questions regarding the volcanic and structural evolution of the caldera. Is the observed seismicity driven by (a) magmatism, (b) hydrothermal activity, (c) accommodation of deformation along a left-stepping fault bend (Hill, 2006), or (d) a combination of all three? The exact drivers remain difficult to evaluate, as the exact location and configuration of magma bodies beneath the resurgent dome and southern parts of the caldera are not well known (Sanders, 1984; Sanders et al., 1995; Battaglia and Vasco, 2006). Deformation data and modeling cannot distinguish between a single large reservoir and several smaller intrusions of magma along existing fractures (Savage and Cockerham, 1984; Langbein, 1989, 2003). Mapping of hypocenters in the southern part of the caldera has revealed active E-W and WNW-ESE striking faults that reflect the ongoing structural evolution of the caldera and the eastern Sierra Nevada fault scarp system (Prejean et al., 2002).

3. Methods

The Picarro instrument is a field-portable cavity ring-down spectrometer which we used to perform carbon isotopic measurements on a daily basis. Typically, we would sample gases during the day and then analyze them in the evening. This approach allowed us to tailor our sampling campaign to important sites for multiple analyses. This type of iterative study allows a high degree of flexibility and freedom.

Gas samples were collected at prominent volcanic and structural sites within and outside the caldera margins. These included Mammoth Mountain, the resurgent dome, Alkali Lake, Hot Creek, the ORMAT geothermal field, the Mono-Inyo chain, Pahoa Island on Mono Lake, the Hilton Creek and Hartley Springs faults, the calderas ring faults and the caldera floor (Figure 1). Our catalogue of sites comprises 220 soil gas samples, three direct measurements of bubbling pools, six soil depth profiles, and a 24h measurement of local atmospheric $\delta^{13}C$. Samples were collected over a 6 week period in July and August 2012, with a small resampling campaign in June 2014.

3.1 Preparation and field sampling

We collected and analyzed gas samples on the same day. The night before a sampling day, we purged and prefilled a select number of 1500 mL Tedlar sampling bags (Analytical Specialties) with CO_2-free air of a known volume (750mL). This was achieved using a standard air pump that passed room air through an alphasolve (NaOH) filter that removed CO_2. The pumping speed was controlled by a flowmeter which allowed us to monitor the volume of air being pumped into the bag. Using this approach, the CO_2 concentrations in the bag at the start of a sampling day were typically between 10 and 20 ppm. This technique produced bags with a known volume of nearly CO_2-free air for gas sample collection the following day. We found that there was no diffusion of air out of or into the bags when they were stored overnight. In the field, soil gases were extracted using a 1m long stainless steel probe coupled with an ADC Systems landfill analyzer (error: ±0.01% at 0-9% and ±0.1% at 10-100%) that measured CO_2, O_2 and CH_4 concentrations (all vol. %). The ADC also served as a pump that extracted the gases from the soil at a low pumping speed, after which they were extracted into a syringe with a stopcock (5 mL, 10 mL, 60 mL syringe by BD, and 140 mL by Monoject). Depending on the concentration of CO_2 in the soil, the volume of gas in the syringe was adjusted to produce a concentration of ~2500 ppm CO_2 in the sample bag. Soil gases that were above 3000 ppm CO_2 were diluted in a prefilled Tedlar bag of CO_2-free air, while soil samples below 3000 ppm were pumped directly into an empty Tedlar bag. Once collected, the gases would remain in the bags for a period of $\leq$ 8h before analysis. Gases were sampled between 30 and 100 cm depth, depending on the soil compaction. Experiments on the role of depth in gas sampling (see section 4.1 below) showed that in order to obtain reliable isotopic samples, depths greater than 30cm were essential. Most soil gases were collected at depths greater than ~60 cm. Soil temperatures were measured by an Omega thermocouple with a precision of ±0.1°C, at the same depth as gas sample collection.

3.2 Sample analysis

Gas samples were analyzed using a Picarro G1101-i cavity ring-down spectrometer (CRDS). This instrument is designed for gas phase analysis of ^{12}C and ^{13}C at atmospheric gas concentrations and has an upper limit of 6000 ppm. Measurement precision is quoted as ±0.5‰ for $\delta^{13}C$, but this precision is dependent on concentration. To address this issue, we analyzed a standard gas at 500ppm intervals between 500 and 5000 ppm and recorded the mean and standard deviation of the $\delta^{13}C$ values over a 10min analysis period (Figure 2a). We found that at ~500 ppm the variability is ±0.85‰ (1σ), and between 2000 and 5000 ppm the variability bottoms out at ±0.30‰ (1σ). In addition to concentration-dependent variability in precision, there is also a known concentration-dependent change in $\delta^{13}C$ which can produce heavier isotopic values at higher concentrations. Using the same standard data (Figure 2a), we quantified this shift as a maximum of 0.6‰ over a concentration range of 500-5000 ppm. To minimize this effect, we analyzed all gas samples at a constant CO_2 concentration of ~2500 ppm when possible. The calibration curve was obtained using four gas standards at a concentration of ~2500 ppm, similar to the average concentration of gas within the sample bags.

To further ensure the accuracy of our Picarro measurements, we compared all gas standards and selected field samples measured by Picarro with duplicate samples analyzed in the Stable Isotope Laboratory at the University of Toronto. Samples that were collected in duplicate were sampled from sites that cover a range of CO_2 concentrations, $\delta^{13}C$ values, temperatures, depths, surface types and H_2S concentrations. The analyses at Toronto were performed on a Finnigan MAT gas source mass spectrometer paired to a gas chromatograph combustion interface with a continuous flow-through system. Carbon isotope ratios were determined by comparing international (National Bureau of Standards (NBS)-18 and NBS-19) and in-house standards, and each gas sample was analyzed 3 times to quantify the analytical error (±0.1‰). The standards and samples that were run by both Picarro and Finnigan MAT instruments show a 1:1 match (Figure 2b), demonstrating that the Picarro instrument is both accurate and precise to sub-per mil levels.

The Picarro analyzer was set up at an altitude of 2155 m inside the laboratory facilities of the Sierra Nevada Aquatic Research Lab (SNARL). Temperatures inside the laboratory ranged from ~20° to 30°C, with an average daytime temperature of 25°C and low relative humidity (<20%). Once the sample bags were brought back to the lab, they were attached directly to the inlet of the analyzer separated by a 1µm Acrodisc CR 25 mm syringe filter to remove any particulate matter that might have entered the bag during field sampling. The instrument sampled gases using a flow-through system taking one measurement every 10s. Once the bag was connected, the instrument displayed a change in ^{12}C and ^{13}C from room-like CO_2 concentrations (background) that typically varied from 100 to 300 ppm above the atmospheric background of ~400 ppm, to a stable, high concentration of ~2500 ppm CO_2 that varied by ~10 ppm or less. Once this plateau was established, we let the instrument analyze for 10min, a time period which we determined to be statistically suitable. An average value of the plateau for ^{12}C and ^{13}C (ppm) was recorded along with H_2O (wt. %), CH_4 (ppm) and the raw $\delta^{13}C$ value (‰). Once the bag was disconnected and the CO_2 concentration and $\delta^{13}C$ returned to background values, we resumed the analysis by attaching the next bag. The time period between successive bags was typically 2-3min. All $\delta^{13}C$ values are reported on the Vienna Pee Dee Belemnite scale.

3.3 H_2S interference

Our isotopic analyses of soil gases identified a small number of samples that produced anomalous $\delta^{13}C$ values of -50 to -150‰. With injection of normal samples the instrument registered a change from atmospheric readings to a steady plateau of CO_2 (ppm) and $\delta^{13}C$ (‰) with time. Anomalous samples displayed a steady plateau of CO_2 but decreasing (more negative) $\delta^{13}C$ with time (see Appendix 2). Resampling of the same site 1-2 m from the original sampling location did not remove the anomaly, indicating it did not reflect from sampling variability. In 2014, repeat samples of these anomalous sites revealed hydrogen sulfide (H_2S) concentrations in excess of 76 ppm. H_2S is commonly detected at hydrothermal areas, and its presence was reported at Casa Diablo at ppb to ppm levels in the past (Sorey et al., 1993). Due to our same day technique of sampling and analysis, we were able to identify the anomalous samples and resample them for mass spectrometer analysis at the University of Toronto Stable Isotope

Laboratory. By comparing our Picarro field measurements of δ^{13}C from anomalous sites (-50 to -100‰) with laboratory analysis of duplicates from Toronto (-4.4‰), we were able to identify the problem as one of instrumental interference. Consultation with Picarro engineers confirmed our suspicion that the presence of an additional gas species was producing the interference signal. Since that time we have developed a method for removing H_2S from our samples by passing the sample gas through a copper tube filled with copper filings (K. Malowany et al., H_2S interference on CO_2 isotopic measurements using a Picarro G1101-I cavity ring-down spectrometer, submitted to Rapid Communications in Mass Spectroscopy, 2015). We found this setup to be successful in removing H_2S so that it would not interfere with our δ^{13}C measurements.

4. Results

4.1 Soil types

Over a span of 6weeks our campaign of soil gas sampling at Long Valley Caldera produced an isotopic characterization of 223 individual sites. After several days of fieldwork, we identified three predominant soil surface types that we termed (a) hydrothermal, (b) rich vegetation, and (c) dry vegetation. Hydrothermal sites are distinct in their lack of vegetation. These areas occur as small patches of dying grass or prominent tree-kill zones such as Horseshoe Lake on the flanks of Mammoth Mountain. Hydrothermal sites commonly feature fumaroles and hot springs that vary in size and output. Prominent hydrothermal sites are generally easy to identify; for those with more subtle surface signatures, we used a hand-held infrared camera to detect small temperature anomalies. The other two soil types are very different from hydrothermal sites since they are both covered by vegetation. Due to the dry summer climate in and around Long Valley, vegetation can be classified as either rich vegetation or dry vegetation. Pine forests, grasslands, and areas near sources of flowing water are grouped as rich vegetation, while arid soils and low bushes with no leaves constitute dry vegetation. The three soil surface types can be seen in Figure 3.

4.2 Carbon isotopes of soil gases

All data are presented in Appendix 1 - Table 1. Soil gases show a large range in CO_2 concentration between 0.04 and 89% by volume and $\delta^{13}C$ from -1.9 to -24.5‰. In order to accurately characterize the different soil surface types, we measured soil gases in a series of depth profiles. Two sites per surface type were selected from six separate sampling sites that best represent dry vegetation, rich vegetation, and hydrothermal sites (Figure 4). All surface types show a reproducible depth profile trend that varies systematically in CO_2 and $\delta^{13}C$. Dry vegetation registers almost no change in concentration (<0.3 vol. %) with depth when compared to rich vegetation, which appears to stabilize at ~4 vol. % at 70 cm depth. The largest amount of variability is seen in the hydrothermal profile with a concentration increase of 12 vol. % from 10 to 80cm depth. All three soil types appear to converge at 0 vol. % at the surface, suggesting mixing with an atmospheric CO_2 end-member. By contrast, dry vegetation registers the largest degree of $\delta^{13}C$ variability with -13‰ at 10 cm and -19‰ at 90 cm depth, while rich vegetation reaches a stable value of ~-22 to -24‰ at 30cm depth. For the hydrothermal profile, the stable value of ~4‰ that begins at 10cm depth gives us confidence that concentrations above ~4 vol. % CO_2 are primarily of hydrothermal origin.

From previous work on CO_2-He relationships (Hilton, 1996), we know that the composition of CO_2 in the hydrothermal system is primarily of magmatic origin with an average $\delta^{13}C$ ratio of -4.5‰ and a $^3He/^4He$ ratio of ~6.5R_A. For the purpose of our three-component mixing model, we assume that the hydrothermal CO_2 source concentration is 100% and that the natural variability of the hydrothermal system forms a range between -2 and -7‰ rather than a single value of ~-4.5‰. Due to a range of vegetation types inside and outside the caldera, we define the biogenic end-member as a range of $\delta^{13}C$ from -19‰ to -24‰ (Clark and Fritz, 1997). We conducted a continuous, 24h experiment of atmospheric CO_2 concentrations and $\delta^{13}C$ values at the SNARL facility which established the atmospheric end-member as ~400±10 ppm CO_2 and $\delta^{13}C$ of -9.0±0.8‰. Using these end-member parameters, nearly every soil gas sample can be modeled as a three-component mixture. To calculate three-component mixing, we use the following equations:

$$1 = f_H + f_A + f_B \tag{1}$$

$$\delta^{13}C_{obs} = f_H(\delta^{13}C_H) + f_A(\delta^{13}C_A) + f_B(\delta^{13}C_B) \tag{2}$$

$$\frac{1}{CO_{2\ obs}} = \frac{f_H}{CO_{2\ H}} + \frac{f_A}{CO_{2\ A}} + \frac{f_B}{CO_{2\ B}} \tag{3}$$

where the subscripts *H*, *A,* and *B* correspond to hydrothermal, atmospheric, and biogenic end-members, respectively. The parameter *f* represents the relative volume fraction for each end-member, $\delta^{13}C$ represents the carbon isotopic signature in per mil notation (‰), and CO_2 represents the concentration of gas in vol. %. In summary, our end-member concentrations of

CO_2 for H, A, and B are 100%, 0.04% and 4%, respectively, while $\delta^{13}C$ ratios are -2 to -7‰, -9‰, and -19 to -24‰, respectively.

Pairing the results of the three-component mixing with the depth profiles and field observations, we can differentiate among four groups of soil gases based on their CO_2 concentrations and $\delta^{13}C$ signatures (Figure 5): (1) hydrothermal, (2) dry vegetation, (3) rich vegetation, and (4) a mixing field. The division between dry vegetation and rich vegetation was made on the basis of the depth profiles and our field notes; there is an overlap between the two fields. The mixing field represents sites whose signatures show mixing between dry vegetation, rich vegetation, atmospheric CO_2, and variable amounts of hydrothermal CO_2.

4.3 Soil temperatures

Soil temperatures in the field area range from a minimum of 5°C at the Earthquake Fault to a maximum of 99°C near the Casa Diablo geothermal field (Figure 6). Air temperatures during the summer ranged between 5° and 30°C, and field sampling was conducted during the day when soil surface temperatures ranged between 15 ° and 25 °C. The soil temperature trends indicate that low-temperature gases tend to be associated with low CO_2 concentrations and high-temperature gases with high CO_2 concentrations (Figure 6). A closer examination of the hydrothermal and mixing fields shows that certain high-temperature gases have low concentrations of CO_2, while other low-temperature gases have high concentrations of CO_2. There is a similar trend observed between temperature and $\delta^{13}C$, as lighter $\delta^{13}C$ gases from dry vegetation and rich vegetation sites tend to have lower temperatures with a more restricted range (~10 to 40°C). There is a considerable variation in temperature for soils with gases exhibiting more positive $\delta^{13}C$ values, with the highest-temperature gases (95°C) registering a $\delta^{13}C$ value of ~-7‰. This is on the more negative end of the proposed -2 to -7‰ range for hydrothermal soil values.

4.4 Spatial distributions

We apply this fourfold division of soil gases (hydrothermal, dry vegetation, rich vegetation and mixing) to their spatial distribution within and near the caldera in order to identify areas where hydrothermal CO_2 is the dominant soil gas species (Figure 7). Hydrothermal and mixing signatures occur within or in close proximity to well-defined hydrothermal zones. These two groups are found along several "hot spots" of hydrothermal activity that progress from west to east in the following sequence: Mammoth Mountain, west and east Casa Diablo, Fumarole Valley, Hot Creek, and Alkali Springs Lake. Other than Mammoth Mountain, which is located on the caldera margin, all other zones are located in the caldera and along the southern margin of the resurgent dome. The distribution of our hydrothermal gas samples within these hot spots reveals a linear trend that parallels the strike of smaller, regional NW-SE faults (Figure 7).

Transects of these faults at right angles reveal heavier $\delta^{13}C$ signatures (~-5‰) close to the fault strand (Figure 8). This change toward heavier values may occur up to 100 m from the fault trace (e.g., Casa Diablo A) or as a single sampling point directly on the fault trace (e.g., Fumarole Valley B). Transects of the Hot Creek area show a large variability of $\delta^{13}C$ values ranging from dry vegetation to hydrothermal signatures. In this area, there is no single fault trace visible in terms of $\delta^{13}C$ but rather a continuous zone of hydrothermal emissions that trends perpendicular to the northern termination of the Hilton Creek fault.

Dry vegetation sites are dominant on the caldera floor, the eastern caldera, and several areas on the resurgent dome, as well as areas north of the caldera. Rich vegetation sites occur in these same areas but tend to be focused on the resurgent dome and along the Hartley Springs fault system, both of which are forested areas. Some rich vegetation sites occur as isolated pockets of vegetation along major fault strands such as the Hilton Creek fault. Transects of these sites reveal that $\delta^{13}C$ values at the fault trace become lighter (~-23‰), suggesting an increase in the biogenic CO_2 component. Natural springs in the area (Big Springs, Hot Creek, and Antelope Valley) are located on or near prominent fault strands. Water rising along these structural features creates isolated pockets of rich vegetation.

Limited sampling of soil gases along the southern shore of Mono Lake and the northeast margin of the North Coulee revealed a faint hydrothermal signature of ~-6.5‰ and CO_2 concentrations of 1-2 vol. %. This is in agreement with recent work by Bergfeld et al. (2015) which examined degassing from Mono Lake and the Mono-Inyo chain of domes. They propose that magmatic $\delta^{13}C$ (~-4.5‰) and $^3He/^3He$ (5-6R_A) ratios in soil gases from the North Coulee reflect the presence of a degassing basaltic intrusion, perhaps associated with Holocene volcanism (Bray, 2014).

5. Discussion

5.1 Sources of CO_2

Using our established end-member compositions for hydrothermal, atmospheric and biogenic sources of carbon, we can account for all samples within the three-component mixing diagram (Figure 5). Samples along the atmospheric-biogenic mixing curve plot in one of the two fields, dry vegetation or rich vegetation. Given the high number of sampling sites at various levels of vegetation cover, these two fields represent variable proportions of mixing between the two end-members with a stronger atmospheric component for dry vegetation. Depth profiles at dry vegetation sites display larger variability in $\delta^{13}C$ values with depth (Figure 4), further demonstrating that a low-concentration biogenic component in the soil is mixing with atmospheric CO_2. The influence of a stronger biogenic source is demonstrated by the rich vegetation depth profile for which the stable $\delta^{13}C$ signature (~-23‰) occurs at a depth of >20 cm when concentrations rise above 0.5vol% CO_2. Our field evidence suggests that the primary controlling factor in determining the presence of abundant vegetation capable of producing a strong biogenic soil CO_2 signature is water. Sites located near streams, freshwater springs, and sites with the availability of surface water can sustain relatively lush vegetation that has a higher rate of metabolism and respiration, deeper roots, and a strong biogenic signature (Clark and Fritz, 1997).

Hydrothermal sites on the other hand have a strong magmatic source of high-concentration CO_2 that generally swamps both the atmospheric and biogenic contributions to produce a stable $\delta^{13}C$ soil profile with depth (Figure 4). While the average $\delta^{13}C$ composition of high CO_2 concentration gas from prominent hydrothermal sites is estimated to be ~-4.5‰ (Hilton, 1996), we find that our end-member composition requires a range in $\delta^{13}C$ between -2 and -7‰ in order to successfully fit all the sample sites within our three-component mixing model (Figure 5). Many of the $\delta^{13}C$ systematics can be explained by batch equilibrium degassing at the source and fractionation through diffusion in a porous medium (Capasso et al., 2001), but to explain the full range of $\delta^{13}C$ in the hydrothermal field also requires a small degree of fractionation through speciation reactions between CO_2 and HCO_3^- in the shallow hydrothermal system (Hilton, 1996). The fact that no $CO_2/^3He$ anomaly is present in hydrothermal fluids suggests that the effect of the shallow hydrothermal system on the $\delta^{13}C$ ratio is small (±1-2 ‰). Given that Long Valley Caldera is a large and complex volcanic system, we attribute our range of $\delta^{13}C$ compositions from numerous hydrothermal zones to a combination of magmatic degassing at depth, secondary fractionation within the hydrothermal system, and a small component of mixing with atmospheric and biogenic sources of carbon near the surface.

Sites that fall within the mixing group represent soil gases with a contribution from all three end-members (Figure 5). They plot in a distinct field removed from the dry vegetation and rich vegetation fields due to a larger proportion of the hydrothermal end-member. Sites that plot within the mixing field are located on or within ~50m of hydrothermal areas, demonstrating that the increased hydrothermal component is due to their proximity to a hydrothermal source of CO_2. This gradual increase in the hydrothermal component can be seen in Figure 8, where soil gases change from dry vegetation $\delta^{13}C$ compositions to mixing compositions and finally peak at a strong hydrothermal composition at the fault trace. They are found at Casa Diablo, Fumarole Valley, Hot Creek and Alkali Lake but are absent from other parts of the caldera where the predominant sources of carbon come from biogenic sources, i.e., the dry vegetation and rich vegetation fields. In 2014 we resampled and reanalyzed key sites from within the mixing field by both CRDS and mass spectroscopy to confirm their lighter signatures. This gives us confidence that the reported $\delta^{13}C$ values in the mixing field are real and not a product of instrumental error or contamination by H_2S.

A small number of sites within the mixing field plot along the mixing line between atmospheric and hydrothermal CO_2, and we interpret them as a mixture between atmospheric CO_2 and a small proportion of hydrothermal CO_2. It is interesting that only two sites (located at Alkali Lake) plot on the mixing line between biogenic and hydrothermal CO_2, but perhaps this is to be expected due to the detrimental effects of elevated CO_2 concentrations on vegetation (e.g., tree kills). In addition, there appears to be no clear correlation between sampling depth and the isotopic composition of the samples within the mixing field. This suggests that the main controlling factors are the presence of organic layers within the soil and the proximity of the site to a hydrothermal source. Small changes in the permeability of the soil due to compaction, hydrothermal alteration, and surface water flow may alter the efficiency of mixing between the three end-members.

5.2 Fluids

The $\delta^{13}C$ and $^3He/^4He$ characteristics of soil gases from Mammoth Mountain and the interior of the caldera suggest that both are sourced from magmatic bodies. Degassing at Mammoth Mountain is restricted to its flanks, while drill hole data indicate that a more general zone of upwelling fluids is present beneath the west moat of the caldera (Goff et al., 1991). It is unclear whether basaltic intrusions responsible for gas recharge beneath Mammoth Mountain (Sorey et al., 1998) are also responsible for this larger zone of upwelling or if a second set of older intrusives is present (Sorey et al., 1991). Likewise, the source of magmatic gas in the interior of the caldera remains a topic of debate (Hough et al., 2000; Pribnow et al., 2003). Magmatic $\delta^{13}C$ ratios and high $^3He/^4He$ values coupled with deformation suggest that an intrusive body 6km beneath the resurgent dome may be the source. However, resistivity measurements from the Long Valley Exploratory Well indicate that the resurgent dome acts as an impermeable cap down to a depth of 2-2.5km, inhibiting vertical and lateral migration of fluids at shallow levels (Farrar et al., 2003; Pribnow et al., 2003). This feature explains the lack of major hydrothermal activity and fluid flow within the interior of this structure, although it does not discount the possibility of downward percolation of meteoric water in the uppermost few hundred meters (100-300 m). Temperature measurements at 3km depth (100°C) and hydrothermal alteration of metasediments favor the presence of a long-lived hydrothermal system which is unaffected by 800°C intrusions at 6-8km depth (Pribnow et al., 2003).

We interpret our results within this framework, where emissions from a source of magmatic volatiles beneath the west moat of the caldera are transported laterally from west to east along preexisting fluid reservoirs in the Bishop Tuff and early rhyolites (Sorey et al., 1991). Groundwater flow that begins as precipitation in the Sierra Nevada migrates from west to east across the caldera as dictated by the regional hydraulic gradient (Sorey et al., 1991). We propose that the west to east distribution of hydrothermal areas within the caldera is a reflection of the interplay between upwelling magmatic fluids in the west, the hydraulic gradient of regional groundwater flow, and the impermeable cap formed by the resurgent dome (Pribnow et al., 2003). As discussed by Hilton (1996), the hydrothermal system has the ability to transport the bulk of magmatic volatiles with little or no modification to the C-He isotopic budget. CO_2 concentrations, $\delta^{13}C$ ratios and temperatures of soil gases presented in this study reflect the interaction among the different types of fluids and spatially distinct sources of magmatic volatiles.

Samples collected from degassing zones on Mammoth Mountain and adjacent tree-kill sites such as Horseshoe Lake are characterized by high CO_2 concentrations (> 10%) and hydrothermal $\delta^{13}C$ values (~-5‰) but low temperatures (< 20°C). “Cold” pockets of CO_2 are well documented in this area (Sorey et al.,1998; Evans et al., 2002) and may form due to absorption of magmatic gases into a shallow groundwater system, resulting in the formation of high-CO_2, low-temperature systems that supply a constant flux of CO_2 (Werner et al., 2014). This flux may increase episodically due to a buildup of pressure or tectonic activity (Giggenbach et al., 1991; Hill and Prejean, 2005).

Samples from the interior of the caldera reflect a larger and more complex mixing configuration. A select set of our samples exhibit high temperatures (70 to 90°C), low CO_2 concentrations (<1vol%) and depleted $\delta^{13}C$ (~-10‰). When plotted within our three-component mixing model, these sites fall within the mixing category. Their high temperatures likely reflect fluid mixtures that have been reheated due to their proximity to high heat flux sites such as Casa Diablo, Fumarole Valley and Hot Creek. These sites exhibit some of the largest heat fluxes within the caldera (Bergfeld et al., 2006). We do not discount the possibility that some gases may be mixing with vaporized meteoric fluids that have percolated down faults and fractures.

The largest manifestation of hydrothermal activity and degassing within the caldera is at Casa Diablo. This locality is also home to a small subset of samples that are characterized by high temperatures (>80°C), high CO_2 concentrations (>2vol%) and $\delta^{13}C$ values of ~-7‰. Given that these sites plot within the hydrothermal field in terms of CO_2-$\delta^{13}C$, the -2.5‰ offset from the average hydrothermal value of -4.5‰ is unusual (Figure 6). Winnett and Janik (1986) presented carbon isotopic data on hydrothermal fluids and gases collected at localities along the resurgent dome. Their results suggested that isotopic equilibrium between CO_2 (gas) and HCO_3^- (aqueous) was achieved in the Hot Creek region but not at Casa Diablo. Different boiling conditions within the hydrothermal system and their host rocks may produce a difference between equilibration and discharge temperatures, resulting in fractionation between CO_2 and HCO^{3-}. They reported a similar range (-4.1 to -7.9‰) in their $\delta^{13}C$ composition of Casa Diablo gases, concluding that this is a result of secondary fractionation processes and does not represent the original carbon source. Our lighter (~-7‰) $\delta^{13}C$ compositions, emissions of H_2S gas (>76ppm) and a high heat flux in the Casa Diablo region suggest three scenarios. (1) The boiling front of the geothermal upflow zone is creating fluid-rock instabilities leading to a possible increase in pH, from 5 to 7 or more. The resulting low-temperature precipitation of CO_2 to carbonates in order to buffer this change in pH may shift $\delta^{13}C$ values toward lighter values (Gilfillan et al., 2009). (2) The -7‰ mean value is an expression of nearly pure carbon from the primary magmatic source, unaffected or less affected by the hydrothermal system. (3) The range reflects the addition of carbon through hydrothermal interactions with metasedimentary rocks (White et al., 1990). These different processes likely contribute to the slightly lighter $\delta^{13}C$ signature observed at Casa Diablo.

5.3 Regional structure

The main regional structures in the greater Long Valley region are the Hilton Creek fault, the Hartley Springs fault and the left-stepping bend that links the two. All three structures are a product of the regional stress regime associated with the continuing evolution of the Basin and Range system and its interaction with the eastern Sierra Nevada. Recent seismicity in the southern parts of the caldera and the adjacent Sierra Nevada block to the south indicate that all three structures continue to be active (Hill, 2006). Despite being prominent features that transect the caldera margins to the northwest and southeast, our data reveal that soil gas compositions along the Hilton Creek and the Hartley Springs faults show no presence of hydrothermal CO_2 (Figure 7). Soil gases from both fault systems plot within the dry vegetation and rich vegetation fields, indicating that the dominant control on gas composition in these areas is surface cover. The Hartley Springs fault passes through a healthy pine forest. As a result, signatures of rich vegetation dominate the soil gases here (~2 vol. % CO_2, -21‰ $\delta^{13}C$). The Hilton Creek fault on the other hand passes through a more arid part of the caldera resulting in dry vegetation soil gas signatures (~<1vol% CO_2, -17‰ $\delta^{13}C$). Both fault systems have several freshwater springs along their length, suggesting that the structures are permeable and allow for zones of upwelling meteoric water. Two transects of the Hilton Creek fault south of the caldera margin demonstrate how the introduction of water to an otherwise dry part of the caldera can alter the surface cover and composition of soil gases (Figure 8). Samples collected several meters from the fault trace plot within the dry vegetation field (-18‰). As one approaches the fault trace, the influence of upwelling water is reflected in a change of surface cover from dry vegetation to rich vegetation, hence a lighter soil gas isotopic signature (-22‰). The increased water supply brings with it the ability to sustain rich vegetation and a stronger biogenic gas component. On the other hand, transects of the Hartley Springs fault are located in forest and do not register a change in soil gas composition because the contrast in surface cover is not as great. The role of the left-stepping bend is discussed below, as its relationship with caldera structure is important.

5.4 Interactions between regional and caldera structures

Long Valley Caldera is a complex volcanic system defined by several stages and styles of volcanic activity. Its present-day caldera structure is subject to ongoing modification due to the interaction between regional structure and the recent magmatic-hydrothermal activity. We now examine the major structures beginning with the topographic margin of the caldera.

The topographic margin is larger than the location of the ring fault due to progressive widening by collapse and erosion (Hildreth, 2004). Excluding Mammoth Mountain, our soil gas measurements from key sites along the topographic margin as well as sites along the approximate position of the ring fault reveal no magmatic gas anomalies. Parts of the margin that are covered by forest show rich vegetation signatures while drier parts display dry vegetation signatures. The tectonomagmatic model of Mammoth Mountain suggests that its location on the southwest topographic margin is a reflection of deep magma intrusions along the calderas ring fracture system (Bailey, 2004; Hill and Prejean, 2005). These fractures provide efficient conduits for the transport of magmatic volatiles to shallow levels where smaller fractures related to the structure of the edifice distribute CO_2 bearing gases along hydrothermal and tree-kill areas such as Horseshoe Lake (Sorey et al., 1998).

The structural and volcanic history of the resurgent dome is important in understanding the present-day distribution of hydrothermal activity. A large majority of the dome is covered and characterized by dry vegetation and rich vegetation soil gas signatures. The southern margin of the resurgent dome is an area of particular interest because it is different from the rest of the dome. Not only is hydrothermal activity focused in this area, but its history of seismicity and uplift is related to fluid flow and hydrothermal CO_2 emissions (Bergfeld et al., 2006). Soil gas samples that plot within the mixing and hydrothermal fields are all located in this region as three large clusters: Casa Diablo, Fumarole Valley, and Hot Creek. These sites are located on major surface expressions of faulting, and their west-east distribution mimics the orientation of the left-stepping fault offset that links the Hilton Creek fault to the Hartley Springs fault.

Leveling surveys and interferometric synthetic aperture radar data suggest that periods of inflation from 1982 to 1999 were centered beneath the resurgent dome with a component of asymmetric uplift (Savage and Cockerham, 1984; Tizzani et al., 2009). Mapping the extent of uplift reveals a steeper gradient along the southern margin of the resurgent dome indicating a higher degree of deformation and rock fracturing in this area. Analogue modeling of caldera resurgence by Acocella et al. (2000) defines the structural margins of resurgent domes as a series of reverse faults which dip steeply toward the center of the dome. Resurgent doming causes these structures to be opened, increasing their permeability and facilitating injection of magma and fluids along the faults (Stix et al., 2003). In the case of the Long Valley resurgent dome, the asymmetric inflation can be thought of as asymmetric trapdoor uplift of the dome along its southern margin (Moon, 1953; Mahood and Hildreth, 1983). Hence, magma and magmatic fluids are mobilized preferentially by the enhanced structural permeability in this area (Figure 9).

By comparing the orientation of resurgence-related faults to the orientation of fault traces mapped using hypocenter locations during the last 30-40years of seismicity in the same region, we see a remarkable degree of similarity. Prejean et al. (2002) mapped several subsurface E-W and WNW-ESE striking strike-slip/normal faults in the south moat which dip steeply to the north-northeast (Figure 9). Hence, this interesting juxtaposition of faults in the southern margin of the resurgent dome and in the south moat includes both east-west trending resurgence-related faults which dip north and tectonic faults which also dip north. As a result, this area represents a zone where the interplay of regional deformation, intrusive uplift, and past resurgence has created a highly fractured and highly permeable setting, suitable for high fluid flow and the formation of shallow hydrothermal zones.

Resistivity studies consider the resurgent dome to be an impermeable structure down to a depth of 2-2.5km (Pribnow et al., 2003; Farrar et al., 2003), consistent with our results that no hydrothermal signatures were detected in the central regions of the dome or over mapped eruptive vents. Because the hydrothermal system is shallow, most fluids tend to flow around the impermeable resurgent dome to the south, where the degree of fracturing and permeability is higher. Soil gas transects of the NW-SE faults along this southern margin reveal magmatic $\delta^{13}C$ anomalies at sites located directly on the fault scarps (Figure 8). This demonstrates that permeability along these faults is high, enabling the ascent of hot fluids and gases from the shallow hydrothermal system. Areas such as Casa Diablo and Fumarole Valley are excellent examples of hydrothermal activity along such structures. Hot Creek on the other hand is located in a zone where the northern extent of the Hilton Creek fault splays and intersects with the left-stepping bend. As a result of this confluence of fault structures, the hydrothermal signatures, as manifested by magmatic $\delta^{13}C$, are not focused along a single fault scarp but instead are more broadly distributed spatially.

The Alkali Lake Springs area represents the easternmost extent of hydrothermal activity in the caldera. Its location does not appear to be related to any obvious volcanic or structural feature. Sampling of fluids from west to east along prominent areas of hydrothermal activity reveals a gradually decreasing Cl content (Sorey et al., 1991; Pribnow et al., 2003), suggesting that Alkali Lake Springs represents a dilute component of hydrothermal fluids carried from west to east by the hydraulic gradient. Soil gas signatures from Alkali Lake that plot within the mixing field, as well as associated low temperatures, suggest that hot hydrothermal fluids rich in magmatic volatiles have mixed with groundwater by the time they reach this area. One sample in the mixing field located on the eastern shore of Lake Crowley demonstrates that trace amounts of hydrothermal fluids are possibly present as far east as the eastern margin of the caldera, at which point they drain into the lake and mix with an abundant freshwater reservoir.

The south moat of the caldera has been subject to high levels of seismicity for more than 30 years, yet no surface manifestations of hydrothermal activity have been observed (Figs. 6 and 9). This seismicity has been attributed to the series of subsurface WNW-ESE oriented normal faults that dip steeply to the north and accommodate slip along the southern caldera block (Hill, 2006). Hypocenter locations associated with these faults define a zone of fractured rock at a depth of 5 to 10 km (Prejean et al., 2002). The south moat is underlain by lacustrine sediments deposited by the Pleistocene age Long Valley Lake and fluvial deposits from erosion of the caldera margins (Bailey et al., 1976). The intracaldera Bishop Tuff is not exposed in this region and was not intersected by a 300 m drill hole, but the unit is reported to be as thick as 1500 m in the caldera (Hildreth and Wilson, 2007). The lacustrine sediments decrease in permeability at 150 m beneath the surface due to the onset of zeolitization and sedimentation (Bailey et al., 1976), and given the substantial thickness of the Bishop Tuff and high temperatures of deposition, the unit is most likely welded. This combination of post caldera sedimentary fill and welded ignimbrite creates an impermeable cap above the southern caldera block. As a result, the lack of surface hydrothermal activity in the south moat is the result of the impermeability imparted by the caldera fill, inhibiting the ascent of fluids and gases to the surface.

6. Conclusions

A total of 223 soil gas samples were collected from sampling sites at Long Valley Caldera in July and August 2012. The objectives of this research were to characterize soil gases along regional faults and volcanic structures (resurgent dome and caldera faults) to explore their controls upon the occurrence of magmatic carbon dioxide gas. We present the following conclusions:

- The Picarro cavity ring-down spectrometer enabled us to perform precise and accurate same day measurements of soil gas compositions (CO_2 vol. %, $\delta^{13}C$) and tailor our sampling strategy on a day-by-day basis. This flexible setup can be applied at other volcanic centers and fracture networks and is suitable for iteratively mapping active and diffuse CO_2 anomalies.

- Carbon dioxide in soil gases in the Long Valley region reflects a mixture of three end-member compositions: magmatic-hydrothermal, atmospheric, and biogenic carbon. On the basis of their CO_2 concentrations and $\delta^{13}C$ compositions, samples plot into hydrothermal, mixing, dry vegetation and rich vegetation fields.

- Deformation along E-W and WNW-ESE trending regional faults, as well as asymmetric resurgent uplift, has formed a zone of highly fractured rock along the southern margin of the resurgent dome. Transects across these faults reveal that they are permeable structures, suitable for fluid flow and the formation of shallow hydrothermal systems.

- The lack of hydrothermal gas signatures in the south moat of the caldera, one of the most seismically active zones in the past 30 years, is likely due to the thick sedimentary and volcanic fill which is impermeable, inhibiting the ascent of magmatic fluids and the formation of shallow hydrothermal systems at the surface.

We propose a model in which volcanic activity associated with intrusive episodes at Mammoth Mountain and along the Inyo-Mono chain of domes has formed a persistent zone of upwelling magmatic fluids beneath the western moat of the caldera. Rising volatiles interact with a shallow hydrothermal system reinforced by groundwater from the Sierra Nevada. The magmatic volatiles are transported from west to east by the hydraulic gradient until they approach the resurgent dome. Given the impermeable nature of most of the resurgent dome, fluid flow is diverted along its southern margin, an ideal setting for fluid transport due to rock fracturing and high permeability associated with subsurface E-W and WNW-ESE trending faults and resurgent uplift. As fluids continue to migrate toward the east, they cluster along several surface expressions of hydrothermal activity including Casa Diablo, Fumarole Valley, Hot Creek and Alkali Lake Springs, finishing their journey at Lake Crowley at which point they mix with an abundant reservoir of fresh water.

Regional faulting and magma intrusion have the potential to expand the network of hydrothermal and degassing zones to now inactive areas such as the interior of the resurgent dome or the Hartley Springs fault system. These, as well as existing areas, are important targets for future geochemical and geophysical studies.

Acknowledgments

The authors would like to thank Brandon Bray and Patrick Beaudry for their assistance in the field. Carbon isotope analyses performed by Barbara Sherwood Lollar and Georges Lacrampe-Couloume at the University of Toronto were instrumental in calibrating and verifying our Picarro measurements. We are grateful for the laboratory facilities and accommodation provided to us by the Sierra Nevada Aquatic Research Laboratory (SNARL). Discussions with Chris Farrar (U.S. Geological Survey) were helpful in the preparatory stages and with planning of sampling locations. We also appreciate discussions with Jeff McKenzie (McGill) on groundwater flow and fluid mixing scenarios. We thank Aaron Van Pelt and Mike Ahern at Picarro Inc. for their assistance with the instrument. We thank Cynthia Werner and one anonymous reviewer for their thoughtful and insightful reviews. This research was made possible with funding to GL from GEOTOP, MAGNET, the Geological Society of America and the Department of Earth and Planetary Sciences, McGill University. This work was also supported by Discovery and CREATE grants to John Stix and in part by a Discovery grant to Boswell Wing, from the Natural Sciences and Engineering Research Council of Canada (NSERC).

References

Acocella, V., F. Cifelli, and R. Funiciello (2000), Analogue models of collapse calderas and resurgent domes, *J. Volcanol. Geotherm. Res.*, *104*(1–4), 81-96, doi:10.1016/S0377-0273(00)00201-8.

Allard, P., et al. (1991), Eruptive and diffuse emissions of CO_2 from Mount Etna, *Nature*, *351*(6325), 387-391, doi:10.1038/351387a0.

Bailey, R. A. (2004), Eruptive history and chemical evolution of the precaldera and postcaldera basalt-dacite sequences, Long Valley, California: implications for magma sources, current seismic unrest, and future volcanism, *Rep.*, 86 pp, Professional Paper 1692, U.S. Geological Survey, Reston, Virginia.

Bailey, R. A., G. B. Dalrymple, and M. A. Lanphere (1976), Volcanism, structure, and geochronology of Long Valley Caldera, Mono County, California, *J. Geophys. Res.*, *81*(5), 725-744, doi:10.1029/JB081i005p00725.

Battaglia, M., P. Segall, and C. Roberts (2003), The mechanics of unrest at Long Valley Caldera, California: 2. Constraining the nature of the source using geodetic and micro-gravity data, *J. Volcanol. Geotherm. Res.*, *127*(3–4), 219-245, doi:10.1016/S0377-0273(03)00171-9.

Battaglia, M., and D. Vasco (2006), The search for magma reservoirs in Long Valley Caldera: Single versus distributed sources, in *Mechanisms of Activity and Unrest at Large Calderas, Spec. Publ*, vol. 269, edited by G. De Natale, C.T. Roise, and C. R. J. Killburn, pp. 173-18, Geol. Soc., London.

Bergfeld, D., and W. C. Evans (2011), Monitoring CO_2 emissions in tree-kill areas near the resurgent dome at Long Valley Caldera, California, *Rep.*, 22 pp.

Bergfeld, D., W. C. Evans, J. F. Howle, and C. D. Farrar (2006), Carbon dioxide emissions from vegetation-kill zones around the resurgent dome of Long Valley Caldera, eastern California, USA, *J. Volcanol. Geotherm. Res.*, *152*(1-2), 140-156, doi:10.1016/j.jvolgeores.2005.11.003.

Bergfeld, D., W. C. Evans, J. F. Howle, and A. G. Hunt (2015), Magmatic gas emissions at Holocene volcanic features near Mono Lake, California, and their relation to regional magmatism, *J. Volcanol. Geotherm. Res.*, *292*, 70-83, doi:10.1016/j.jvolgeores.2015.01.008.

Bray, B. A. (2014), Mafic replenishment of multiple felsic reservoirs at the Mono domes and Mono Lake islands, California, M.Sc. Thesis, McGill University, Montreal.

Brown, S. T., B. M. Kennedy, D. J. DePaolo, S. Hurwitz, and W. C. Evans (2013), Ca, Sr, O and D isotope approach to defining the chemical evolution of hydrothermal fluids: Example from Long Valley, CA, USA, Geochim. Cosmochim. Acta, 122(0), 209-225, doi:http://dx.doi.org/10.1016/j.gca.2013.08.011

Burton, M. R., G. M. Sawyer, and D. Granieri (2013), Deep carbon emissions from volcanoes, *Rev. Mineral. Geochem.*, *75*(1), 323-354, doi:10.2138/rmg.2013.75.11.

Capasso, G., W. D'Alessandro, R. Favara, S. Inguagguato, and F. Parello (2001), Kinetic isotope fractionation of CO_2 carbon due to diffusion processes through the soil, in *Proceedings of the 10th International Symposium on Water Rock Interactions*, edited by R. Cidu, pp. 1497-1499, Italy.

Chiodini, G., A. Baldini, F. Barberi, M. L. Carapezza, C. Cardellini, F. Frondini, D. Granieri, and M. Ranaldi (2007), Carbon dioxide degassing at Latera caldera (Italy): Evidence of geothermal reservoir and evaluation of its potential energy, *Journal of Geophysical Research: Solid Earth*, *112*, B12204, doi:10.1029/2006JB004896.

Chiodini, G., S. Caliro, C. Cardellini, R. Avino, D. Granieri, and A. Schmidt (2008), Carbon isotopic composition of soil CO_2 efflux: A powerful method to discriminate different sources feeding soil CO_2 degassing in volcanic-hydrothermal areas, *Earth Planet. Sci. Lett.*, *274*(3-4), 372-379, doi:10.1016/j.epsl.2008.07.051.

Chiodini, G., R. Cioni, M. Guidi, B. Raco, and L. Marini (1998), Soil CO_2 flux measurements in volcanic and geothermal areas, Appl. Geochem., 13(5), 543-552, doi:10.1016/S0883-2927(97)00076-0.

Chiodini, G., F. Frondini, C. Cardellini, D. Granieri, L. Marini, and G. Ventura (2001), CO_2 degassing and energy release at Solfatara volcano, Campi Flegrei, Italy, *J. Geophys. Res.*, *106*(B8), 16,213-16,221, doi:10.1029/2001jb000246.

Clark, I. D., and P. Fritz (1997), Tracing the carbon cycle, in *Environmental isotopes in hydrogeology*, edited by A. W. Starkweather, pp. 111-134, Lewis Publishers, New York.

Evans, W. C., M. L. Sorey, A. C. Cook, B. M. Kennedy, D. L. Shuster, E. M. Colvard, L. D. White, and M. A. Huebner (2002), Tracing and quantifying magmatic carbon discharge in cold groundwaters: lessons learned from Mammoth Mountain, USA, *J. Volcanol. Geotherm. Res.*, *114*(3–4), 291-312, doi:10.1016/S0377-0273(01)00268-2.

Farrar, C. D., J. M. Neil, and H. L. Howle (1999), Magmatic carbon dioxide emissions at Mammoth Mountain, California, *U.S. Geological Survey Water-Resources Investigations Report 98-4217*, Sacramento, Calif., p. 34.

Farrar, C. D., M. L. Sorey, W. C. Evans, J. F. Howle, B. D. Kerr, B. M. Kennedy, C. Y. King, and J. R. Southon (1995), Forest-killing diffuse CO_2 emission at Mammoth Mountain as a sign of magmatic unrest, *Nature*, *376*(6542), 675-678, doi:10.1038/376675a0.

Farrar, C. D., M. L. Sorey, E. Roeloffs, D. L. Galloway, J. F. Howle, and R. Jacobson (2003), Inferences on the hydrothermal system beneath the resurgent dome in Long Valley Caldera, east-central California, USA, from recent pumping tests and geochemical sampling, *J. Volcanol. Geotherm. Res.*, *127*(3–4), 305-328, doi:10.1016/S0377-0273(03)00174-4.

Farrar, C. D., M. L. Sorey, S. A. Rojstaczer, A. C. Steinemann, and M. D. Clark (1989), Hydrologic and geochemical monitoring in Long Valley Caldera, Mono County, California, 1989, *U.S. Geol. Surv. Water-resources investigations report 89-4033*, p. 69.

Fischer, T. P., G. B. Arehart, N. C. Sturchio, and S. N. Williams (1996), The relationship between fumarole gas composition and eruptive activity at Galeras Volcano, Colombia, *Geology*, *24*, 531-534, doi:10.1130/0091-7613(1996)024<0531:TRBFGC>2.3.CO;2.

Geis, S. (2006), 3 die from toxic gases at California sky resort, in *Nation*, edited by, The Washington Post, Washington, D. C. The Washington Post.

Gerlach, T. M., M. P. Doukas, K. A. McGee, and R. Kessler (1998), Three-year decline of magmatic CO_2 emissions from soils of a Mammoth Mountain Tree Kill: Horseshoe Lake, CA, 1995-1997, *Geophys. Res. Lett.*, *25*(11), 1947-1950, doi:10.1029/98gl01298.

Gerlach, T. M., M. P. Doukas, K. A. McGee, and R. Kessler (2001), Soil efflux and total emission rates of magmatic CO_2 at the Horseshoe Lake tree kill, Mammoth Mountain, California, 1995–1999, *Chem. Geol.*, *177*(1–2), 101-116, doi:10.1016/S0009-2541(00)00385-5.

Giggenbach, W. F., Y. Sano, and H. U. Schmincke (1991), CO_2-rich gases from Lakes Nyos and Monoun, Cameroon; Laacher See, Germany; Dieng, Indonesia, and Mt. Gambier, Australia—Variations on a common theme, *J. Volcanol. Geotherm. Res.*, *45*(3–4), 311-323, doi:10.1016/0377-0273(91)90065-8.

Gilfillan, S. M., et al. (2009), Solubility trapping in formation water as dominant CO_2 sink in natural gas fields, *Nature*, *458*(7238), 614-618, doi:10.1038/nature07852.

Goff, F., H. A. Wollenberg, D. C. Brookins, and R. W. Kistler (1991), A Sr-isotopic comparison between thermal waters, rocks, and hydrothermal calcites, Long Valley Caldera, California, *J. Volcanol. Geotherm. Res.*, *48*(3–4), 265-281, doi:10.1016/0377-0273(91)90046-3.

Granieri, D., M. L. Carapezza, G. Chiodini, R. Avino, S. Caliro, M. Ranaldi, T. Ricci, and L. Tarchini (2006), Correlated increase in CO_2 fumarolic content and diffuse emission from La Fossa crater (Vulcano, Italy): Evidence of volcanic unrest or increasing gas release from a stationary deep magma body?, *Geophys. Res. Lett.*, *33*, doi:10.1029/2006gl026460.

Hildreth, W. (2004), Volcanological perspectives on Long Valley, Mammoth Mountain, and Mono Craters: several contiguous but discrete systems, *J. Volcanol. Geotherm. Res.*, *136*(3-4), 169-198, doi:10.1016/j.jvolgeores.2004.05.019.

Hildreth, W., and C. J. N. Wilson (2007), Compositional zoning of the Bishop Tuff, *J. Petrol.*, *48*(5), 951-999, doi:10.1093/petrology/egm007.

Hill, D. P. (2006), Unrest in Long Valley Caldera, California, 1987-2004, in *Mechanisms of activity and unrest at large calderas*, *Spec. Publ.,* edited by C. Troise, G. D. Natale and C. R. J. Kilburn, pp. 1-24, Geological Society, London.

Hill, D. P., and S. Prejean (2005), Magmatic unrest beneath Mammoth Mountain, California, *J. Volcanol. Geotherm. Res.*, *146*(4), 257-283, doi:10.1016/j.jvolgeores.2005.03.002.

Hilton, D. R. (1996), The helium and carbon isotope systematics of a continental geothermal system: Results from monitoring studies at Long Valley Caldera (California, U.S.A.), *Chem. Geol.*, *127*(4), 269-295, doi:10.1016/0009-2541(95)00134-4.

Hilton, D. R., C. J. Ramirez, R. Mora-Amador, T. P. Fischer, E. Fueri, P. H. Barry, and A. M. Shaw (2010), Monitoring of temporal and spatial variations in fumarole helium and carbon dioxide characteristics at Poas and Turrialba volcanoes, Costa Rica (2001-2009), *Geochem. J.*, *44*(5), 431-440.

Hough, S. E., R. S. Dollar, and P. Johnson (2000), The 1998 earthquake sequence south of Long Valley Caldera, California: hints of magmatic involvement, *Bull. Seismol. Soc. Am.*, *90*(3), 752-763, doi:10.1785/0119990109.

Langbein, J. (1989), Deformation of the Long Valley Caldera, eastern California from mid-1983 to mid-1988: Measurements using a two-color geodimeter, *Journal of Geophysical Research: Solid Earth*, *94*(B4), 3833-3849, doi:10.1029/JB094iB04p03833.

Langbein, J. O. (2003), Deformation of the Long Valley Caldera, California: inferences from measurements from 1988 to 2001, *J. Volcanol. Geotherm. Res.*, *127*(3-4), 247-267, doi:10.1016/s0377-0273(03)00172-0.

Lucic, G., J. Stix, B. Sherwood Lollar, G. Lacrampe-Couloume, A. Muñoz, and M. I. Carcache (2014), The degassing character of a young volcanic center: Cerro Negro, Nicaragua, *Bull. Volcanol.*, *76*(9), doi:10.1007/s00445-014-0850-6.

Mahood, G., and W. Hildreth (1983), Nested calderas and trapdoor uplift at Pantelleria, Strait of Sicily, *Geology*, *11*(12), 722-726, doi:10.1130/0091-7613(1983)11<722:ncatua>2.0.co;2.

Moon, C. G. (1953), Geology of Agua Fria quadrangle, Brewster County, Texas, *Bull. Geol. Soc. Am.*, *64*(2), 151-196, doi:10.1130/0016-7606(1953)64[151:GOAFQB]2.0.CO;2.

Oppenheimer, C. (2003), Volcanic degassing, in *Treatise on geochemistry*, edited by H. D. Holland and K. K. Turekian, pp. 123-166, Pergamon, Oxford.

Prejean, S. (2002), Fault structure and kinematics of the Long Valley Caldera region, California, revealed by high-accuracy earthquake hypocenters and focal mechanism stress inversions, *J. Geophys. Res.*, *107*(B12), 1397, doi:10.1029/2001jb001168.

Pribnow, D., C. Schütze, S. J. Hurter, and C. Flechsig (2003), Fluid flow in the resurgent dome of Long Valley Caldera: implications from thermal data and deep electrical sounding, *J. Volcanol. Geotherm. Res.*, *127*, 329-345, doi:10.1016/S0377-0273(03)00175-6.

Rissmann, C., B. Christenson, C. Werner, M. Leybourne, J. Cole, and D. Gravley (2012), Surface heat flow and CO_2 emissions within the Ohaaki hydrothermal field, Taupo Volcanic Zone, New Zealand, *Appl. Geochem.*, *27*(1), 223-239, doi:10.1016/j.apgeochem.2011.10.006.

Roggensack, K., R. L. Hervig, S. B. McKnight, and S. N. Williams (1997), Explosive basaltic volcanism from Cerro Negro volcano: influence of volatiles on eruptive style, *Science*, *277*, 1639-1642, doi:10.1126/science.277.5332.1639.

Rogie, J. D., D. M. Kerrick, M. L. Sorey, G. Chiodini, and D. L. Galloway (2001), Dynamics of carbon dioxide emission at Mammoth Mountain, California, *Earth Planet. Sci. Lett.*, *188*(3–4), 535-541, doi:10.1016/S0012-821X(01)00344-2.

Sanders, C. O., and S. Collected Reprint (1984), Location and configuration of magma bodies beneath Long Valley, California, determined from anomalous earthquake signals, in *1984, Calderas and Associate Igneous Rocks*, edited, pp. 8287-8302, American Geophysical Union, Washington D.C.

Sanders, C. O., S. C. Ponko, L. D. Nixon, and E. A. Schwartz (1995), Seismological evidence for magmatic and hydrothermal structure in Long Valley Caldera from local earthquake attenuation and velocity tomography, *Journal of Geophysical Research: Solid Earth*, *100*(B5), 8311-8326, doi:10.1029/95JB00152.

Savage, J. C., and R. S. Cockerham (1984), Earthquake swarm in Long Valley Caldera, California, January 1983: Evidence for dike inflation, *J. Geophys. Res.*, *89*(B10), 8315-8324, doi:10.1029/JB089iB10p08315.

Sorey, M. L., W. C. Evans, B. M. Kennedy, C. D. Farrar, L. J. Hainsworth, and B. Hausback (1998), Carbon dioxide and helium emissions from a reservoir of magmatic gas beneath Mammoth Mountain, California, *Journal of Geophysical Research: Solid Earth*, *103*(B7), 15303-15323, doi:10.1029/98JB01389.

Sorey, M. L., B. M. Kennedy, W. C. Evans, C. D. Farrar, and G. A. Suemnicht (1993), Helium isotope and gas discharge variations associated with crustal unrest in Long Valley Caldera, California, 1989–1992, *Journal of Geophysical Research: Solid Earth*, *98*(B9), 15871-15889, doi:10.1029/93JB00703.

Sorey, M. L., V. S. McConnell, and E. Roeloffs (2003), Summary of recent research in Long Valley Caldera, California, *J. Volcanol. Geotherm. Res.*, *127*(3-4), 165-173, doi:10.1016/s0377-0273(03)00168-9.

Sorey, M. L., G. A. Suemnicht, N. C. Sturchio, and G. A. Nordquist (1991), New evidence on the hydrothermal system in Long Valley Caldera, California, from wells, fluid sampling, electrical geophysics, and age determinations of hot-spring deposits, *J. Volcanol. Geotherm. Res.*, *48*(3–4), 229-263, doi:10.1016/0377-0273(91)90045-2.

Stix, J., B. Kennedy, M. Hannington, H. Gibson, R. Fiske, W. Mueller, and J. Franklin (2003), Caldera-forming processes and the origin of submarine volcanogenic massive sulfide deposits, *Geology*, *31*(4), 375-378, doi:10.1130/0091-7613(2003)031<0375:cfpato>2.0.co;2.

Tizzani, P., M. Battaglia, G. Zeni, S. Atzori, P. Berardino, and R. Lanari (2009), Uplift and magma intrusion at Long Valley Caldera from InSAR and gravity measurements, *Geology*, *37*(1), 63-66, doi:10.1130/g25318a.1.

Troll, V. R., D. R. Hilton, E. M. Jolis, J. P. Chadwick, L. S. Blythe, F. M. Deegan, L. M. Schwarzkopf, and M. Zimmer (2012), Crustal CO_2 liberation during the 2006 eruption and earthquake events at Merapi volcano, Indonesia, *Geophys. Res. Lett.*, *39*, L11302, doi:10.1029/2012GL051307.

Werner, C., D. Bergfeld, C. D. Farrar, M. P. Doukas, P. J. Kelly, and C. Kern (2014), Decadal-scale variability of diffuse CO_2 emissions and seismicity revealed from long-term monitoring (1995–2013) at Mammoth Mountain, California, USA, *J. Volcanol. Geotherm. Res.*, *289*, 51-63, doi:10.1016/j.jvolgeores.2014.10.020.

Werner, C., and S. Brantley (2003), CO_2 emissions from the Yellowstone volcanic system, *Geochem. Geophys. Geosyst.*, *4*(7), 1061, doi:10.1029/2002GC000473.

Werner, C., and C. Cardellini (2006), Comparison of carbon dioxide emissions with fluid upflow, chemistry, and geologic structures at the Rotorua geothermal system, New Zealand, *Geothermics*, *35*(3), 221-238, doi:10.1016/j.geothermics.2006.02.006.

White, A. F., M. L. Peterson, H. Wollenberg, and S. Flexser (1990), Sources and fractionation processes influencing the isotopic distribution of H, O and C in the Long Valley hydrothermal system, California, U.S.A, *Appl. Geochem.*, *5*(5–6), 571-585, doi:10.1016/0883-2927(90)90057-C.

Winnett, T., and C. J. Janik (1986), Isotopic composition of carbon in fluids from the Long Valley geothermal system, California, in *Proceedings of the second workshop on hydrologic and geochemical monitoring in the Long Valley Caldera*, edited by M. L. Sorey, C. D. Farrar and H. A. Wollenberg, p. 83.

Figures

Figure 1

Map of the greater Long Valley region displaying major lava dome complexes, the topographic margin of the caldera (dashed line), regional faults (solid lines), and key sampling localities (black dots). Site abbreviations from west to east are HSF (Hartley Springs Fault), EF (Earthquake Fault), CD (Casa Diablo), SM (South Moat), FV (Fumarole Valley), LHC (Little Hot Creek), HC (Hot Creek), HCF (Hilton Creek Fault), and AL (Alkali Lake). Small V symbols represent the locations of active fumarolic vents.

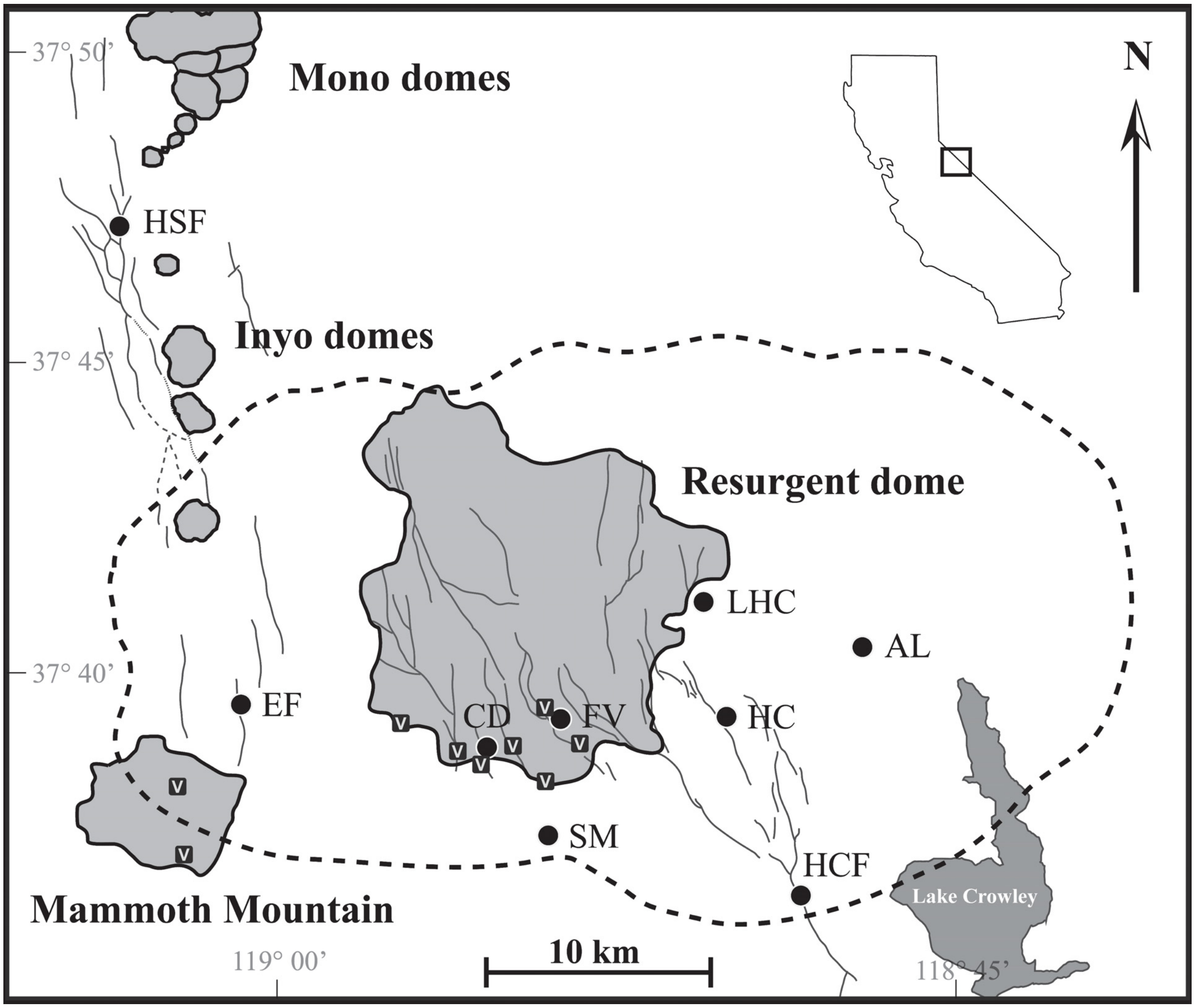
37° 50'
Mono domes
N
HSF
Inyo domes
37° 45'
Resurgent dome
LHC
AL
37° 40'
EF
CD
FV
HC
V
SM
HCF
Lake Crowley
Mammoth Mountain
119° 00'
10 km
118° 45'

Figure 2

Gas standard calibrations using the Picarro cavity ring-down spectrometer and a gas source mass spectrometer at the University of Toronto. (a) Repeat measurements of the same gas standard at different CO_2 concentrations show excellent agreement in $\delta^{13}C$ relative to the reported value of -11.4‰ (dashed line). Errors in measured $\delta^{13}C$ are 2σ. (b) Plot of standards and samples measured by both Picarro cavity ring-down spectrometry and gas source mass spectrometry. There is excellent correspondence between the two datasets.

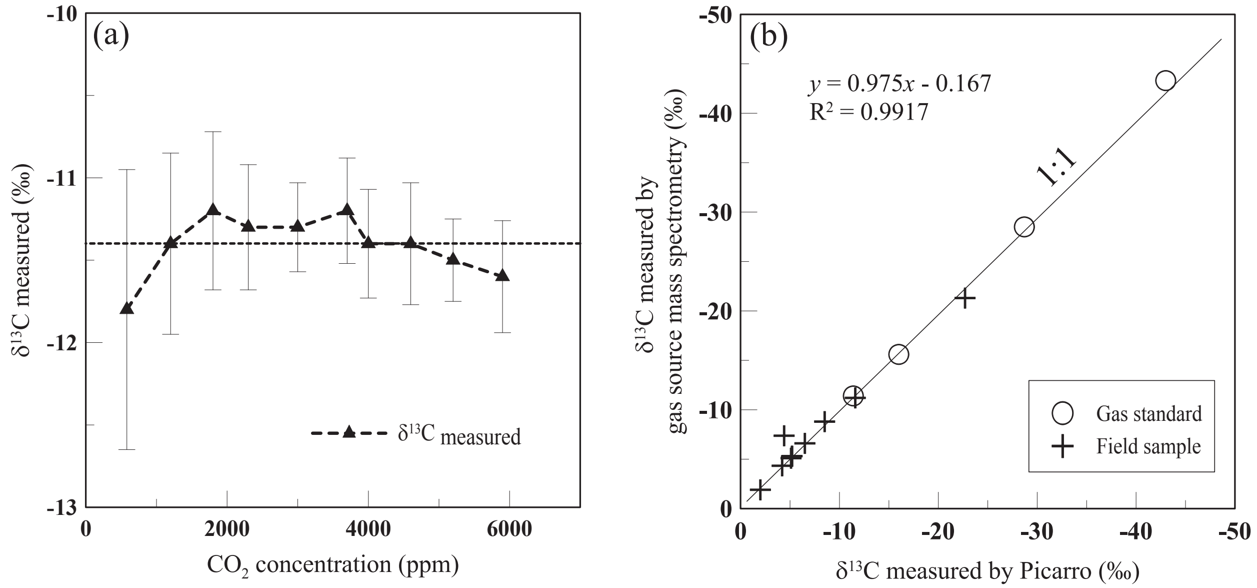
(a)
-10
-11
-12
-13
0
2000
4000
6000
δ13C measured (‰)
CO2 concentration (ppm)
δ13C measured
(b)
y = 0.975x - 0.167
R2 = 0.9917
1:1
-50
-40
-30
-20
-10
0
δ13C measured by gas source mass spectrometry (‰)
δ13C measured by Picarro (‰)
Gas standard
Field sample

Figure 3

Field photographs of representative soil surface types: (a) rich vegetation, (b) dry vegetation, and (c) hydrothermal. Photos were taken at the resurgent domes interior, the north caldera floor, and Fumarole Valley, respectively.

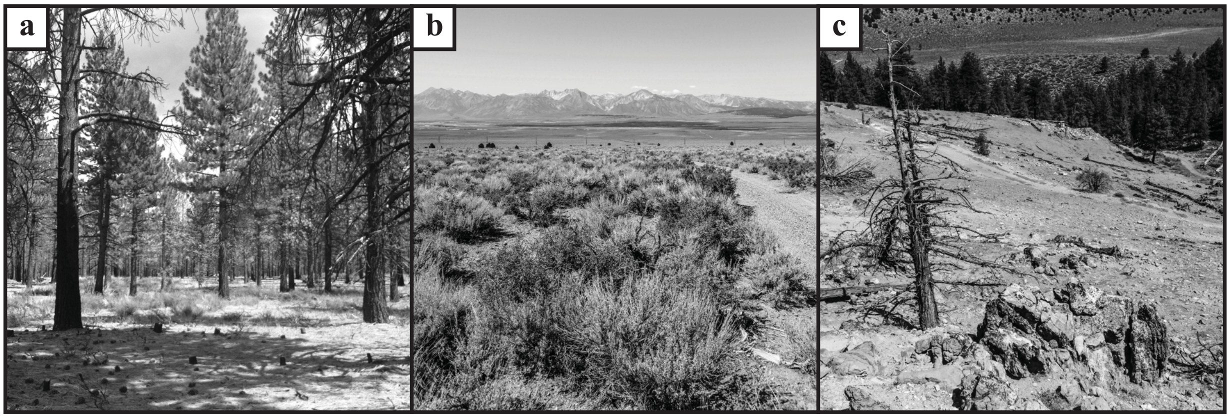
a
b
c

Figure 4

(a) CO_2 concentration and (b) $\delta^{13}C$ soil depth profiles of rich vegetation, dry vegetation, and hydrothermal soil surface types. Two depth profiles per surface type were measured at various sites, for a total of six profiles. White circles represent individual measurements at 10cm intervals. Sampling locations are LV76, LV30, LV213, LV67, LV25, and LV166 for hydrothermal, dry vegetation, and rich vegetation, respectively (see Table S1).

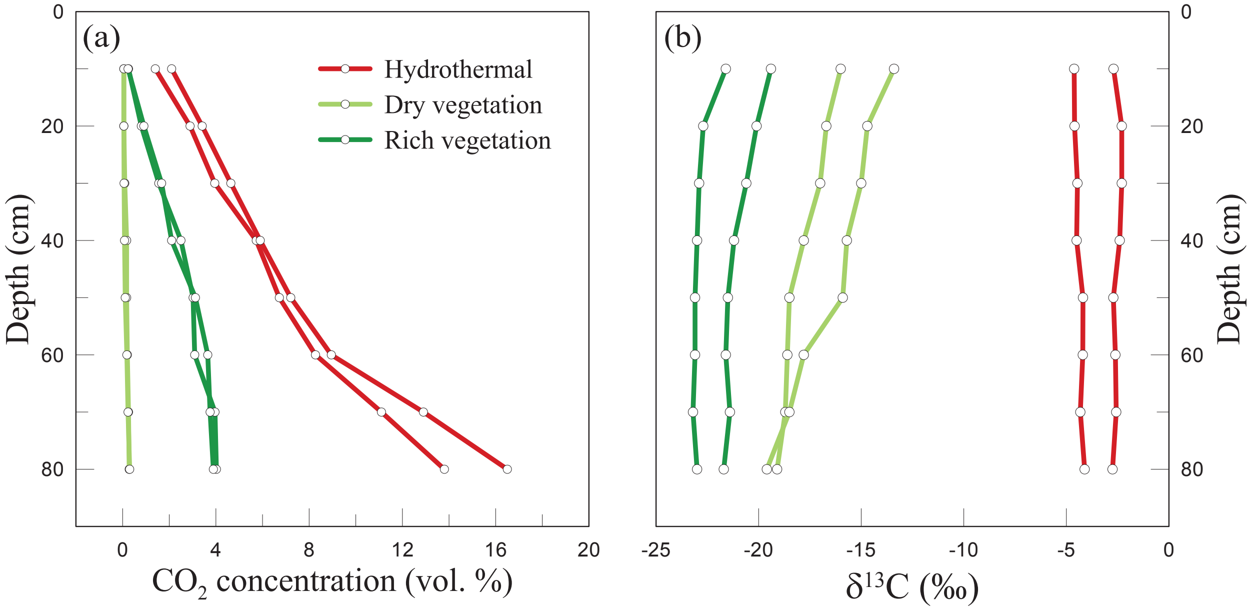
(a)
Hydrothermal
Dry vegetation
Rich vegetation
Depth (cm)
0
20
40
60
80
0
4
8
12
16
20
CO$_2$ concentration (vol. %)
(b)
-25
-20
-15
-10
-5
0
δ^{13}C (‰)
Depth (cm)

Figure 5

Three-component mixing diagram of soil gas samples with CO_2 concentrations plotted against $\delta^{13}C$ compositions. End-members are defined as A (atmospheric), B (biogenic), and H (hydrothermal). Samples are divided into hydrothermal (red), mixing (orange), dry vegetation (light green), and rich vegetation (dark green) fields. Solid lines represent mixing paths between principal end-members. The grey fields show expanded mixing paths between the lightest and heaviest end-member compositions.

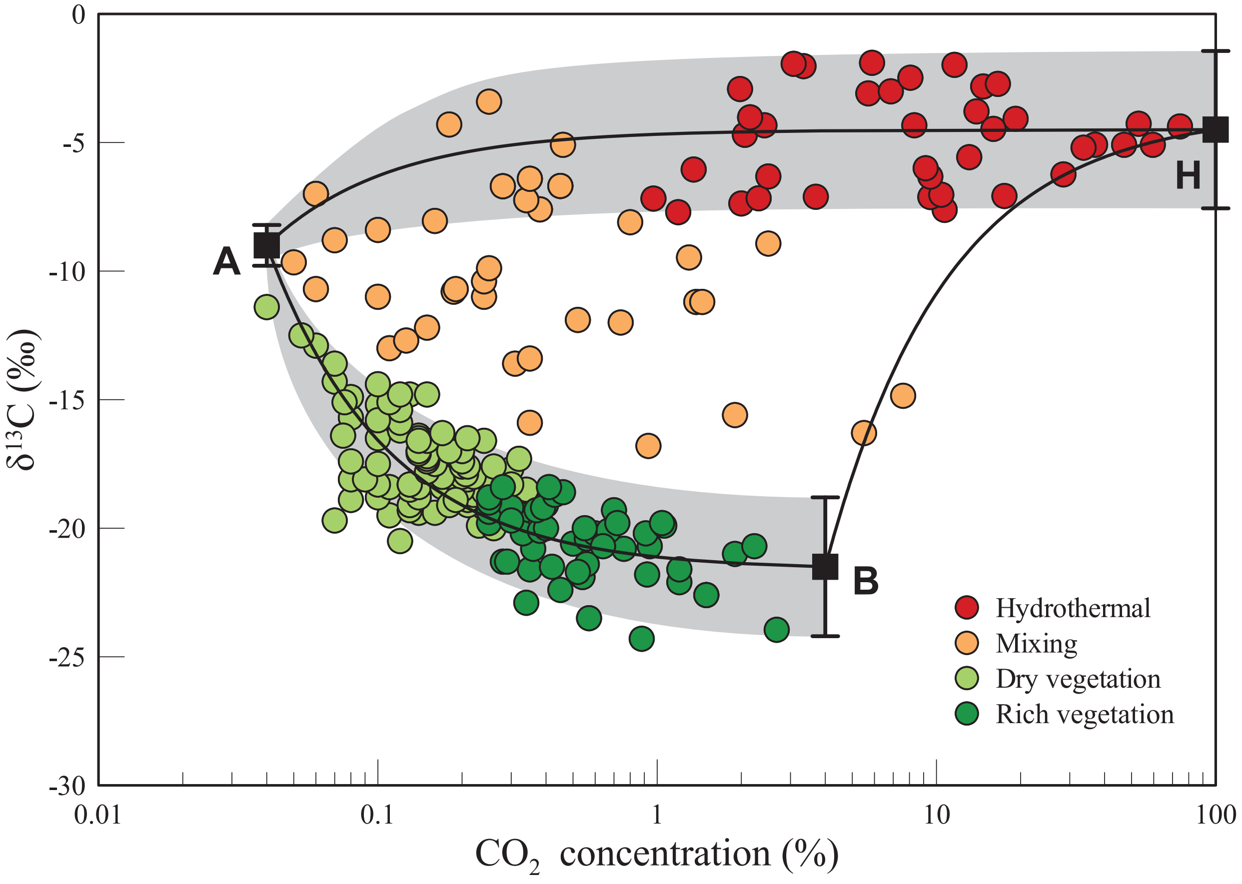

0
-5
-10
-15
-20
-25
-30
δ13C (‰)
0.01
0.1
1
10
100
CO2 concentration (%)
A
B
H
Hydrothermal
Mixing
Dry vegetation
Rich vegetation

Figure 6

Plot of temperature versus $\delta^{13}C$ for samples in the hydrothermal and mixing fields. Individual samples are color coded based on their CO_2 concentration. Circled samples represent a cluster of sites located on Mammoth Mountain. Samples bounded by a rectangle represent a series of sites from Casa Diablo, Fumarole Valley, and Hot Creek that exhibit anomalous temperature and $\delta^{13}C$ values.

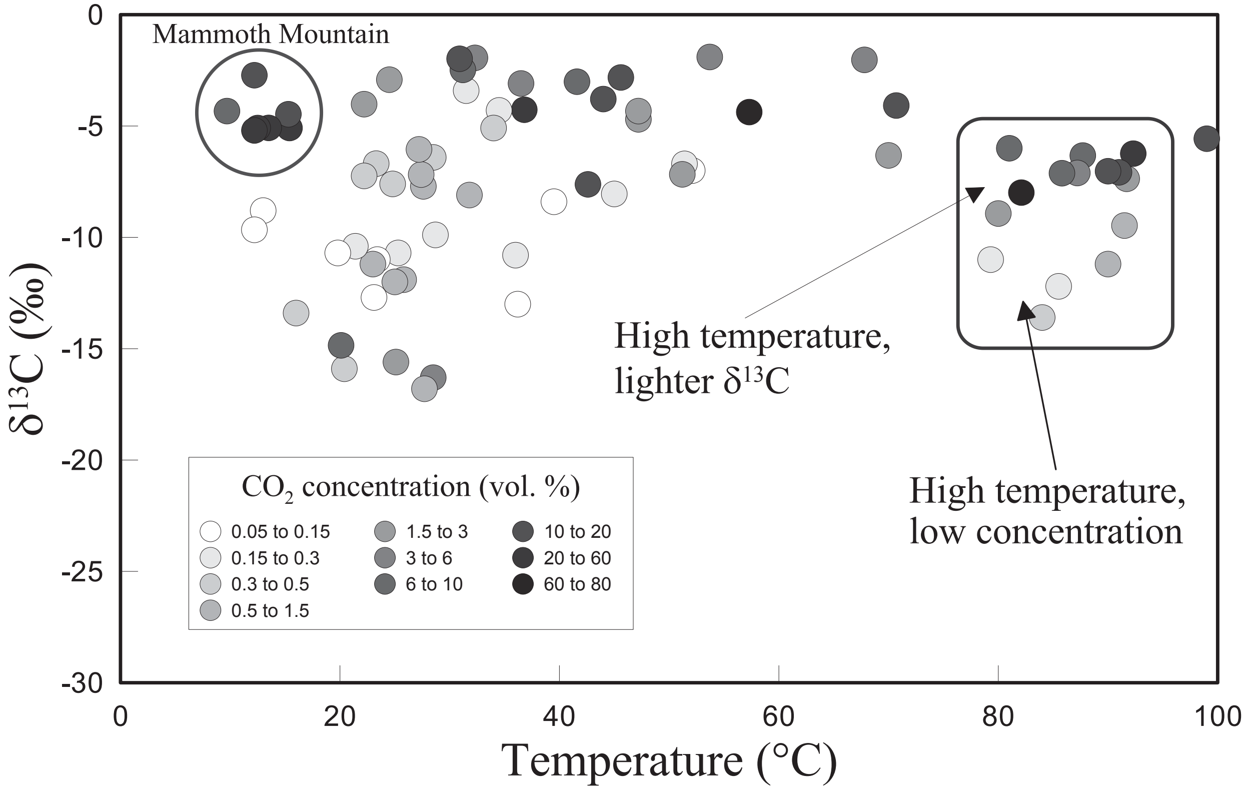
Mammoth Mountain
High temperature,
lighter δ13C
High temperature,
low concentration
CO2 concentration (vol. %)
0.05 to 0.15
0.15 to 0.3
0.3 to 0.5
0.5 to 1.5
1.5 to 3
3 to 6
6 to 10
10 to 20
20 to 60
60 to 80
δ13C (‰)
0
-5
-10
-15
-20
-25
-30
Temperature (°C)
0
20
40
60
80
100

Figure 7

(a) Areal distribution of dry and rich vegetation sites in Long Valley Caldera. (b) Distribution of hydrothermal and mixing, which are restricted to Mammoth Mountain and the southern margin of the resurgent dome. Unlike samples in Figure 7a, they occur predominantly in close proximity to E-W and NW-SE surface expressions of faulting (grey lines). (HSF=Hartley Springs Fault and HCF=Hilton Creek Fault)

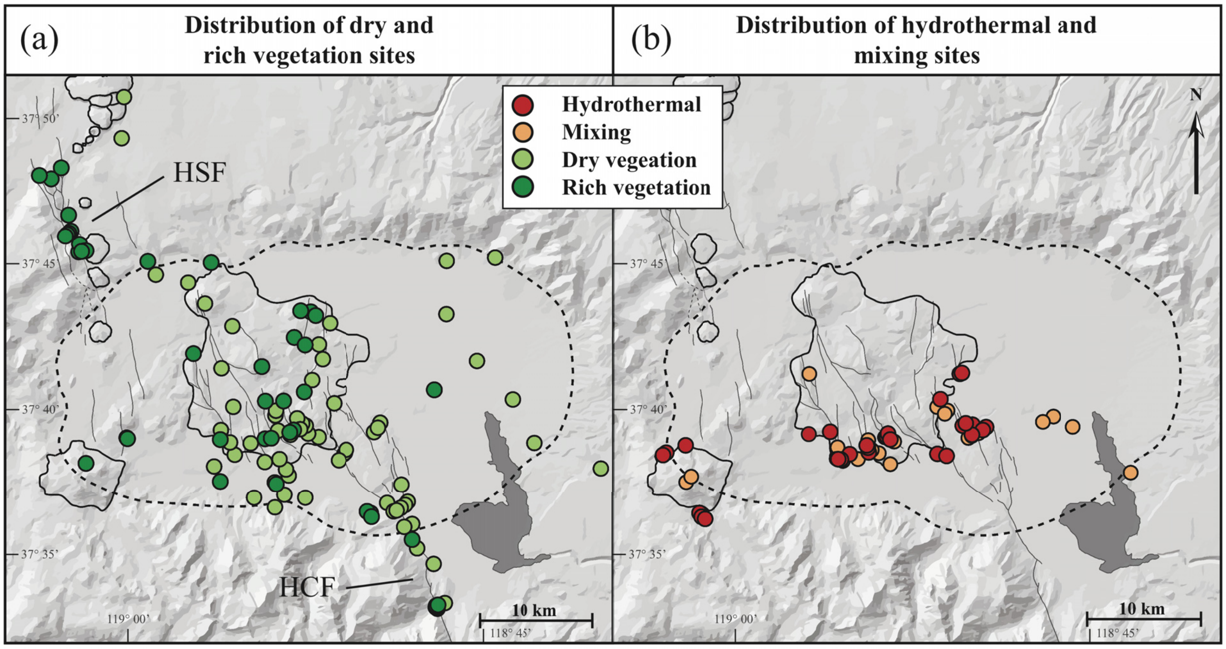
(a)
Distribution of dry and rich vegetation sites
(b)
Distribution of hydrothermal and mixing sites
Hydrothermal
Mixing
Dry vegeation
Rich vegetation
HSF
HCF
N
37° 50'
37° 45'
37° 40'
37° 35'
119° 00'
118° 45'
10 km
10 km

Figure 8

Transects across prominent fault traces at localities along the south margin of the resurgent dome and the Hartley Springs and Hilton Creek regional fault systems to the NW and SE, respectively. Samples marked in red represent transects that display a heavy $\delta^{13}C$ anomaly at the fault trace. Samples marked in black represent transects that display a light $\delta^{13}C$ anomaly at the fault trace.

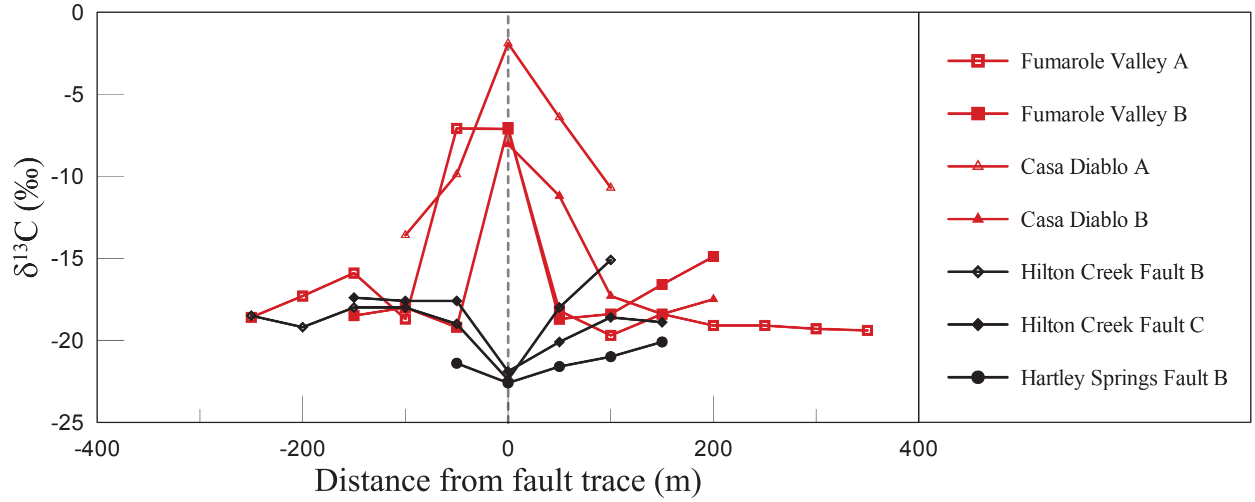
0
-5
-10
-15
-20
-25
$\delta^{13}C$ (‰)
-400
-200
0
200
400
Distance from fault trace (m)
Fumarole Valley A
Fumarole Valley B
Casa Diablo A
Casa Diablo B
Hilton Creek Fault B
Hilton Creek Fault C
Hartley Springs Fault B

Figure 9

A conceptual model for the formation of hydrothermal areas within the caldera. (a) Select epicenter locations (grey dots) from 1997 to 1998 (Hill, 2006) reveal the presence of subsurface E-W and WNW-ESE striking, north dipping normal and strike-slip faults. The permeability of these zones is enhanced by deformation associated with the asymmetric uplift of the resurgent dome (shown in green) following two recent intrusive episodes (Savage and Cockerham, 1984; Tizzani et al., 2009). (b) These structures act as permeable pathways for the migration of magmatic fluids sourced from the west moat (blue arrows) toward the east around the otherwise impermeable resurgent dome (Pribnow et al., 2003). Hydrothermal and mixing gas samples (red and orange circles, respectively) are focused along this deformed and permeable southern margin of the resurgent dome (CD=Casa Diablo, FV=Fumarole Valley and HC=Hot Creek). (c) A schematic cross section across the southern margin of the resurgent dome from west to east that illustrates the interplay between fluids and permeable structures (after Brown et al., 2013). The layered Bishop Tuff and overlying caldera fill (Sorey et al., 1991) enable the lateral flow of fluids that rise to the surface only when regional and volcanic faults provide suitable pathways. Some downward percolation of meteoric fluids along these structures is likely (Pribnow et al., 2003).

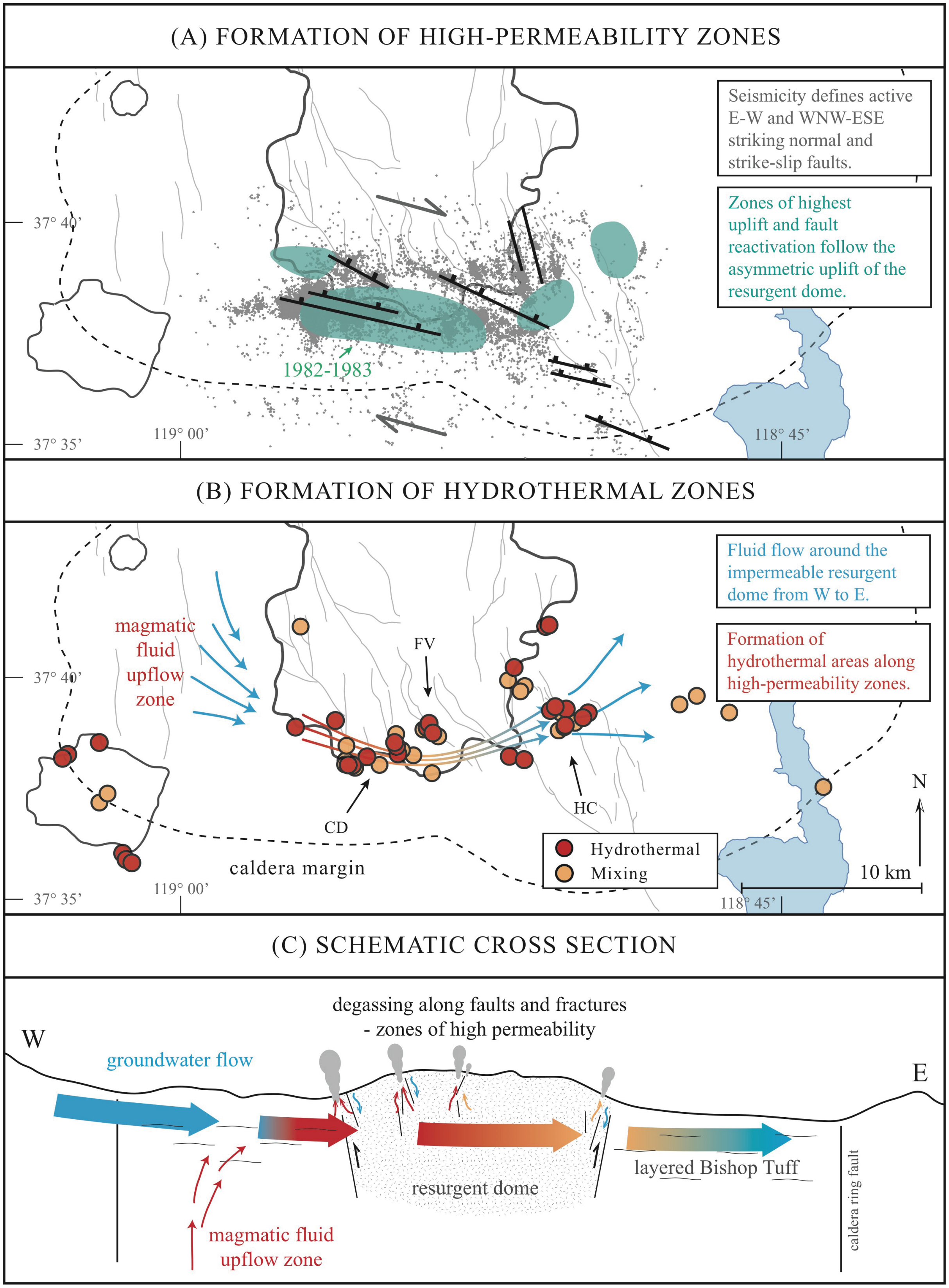

(A) FORMATION OF HIGH-PERMEABILITY ZONES

(B) FORMATION OF HYDROTHERMAL ZONES

(C) SCHEMATIC CROSS SECTION

Appendix 1

Supplementary Table 1. CO_2 concentration, temperature and carbon isotope data for soil gases collected in July-August, 2012. H_2S data collected in June, 2014.

Sample ID	Locality	Lat.	Long.	CO_2 (vol. %)	Temp. (°C)	$\delta^{13}C$ (‰)	H_2S (ppm)
Hydrothermal							
LV66	Casa Diablo	330659	4168254	8.1	31	-2.5	
LV104	E Casa Diablo	331774	4168513	2.5	70	-6.3	
LV105	E Casa Diablo	331738	4168411	13.1	99	-5.6	1
LV107	Fish Creek	335875	4168323	11.6	31	-2.0	
LV111	Fish Creek	336456	4168220	10.4	90	-7.0	
LV26	Horse Shoe Lake	321492	4164871	37.0	14	-5.1	
LV27	Horse Shoe Lake	321545	4164703	47.0	15	-5.1	
LV28	Horse Shoe Lake	321719	4164573	16.0	15	-4.5	
LV3	Hot Creek	338725	4169780	2.4	47	-4.3	
LV9	Hot Creek	328434	4169616	70.0	82	-8.0	20
LV95	Hot Creek	338615	4169591	6.9	42	-3.0	
LV96	Hot Creek	338664	4169724	2.1	47	-4.7	
LV1	Hot Creek	338813	4169920	9.5	88	-6.3	
LV17	Little Hot Creek	337387	4173090	10.7	43	-7.6	
LV150	Mammoth Mountain	320857	4167223	16.6	12	-2.7	
LV153	Mammoth Mountain	320607	4169080	8.3	10	-4.3	
LV154	Mammoth Mountain	319280	4168532	59.5	13	-5.1	
LV155	Mammoth Mountain	319462	4168641	33.6	12	-5.2	
LV123	Mono Domes	321623	4199285	1.0	27	-7.2	
LV124	Mono Domes	321630	4199292	1.2	28	-7.7	
LV50	SW Fumarole Valley	332910	4169410	9.5	86	-7.1	
LV51	SW Fumarole Valley	332956	4169331	28.5	92	-6.2	
LV54	SW Fumarole Valley	333098	4169165	2.3	51	-7.2	
LV6	SW Fumarole Valley	332888	4169548	3.7	87	N/A	
LV7	SW Fumarole Valley	332845	4169498	2.0	92	-7.4	
LV8	SW Fumarole Valley	332857	4169427	17.5	91	-7.1	
LV212	Tuffa Towers Beach	322479	4201126	1.4	27	-6.1	
LV30	W Casa Diablo	329965	4168211	19.2	71	-4.1	
LV32	W Casa Diablo	329837	4168085	88.9	90	-5.3	> 76
LV33	W Casa Diablo	329717	4168045	2.2	22	-4.0	
LV35	W Casa Diablo	329401	4169769	9.2	81	-6.0	
LV76	W Casa Diablo	330018	4168097	14.5	54	-1.9	

LV78	W Casa Diablo	330022	4168035	3.1	32	-1.9	
LV85	W Casa Diablo	330016	4168226	3.3	68	-2.0	
LV86	W Casa Diablo	330005	4168287	14.7	46	-2.8	
LV87	W Casa Diablo	329993	4168346	5.7	37	-3.1	
LV138	W Hot Creek	336144	4171603	13.9	44	-3.8	
LV144	W Hot Creek	337449	4170012	2.0	25	-2.9	
LV145	W Hot Creek	337594	4169941	74.5	57	-4.4	7
LV147	W Hot Creek	337999	4169998	53.0	37	-4.3	
Mixing							
LV137	Alkali Lake	344036	4169678	5.5	29	-16.3	
LV202	Alkali Lake	342823	4170355	1.9	25	-15.6	
LV116	Aqua Dome	343012	4179907	0.2	n/a	-11.4	
LV214	Bishop	360673	4145473	1.5	23	-11.2	
LV201	E Caldera	348171	4168725	0.0	24	-12.9	
LV120	E Caldera Floor	347499	4166833	0.7	25	-12.0	
LV121	E Caldera Rim	352116	4167142	0.1	25	-15.2	
LV100	E Casa Diablo	331588	4169116	1.4	90	-11.2	
LV101	E Casa Diablo	331652	4168908	0.2	45	-8.1	
LV102	E Casa Diablo	331714	4168814	2.5	80	-8.9	
LV106	E Casa Diablo	331754	4167959	0.4	24	-16.6	
LV81	E Casa Diablo	333027	4167457	0.1	25	-14.3	
LV82	E Casa Diablo	332894	4167656	0.3	86	-12.2	
LV83	E Casa Diablo	332647	4168083	0.1	23	-16.4	
LV84	E Casa Diablo	332250	4168380	1.3	92	-9.5	2
LV103	E Casa Diablo	331724	4168720	70.0	95	N/A	
LV114	Fish Creek	336633	4168441	0.1	25	-16.6	
LV115	Fish Creek	336692	4168521	0.1	24	-14.9	
LV37	Fumarole Valley	334008	4169915	0.3	22	-17.0	
LV195	Hilton Creek Fault	340318	4165282	0.1	23	-14.8	
LV2	Hot Creek	338757	4169834	0.3	51	-6.7	
LV90	Hot Creek	338024	4169144	0.1	30	-14.4	
LV91	Hot Creek	338159	4169234	0.0	40	-8.4	
LV92	Hot Creek	338283	4169310	0.1	36	-13.0	
LV93	Hot Creek	338401	4169372	0.1	29	-14.8	
LV99	Hot Creek	338044	4168857	0.1	23	-12.7	
LV89	Hot Creek	337883	4169029	0.0	32	-3.4	
LV94	Hot Creek	338506	4169471	0.1	35	-4.3	20
LV96	Hot Creek	338664	4169724	0.1	52	-7.0	
LV5	Little Alkali Spring	342206	4170032	7.6	20	-14.9	

LV148	Mammoth Mountain	320560	4166814	0.2	13	-8.8
LV149	Mammoth Mountain	320528	4166833	0.2	12	-9.7
LV152	Mammoth Mountain	321139	4167921	0.1	11	-20.0
LV151	Mammoth Mountain	320909	4167488	64.3	81	-14.6
LV125	Mono Domes	323733	4190271	0.2	23	-16.3
LV117	N Caldera Floor	342927	4176676	0.0	30	-13.6
LV69	N Casa Diablo	328185	4173236	0.5	16	-13.4
LV118	NE Caldera Floor	344714	4173751	0.3	30	-15.7
LV15	NE Fumarole Valley	333750	4170547	0.3	19	-16.5
LV12	NE Fumarole Valley	334406	4169596	0.0	24	N/A
LV217	ORMAT	332716	4169362	0.3	20	-15.9
LV223	ORMAT	330993	4167965	65.3	94	N/A
LV53	SW Fumarole Valley	333028	4169162	0.5	26	-11.9
LV55	SW Fumarole Valley	333153	4169039	0.2	79	-11.0
LV34	W Casa Diablo	329147	4169790	0.1	22	-14.8
LV36	W Casa Diablo	329713	4169106	0.0	20	-10.7
LV71	W Casa Diablo	330102	4168196	0.2	25	-10.7
LV75	W Casa Diablo	329853	4168141	0.3	N/A	-13.6
LV77	W Casa Diablo	330063	4168105	0.3	29	-6.4
LV79	W Casa Diablo	330035	4167965	0.4	25	-7.6
LV80	W Casa Diablo	329942	4168088	0.2	29	-9.9
LV88	W Casa Diablo	329981	4168416	0.1	23	-11.0
LV29	W Casa Diablo	329701	4168165	62.0	92	N/A
LV31	W Casa Diablo	329976	4168148	70.0	89	N/A
LV32	W Casa Diablo	329837	4168085	59.5	93	N/A
LV72	W Casa Diablo	330036	4168163	0.4	34	-5.1
LV139	W Hot Creek	335842	4171183	0.9	28	-16.8
LV140	W Hot Creek	335863	4171125	0.2	21	-10.4
LV141	W Hot Creek	336016	4171387	0.3	22	-17.7
LV142	W Hot Creek	336390	4170861	0.8	32	-8.1
LV143	W Hot Creek	336304	4170814	0.4	23	-6.7
LV146	W Hot Creek	337672	4169900	0.2	22	-7.2
Dry Vegetation						
LV191	Big Spring	329021	4179931	0.2	9	-19.4
LV21	Dry Creek	329992	4176103	0.0	20	-15.1
LV119	E Caldera Floor	346916	4171357	0.2	25	-18.3
LV122	E Outside Caldera	357901	4166031	0.1	25	-17.2
LV156	Earthquake Fault	323563	4169404	0.1	5	-19.9
LV108	Fish Creek	336236	4168009	0.3	19	-18.5

LV109	Fish Creek	336315	4168085	0.1	25	-18.0
LV112	Fish Creek	336514	4168288	0.2	26	-18.7
LV113	Fish Creek	336566	4168361	0.2	25	-18.4
LV110	Fish Creek	336395	4168164	0.4	25	-19.2
LV135	HCF Church	339171	4165200	0.2	22	-17.1
LV127	Hilton Creek Fault	340062	4163734	0.2	22	-18.5
LV128	Hilton Creek Fault	340170	4163811	0.2	24	-19.2
LV129	Hilton Creek Fault	340251	4163811	0.1	20	-18.0
LV130	Hilton Creek Fault	340346	4163837	0.1	22	-19.0
LV132	Hilton Creek Fault	340470	4163857	0.1	23	-18.0
LV133	Hilton Creek Fault	340527	4163934	0.0	26	-15.1
LV134	Hilton Creek Fault	340602	4163984	0.0	25	-15.4
LV158	Hilton Creek Fault	342090	4158699	0.2	21	-17.4
LV159	Hilton Creek Fault	342140	4158808	0.2	20	-17.6
LV160	Hilton Creek Fault	342185	4158899	0.1	20	-17.6
LV161	Hilton Creek Fault	342347	4159105	0.1	18	-18.9
LV162	Hilton Creek Fault	342279	4159015	0.2	19	-18.6
LV167	Hilton Creek Fault	341838	4161507	0.2	22	-17.8
LV168	Hilton Creek Fault	340889	4162505	0.2	22	-18.7
LV196	Hilton Creek Fault	340197	4165186	0.1	24	-18.3
LV197	Hilton Creek Fault	340084	4165113	0.1	23	-18.9
LV198	Hilton Creek Fault	339963	4165025	0.1	24	-17.4
LV199	Hilton Creek Fault	339862	4164961	0.1	25	-19.7
LV200	Hilton Creek Fault	339739	4164888	0.1	22	-18.1
LV97	Hilton Creek Fault	338808	4170087	0.1	28	-15.9
LV65	Little Antelope Valley	334756	4172829	0.1	16	-18.4
LV22	Lookout Mountain	328381	4177504	0.0	23	-18.3
LV126	Mono Domes	323397	4187860	0.0	22	-16.4
LV4	N Caldera	345948	4180113	0.0	18	-17.9
LV10	NE Fumarole Valley	334052	4170194	0.1	20	-18.5
LV11	NE Fumarole Valley	334136	4169974	0.1	20	-18.3
LV13	NE Fumarole Valley	335019	4169367	0.1	26	-15.8
LV14	NE Fumarole Valley	334277	4170052	0.2	29	-17.4
LV38	NE Fumarole Valley	333875	4169863	0.2	21	-18.0
LV41	NE Fumarole Valley	333532	4169695	0.2	22	-19.4
LV42	NE Fumarole Valley	333422	4169642	0.2	23	-19.3
LV43	NE Fumarole Valley	333309	4169582	0.2	24	-19.1
LV44	NE Fumarole Valley	333201	4169540	0.2	23	-18.4
LV46	NE Fumarole Valley	332982	4169441	0.2	26	-18.2
LV60	NE Resurgent Dome	335865	4176250	0.2	24	-18.1

LV63	NE Resurgent Dome	335144	4174963	0.3	22	-18.8
LV64	NE Resurgent Dome	335426	4174065	0.1	19	-18.8
LV194	NW Caldera	325443	4179405	0.2	20	-19.9
LV218	ORMAT	332527	4169300	0.1	20	-17.3
LV220	ORMAT	332112	4169224	0.1	18	-17.5
LV222	ORMAT	331701	4169084	0.2	21	-17.3
LV67	Smokie Bear	329943	4171271	0.2	17	-17.6
LV68	Smokie Bear	329238	4173607	0.0	19	-19.1
LV213	SNARL	339446	4164667	0.3	24	-18.5
LV203	South Moat	333150	4167040	0.0	20	-16.5
LV204	South Moat	332331	4165079	0.1	21	-19.2
LV205	South Moat	332572	4166565	0.0	25	-16.5
LV207	South Moat	331087	4165694	0.1	25	-18.8
LV208	South Moat	332934	4165886	0.0	25	-18.1
LV209	South Moat	334171	4165608	0.1	25	-17.5
LV210	South Moat	328712	4167638	0.1	25	-19.5
LV211	South Moat	329286	4166607	0.1	25	-20.5
LV47	SW Fumarole Valley	332416	4170807	0.2	20	-17.0
LV48	SW Fumarole Valley	332470	4170998	0.2	22	-16.9
LV56	SW Fumarole Valley	332639	4169727	0.0	16	-16.2
LV73	W Casa Diablo	329895	4168242	0.1	19	-16.6
LV74	W Casa Diablo	329885	4168338	0.1	18	-17.0
LV136	Whitmore Spring	340061	4166356	0.0	26	-17.0
Rich Vegetation						
LV16	Big Alkali Lake	342349	4172004	0.9	13	-24.3
LV190	Big Spring	329101	4179855	0.6	18	-20.4
LV215	Bishop	352777	4158371	0.4	22	-19.5
LV157	Earthquake Fault	323658	4169404	0.5	17	-20.6
LV39	Fumarole Valley	333765	4169812	0.3	20	-18.8
LV40	Fumarole Valley	333641	4169744	0.3	22	-19.1
LV45	Fumarole Valley	333090	4169493	0.4	22	-19.7
LV20	Gilbert Peak	331935	4173607	0.3	20	-20.0
LV170	Hartley Springs Fault	321392	4180943	0.4	14	-21.5
LV171	Hartley Springs Fault	321349	4180926	1.2	15	-22.1
LV172	Hartley Springs Fault	321319	4180936	0.9	17	-20.2
LV173	Hartley Springs Fault	321280	4180930	0.9	16	-20.7
LV174	Hartley Springs Fault	321225	4180928	1.0	16	-19.8
LV175	Hartley Springs Fault	321183	4180928	0.6	13	-20.2
LV176	Hartley Springs Fault	321133	4180906	0.7	15	-19.3

LV177	Hartley Springs Fault	320248	4181974	1.5	7	-22.6
LV178	Hartley Springs Fault	320199	4181933	0.6	11	-21.4
LV179	Hartley Springs Fault	320346	4182017	0.5	10	-21.6
LV180	Hartley Springs Fault	320432	4182106	1.9	12	-21.0
LV181	Hartley Springs Fault	320531	4182178	0.7	13	-20.1
LV185	Hartley Springs Fault	318726	4185804	0.5	14	-19.1
LV186	Hartley Springs Fault	319962	4186039	1.1	15	-19.9
LV187	Hartley Springs Fault	319400	4185290	0.8	15	-20.8
LV188	Hartley Springs Fault	320414	4183131	0.9	13	-21.8
LV189	Hartley Springs Fault	320989	4181368	2.2	13	-20.7
LV131	Hilton Creek Fault	340419	4163846	0.3	23	-22.4
LV163	Hilton Creek Fault	342208	4158936	0.4	19	-20.1
LV164	Hilton Creek Fault	342201	4158922	0.5	16	-21.9
LV165	Hilton Creek Fault	342243	4158844	1.5	15	-22.6
LV166	Hilton Creek Fault	342299	4158732	3.8	15	-21.6
LV169	Hilton Creek Fault	340782	4162874	0.4	14	-22.9
LV98	Hot Creek	338869	4170218	0.3	23	-19.8
LV18	Little Antelope Spring	334438	4171976	0.4	18	-23.5
LV70	N Casa Diablo	327782	4174522	0.3	19	-20.0
LV19	N Fumarole Valley	333200	4171518	0.4	19	-20.7
LV57	NE Resurgent Dome	334365	4176948	0.3	22	-18.4
LV58	NE Resurgent Dome	334908	4176881	0.3	23	-20.2
LV59	NE Resurgent Dome	335255	4176655	0.3	23	-18.9
LV61	NE Resurgent Dome	333908	4175344	0.4	20	-20.8
LV62	NE Resurgent Dome	334543	4174894	0.3	18	-19.3
LV192	NW Caldera	327383	4178841	0.7	17	-19.8
LV193	NW Caldera	325147	4180150	0.3	17	-19.2
LV216	ORMAT	332841	4169406	0.3	22	-18.7
LV219	ORMAT	332359	4169307	0.4	18	-18.6
LV221	ORMAT	331895	4169229	0.3	18	-18.4
LV23	SNARL	338318	4164456	0.1	20	-21.3
LV24	SNARL	338109	4164573	0.3	16	-21.7
LV25	SNARL	338273	4164575	0.1	23	-21.3
LV206	South Moat	332601	4166417	2.7	16	-24.0
LV49	SW Fumarole Valley	332122	4171564	0.3	16	-19.0
LV52	SW Fumarole Valley	332975	4169282	0.3	22	-19.4

GPS datum WGS 84, UTM, Zone 11S

Errors: Concentration (± 0.01 % at 0-9 % and ± 0.1 % at 10-100 %), Temperature (± 0.1°C), $\delta^{13}C$ (±0.5 ‰), H_2S (±1 ppm)

Appendix 2

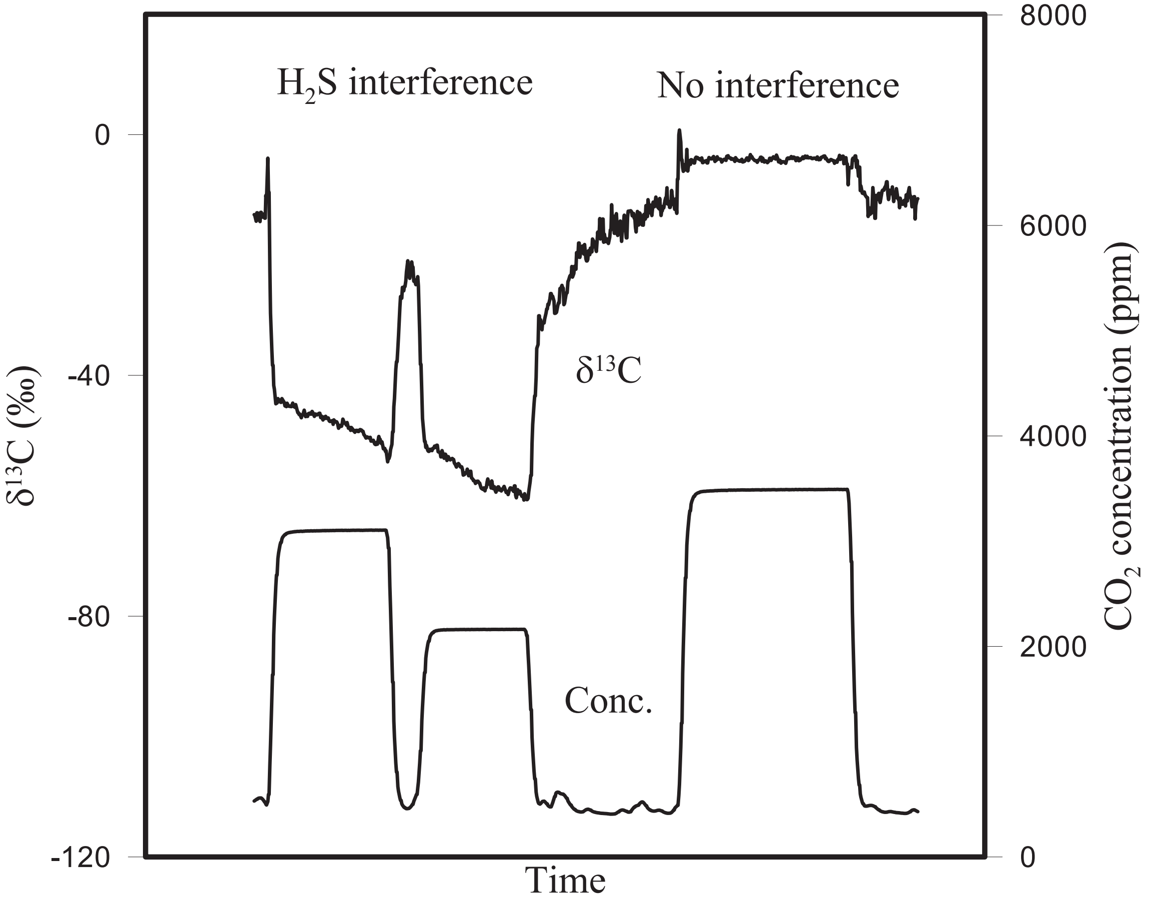

Supplementary Figure 1. Continuous measurements of three field samples from the Casa Diablo power-plant area. All three samples display flat concentration plateaus, but only one displays a flat δ^{13}C profile. The negative δ^{13}C slope of the first two samples is characteristic of 1-2 ppm of H$_2$S interference.

Link to Chapter 2

In Chapter 1, I highlight how both regional and volcanic structures contribute to the permeability of a volcanic system. Magmatic gases reaching the surface are not released from a central conduit, but instead are distributed over a wider area via an intricate network of faults and fractures. These structures vary in size and morphology, and their permeability may change with time under the influence of caldera and regional tectonics. I highlight that at the surface our measurements of stable carbon isotopes can be affected by contributions from atmospheric and biogenic sources of carbon. Is is therefore essential that all possible contributions to gases are characterized when a new area is being investigated, so that surface influences are not mistaken for changes occurring in the magmatic-hydrothermal system.

In the following chapter, I expand on the characterization of soil and fumarolic gases by complementing stable carbon isotopes with helium, oxygen and deuterium isotopes, as well as measurements of CO_2 soil flux. This study of active and diffuse degassing at Cerro Negro volcano in Nicaragua sheds light on the variability of these isotopes systems in both space and time. I use this dataset to identify primary degassing conduits on the main volcanic edifice as well as secondary conduits on its flanks. Using this soil gas characterization, I am able to recognize that despite its small size, Cerro Negro is an efficient conduit for the release of magmatic gas from great depth and perhaps even the mantle. Variations in the isotopic composition of these gases may serve as powerful indicators of change within the subsurface plumbing network, and they may signify the arrival of new magma in the future.

Chapter 2

The degassing character of a young volcanic center: Cerro Negro, Nicaragua

Gregor Lucic[1], John Stix[1], Barbara Sherwood Lollar[2], Georges Lacrampe-Couloume[2], Angélica Muñoz[3], Martha Ibarra Carcache[3]

[1] Department of Earth and Planetary Sciences, McGill University, 3450 University Street, Montreal, QC, H3A 0E8, Canada
[2] Department of Earth Sciences, University of Toronto, 22 Russell Street, Toronto, ON, M5S 3B1, Canada
[3] Instituto Nicaragüense de Estudios Territoriales (INETER), Frente a Hospital Solidaridad. Apartado postal 2110, Managua, Nicaragua

---

Manuscript II – published as:

Lucic, G., J. Stix, B. Sherwood Lollar, G. Lacrampe-Couloume, A. Muñoz, and M. I. Carcache (2014), The degassing character of a young volcanic center: Cerro Negro, Nicaragua, *Bull. Volcanol.*, *76*(9), doi:10.1007/s00445-014-0850-6

Abstract

Cerro Negro volcano is a young basaltic cinder cone which is part of the Nicaraguan volcanic arc. Eruptive activity at Cerro Negro is characterized by explosive strombolian to subplinian eruptions driven by volatile-rich basaltic magma ascending rapidly from various crustal depths (>15 to 6 km) resulting in the onset of precursory activity only ~30 minutes before an eruption. In this paper we present a comprehensive degassing characterization of the volcano over a 4-year period aimed at improving our understanding of the magmatic plumbing network and its relationship with regional tectonics. A total of 124 individual soil gas samples were collected between 2010 and 2013 and analyzed for stable carbon isotopes ($\delta^{13}C$) from CO_2. High-temperature fumaroles were sampled for $\delta^{18}O$, δD and $^3He/^4He$ isotope analysis, and major degassing zones were mapped using soil CO_2 flux measurements. Gases at Cerro Negro are characterized by a strong $^3He/^4He$ mantle signature (6.3 to 7.3 R_A), magmatic $\delta^{13}C$ ratios (-2.3 to -3.0 ‰), meteoric $\delta^{18}O$ and δD ratios, and stable CO_2 fluxes (31 t d^{-1}). The lack of $\delta^{13}C$ fractionation, and an increase in the relative mantle component from 2002 to 2012 suggests that the volatile flux at Cerro Negro originates from the mantle and ascends to the surface via a series of crustal fractures that act as permeable conduits. Despite the lack of new eruptions, the hydrothermal system of Cerro Negro continues to evolve due to seasonal inputs of meteoric water, slope failures that expose and bury sites of active degassing, and bursts of regional seismicity that have the potential to open up new conduits for gas release as well as magma. Continuing geophysical and geochemical monitoring of the main edifice and the recently formed south zone is essential, as the volcano remains overdue to erupt.

1. Introduction

Our ability to reduce loss of life due to volcanic hazards is dependent on our ability to recognize complex processes that drive eruptions. Despite technological and theoretical advances, our network of early-warning techniques remains unreliable. While part of this unreliability stems from our lack of data and understanding, a large part can be attributed to the inherently unpredictable behavior of volcanoes. To complicate matters even more, there are certain volcanoes that display little to no precursory activity. Eruptions from these types of volcanoes are extremely difficult to forecast. Hence warnings of an impending eruption are very short. Cerro Negro in Nicaragua and Hekla in Iceland are two examples of such problematic volcanoes that exhibit precursory activity only 30 minutes to 1-2 hours prior to an explosive eruption.

Volcanic gases are useful indicators of magmatic and hydrothermal activity as they provide a window into processes operating at depth. Increased SO_2 gas emissions before the 1991 Pinatubo eruption were attributed to renewed magmatic activity (Dagg et al., 1996). During the 2000 Miyakejima caldera-forming eruption, SO_2 emissions provided constraints on the size of the magma body, and the onset of degassing showed a close relationship between magma ascent and caldera collapse (Kazahaya et al., 2004). Stable carbon isotopes collected from summit gases at Merapi before the 2006 eruption showed a trend towards more ^{13}C-enriched values from devolatization of crustal carbonates by newly intruded magma (Troll et al., 2012). These and other studies have shown that changes in the volcano's degassing character occur due to a variety of magmatic and physical processes (Fischer et al., 1997; Hilton et al., 2010; Chiodini et al., 2008; Shinohara et al., 2008; Oppenheimer et al., 2011; Sparks et al., 2012). In this paper we explore the potential application of carbon dioxide gas and its stable isotopes as an indicator of magmatic activity. CO_2 is an important volatile component in magmas. Due to its low solubility, it is commonly one of the first volatile species to begin degassing (Blundy et al., 2010; Chiodini et al., 2011). At volcanic centers where traditional real-time monitoring techniques are unable to detect changes in the magmatic plumbing network, and at centers where precursory activity is rare, the early release of CO_2 from depth is potentially a powerful indicator of upcoming eruptions or other changes in volcanic activity (Aiuppa et al., 2007).

The motivation for this paper is to determine the degassing character of Cerro Negro volcano, to characterize the style of gas release from the volcano, and to identify changes in its magmatic and hydrothermal system that might occur prior to an eruption. To increase the chances of detecting such changes, we selected Cerro Negro as it may be overdue for eruption and has a history of volatile-driven eruptions. We present four datasets collected over a period of four years (2010, 2011, 2012, 2013). Soil gas samples demonstrate how spatial and temporal variability in stable carbon isotopes ($\delta^{13}C$) might arise due to magma chamber degassing and migration of magmatic gas sources beneath Cerro Negro. Measurements of soil CO_2 flux help identify magmatic and structural controls on the locations of degassing zones. Oxygen and hydrogen isotopes ($\delta^{18}O$, δD) collected from condensate and water samples identify the major sources of water in the hydrothermal system. Helium isotopes ($^3He/^4He$) obtained from fumarole gases constrain relative source carbon contributions. These combined datasets are used to characterize the degassing character of Cerro Negro. Such an approach can be applied to other shield and scoria cone volcanoes where short warning times prior to an eruption pose an ongoing challenge.

We propose a model for Cerro Negro that is characterized by a homogeneous magma source located deep within the crust or the upper mantle. Long-term monitoring of fumarolic gases shows little variation in $\delta^{13}C$ through time, consistent with a continuous supply of gas via an interconnected network of faults and fractures resulting from N-S striking extension. Regional stress fields exert an important control on the permeability of these conduits, restricting or enabling the ascent of magma and gas, creating new zones of degassing, and shutting off others. These volcano-tectonic interactions are important drivers at Cerro Negro and possibly other volcanoes in the region.

2. Cerro Negro volcano

Cerro Negro is a young, 350 m high basaltic cinder cone that represents one of the most active volcanic centers in the Nicaraguan volcanic arc (Figure 1). It first appeared in April 1850, and since then the volcano has erupted 23 times with an average recurrence interval of one eruption every 5 years over the last 50-year period. In the last 70 years eruptions tend to occur in clusters of 3 to 4 over a span of 5 years, separated by longer quiescent periods. Eruptions are strombolian and sub-plinian in nature, tend to be low-moderate intensity (VEI 1-3), feature blocky aa flows and can produce 7 km high eruptive columns (Hill et al., 1998; McKnight, 1995; McKnight and Williams, 1997, Courtland et al., 2012). Quiescent periods between eruptions are distinct for their lack of seismicity and deformation. In the past, poor seismic coverage from one station and yearly CO_2 flux measurements were able to resolve precursory activity in the form of increased seismicity and degassing only 30 minutes to ~1 hour prior to the onset of eruption. In response, the monitoring network has been expanded and as of May, 2014 consists of 5 seismic stations and 2 continuous, 7 semi-continuous and 4 episodic GPS stations (Geirsson, 2014, pers.

comm.). Temperature and CO_2 flux measurements are collected from fumaroles in the main crater on a bi-monthly basis by the Instituto Nicaragüense de Estudios Territoriales (INETER).

Basaltic volcanism is commonly associated with effusive, low-intensity eruptions, yet Cerro Negro is a basaltic system that has experienced frequent violent, explosive eruptions. The energetic nature of the 1992 eruption has been attributed to magma with high volatile contents (maximum H_2O 6.08 wt. %, CO_2 1040 ppm) that rapidly ascended to the surface from a depth of 6 km (Roggensack et al., 1997). This event contrasts with the 1995 effusive eruption that was fueled by magma that underwent a higher degree of degassing through a slower ascent rate, resulting in lower volatile contents before erupting from a depth of 1-2 km. It is believed that the primary source of magma is located at a depth of 10-15 km (Roggensack et al., 1997; Portnyagin et al., 2012).

While degassing dynamics control magmatic overpressure and explosivity, the tectonic setting may facilitate eruption triggers through modifications to the local stress regime (Manga and Brodsky, 2006). Cerro Negro is the youngest manifestation of volcanic activity in a N-S alignment of cinder cones called the Cerro La Mula-Cerro Negro alignment (Figure 2) (McKnight and Williams, 1997). This volcanic lineament, along with other prominent volcanic centers such as the Managua graben (Girard and van Wyk de Vries, 2005), formed due to extension in the upper crust enabled by N-S trending faults and fractures that accommodate trench-parallel dextral shear within the Nicaraguan forearc (Figure 1) (LaFemina et al., 2002). The low-volume, low-intensity 1999 effusive eruption at Cerro Negro was a result of static stress changes along one such N-S fracture system that squeezed magma towards the surface by a combination of contraction at depth and extension at the surface, similar to the toothpaste analogy (Diez et al., 2005; LaFemina et al., 2004). The eruption was centered on the southern flank of Cerro Negro at a secondary vent called the Cristo Ray crater (Figure 2). It was accompanied by the formation of a new thermal anomaly located 1 km south of this crater, a zone we refer to as the south zone of hydrothermal activity (Zone S, Figure 2). Volcanic activity has been gradually moving southward along the Cerro La Mula-Cerro Negro alignment, and this anomaly represents the southernmost extent of volcanic activity along this alignment.

Cerro Negro has been the site of five previous degassing studies. The first study mapped out a ^{222}Rn anomaly in soil gases that was attributed to a degassing pulse during the initial stages of the low-energy, low-volume 1995 eruption (Connor et al., 1996). The second study looked at diffuse CO_2 gas emissions and presented a $\delta^{13}C$ characterization of soil gases of the main volcanic edifice, highlighting zones of elevated CO_2 flux along discrete fissures (Salazar et al., 2001). The third study examined regional helium-carbon relationships along the Nicaragua-Costa Rica volcanic arc and concluded that $^3He/^4He$ ratios in Nicaragua have MORB-like values with He-CO_2 systematics indicating an increased component of slab-derived carbon to the magmatic supply beneath Nicaragua (Shaw et al., 2003, 2006). The fourth study reported nitrogen abundances and isotope ratios from geothermal gases, thermal waters and vapor condensates, and concluded that nitrogen content in volcanic gases is higher than previously estimated due to sediment-derived volatile contributions from the subducting slab (Elkins et al., 2006). The fifth is an ongoing degassing study by Barrancos et al. (2013) to measure how CO_2 fluxes on Cerro Negro's main cone evolve in space and time.

3. Methods

3.1 Sampling sites

Sampling took place in September 2010, January 2011, January-February 2012 and May 2013 at three principal localities on and around Cerro Negro that correspond to three zones of hydrothermal activity (Figure 2). Active degassing is used to describe prominent degassing features such as fumaroles and sites where gases can be seen rising from the soil. Diffuse degassing is used to describe areas where no gases can be seen, but there are surface indications of elevated CO_2 concentrations (e.g., vegetation kill, mineral precipitation). The first locality is part of the Cerro La Mula volcanic complex, located 0.9-1.3 km north of Cerro Negro's main vent (Zone N). This zone consists of a series of eroded cinder cones that vary in size and age. There is no historic record of volcanic activity from Cerro La Mula since Cerro Negro formed in 1850. At present the area is experiencing active and diffuse degassing along a series of small fractures associated with the cones in this zone. There is one major fumarole, an area of hydrothermal alteration, a number of surface thermal anomalies (>35°C) and several minor areas of vegetation kill. The vegetation in this area is mostly grass with a few sparsely forested areas.

The second locality is the main edifice of Cerro Negro volcano (Zone C). Sampling here was divided into three sub-zones. The first sub-zone is located on the central cone, displays heavy hydrothermal alteration of soils and rocks, secondary mineral precipitation of calcite and sulfur, several thermal anomalies and is experiencing both active and diffuse degassing. The second sub-zone comprises part of the outer crater and is the largest and most prominent hydrothermal zone in the study area. It has two large fumaroles (Figure 2), active and diffuse degassing, extensive secondary mineral precipitation, chemical alteration and several thermal anomalies. Hydrothermal activity in this zone is controlled by a prominent NE-SW fracture that is visible due to a series of slope failures. The third sub-zone is the Cristo Rey crater which was formed on the south flank of Cerro Negro during the 1968 eruption. At present this area consists of two larger craters 50 m in diameter and a smaller crater 15 m in diameter. Minor diffuse degassing and a few small thermal anomalies are observed in this area. However, there is evidence of past chemical alteration and mineral precipitation.

The third locality is the southern zone of hydrothermal activity that formed during the 1999 eruption series (Zone S). LaFemina et al. (2004) proposed that extension and offset of surface blocks led to the development of a NW-SE trending fracture system. This fracture penetrated a possible pre-existing shallow geothermal system associated with the Las Pilas – El Hoyo volcanic complex (Figure 1). The result was a new hydrothermal zone approximately ~16,300 m^2 in size and distinguished from its surroundings by intense to moderate vegetation kill. At present the zone is experiencing active and diffuse degassing, has several thermal anomalies and a central zone of chemical alteration and mineral precipitation. Zone S is surrounded by a combination of forest, bush and grasslands. The central part of zone S, ~1,400 m^2 in size, is devoid of vegetation and has several small yet visible actively degassing areas. There is no evidence of eruptive activity at zone S.

Soil gas and soil flux sampling covered zones N, C, S as well as background sites away from the volcano, while helium, oxygen and deuterium isotope samples were collected at the two largest fumaroles located in zone C (Figure 2). These fumaroles were selected for their high gas fluxes, high CO_2 concentrations, and high temperatures.

3.2 Carbon isotopes

Soil gas measurements were made using a 1 m-long titanium-alloy soil probe connected to a portable gas monitor using Tygon tubing. We used an ADC Systems landfill analyzer that measures CO_2 concentrations (error: ± 0.01 % at 0-9 % and ± 0.1 % at 10-100 %; all vol. %), and a Crowcon gas analyzer that measures CO_2 (vol. %, ±0.01%) and H_2 (ppm, ± 1 ppm). Soil temperatures were collected using an Omega thermocouple (°C, ± 0.1°C).

Soil gas samples were collected between 30 and 90 cm depth in order to minimize atmospheric gas contamination (Camarda et al., 2007). Gases were extracted from the soil using a syringe and injected into 30 cm^3 culture tubes, evacuated to 150 millitorr and pretreated with 0.2 μl of $HgCl_2$ to prevent bacterial respiration and eliminate any isotopic fractionation while in storage. In addition to collecting duplicate samples at important sampling sites to test for reproducibility, we collected samples at different times of the day and at the end of a 1-month field campaign to test for natural variability in soil gas emissions. Gas samples were analyzed at the University of Toronto's Stable Isotope Lab for $\delta^{13}C$ values using a Finnigan MAT gas source mass spectrometer paired to a gas chromatograph combustion interface with a continuous flow through system. Carbon isotope ratios were determined by comparing international (NBS 18 and NBS 19) and in-house standards, and each gas sample was analyzed three times to quantify the analytical precision (±0.1‰). All $\delta^{13}C$ values reported in this paper are relative to V-Pee Dee Belemnite (V_{PDB} = 0‰).

3.3 *Soil CO_2 flux*

For soil flux sampling we used two (16.1 and 6.1 liters) modified 5-gallon water containers depending on whether fluxes were high or low. These chambers were designed for return-flow sampling using a low flow rate to minimize the effects of soil permeability (Camarda et al., 2007) and had a pressure release valve and built-in thermocouple to measure air temperature inside the chamber (Chiodini et al., 1998). The ADC gas analyzer and thermocouple recorded CO_2 concentrations and temperatures, respectively, at 15 s (at high flux sites) and 30 s (at low flux sites) time intervals. Sampling stopped when CO_2 concentrations began to plateau, signifying that chamber saturation had occurred. Multiple measurements at a single site were conducted to ensure good reproducibility in the accumulation of gas within the chamber. The final soil flux value (g m^{-2} d^{-1}) was obtained using the mean temperature inside the chamber and calculated using the following equation:

$$flux_{CO_2} = \left(\frac{\Delta_{CO_2}}{\Delta_t}\right) \times \left(\frac{1}{M_{Air}}\right) \times \left(M_{CO_2}\right) \times \left(V_c\right) \times \left(\frac{1}{A_c}\right) \times \left(\frac{0.348 \times P_{Air}}{T_{Air}}\right) \times \left(\frac{1000\ mg}{g}\right) \times \left(10^{-6}\ ppm\right) \qquad (1)$$

where $\frac{\Delta_{CO_2}}{\Delta_t}$ is the slope obtained from plotting the change in CO_2 concentration (ppm) versus time (t, min), M_{Air} is the molecular weight of air (g mol^{-1}), M_{CO_2} is the molecular weight of CO_2 (g mol^{-1}), V_c is the chamber volume (l), A_c is the chamber area (m^2), P_{Air} is barometric air pressure (mbar), and T_{Air} is the temperature of air in the chamber (K). Three soil flux measurements were collected at every site to ensure good reproducibility. For each one of these measurements we used low, high and mean chamber temperatures in equation 1. This gave us a total of 9 flux values per measurement site. These values were then averaged into a single soil flux value representative of that site. The majority of sites are reproducible on the order of ±15%.

Contour maps of CO_2 flux were constructed using our sample location map combined with field observations of active degassing and zones of recent vegetation kill. Areas that were not covered by flux sites were assessed in terms of their proximity to major zones of degassing, surface alteration and mineral precipitation, visible degassing and vegetation cover. These considerations were taken into account when making the final contour map. We selected two prominent areas of vegetation kill in zone S and determined their perimeters using a portable GPS unit (Garmin GPSMAP 62s) that calculated surface areas. The graphic representations of these two areas were used as references for calculating the surface areas of our contour maps.

3.4 Oxygen and deuterium isotopes

Water condensates were collected from two of the main fumaroles (Figure 2, fumaroles A and B) using a glass pyrex condenser, a thermos bottle filled with ice and positive gas flow through the system. Collection took place from high temperature, high CO_2 concentration fumaroles where positive gas flow could be established, minimizing the need for manual pumping and atmospheric contamination. Samples were stored in special glass containers that removed any excess air in order to eliminate fractionation between bubbles of atmospheric gas and the sample. An additional background water sample was collected from a local freshwater well located 8 km from Cerro Negro’s main cone (zone C). The analyses were conducted at the Université du Québec à Montréal (UQAM) in the stable isotope laboratory. The water samples were analyzed using a Micromass Isoprime dual inlet mass spectrometer paired to an Aquaprep particle size analysis water preparation system (errors: $\delta^{18}O$ vs VSMOW = ±0.05 ‰, δD vs. VSMOW = ±1 %).

3.5 *Helium isotopes*

A total of four gas samples were collected for helium isotope analysis. Duplicates were collected from the same two fumaroles used for oxygen and deuterium sampling (fumaroles A and B). The same sampling criteria of high CO_2 concentration and positive gas flow were applied. The gas samples were stored in 1/4 in. diameter copper tubes to prevent helium diffusion and clamped with refrigeration clamps in order to prevent leakage and contamination with atmospheric gas. Gas samples were analyzed at the Scripps Institution of Oceanography using a MAP215E noble gas mass spectrometer (errors: $\delta^{13}C$ = ±0.5‰, $^{3}He/^{4}He$ = ±0.17-0.22 at $2\boldsymbol{\sigma}$ uncertainty, $CO_2/^{3}He$ = ±5%).

4. Results

4.1 *Carbon isotopes*

Over a four-year period (2010-2013), a total of 124 soil gas samples were collected and analyzed for stable carbon isotopes (Tables 1, 2, 3 and Figure 3). $\delta^{13}C$ ratios for all three zones range between -0.7‰ and -10‰, with four samples between -10 ‰ to -32.8 ‰ (Figure 4). The majority of samples cluster between -2‰ to -5.5 ‰, with a large peak in the -3 to -3.5‰ range, and a mean $\delta^{13}C$ ratio of -4.2 ‰ for the entire field area over the four-year period. $\delta^{13}C$ ratios at hydrothermal areas located within zone N range between -2.5 ‰ to -4.5 ‰, with a background soil gas ratio of -19.4 ‰. Zone C is characterized by a wide spread of data in 2010 (-3.5 ‰ to -

9.5 ‰), a tight cluster in 2011 (-1.5 ‰ to -5 ‰), and a prominent peak in 2012 (-2.5 ‰ to -3.5 ‰) accompanied by a range of more depleted $\delta^{13}C$ values as low as -9.7 ‰. At zone S, both the 2011 and the 2012 datasets display a large range in $\delta^{13}C$ values (-0.9 ‰ to -10.3 ‰ in 2011; -0.8 ‰ to -33 ‰ in 2012, Figure 4), with major clusters in 2011 (-2.5 ‰ to -3 ‰) and 2012 (-3 ‰ to -3.5 ‰). Resampling of key hydrothermal areas from zones C and S in 2013 shows a tight grouping of values around -2.7 ‰ and an average value of -3.5 ‰ for zone C and -3.5 ‰ for zone S. The long-term mean $\delta^{13}C$ ratio is -4.6 ‰ at zone N (3 years of sampling), -4.0 ‰ at zone C (4 years) and -4.3 ‰ at zone S (3 years). Repeat sampling of hydrothermal zones reveals little short-term variation in $\delta^{13}C$ from successive samples (~15 min, -3.1 ‰ vs. -3.2 ‰) and over the duration of a sampling campaign (~20 days, -2.9 ‰ vs. -2.6 ‰).

Variability in the number of sampling sites for each zone is a byproduct of our sampling strategy that focused on zones of hydrothermal activity; since the scale of activity varies among the zones, so does the number of samples from each zone. Spatial distribution and variability of $\delta^{13}C$ ratios within the hydrothermal areas are also a function of scale. Many adjacent sampling sites are separated by 5 to 10 m and display changes of 1.0 to 1.5 ‰. Rarely, adjacent sites located in zones C and S display changes as large as 3‰. Sites located on the margins of hydrothermal areas and in close proximity to vegetation tend to display larger variations in $\delta^{13}C$ ratios. Major hydrothermal features such as fumaroles, sites of active degassing and mineral precipitation, and areas with high concentrations of CO_2 (>30 %) tend to show lower $\delta^{13}C$ variability in space (Figure 4b). To assess long-term (2010-2013) temporal variability in carbon isotopes, 7 key hydrothermal sites at zone C were selected for repeat measurements (Table 4). The largest change is observed between September 2010 (7 sites, mean -6.7 ‰) and January 2011 (-3.3 ‰) with a strong trend towards heavier isotopic signatures from September to

January. A change in isotopic trends among these 7 sites is not evident for January 2011 (-3.3 ‰), January 2012 (-3.6 ‰) and May 2013 (-3.7 ‰). In addition, these small changes fall within the short-term temporal variability of the hydrothermal system from repeat samples within a single sampling campaign. In 2011, 2012 and 2013 repeat samples were extended to zones N and S, yet no long-term trends were observed (Table 4).

4.2 Temperature and CO_2 concentration

Temperatures within sampling zones range from 30°C to 100°C. Temperatures higher than 100°C are associated with prominent hydrothermal features such as fumaroles A and B in zone C (240°C and 220°C, respectively, in 2010). There is a tight cluster of points in zone C and zone S from 80°C to 100°C. A secondary cluster of samples from zone S ranges between 40°C and 60°C. Long-term temperature trends in the field area which include prominent hydrothermal zones show a steady decrease in temperature from 2010 to 2013. Fumaroles A and B show a 4-year decrease in temperature from 240°, 180°, 145° to 90°C and from 221°, 270°, 155° to 100°C, respectively. The complete 4-year (2010-2013) record from zone C shows a general decrease in mean soil gas temperatures from 170°, 158°, 120° to 100°C. Comparisons between key sites sampled in 2011 and 2012 at Zone N show a decrease in temperature (mean of 74.3°C in 2011 to 61.5°C in 2012), as well as decreases in temperature in zone S (mean of 68.2°C in 2011 to 60.8°C in 2012). Overall, soil gas temperatures in the greater Cerro Negro area have been decreasing by 5 to 50°C per year since 2010. Atmospheric temperatures at the time of sampling varied between 24°C and 32°C. Background sites removed from any hydrothermal heat sources register a minimum temperature of 23.7°C at a depth of 90 cm measured at mid-day. The temperature range between this minimum and 40°C is a function of sampling depth (10-90 cm) and surface heating.

CO_2 concentrations of soil gases are variable amongst the three zones (Figure 4b), with zone C displaying both increases and decreases over the 4-year period, and zone N displaying a 50% decrease between 2011 and 2012 (mean of 7.6 % to 3.3 %, respectively). In 2011, Zone S displayed 7 sites whose concentrations reached 100% CO_2. In 2012 and 2013, the highest CO_2 concentration at zone S was ~30 %. Overall, CO_2 concentrations measured over a four-year period are characterized by a full range between 0 % to 100 % and a strong isotopic clustering between -3.2 ‰ and -3.4 ‰. Zone C has the highest number of high-concentration sites in the field area with a concentration gap from 17 % to 54 % CO_2. Zone S displays a continuous range of concentrations from 0 % to 61 % CO_2, followed by a concentration gap and 7 sites at 100 % (Figure 5), and shares a cluster similar to zones C and N from 0% to 10 % CO_2. Zone N on the other hand is dominated by low CO_2 concentrations and a complete lack of sites above 10 % CO_2, except for a single site (30.1 %) located within an eroded crater at Cerro La Mula.

Figure 5 presents temperature, hydrogen, CO_2 and carbon isotope data collected in January 2011 along a 50 m transect that intersects zone S at right angles. The most striking feature is a 10 m long plateau of 100% CO_2 emissions, accompanied by elevated hydrogen (peak = 72 ppm), enriched $\delta^{13}C$ ratios (-2.8 ‰) and elevated temperatures (mean 88°C). This transect is located across the most prominent segment of hydrothermal activity in zone S (Figure 6).

4.3 Soil CO_2 flux

Soil flux data comprise 51 samples that cover the major hydrothermal areas and background sites in all three zones (Figure 6). The dataset is divided into three groups: (1) low flux measurements from background sites distant from hydrothermal areas (0-500 g $m^{-2}d^{-1}$) and sites close to their boundaries, (2) a selection of intermediate-high sites that increase in flux with proximity to major zones of active degassing (500-9,000 g $m^{-2}d^{-1}$), and (3) a small number of very high flux sites dominated by active degassing and large fumaroles (>9,000 g $m^{-2}d^{-1}$). Statistical analyses to determine these thresholds used a normal probability plot as described in Sinclair (1974) and Chiodini et al. (1998). Ultimately, the distinction between background/biogenic and hydrothermal populations was made on the basis of both CO_2 fluxes and $\delta^{13}C$ compositions (see section 5.4). The highest flux measurements, belonging to group (3), are recorded at fumaroles A and B located in zone C (Figure 6b) (24,040 and 29,160 g $m^{-2}d^{-1}$) and one measurement at the most hydrothermally active part of zone S (Figure 6c) (21,540 g $m^{-2}d^{-1}$). It is probable that fumaroles A and B have even larger fluxes than measured, as sampling of the main fumarole outlet was difficult due to very high gas flux and temperature. Hence these are minimum values. The lowest flux in the region was obtained at a background site located on the tephra blanket 3 km west of zone S where no flux was recorded over a measurement period of 30 minutes. Much of the edifice of Cerro Negro is covered by loose scoria, which makes soil flux sampling difficult due to the high permeability, uneven terrain and windy conditions. Measurements were attempted in these areas, but reproducibility between repeat samples could not be achieved due to atmospheric contamination.

The CO_2 flux dataset was used to produce three flux maps that correspond to the three sampling zones (Figure 6). These maps were constructed using a combination of flux measurements and field observations of visible zones of active degassing. The total flux per zone was calculated by combining the surface area of the contours with results from our soil flux measurements into a total emission of CO_2 gas in tons per day. We found that modifications to the surface areas of contours produced minor variations in the total flux per zone. Ultimately we decided on a high detail of contour groups to highlight fumarole and fracture locations. These are features that may be of interest in the future as the hydrothermal zones evolve. The combined minimum total CO_2 flux from zones N, C and S in 2012 was 31 ± 5 metric tons per day (zone N = 0.2, zone C = 16.7, zone S =14.1 tons per day).

The relationship between CO_2 flux and carbon isotopes is presented in Figure 4c. Sites with flux values higher than 100-200 g $m^{-2}d^{-1}$ form a well-defined horizontal array at -2.0 to -4.5 ‰. Except for one site located on the edge of a hydrothermal area, zone C is dominated by flux values above 100 g $m^{-2}d^{-1}$. Zones S and N have a larger proportion of samples from background sites and sites that border hydrothermal areas, so they display a much larger variation in both flux and $\delta^{13}C$. Sites with flux values lower than 200 g $m^{-2}d^{-1}$ tend to have lower temperatures and lower CO_2 concentrations. Their isotopic signatures tend to be more depleted in ^{13}C with a greater degree of variability and two distinct outliers. Two points from zone S and N represent the first of these outliers with $\delta^{13}C$ ratios of -18.8 ‰ and -19.4 ‰ and fluxes of 10 and 12 g $m^{-2}d^{-1}$. The second outlier has a $\delta^{13}C$ ratio of -32.8 ‰ and a flux value of 10 g $m^{-2}d^{-1}$. The first two sites are located in poorly vegetated areas removed from hydrothermal zones while the third point, the second outlier, was measured within a densely forested area. In all cases these more depleted values are consistent with a greater contribution of soil-derived biogenic CO_2.

4.4 Oxygen and hydrogen isotopes

Fumaroles A and B in zone C and a water well located 8 km southwest of Cerro Negro were sampled for $\delta^{18}O$ and δD isotopes (Figure 7). Each sampling site is represented by two water samples (duplicates) collected in close succession. Three fumarole samples form a cluster with an average $\delta^{18}O$ = -4.7 ‰ and δD = -49.6 ‰. One of the fumarole samples (Fumarole B) is offset slightly towards heavier oxygen and deuterium values ($\delta^{18}O$ = -3.32 ‰ and δD = -40.3 ‰). One water well sample plots on the global meteoric water line (GMWL), which is similar to the local meteoric water line for Nicaragua ($\delta^{18}O$ = -7.3 ‰ and δD = -48.6 ‰), while the other sample is offset to the right and may form a secondary linear trend. None of the fumarolic samples approach the andesitic/arc-related water field defined by Giggenbach (1992) or the primary magmatic water in equilibrium with plutonic formations defined by Sheppard and Epstein et al. (1970), suggesting a dominantly meteoric component. Given the steep slope of this secondary mixing trend, a small degree of mixing between magmatic vapor and meteoric water is possible (Giggenbach, 1992). There is no past fumarole data on Cerro Negro; however, we included two measurements of $\delta^{18}O$ and δD from fumarole condensates at Momotombo and Mombacho volcano in Figure 7 (Elkins et al., 2006). The authors suggest that their data falling between the meteoric line and the arc-related water field are related to the evaporation of meteoric water rather than mixing.

4.5 Helium isotopes

Table 5 lists air-corrected helium results from fumaroles A and B sampled in zone C. Duplicates were collected at each site; one sample from fumarole B leaked during analysis and is not presented. Williams et al. (1987) demonstrated that air contamination can influence the $^3He/^4He$ ratio, while also demonstrating that the dominant control is magmatic input or dilution from crustal radiogenic He (Craig et al., 1978; Sano and Fischer, 2012). The $^4He/^{20}Ne$ ratio for fumarole B (38.2) is significantly larger than that of fumarole A (11.6 and 12.9) and samples collected in 2002 (14.1). All these values are much higher than the atmospheric $^4He/^{20}Ne$ ratio of 0.032 (Shaw et al., 2003; Elkins et al., 2006; Gilfillan et al., 2008), indicating that both atmospheric contamination and the air correction have very little effect on the $^3He/^4He$ ratio. Therefore, the difference between our data and previously reported $^3He/^4He$ values is real. Duplicates from fumarole A display agreement in $^3He/^4He$ (6.77 and 6.37 ±0.2 R_A), $CO_2/^3He$ (16.4 and 13.8×10^9) and $\delta^{13}C$ ratios (-3.1 and -3.0 ‰). Fumarole B shows an increase in $^3He/^4He$ (7.38±0.2 R_A) relative to fumarole A, with similar $CO_2/^3He$ (14.5×10^9) and slightly lighter $\delta^{13}C$ (-3.5 ‰). $\delta^{13}C$ ratios obtained at fumarole A from copper tubes used for helium sampling (-3.1 ‰) agree within the daily variability of $\delta^{13}C$ obtained from regular soil gas sampling (-3.0 ‰). Comparisons with data obtained in 2002 (Figure 8) show a large decrease in the $CO_2/^3He$ ratio from 31×10^9 to 15×10^9, an increase in the $^3He/^4He$ ratio from 6.99 to 7.38 and no change in $\delta^{13}C$ ratios.

In order to assess relative source contributions for CO_2, the high $^{4}He/^{20}Ne$ samples are used to calculate three-component mixing as detailed by Sano and Marty (1995) (Table 6). They divide carbon source contributions based on He-C relationships into three principal components: mantle (M), limestone or marine carbonate (L) and sedimentary organic C (S). Relative contributions are calculated as:

$$(^{13}C/^{12}C)_{obs} = f_M(^{13}C/^{12}C)_M + f_L(^{13}C/^{12}C)_L + f_S(^{13}C/^{12}C)_S \qquad (2)$$

$$1/(^{12}C/^{3}He)_{obs} = f_M/(^{12}C/^{3}He)_M + f_L/(^{12}C/^{3}He)_L + f_S(^{12}C/^{3}He)_S \qquad (3)$$

$$1 = f_M + f_L + f_S \qquad (4)$$

The relative fraction is represented by f, and end-member compositions are obtained from previous studies on fumarolic gas from island arcs (Sano and Marty, 1995; Shaw et al., 2003); M: $\delta^{13}C$ = -6.5 ‰, $C/^{3}He = 1.5\times10^{9}$; L: $\delta^{13}C$ = 0 ‰, $C/^{3}He = 10^{13}$; S: $\delta^{13}C$ = -30 ‰, $C/^{3}He$ = 10^{13}). These components represent worldwide averages from subduction margins. Results using these principal components suggest an increase in mantle (M) carbon between 2002 and 2012 from 5 % to 10 %, a decrease in limestone/marine carbonate (L) from 89 % to 82 %, and similar sedimentary organic (S) ratios of 6-8 % (Table 6). In an attempt to investigate the variation in total organic carbon (TOC) and total nitrogen along the Central American subduction zone, Li and Bebout (2005) updated the carbon and nitrogen isotopic composition of subducting sediments from drill cores located offshore of Costa Rica. Hence we also ran our three-component mixing model using these new estimates (S: $\delta^{13}C$ = -22 ‰; L: $\delta^{13}C$ = +1.9 ‰). When the principal components from Li and Bebout (2005) are used, the proportion of marine carbonate decreases from 82 % to 73 %, the sedimentary organic component increases from 8 % to 17 %, and mantle (M) carbon components remain comparable at 10 % (Table 6).

5. Discussion

5.1 Present-day degassing state of Cerro Negro

Cerro Negro last erupted in 1999. Since that time its degassing character has changed significantly. Thanks to early work conducted by Salazar et al. (2001) and unpublished results from Barrancos et al. (2013), we know that in the months following the 1999 eruption, Cerro Negro experienced relatively high levels of soil CO_2 flux of 1,870-2,800 t d^{-1} from the main edifice (zone C). In the following years emissions dropped to 430 t d^{-1} in 2002, 10 t d^{-1} in 2008 with an exceptional increase to 260 t d^{-1} in 2004 following a small seismic crisis (Barrancos et al., 2013). 2008 marks an important change in Cerro Negro's degassing character when CO_2 fluxes began to plateau in the 10-40 t d^{-1} range. Over the same time period the number of active fumaroles in zone C decreased from 8 to 4 and their temperatures fell from 700°C to a range of 50-250°C (INETER 2012; 2013). The behavior of zone C in terms of CO_2 flux and temperature at the time of sampling in 2010-2013 is consistent with this plateau, with ~17 t d^{-1} CO_2 for zone C and temperatures in the range of 100-200°C from fumaroles A and B.

The evolution of CO_2 flux zones at Cerro Negro varies with time and importantly, with space. Prior to this study, there were no historic accounts nor measurements of degassing from zone N. The lack of recent eruptive activity and low CO_2 flux in this zone (0.2 t d^{-1}) suggest that the present day hydrothermal system is a remnant of a once active volcanic complex that became dormant when volcanism migrated south towards Cerro Negro. The present day distribution of degassing and of soil alteration mimic what appear to be a series of fractures associated with the eroding scoria cones of the Cerro La Mula complex (Figure 6).

Zone C is divided into two hydrothermal areas that represent the largest and most prominent areas of hydrothermal activity within the greater Cerro Negro region (Figure 6b). The first area is smaller in size and mimics the circular shape of Cerro Negro's inner crater. Emissions are focused around the summit and on the inner slopes of the crater. The northern crater edge is an interesting area of degassing where irregular fracturing along the rim releases high temperature and high CO_2 gas. Flux sampling in this area is not reliable due to the rocky terrain and windy conditions. The second area is the largest and most prominent hydrothermal feature of the field area. Its emission map is elongated along a NE-SW trend and is unique for its two large fumaroles marked with red flux contours on Figure 6b. The development of new, moderate flux, high CO_2 and high temperature fractures between 2011 and 2012 indicates that the emissions of CO_2 soil gas in the area are an evolving and dynamic process. In addition, evidence from early soil flux studies (Salazar et al., 2001; Barrancos et al., 2013), as well as observations of secondary mineral precipitation and soil alteration in zone C, suggest that prominent degassing areas within zone C migrate with eruptive activity and time. For example, after 1999, high levels of degassing were measured on the inner flanks of Cerro Negro's main crater. Since that time and up to the present day, activity has gradually migrated southeast to the hydrothermal area where fumaroles A and B are located. Minor changes to the distribution of degassing areas occur after periods of slope failure along this NE-SW structural feature within the outer crater. This either exposes new fractures or clogs older sites of degassing with debris.

Reports from local guides suggest that during the rainy season and for a short period afterward, the amount of visible degassing from fumaroles and fractures in zone C increases.

Zone S is a narrow, NW-SE oriented linear feature that is composed of two high flux segments separated by a small area of low flux (Figure 6c). The southeastern segment is larger and also hydrothermally more active. High fluxes are focused along a small area at the center of zone S, yet its linear nature extends further southeast towards the El Hoyo-Las Pilas complex. Eruptive activity in 1999 was accompanied by the formation of zone S, which until this study remained unsampled. Its current soil CO_2 flux is 14 t d^{-1}, which is comparable to zone C. Degassing and hydrothermal activity at zone C occurs in an elongate pattern similar to zone S, suggesting that both are controlled by structural features related to volcanic or regional structure. However, zone C is older, has prominent fumarolic activity and a higher degree of active degassing when compared to zone S. LaFemina (2013, pers. comm.) reported a CO_2 anomaly in the Cristo-Rey crater area prior to the 1999 eruption. It is possible that the anomaly persisted in the months following the eruption, but it was not present in 2012.

Areas outside of zones N, C and S have low background CO_2 flux (0-100 g $m^{-2}d^{-1}$) and show no signs of mineral precipitation or vegetation kill, suggesting there is no large-scale CO_2 anomaly. Emissions in the greater Cerro Negro region appear to be confined to the established volcanic structures and regional faults and fractures.

5.2 The role of regional structure

LaFemina et al. (2002) and Carr et al. (2003) addressed the nature of subduction along the Nicaraguan plate boundary. They concluded that oblique subduction and a relatively thin crust (~34 km) lead to the formation of several zones of N-S striking extension within the fore-arc region. It was proposed that these zones act as efficient pathways for rapid ascent of magma from deep within the crust or the upper mantle (Carr et al. 2003). LaFemina et al. (2004) proposed that the 1999 tectonically-induced eruption from Cerro Negro was a response to changes in regional stress along one such zone of extension. We propose that in addition to ascending magma, these pathways act as efficient conduits for the ascent of magmatic gases from deep within the crust or perhaps even the upper mantle. Furthermore, changes in the regional stress regime play an important role in controlling the permeability of the fracture network by dilating or constricting conduits for gas ascent. Barrancos et al. (2013) reported a steady trend of decreasing CO_2 flux emissions from zone C between 1999 and 2008. He noted an exceptional increase in emissions following a small seismic crisis in 2004, suggesting that a temporary modification of the local stress field opened new gas pathways to the surface. Small bursts of seismicity are common in the area around Cerro Negro and the neighboring Las Pilas-El Hoyo complex, indicating that the entire region is tectonically active.

Tectonic influence on degassing may be separated into two scales of structural features. The first scale is the large N-S striking extensional structure that represents the Cerro La Mula-Cerro Negro lineament. Pressure estimates from melt inclusion studies indicate the location of a deep, primary magma reservoir at ~15 km depth (Roggensack et al., 1997), suggesting that this extensional structure likely extends to mid-crustal levels and channels magma and gas to the surface. The long-term, large-scale migration of volcanic and degassing activity from north to south suggests that the regional stress field is slowly closing old crustal fractures beneath Cerro La Mula and opening new fractures beneath zone S. The second scale is represented by smaller surface faults and fractures visible through collapse (NE-SW structure, zone C) and the elongate patterns of degassing zones (fractures in zone N and the NW-SE oriented zone S). This second scale is limited to the uppermost crust and is responsible for localized delivery of gas to the surface. An excellent example of such a structure is the elongate nature of the hydrothermal area in zone S (Figure 6c). The transect across it shows a sharp plateau of 100% CO_2 gas in 2011 (Figure 5), indicating that this surface fracture acts as a focused conduit to the lower crust tapping a source of magmatic CO_2. The final result is a series of discontinuous hydrothermal zones that evolve with changes in the local stress regime. We propose that short-term variations in the supply of gas to the surface and the zone-like distribution of degassing areas are a result of the evolution and maturity of this second scale of structural features.

5.3 The meteoric component

Fluids and gases in the hydrothermal system of a volcano may be of magmatic and non-magmatic origin. The balance between the two is a dynamic process that reflects seasonal changes in precipitation and the availability of groundwater. Similarly, the supply of magmatic volatiles varies through time as a function of magma degassing, magma recharge and changes in the permeability of faults and fractures and other pathways of magma and gas ascent (Pribnow et al., 2003). The amount of visible degassing from fumaroles and fractures at Cerro Negro varies throughout a single year. Reports from local guides and our own observations from different periods during the year suggest higher amounts of visible degassing occur after periods of high rainfall. Oxygen and hydrogen isotopic data from fumaroles A and B located in zone C, where high CO_2 concentration gas is being emitted, plot close to the local meteoric water line at -48.4 ‰ δD and -5 ‰ δ^{18}O (Figure 7), indicating that a large percentage of the water supplied to the hydrothermal system is non-magmatic in origin. The suite of samples appear to fall on a mixing line between the GMWL and the arc-related water field defined by Giggenbach (1992), suggesting the involvement of a small amount of magmatic water. However, it is possible that the mixing line is an analytical artifact, or is actually an offset from the GMWL that occurs due to oxygen isotopic exchange between meteoric water and hot rock enriched in ^{18}O. Such a process has been proposed at Showa-Shinzan (Mizutani, 1978), Kudriavy (Taran et al., 1995) and Galeras volcanoes (Fischer et al., 1997). Low temperature fumaroles, meteoric δD and δ^{18}O values, and changes in the amount of visible degassing after rainy periods suggest that the water table is close to the surface (Garofalo et al., 2007). Fractures on the main edifice of Cerro Negro likely provide zones of high permeability, facilitating downward migration of meteoric fluids.

The interaction between magmatic and meteoric fluids likely takes place in a shallow hydrothermal system. Rising magmatic gases are diluted by vaporization of meteoric water leading to a shift in the chemical composition of fumarolic gas (Fischer et al., 1996). In addition, this dilution has the potential to affect the carbon isotopic ratio if rising CO_2 gas mixes with vaporized organic-rich groundwater in the hydrothermal system (Pinti et al., 2013). It is likely that soil gas δ^{13}C values reported in September 2010 are more ^{13}C-depleted due to mixing between magmatic gas and a stronger meteoric/groundwater component in the hydrothermal system following the rainy period.

Hydrogen (H_2) is often a useful component of volcanic gases, one that can move freely through the crust with little risk of atmospheric contamination due to its low concentration in air (0.5 ppm) (Oppenheimer, 2003; Melián et al., 2007). As such, it often takes advantage of high permeability zones. Diffuse H_2 degassing data were collected at prominent degassing sites in Zones C and S. Hydrogen concentrations correlate with high heat flux and high CO_2 concentrations. In zone C, both fumaroles A and B saturated our instrument with high H_2 concentrations (> 2500 ppm) and in zone S samples along the transect register a ~ 70 ppm H_2 anomaly (Figure 5). Infiltration of groundwater into the hydrothermal system can lead to reducing conditions which favor H_2 production through boiling water-rock interactions (Giggenbach ,1987; Aiuppa et al., 2011). When we compare our results to concentrations of diffuse H_2 emissions from Teide volcano, Spain (Hernández et al., 2000), and Poás volcano, Costa Rica (Melián, et al., 2007), we find that our high H_2 concentrations (> 2500 ppm) with positive correlations with temperature and CO_2 concentrations indicate an important contribution of magmatic H_2 to the hydrothermal system, in addition to H_2 sourced from water-rock interactions. Future degassing studies at Cerro Negro should consider H_2 an important tool for monitoring changes in the magmatic-hydrothermal system.

5.4 The carbon isotopic character of Cerro Negro

Soil gases at Cerro Negro can be grouped into three fields defined by Chiodini et al. (2008) on the basis of $\delta^{13}C$ values and CO_2 flux: hydrothermal, biogenic and a mixture between the two (Figure 4c). Biogenic $\delta^{13}C$ values ($\delta^{13}C$ = -32.8 ‰), the most ^{13}C-depleted values in the dataset, were measured within a forested site dominated by C_3 vegetation (-22 to -35 ‰, Clark and Fritz, 1997). Two sites selected to obtain the background $\delta^{13}C$ displayed values of -18.8 and -19.4 ‰ that fall within the mixing field. We propose that the mixing field at Cerro Negro is characterized by $\delta^{13}C$ values representing a mixture of two end members, biogenic and magmatic-hydrothermal CO_2 (Chiodini et al., 2008). While only two sites fall distinctly within this mixing field, several other sites with relatively light $\delta^{13}C$ values (-6 to -10 ‰) and low CO_2 flux (< 200 g $m^{-2}d^{-1}$) represent various degrees of mixing between the two end members. Soil gas samples that fall within the hydrothermal field are defined by CO_2 flux values higher than 200 g $m^{-2}d^{-1}$ and an average soil gas $\delta^{13}C$ in the -3 to -3.5 ‰ range over a period of 4 years (2010-2013). These values are more enriched than pure mantle signatures (-5 to -7 ‰), probably due to a marine carbonate component incorporated from melting of the subducted slab with an estimated end-member $\delta^{13}C$ of ~1.9‰ (Li and Bebout, 2005). Such $\delta^{13}C$ values are common for the Central American Volcanic Arc (CAVA) and arc-related volcanism in general (Shaw et al., 2003; Javoy et al., 1986).

Looking at the short-term degassing trend in $\delta^{13}C$, temporal variability from 2011-2013 is practically non-existent, with small variations on the order of 1 ‰, attributed to natural variability of the magmatic-hydrothermal system (Table 4). Based on 7 key samples from zone C, there is a trend towards heavier values from September 2010 to January 2011, which we attribute to decreased meteoric input and groundwater flux through the hydrothermal system during the dry season in January 2011. The long-term temporal $\delta^{13}C$ variability and flux measurements from zone C indicate that Cerro Negro is presently in a steady-state, post-eruptive degassing stage that started in 2008 when soil fluxes decreased to a plateau of 10-40 t d^{-1} (Figure 8a). Long-term $\delta^{13}C$ values at fumarole B from 1992 to 2013 show minor degrees of variation, with -2.5 ‰ in 1992 (Sano and Williams, 1996), -3.0 ‰ in 1999 (Salazar et al., 2001), -2.3 ‰ in

2002 (Shaw et al., 2003), -7.6 ‰ in 2010, -2.5 ‰ in 2011, -3.1 ‰ in 2012 and -2.6 ‰ in 2013 (Figure 8).

Javoy et al. (1986) and Gerlach and Taylor (1990) suggested that stable carbon isotopes and their evolution through time as a result of degassing might be used to distinguish between volatile-rich and volatile-poor magma batches. Hence, measurements of $\delta^{13}C$ could be used to monitor the extent of magmatic degassing, magma replenishment and movement of magma within the volcano's plumbing network. Gerlach and Taylor (1990) modeled closed-system degassing and showed a theoretical decrease in $\delta^{13}C$ of -4 ‰ through complete loss of CO_2 through degassing. Open-system degassing resulted in a much larger decrease of ~ -40 ‰. Given that over the last 20-year period there has been little to no fractionation at Cerro Negro, we propose that the magmatic network beneath Cerro Negro is supplied by a continuous source of gas from the upper mantle, or a large deep reservoir of ponding magma in the crust which is continuously fed from the upper mantle. Furthermore, despite minor variations in $\delta^{13}C$ between adjacent sites within a single zone and mixing due to groundwater interaction, the overall spatial distribution of $\delta^{13}C$ between zones N, C and S is relatively constant at a mean of -3 to -3.5 ‰ over a four-year period (2010-2013). Values were remarkably constant in 2013; every site in zone C and S above 10 % CO_2 soil gas exhibited a $\delta^{13}C$ ratio of 2.7 ± 0.1 ‰. Such a tight distribution across all three zones is best explained by a primary source of magma deep within the crust and/or upper mantle coupled to a network of overlying fractures that supply gas to a shallow magmatic-hydrothermal system with a distribution of degassing zones at the surface.

5.5 Nature of the gas source beneath Cerro Negro

To determine the deep sources of magmatic gases and identify processes that might affect CO_2 gas on its way to the surface, we examine CO_2-He relationships. Our synthesis includes CO_2 and helium data from April 1992 (Sano and Williams, 1996), December 1999 (Salazar et al., 2001), 1999-2011 (Barrancos et al., 2013), 2002 (Shaw et al., 2003) and 2010-2012 (this study) (Figure 8b and 8c), and is divided into three sections to illustrate three processes that have the potential to affect $^3He/^4He$, $\delta^{13}C$ and $CO_2/^3He$: hydrothermal circulation, magmatic degassing, and crustal and mantle processes (Hilton et al., 2010). In this study we sampled two fumaroles (A and B) that differ in their $^3He/^4He$ ratio from 6.77 ± 0.22 and 6.37 ± 0.21 R_A for fumarole A to 7.38 ±0.17 R_A for fumarole B. For the purpose of this discussion we take fumarole B as the more representative sample due to its higher $^4He/^{20}Ne$ ratio, hence the least amount of air contamination. Samples from 1992 and 1999 were collected days to months after an eruption, samples from 2002 were collected after 3 years, and samples collected by this study represent a repose period of 13 years without any new eruptive activity.

Increased water circulation through the hydrothermal system can lower fumarole temperatures and decrease $CO_2/^3He$ values as a result of higher CO_2 solubility in water and greater partitioning of He in the vapor phase (Wilhelm et al., 1977). At Cerro Negro, fumarole temperatures have decreased by ~500°C since the last eruption in 1999, while the $CO_2/^3He$ ratio remained relatively stable from 33.3×10^9 in April 1992 (Sano and Williams, 1996) to 30.9×10^9 in December 1999 (Salazar et al., 2001), 31×10^9 in January 2002 (Shaw et al., 2003), but showed a decrease to 14.5×10^9 in January 2012 (this study). Such a decrease in temperature and $CO_2/^3He$

is consistent with groundwater-hydrothermal interaction, and near-meteoric $\delta^{18}O$ and δD values from fumaroles support this model.

Gilfillan et al. (2009) showed that under certain pH conditions the dissolution of CO_2 or its precipitation as carbonate can modify the $\delta^{13}C$ ratio. At Cerro Negro, zones of active degassing in the main crater posses a range of pH values (1-6) with gypsum, calcite, and sulfur as the major precipitating phase between sites (Hynek et al., 2013). Low pH (~ -1 to 1) and high temperature (> 100°C) fumaroles tend to be dominated by sulfur, while high pH (~ 6) and low temperature sites (~ 60°C) tend to be dominated by calcite. This range in pH values is likely due to an increased component of meteoric water in the hydrothermal system (Hynek et al., 2013). Given these variable pH and temperature conditions, we should observe a $\delta^{13}C$ shift on the order of 1 - 3 ‰. However, the $\delta^{13}C$ data consistently show a very narrow range, both spatially and temporally.

Magmatic degassing can decrease $CO_2/^3He$ (Hilton et al., 2010) and $\delta^{13}C$ (Javoy et al., 1986; Gerlach and Taylor, 1990; Ray et al., 2009) by a factor of two or more for tholeiitic melt subject to open or closed system degassing. The $CO_2/^3He$ decrease from 33.9×10^9 to 14.5×10^9 is in agreement with closed system degassing, yet the lack of significant change in $\delta^{13}C$ between April 1992 and May 2013 (Figure 8c) suggests that magmatic degassing alone cannot account for the changes in $CO_2/^3He$.

Magmas in arc regions tend to release gases that are high in $^3He/^4He$ (8±1 $R_{A,}$ Graham, 2002) with a range of $\delta^{13}C$ (-2 to -10 ‰) that tends not to vary by more than ±2 ‰ at a single volcano (Javoy et al., 1986). Melting of crustal material by ponding or ascending magma can lead to a decrease in $^3He/^4He$ as well as a modification of the $\delta^{13}C$ ratio. In 1992 the $^3He/^4He$ ratio was 6.8±0.18 R_A, in December 1999 6.82±0.09 R_A, in January 2002 6.99±0.07 R_A (Shaw et al., 2003), and in January 2012 7.38 ± 0.17 R_A. Hence the ratio has been increasing slowly but steadily for >20 years since 1992 without any significant change in $\delta^{13}C$. This excludes crustal melting which would decrease the $^3He/^4He$ ratio. Our trends are consistent with regional CO_2-He systematics (Shaw et al., 2003; and 2006), which suggests minimal crustal interaction of rapidly ascending magma (Roggensack et al., 1997) due to a well-established conduit network provided by N-S striking extension (LaFemina et al., 2004).

Using the three-component mixing analysis presented in section 4.5, we can compare relative abundances of mantle (M), limestone/marine carbonate (L) and sedimentary organic (S) carbon within the fumarolic gas (Table 6). By plotting $\delta^{13}C$ against $CO_2/^3He$, we observe an increase in mantle carbon between 2002 and 2012 (Figure 9). Samples from 2012 form a distinct cluster of points that, when combined with the cluster of data from 1992-2002, follow a trend defined by the two-component mixing line between MORB and lithospheric/carbonate carbon. However, the clusters do not fall on the mixing curve even when the optimal end-member compositions are selected (dashed line, Figure 9), signifying that a small but constant component of sedimentary carbon is present (S). The change between 2002 and 2012 corresponds to a 5 % mantle increase and a ~1 ‰ change towards more negative $\delta^{13}C$ values. This change in $\delta^{13}C$ is within the natural variability of the hydrothermal system, defined by a range of ±1 ‰ at a single site over the timespan of our field campaign. Yet when coupled with the change in $CO_2/^3He$, the increase in mantle contributions is noteworthy.

By eliminating shallow crustal processes capable of altering the CO_2-He relationship, the data suggest that between 2002 and 2012 the deep crustal CO_2 supply to the hydrothermal system increased its mantle component. Shaw et al. (2006) undertook a comprehensive comparison between degassing data (Sano and Williams, 1996; Shaw et al., 2003) and geochemical data from major phenocryst phases from past eruptions at Cerro Negro (Roggensack et al., 1997; Roggensack, 2001). They discovered no major differences in $^3He/^4He$ contents among olivines, pyroxenes and geothermal data, and concluded that magmas at Cerro Negro are homogeneous and sourced via a deep dyke from a common reservoir of magma at great depth (>14 km) (Portnyagin et al., 2012) with minimal crustal interaction. They acknowledged the possibility of an intricate network of shallow crustal chambers and dikes. In this regard, the 1999 eruption was fundamentally different from all other Cerro Negro eruptions in that it formed zone S, which represents the southernmost extent of activity along the Cerro La Mula-Cerro Negro alignment. The low volume of erupted material may be a reflection of extension and subsurface accommodation of magma south of Cerro Negro's main edifice (LaFemina, 2013, pers. comm.). We propose that a change in the permeability of the magmatic plumbing network along with continued influence from the local stress regime has the potential to reconfigure pathways of gas ascent in order to supply a slightly larger proportion of mantle (M) derived CO_2 and modify the relative contributions of carbonate (L) and sedimentary (S) CO_2 sources.

5.5 Degassing model

The occurrence of several volcanic centers in Nicaragua is closely related to areas of N-S striking extension in the fore-arc and arc graben system. Based on the location of inactive cones and the lack of historic eruptions, we consider Cerro La Mula as the first manifestation of activity along a region of local extension that eventually became the Cerro La Mula-Cerro Negro alignment. As the local stress field evolved, extension began migrating south, creating new fracture systems for the ascent of magma and gas. In 1850, a new magmatic pathway was established at Cerro Negro, shifting volcanic activity away from Cerro La Mula. Through numerous eruptions over the following years, the fracture network beneath Cerro Negro developed into an efficient conduit system capable of sourcing magma and gas from the lower crust and upper mantle. In 1968, the Cristo Ray craters formed on the south flank of Cerro Negro, indicating that regional extension was creating new pathways south of the main edifice. The formation of zone S, 1 km south of the Cristo Ray craters after the 1999 eruption, is further evidence that activity is migrating southward along the Cerro La Mula-Cerro Negro alignment. The lack of major gas and thermal anomalies between zones N, C and S indicates that the uppermost crustal fracture network supplying volcanic gases to the surface is discontinuous. However, the similar $\delta^{13}C$ soil gas signatures at all three zones also demonstrate that the surface fractures are tapping a deeper, common source of magmatic CO_2.

After the 1999 eruption, CO_2 fluxes and fumarole temperatures on the main edifice were at elevated values due to the presence of fresh magma and a rejuvenated fracture system. Stable $\delta^{13}C$ values and minor variations in the $^3He/^4He$ ratio suggest that small amounts of crustal melting and/or assimilation took place during magma ascent or emplacement associated with the

1999 eruption. In the years after the eruption, CO_2 fluxes decreased while prominent zones of degassing on the main edifice migrated to their present day position until steady state degassing was achieved around 2008. The presently low CO_2 flux values, stable $\delta^{13}C$, decrease in $CO_2/^3He$ and small increase in the $^3He/^4He$ ratio together reveal that the fracture network beneath Cerro Negro has been reconfigured to provide a low-volume, steady supply of gas composed of a higher fraction of upper mantle CO_2. During this low level of CO_2 flux, the hydrothermal system becomes an important controlling factor on gas chemistry. Its near-meteoric $\delta^{18}O$ and δD values demonstrate that most of the water in the hydrothermal system is sourced via precipitation, which during periods of high rainfall has the potential to offset $\delta^{13}C$ signatures to depleted values as a result of mixing between magmatic and vaporized meteoric fluids. At present, the stable CO_2 flux output and $\delta^{13}C$ values from soil gases indicate that Cerro Negro and its hydrothermal system remain in a steady state of degassing. Future monitoring efforts must account for seasonal variations in precipitation which can vary the input of meteoric water to the hydrothermal system. In addition, small segments of flank collapse may bury old degassing zones and expose new ones, modifying their shape and distribution, and bursts of seismicity have the potential to modify the local stress field, changing the permeability of fault and fractures. If hydrothermal activity at Cerro Negro and other volcanic centers that share its degassing character is to be used as a forecasting tool for future eruptions, such processes must be taken into consideration.

6. Conclusions

Our 4-year gas sampling campaign at Cerro Negro volcano has produced a carbon isotopic characterization of a young basaltic cinder cone. In hopes of improving our understanding of the degassing characteristics and the magmatic plumbing network at Cerro

Negro and at other similar volcanoes, we examined $\delta^{13}C$ and CO_2 fluxes from soil gases and hydrothermal zones on and around Cerro Negro. In addition, we collected condensates for $\delta^{18}O$ and δD analyses, and fumarole gas samples for helium isotope analysis. Our conclusions are as follows:

1. A zone of north-south striking extension controls the distribution of hydrothermal areas at Cerro Negro. This structure has the ability to tap deep pockets of magma, enabling rapid ascent of magma and gas from various depths. Long-term changes in the regional stress field are responsible for the progressive migration of activity from north to south, while short-term stress changes can alter the permeability of upper crustal fractures.

2. Since the last eruption in 1999, the total flux of CO_2 at Cerro Negro decreased until 2008 when it began to plateau at low levels (10-40 t d^{-1}). In 2012, Zone N had a flux of 0.2 t d^{-1}, while zones C and S were emitting 16.7 and 14.1 t d^{-1}, respectively, for a total CO_2 flux of 31 t d^{-1}. High flux values for zone S illustrate that areas of diffuse degassing on the flanks of the volcano are important contributors to the total output of CO_2.

3. Between 2010-2013, the predominant $\delta^{13}C$ soil gas signatures occupy a range between -3 to -3.5 ‰, consistent with a strong magmatic-hydrothermal source. The full range of $\delta^{13}C$ compositions is a function of mixing between two end members, deep magmatic and surface biogenic carbon.

4. Similar $\delta^{13}C$ fumarole values from zone C between 1992 and 2012 indicate a continuous supply of gas from depth. Relatively stable trends in $^3He/^4He$ ratios from 6.8 ± 0.18 R_A

(1992) to 7.38 ± 0.17 R_A (2012) and $CO_2/^3He$ from 33.3×10^9 (1992) to 14.5×10^9 (2012) reinforce the notion of a near-constant mantle source of volatiles, with minimal crustal interaction along a well-established conduit system provided by the N-S striking extension.

5. We propose a degassing model in which regional zones of extension and surface fracturing provide a window into the lower crust and possibly the upper mantle. Rising magmatic volatiles supply the shallow hydrothermal system with a stable, long-term supply of magmatic carbon. Changes in the permeability of upper crustal fractures in response to regional seismicity may lead to changes in CO_2 flux and a continually evolving distribution of hydrothermal zones. Nevertheless, the isotopic signature of the CO_2 gas remains stable, except during periods of high rainfall.

Cerro Negro volcano remains overdue to erupt. We propose that a more extensive network composed of geophysical and gas monitoring instruments be established in order to provide a comprehensive data set that will help our understanding of future eruptive activity at Cerro Negro. It is essential that measurements of gas flux, temperature, gas chemistry and gas isotopes continue to be made on the main edifice and in areas to the south, especially zone S. This zone is an area of great interest and should be closely monitored geophysically and geochemically in the years to come.

Acknowledgements

We thank Marc-Antoine Longpré and Jack Wilcock for their help with fieldwork and sample collection. Reviews and discussions with Dr. Boswell Wing were very helpful and much appreciated. We are most grateful to Dave Hilton for analyzing helium isotopes and Jean-François Hélie for the analysis of oxygen and deuterium isotopes. We would like to thank the staff at the Stable Isotope Laboratory, University of Toronto, for their help with sample preparation and debates regarding carbon isotopes. We thank Pete LaFemina for his insight into Nicaraguan tectonics, Allison Shaw for providing additional data and Tobias Fischer for discussions on Cerro Negro's hydrothermal system. This research was made possible with funding to Gregor Lucic from GEOTOP, MAGNET and the Department of Earth and Planetary Sciences at McGill. This work was also supported by Discovery Grants to John Stix and Barbara Sherwood Lollar from the Natural Sciences and Engineering Research Council of Canada (NSERC), and by an NSERC CREATE grant to Stix and Sherwood Lollar.

Bibliography

Aiuppa A, Franco A, von Glasow R, Allen AG, Alessandro W, Mather TA, Pyle DM, Valenza M (2007) The tropospheric processing of acidic gases and hydrogen sulphide in volcanic gas plumes as inferred from field and model investigations. Atmos Chem Phys 7:1441-1450. doi:10.5194/acp-7-1441-2007

Aiuppa A, Shinohara H, Tamburello G, Giudice G, Liuzzo M, Moretti R (2011) Hydrogen in the gas plume of an open-vent volcano, Mount Etna, Italy. J Geophys Res 116:B10204. doi:10.1029/2011jb008461

Barrancos J, Ibarra M, Melián G, Álvarez J, Rodriguez F, Nolasco D, Padilla G, Calvo D, Dionis S, Padron E, Hernández PA, Pérez NM, Munoz A (2013) Diffuse CO_2 monitoring at Cerro Negro volcano, Nicaragua. International Association of Volcanology and Chemistry of the Earth's Interior (IAVCEI) Scientific Assembly, Kagohsima, 3W_2G-P11, Abstract

Blundy J, Cashman KV, Rust A, Witham F (2010) A case for CO_2-rich arc magmas. Earth Planet Sci Lett 290:289-301. doi:10.1016/j.epsl.2009.12.013

Camarda M, De Gregorio S, Favara R, Gurrieri S (2007) Evaluation of carbon isotope fractionation of soil CO_2 under an advective–diffusive regimen: A tool for computing the isotopic composition of unfractionated deep source. Geochim Cosmochim Acta 71:3016-3027. doi:10.1016/j.gca.2007.04.002

Carr MJ, Feigenson MD, Patino LC, Walker JA (2003) Volcanism and geochemistry in Central America: Progress and problems. In: Inside the Subduction Factory, vol 138. Geophys. Monogr. Ser. AGU, Washington, DC, pp 153-174. doi:10.1029/138GM09

Chiodini G, Caliro S, Aiuppa A, Avino R, Granieri D, Moretti R, Parello F (2011) First $^{13}C/^{12}C$ isotopic characterization of volcanic plume CO_2. Bull Volcanol 73:531-542. doi:10.1007/s00445-010-0423-2

Chiodini G, Caliro S, Cardellini C, Avino R, Granieri D, Schmidt A (2008) Carbon isotopic composition of soil CO_2 efflux, a powerful method to discriminate different sources feeding soil CO_2 degassing in volcanic-hydrothermal areas. Earth Planet Sci Lett 274:372-379. doi:10.1016/j.epsl.2008.07.051

Chiodini G, Cioni R, Guidi M, Raco B, Marini L (1998) Soil CO_2 flux measurements in volcanic and geothermal areas. Appl Geochem 13:543-552. doi:10.1016/S0883-2927(97)00076-0

Clark ID, Fritz P (1997) Tracing the carbon cycle. In: Starkweather AW (ed) Environmental isotopes in hydrogeology. Lewis Publishers, New York, pp 111-134

Connor C, Hill B, LaFemina P, Navarro M (1996) Soil ^{222}Rn pulse during the initial phase of the June–August 1995 eruption of Cerro Negro, Nicaragua. J Volcanol Geotherm Res 73:119-127. doi:10.1016/0377-0273(96)00020-0

Courtland LM, Kruse SE, Connor CB, Connor LJ, Savov IP, Martin KT (2012) GPR investigation of tephra fallout, Cerro Negro volcano, Nicaragua: a method for constraining parameters used in tephra sedimentation models. Bull Volcanol 74:1409-1424. doi:10.1007/s00445-012-0603-3

Craig H, Lupton JE, Horibe Y (1978) A mantle helium component in Circum-Pacific volcanic gases: Hakone, the Marianas, and Mt. Lassen. Terrestrial Rare Gases:3-16

Dagg AS, Tubianosa BS, Newhall CG, Tungol NM, Javier D, Dolan MT, Reyes PJD, Arboleda RA, Martinez MMA, Regalado MTM (1996) Monitoring sulphur dioxide emission at Mount Pinatubo. In: Newhall CG, Punongbayan RS (eds) Fire and mud: Eruptions and lahars of Mount Pinatubo. Phivolcs/U of Washington Press, pp 409-414

Díez M, LaFemina PC, Connor CB, Strauch W (2005) Evidence for static stress changes triggering the 1999 eruption of Cerro Negro Volcano, Nicaragua and regional aftershock sequences. Geophys Res Lett 32:1-4. doi:10.1029/2004GL021788

Elkins LJ, Fischer TP, Hilton DR, Sharp ZD, McKnight S, Walker J (2006) Tracing nitrogen in volcanic and geothermal volatiles from the Nicaraguan volcanic front. Geochim Cosmochim Acta 70:5215-5235. doi:10.1016/j.gca.2006.07.024

Fischer TP, Arehart GB, Sturchio NC, Williams SN (1996) The relationship between fumarole gas composition and eruptive activity at Galeras Volcano, Colombia. Geology 24:531-534. doi:10.1130/0091-7613(1996)024<0531:TRBFGC>2.3.CO;2

Fischer TP, Sturchio NC, Stix J, Arehart GB, Counce D, Williams SN (1997) The chemical and isotopic composition of fumarolic gases and spring discharges from Galeras Volcano, Colombia. J Volcanol Geotherm Res 77:229-253. doi:10.1016/S0377-0273(96)00096-0

Garofalo K, Tassi F, Vaselli O, Delgado-Huertas A (2007) Fumarolic gases at Mombacho volcano (Nicaragua): presence of magmatic gas species and implications for volcanic surveillance. Bull Volcanol 69:785-795. doi:10.1007/s00445-006-0108-z

Gerlach TM, Taylor BE (1990) Carbon isotope constraints on degassing of carbon-dioxide from Kilauea volcano. Geochim Cosmochim Acta 54:2051-2058. doi:10.1016/0016-7037(90)90270-U

Giggenbach WF (1987) Redox processes governing the chemistry of fumarolic gas discharges from White Island, New Zealand. Appl Geochem 2:143-161. doi:10.1016/0883-2927(87)90030-8

Giggenbach WF (1992) Isotopic shifts in waters from geothermal and volcanic systems along convergent plate boundaries and their origin. Earth Planet Sci Lett 113:495-510. doi:10.1016/0012-821X(92)90127-H

Gilfillan S, Ballentine CJ, Holland G, Blagburn D (2008) The noble gas geochemistry of natural CO_2 gas reservoirs from the Colorado Plateau and Rocky Mountain provinces, USA. Geochim Cosmochim Acta 72:1174-1198. doi:10.1016/j.gca.2007.10.009

Gilfillan SM, Lollar BS, Holland G, Blagburn D, Stevens S, Schoell M, Cassidy M, Ding Z, Zhou Z, Lacrampe-Couloume G, Ballentine CJ (2009) Solubility trapping in formation water as dominant CO_2 sink in natural gas fields. Nature 458:614-618. doi:10.1038/nature07852

Girard G, van Wyk de Vries B (2005) The Managua Graben and Las Sierras-Masaya volcanic complex (Nicaragua); pull-apart localization by an intrusive complex: results from analogue modeling. J Volcanol Geotherm Res 144:37-57. doi:10.1016/j.jvolgeores.2004.11.016

Graham DW (2002) Noble gas isotope geochemistry of mid-ocean ridge and ocean island basalts; characterization of mantle source reservoirs. Rev Mineral Geochem 47:247-317. doi:10.2138/rmg.2002.47.8

Hernández PA, Pérez NM, Salazar JML, Sato M, Notsu K, Wakita H (2000) Soil gas CO_2, CH_4 and H_2 distribution in and around Las Cañadas caldera, Tenerife, Canary Islands, Spain. J Volcanol Geotherm Res 103:425-438. doi:10.1016/S0377-0273(00)00235-3

Hill BE, Connor CB, Jarzemba MS, LaFemina PC, Navarro M, Strauch W (1998) 1995 eruptions of Cerro Negro volcano, Nicaragua, and risk assessment for future eruptions. Geol Soc Am Bull 110:1231-1241. doi:10.1130/0016-7606(1998)110<1231:EOCNVN>2.3.CO;2

Hilton DR, Ramirez CJ, Mora-Amador R, Fischer TP, Fueri E, Barry PH, Shaw AM (2010) Monitoring of temporal and spatial variations in fumarole helium and carbon dioxide characteristics at Poas and Turrialba volcanoes, Costa Rica (2001-2009). Geochem J 44:431-440

Hynek BM, McCollom TM, Marcucci EC, Brugman K, Rogers KL (2013) Assessment of environmental controls on acid-sulfate alteration at active volcanoes in Nicaragua: Applications to relic hydrothermal systems on Mars. Journal of Geophysical Research: Planets 118:2083-2104. doi:10.1002/jgre.20140

INETER (2012) Sismos y volcanes de Nicaragua. Tenorio V (ed), In Catálogo Anual, 2012, pp 66, http://www.ineter.gob.ni/articulos/comunicaciones/boletines/boletin-sismologico.html

INETER (2013) Sismos y volcanes de Nicaragua. Tenorio V (ed), In Catálogo Anual, 2013, pp 53, http://www.ineter.gob.ni/articulos/comunicaciones/boletines/boletin-sismologico.html

International Atomic Energy Agency (IAEA) (2004) Global network of isotopes in precipitation. http://www-naweb.iaea.org/napc/ih/IHS_resources_gnip.html. Accessed April 17th 2013

Javoy M, Pineau F, Delorme H (1986) Carbon and nitrogen isotopes in the mantle. Chem Geol 57:41-62. doi:10.1016/0009-2541(86)90093-8

Kazahaya K, Shinohara H, Uto K, Odai M, Nakahori Y, Mori H, Iino H, Miyashita M, Hirabayashi J (2004) Gigantic SO_2 emission from Miyakejima volcano, Japan, caused by caldera collapse. Geology 32:425-428. doi:10.1130/g20399.1

LaFemina PC, Connor CB, Hill BE, Strauch W (2004) Magma–tectonic interactions in Nicaragua: the 1999 seismic swarm and eruption of Cerro Negro volcano. J Volcanol Geotherm Res 137:187-199. doi:10.1016/j.jvolgeores.2004.05.006

LaFemina PC, Dixon TH, Stauch W (2002) Bookshelf faulting in Nicaragua. Geology 30:751-754. doi:10.1130/0091-7613(2002)030<0751:BFIN>2.0.CO;2

Li L, Bebout GE (2005) Carbon and nitrogen geochemistry of sediments in the Central American convergent margin: Insights regarding subduction input fluxes, diagenesis, and paleoproductivity. J Geophys Res 110:1-17. doi:10.1029/2004JB003276

Manga M, Brodsky E (2006) Seismic triggering of eruptions in the far field: Volcanoes and geysers. Annual Review of Earth and Planetary Sciences 34:263-291. doi:10.1146/annurev.earth.34.031405.125125

McKnight SB (1995) Geology and petrology of Cerro Negro volcano, Nicaragua. MS Thesis, Arizona State University, Tempe

McKnight SB, Williams SN (1997) Old cinder cone or young composite volcano?: The nature of Cerro Negro, Nicaragua. Geology 25:339-342. doi:10.1130/0091-7613(1997) 025<0339:OCCOYC>2.3.CO;2

Melián GV, Galindo I, Pérez NM, Hernández PA, Fernández M, Ramírez C, Mora R, Alvarado GE (2007) Diffuse emission of hydrogen from Poás volcano, Costa Rica, America Central. Pure Appl Geophys 164:2465-2487. doi:10.1007/s00024-007-0282-8

Mizutani Y (1978) Isotopic compositions of volcanic steam from Showashinzan volcano, Hokkaido, Japan. Geochem Journal 12:57-63.

Oppenheimer C (2003) Volcanic degassing. In: Holland HD, Turekian KK (eds) Treatise on geochemistry. Pergamon, Oxford, pp 123-166. doi:10.1016/B0-08-043751-6/03020-6

Oppenheimer C, Scaillet B, Martin RS (2011) Sulfur degassing from volcanoes: source conditions, surveillance, plume chemistry and earth system impacts. Rev Mineral Geochem 73:363-421. doi:10.2138/rmg.2011.73.13

Pinti DL, Castro MC, Shouakar-Stash O (2013) Evolution of the geothermal fluids at Los Azufres, Mexico, as traced by noble gas isotopes, $\delta^{18}O$, δD, $\delta^{13}C$ and $^{87}Sr/^{86}Sr$. J Volcanol Geotherm Res 249:1-11. doi:10.1016/j.jvolgeores.2012.09.006

Portnyagin MV, Hoernle K, Mironov NL (2012) Contrasting compositional trends of rocks and olivine-hosted melt inclusions from Cerro Negro volcano (Central America): implications for decompression-driven fractionation of hydrous magmas. Int J Earth Sci doi:10.1007/s00531-012-0810-3

Pribnow D, Schütze C, Hurter SJ, Flechsig C (2003) Fluid flow in the resurgent dome of Long Valley Caldera: implications from thermal data and deep electrical sounding. J Volcanol Geotherm Res 127:329-345. doi:10.1016/S0377-0273(03)00175-6

Ray MC, Hilton DR, Muñoz J, Fischer TP, Shaw AM (2009) The effects of volatile recycling, degassing and crustal contamination on the helium and carbon geochemistry of hydrothermal fluids from the Southern Volcanic Zone of Chile. Chem Geol 266:38-49. doi:10.1016/j.chemgeo.2008.12.026

Roggensack K (2001) Sizing up crystals and their melt inclusions: a new approach to crystallization studies. Earth Planet Sci Lett 187:221-237. doi:10.1016/S0012-821X(01)00269-2

Roggensack K, Hervig RL, McKnight SB, Williams SN (1997) Explosive basaltic volcanism from Cerro Negro volcano: influence of volatiles on eruptive style. Science 277:1639-1642. doi:10.1126/science.277.5332.1639

Salazar JML, Hernández PA, Pérez NM, Melián G, Álvarez J, Segura F, Notsu K (2001) Diffuse emission of carbon dioxide from Cerro Negro Volcano, Nicaragua, Central America. Geophys Res Lett 28:4275-4278. doi:10.1029/2001GL013709

Sano Y, Fischer TP (2012) The analysis and interpretation of noble gases in modern hydrothermal systems. In: Burnard P (ed) The noble gases as geochemical tracers, advances in isotope geochemistry. Chapter 10. Springer Berlin Heidelberg, Berlin, Heidelberg, pp 249-317. doi:10.1007/978-3-642-28836-4_10

Sano Y, Marty B (1995) Origin of carbon in fumarolic gas from island arcs. Chem Geol 119:265-274. doi:10.1016/0009-2541(94)00097-R

Sano Y, Williams SN (1996) Fluxes of mantle and subducted carbon along convergent plate boundaries. Geophys Res Lett 23:2749-2752. doi:10.1029/96GL02260

Shaw AM, Hilton DR, Fischer TP, Walker JA (2003) Contrasting He–C relationships in Nicaragua and Costa Rica: insights into C cycling through subduction zones. Earth Planet Sci Lett 214:499-513. doi:10.1016/S0012-821X(03)00401-1

Shaw AM, Hilton DR, Fischer TP, Walker JA (2006) Helium isotope variations in mineral separates from Costa Rica and Nicaragua: Assessing crustal contributions, timescale variations and diffusion-related mechanisms. Chem Geol 230:124-139. doi:10.1016/j.chemgeo.2005.12.003

Sheppard S, Epstein S (1970) D/H and $^{18}O/^{16}O$ ratios of minerals of possible mantle or lower crustal origin. Earth Planet Sci Lett 9:232-239. doi:10.1016/0012-821X(70)90033-6

Shinohara H, Ohba T, Kazahaya K, Takahashi H (2008) Origin of volcanic gases discharging from a cooling lava dome of Unzen volcano, Japan. J Volcanol Geotherm Res 175:133-140. doi:10.1016/j.jvolgeores.2008.03.024

Sinclair AJ (1974) Selection of threshold values in geochemical data using probability graphs. J Geochem Explor 3:129-149.

Sparks RSJ, Biggs J, Neuberg JW (2012) Monitoring volcanoes. Science 335:1310-1311. doi:10.1126/science.1219485

Taran YA, Hedenquist JW, Korzhinsky MA, Tkachenko SI, Shmulovich KI (1995) Geochemistry of magmatic gases from Kudryavy volcano, Iturup, Kuril islands. Geochim Cosmochim Acta 59:1749-1761. doi:10.1016/0016-7037(95)00079-F

Troll VR, Hilton DR, Jolis EM, Chadwick JP, Blythe LS, Deegan FM, Schwarzkopf LM, Zimmer M (2012) Crustal CO_2 liberation during the 2006 eruption and earthquake events at Merapi volcano, Indonesia. Geophys Res Lett 39:L11302. doi:10.1029/2012GL051307

Weiss RF (1971) Solubility of helium and neon in water and seawater. Journal of Chemical & Engineering Data 16:235-241. doi:10.1021/je60049a019

Wilhelm E, Battino R, Wilcock RJ (1977) Low-pressure solubility of gases in liquid water. Chemical Reviews 77:219-262. doi:10.1021/cr60306a003

Williams SN, Sano Y, Wakita H (1987) Helium-3 emission from Nevado Del Ruiz Volcano, Colombia. Geophys Res Lett 14:1035-1038. doi:10.1029/GL014i010p01035

World Meteorological Organization (WMO) (2004) Global precipitation data sets. http://www.wmo.int/pages/themes/climate/climate_data_and_products.php. Accessed April 17th 2013

Tables

Table 1

Table 1 Compilation of temperature, CO_2 concentration, $\delta^{13}C$ and CO_2 flux measurements from zone N

	GPS (NAD27)			**Temperature (°C)**			**CO_2 Concentration (%)**			**$\delta^{13}C$ (‰)**			**CO_2 Flux ($g\ m^{-2}\ d^{-1}$)**
Site ID	**Latitude**	**Longitude**	**Altitude (m)**	**2010**	**2011**	**2012**	**2010**	**2011**	**2012**	**2010**	**2011**	**2012**	**2012**
CN-10	0532264	1383907	441	78	93	76.5	5.4	6.9	4.9	-6.7	-3.9	-3.5	65
CN-13	0532072	1383834	465		86	33.4		30.1	6.1		-4.0	-3.5	
CN-14	0532253	1383955	448		68	66.5		3.2	4.5		-3.4	-4.4	
CN-15	0532160	1383722	473		73	68.2		5.2	2.9		-3.4	-3.2	10380
CN-16	0532097	1383647	512		86.5	78.1			3.5			-2.9	326
CN-17	0532151	1383634	490		67	38.1		3.3	2.5		-3.3	-3.2	0
CN-18	0532108	1383588	490		80	72.1		3.1	2.2		-3.8	-3.8	305
CN-19	0532061	1383381	466		42.6	72.1		1.6	4.4		-3.7	-2.8	
CN-20	0532067	1383342	475		72.2	79.8			1.8			-2.9	512
CN-59	0532035	1383120	532			30.4			0.4			-19.4	13

Errors: T ±0.1°C, CO_2 vol. ±0.1 %, $\delta^{13}C$ ±0.1 ‰, CO_2 flux ±15 %

Table 2

Table 2 Compilation of temperature, CO_2 concentration, $\delta^{13}C$ and CO_2 flux measurements from zone C

	GPS (NAD27)			Temperature (°C)				CO_2 Concentration (%)				$\delta^{13}C$ (‰)				CO_2 Flux (g m^{-2} d^{-1})
Site ID	**Latitude**	**Longitude**	**Altitude (m)**	**2010**	**2011**	**2012**	**2013**	**2010**	**2011**	**2012**	**2013**	**2010**	**2011**	**2012**	**2013**	**2012**
CN-2	0532257	1382527	687	247	85	85.1	95.6	6.0	0.4	3.3	1.6	-9.3	-4.2	-3.4	-3.9	379
CN-5	0532341	1382527	617	94	91	96.7	95	20.0	2.1	53.7	16.4	-8.4	-3.5	-3.0	-2.8	3201
CN-6	0532367	1382406	592	97	98	97.4	97.3	88.0	99.4	100.0	89.0	-7.5	-3.1	-3.0	-2.7	6774
CN-7	0532423	1382435	602	240	180	145	205	83.0	67.0	80.9	80.0	-6.6	-1.6	-3.1	-2.6	24037
CN-8	0532455	1382448	591	221	270	155	188	73.0	17.0	76.4	83.0	-7.6	-2.5	-2.7	-2.6	29157
CN-9	0532508	1382532	596	79	91	81.1	81	1.2	1.4	1.5	2.5	-3.8	-4.4	-3.8	-3.3	
CN-12	0532222	1382531	692	104	189	87.7	79.8	5.3	1.4	3.6	1.5	-5.2	-4.0	-7.1	-8.3	1426
CN-51	0532395	1382437	631			87.8				2.9				-3.5		1168
CN-52	0532348	1382323	651			86.6				7.3				-4.7		442
CN-53	0532270	1382329	657			91.5				10.0				-3.2		1533
CN-55	0532278	1382617	673			86.6				4.7				-2.9		
CN-56	0532432	1382473	622			84.3				2.5				-3.1		252
CN-57	0532510	1382524	620			81.1				0-10				-3.8		2423
CN-58	0532491	1382615	616			64.6				0.4				-4.5		213
CN-60	0532357	1382405	600			23.7				0.0				-9.7		54
CN-61	0532395	1382409	606			97.5				89.5				-3.0		1192
CN-62	0532400	1382411	609			96.5				100.0				-2.8		389
CN-63	0532413	1382434	621			43.1				2.7				-2.6		113
CN-64	0532442	1382458	621			97.2				44.8				-2.9		998
CN-65	0532469	1382491	623			25.1				0.1						262
CN-66	0532358	1382310	683			67.1				1.5				-4.7		572
CN-67	0532300	1382317	676			66.4				1.9				-3.2		1533

Errors: T ±0.1°C, CO_2 vol. ±0.1 %, $\delta^{13}C$ ±0.1 ‰, CO_2 flux ±15 %

Table 3

Table 3 Compilation of temperature, CO_2 concentration, $\delta^{13}C$ and CO_2 flux measurements from zone S

	GPS (NAD27)												**CO_2 Flux (g m^{-2} d^{-1})**
Site ID	**Latitude**	**Longitude**	**Altitude (m)**	**2011**	**2012**	**2013**	**2011**	**2012**	**2013**	**2011**	**2012**	**2013**	**2012**
CN-21	0532279	1380828	450	45.3			1.8			-10.4			
CN-22	0532287	1381030	451	47.2			3.3						
CN-23	053288	1381032	452	54.7			5.4						
CN-24	0532289	1381033	452	64.3			6.0						
CN-26	0532291	1381037	453	63.2			2.7						
CN-27	0532292	1381039	453	66.2			2.8						
CN-28	0532293	1381041	453	70.7			4.7						
CN-29	0532294	1381042	453	74.6			15.3						
CN-30	0532289	1380842	453	81.1			46.8			-3.1			
CN-31	0532297	1381045	453	81.4			100.2						
CN-32	0532297	1381045	453	91.2			100.6						
CN-33	0532300	1381051	452	92			100.5						
CN-35	0532302	1381054	451	93			100.5						
CN-36	0532296	1380953	451	88.5			99.8			-2.8			
CN-37	0532298	1380856	451	91.2			60.6			-2.4			
CN-38	0532298	1380858	451	91.1			50.4			-2.7			
CN-40	0532301	1380861	450	87.3			21.6			-2.6			
CN-41	0532303	1380863	450	76.5			13.8						
CN-42	0532311	1381067	450	62.5			12.6						
CN-43	0532312	1381070	449	50.9			11.6						
CN-44	0532312	1381070	449	53			9.1						
CN-45	0532309	1380869	449	45			6.3			-0.9			
CN-46	0531996	1381025	438	38.5									
CN-48	0532032	1381049	441	55.1			4.0			-3.7			
CN-50	0532070	1381085	445	35.4			0.4			-3.6			
CN-68	0532023	1381027	452	59.7	48.2	58.5	6.3	2.8	4.4	-3.3	-4.2	-3.2	466
CN-69	0532129	1381060	459		47			4.0			-3.9		218
CN-70	0532194	1380999	434		46.4			2.3			-5.0		164
CN-71	0532234	1380944	469		39.9			1.2			-4.7		0
CN-72	0532271	1380906	472		43.6			5.4			-2.1		0
CN-73	0532250	1380882	472		77.2			11.5			-3.3		1804
CN-74	0532229	1380856	473		52.3			0.9			-3.5		167
CN-75	0532316	1380882	475		27.2			1.5			-32.8		0
CN-76	0532300	1380860	478	88.6	87.5	87.5	41.7	20.9	10.8	-2.6	-3.3	-2.7	1638
CN-77	0532295	1380851	470	91.4	91.8	91.7	100.5	33.6	30.6	-2.4	-3.0	-2.6	21539
CN-78	0532277	1380823	473	63.1	70.5	76.8	7.0	4.1	3.7	-5.2	-3.8	-5.1	756
CN-79	0532344	1380824	482		51.6			30.0			-1.5		258
CN-80	0532341	1380797	484		49.6			8.1			-3.1		306
CN-81	0532341	1380797	484		36.1			1.5			-4.6		17
CN-82	0532391	1380798	496		69.1			25.0			-3.1		703
CN-83	0532450	1380760	521		56			16.3			-3.2		656
CN-84	0532000	1380803	567		59			20-30			-2.2		2812
CN-85	0532274	1380868	471		87.2			26.1			-3.2		749
CN-86	0532268	1380858	464		70.8			2.7			-7.4		86
CN-87	0532277	1380854	576		83.2			7.9			-3.9		9295
CN-88	0532287	1380878	469		70			10.5			-3.5		509
CN-89	0532056	1381073	451	41.1	41	44.6	1.0	2.2	2.9	-4.1	-4.7	-3.9	118
CN-90	0532074	1381024	456		46.7			3.9			-3.6		5631
CN-91	0532167	1380977	450		54.8			2.6			-4.1		476
CN-92	0532321	1380837	460		80.1			17.1			-3.3		1127
CN-93	0532313	1380824	455		62.5			10.1			-3.7		1440
CN-94	0532336	1380821	463		83.8			12.4			-3.5		3223
CN-95	0532370	1380810	468		51.1			25.4			-0.8		1230
CN-96	0532363	1380795	482		56.1			9.2			-3.6		388
CN-97	0532384	1380824	480		35.7			2.4			-2.1		49
CN-98	0532422	1380782	508		74.1			25.9			-3.1		606
HOLE	0528759	1380890	309		26.1			0.0			-18.8		0

Errors: T ±0.1°C, CO_2 vol. ±0.1 %, $\delta^{13}C$ ±0.1 ‰, CO_2 flux ±15 %

Table 4

Table 4 Analysis of $\delta^{13}C$ samples from soil gas measurements in zones N, C and S collected in 2010, 2011, 2012 and 2013

Zone ID	Site ID	GPS (NAD27)		September 2010	January 2011	January 2012	May 2013
		Latitude	Longitude	(‰)	(‰)	(‰)	(‰)
Zone N	CN-13	0532072	1383834		-3.5	-3.5	
	CN-10	0532264	1383907	-6.7	-3.9	-3.5	
	CN-14	0532253	1383955		-3.4	-4.4	
	CN-15	0532160	1383722		-3.4	-3.2	
	CN-17	0532151	1383634		-3.3	-3.2	
	CN-18	0532108	1383588		-3.8	-3.8	
	CN-19	0532061	1383381		-3.8	-2.8	
Zone C	CN-9	0532508	1382532	-3.8	-4.4	-3.8	-2.6
	CN-12	0532222	1382531	-5.2	-4.0	-7.1	-8.3
	CN-8	0532455	1382448	-7.6	-2.5	-2.9	-2.7
	CN-7	0532423	1382435	-6.6	-1.6	-3.1	-2.6
	CN-6	0532367	1382406	-7.5	-3.1	-3.0	-2.7
	CN-5	0532341	1382527		-3.5	-3.0	-2.8
	CN-2	0532257	1382527	-9.3	-4.2	-3.4	-3.9
Zone S	CN-71	0532277	1380823		-5.2	-3.8	-5.1
	CN-77	0532295	1380851		-2.4	-3.0	-2.6
	CN-76	0532300	1380860		-2.6	-3.3	-2.7
	CN-68	0532023	1381027		-3.3	-4.2	-3.2
	CN-89	0532056	1381073		-4.1	-4.7	-3.9

Table 5

Table 5 Helium isotope data from 2012, collected at fumaroles A and B in zone C

Sample Site	**GPS (NAD27)**		**Site ID**	**$^4He/^{20}Ne$ [a]**	**$^3He/^4He$ [b]**	**$CO_2/^3He$ ($x10^9$)**	**Fumarole $\delta^{13}C$ (‰)**	**Soil $\delta^{13}C$ (‰)**
	Latitude	**Longitude**						
Fumarole A1	0532455	1382448	CN-7	11.6	6.77 ± 0.22	16.4	-3.1	-3.0
Fumarole A2	0532455	1382448	CN-7	12.9	6.37 ± 0.21	13.8	-3.0	-3.0
Fumarole B	0532423	1382435	CN-8	38.3	7.38 ± 0.17	14.5	-3.5	-3.1
Shaw et al. (2003):								
Fumarole A	0532455	1382448		14.1	6.99 ± 0.07	31	-2.3	

Results from Shaw et al. (2003) were sampled from fumarole A in January 2002

$CO_2/^3He$ uncertainty = ± 5%, $^3He/^4He$ uncertainty = ±0.17-0.22 at 2σ

Soil $\delta^{13}C$: from gas sampling with glass vials (± 0.1 ‰); **Fumarole $\delta^{13}C$:** from gas sampling with copper tubes (± 0.5 ‰)

[a] **$^4He/^{20}Ne$** = $[(^4He/^{20}Ne)_{measured}/(^4He/^{20}Ne)_{air}]$ x (βNe/βHe) β = Bunses coefficient from Weiss (1971) = GWDR T = 15°C

[b] **$^3He/^4He$:** air-corrected $^3He/^4He$ isotope ratio (R_C/R_A)

Table 6

Table 6 Three-component mixing results using principal end-members from Sano and Marty (1995) and Li and Bebout (2005)

	Sano and Marty (1995) end-members		
Sample	*M (-6.5 ‰)*	*L (-0 ‰)*	*S (-30 ‰)*
Fumarole A1	10	82	8
Fumarole A2	11	82	7
Fumarole B	10	80	10
	Li and Bebout (2005) end-members		
	M (-6.5 ‰)	*L (1.9 ‰)*	*S (-22 ‰)*
Sample			
Fumarole A1	9	73	18
Fumarole A2	11	73	16
Fumarole B	10	71	19
Result from Shaw et al. (2003)			
	M (-6.5 ‰)	*L (-0 ‰)*	*S (-30 ‰)*
Cerro Negro	5	89	6
Nicaragua mean	6	87	8
Costa Rica mean	9	82	9
Worldwide mean	13	75	13

Mantle (M), Marine carbonate (L) and Sedimentary (S) proportions (in %)

Nicaraguan and Costa Rican volcanic arcs, and the worldwide mean for subduction zones from Shaw et al. (2003), using end-members from Sano and Marty (1995)

Figures

Figure 1

Topographic map of northwestern Nicaragua and prominent volcanic centers which are part of the NW-SE trending Central American Volcanic Arc (CAVA) (Google Earth terrain data, 2013).

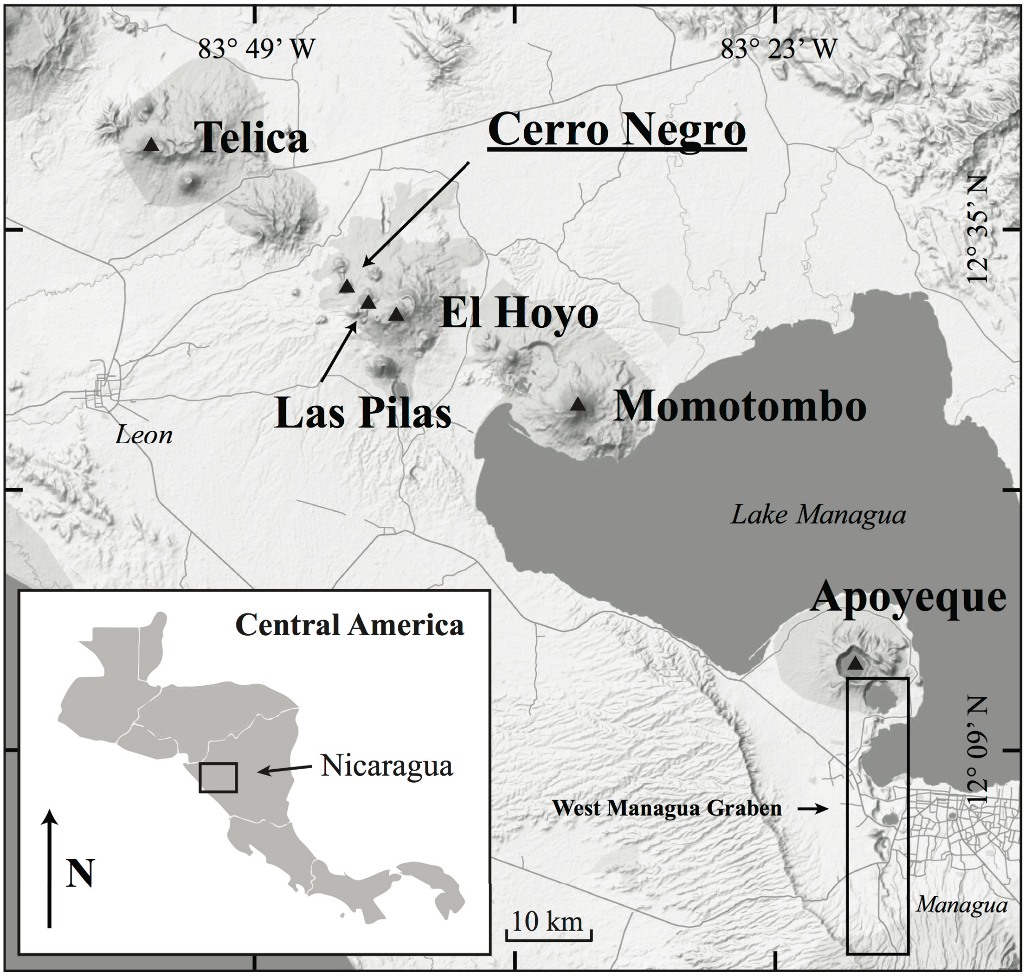
83° 49' W
83° 23' W
Telica
Cerro Negro
12° 35' N
El Hoyo
Las Pilas
Leon
Momotombo
Lake Managua
Apoyeque
12° 09' N
Central America
Nicaragua
N
West Managua Graben
10 km
Managua

Figure 2

Regional map of Cerro Negro volcano, Cerro La Mula cinder cones and the Cristo Rey craters. Shown on the map are major thermal zones (in red) and the associated division of sampling localities (zone N, zone C and zone S). Note the north-south alignment of volcanic centers known as the Cerro La Mula-Cerro Negro alignment.

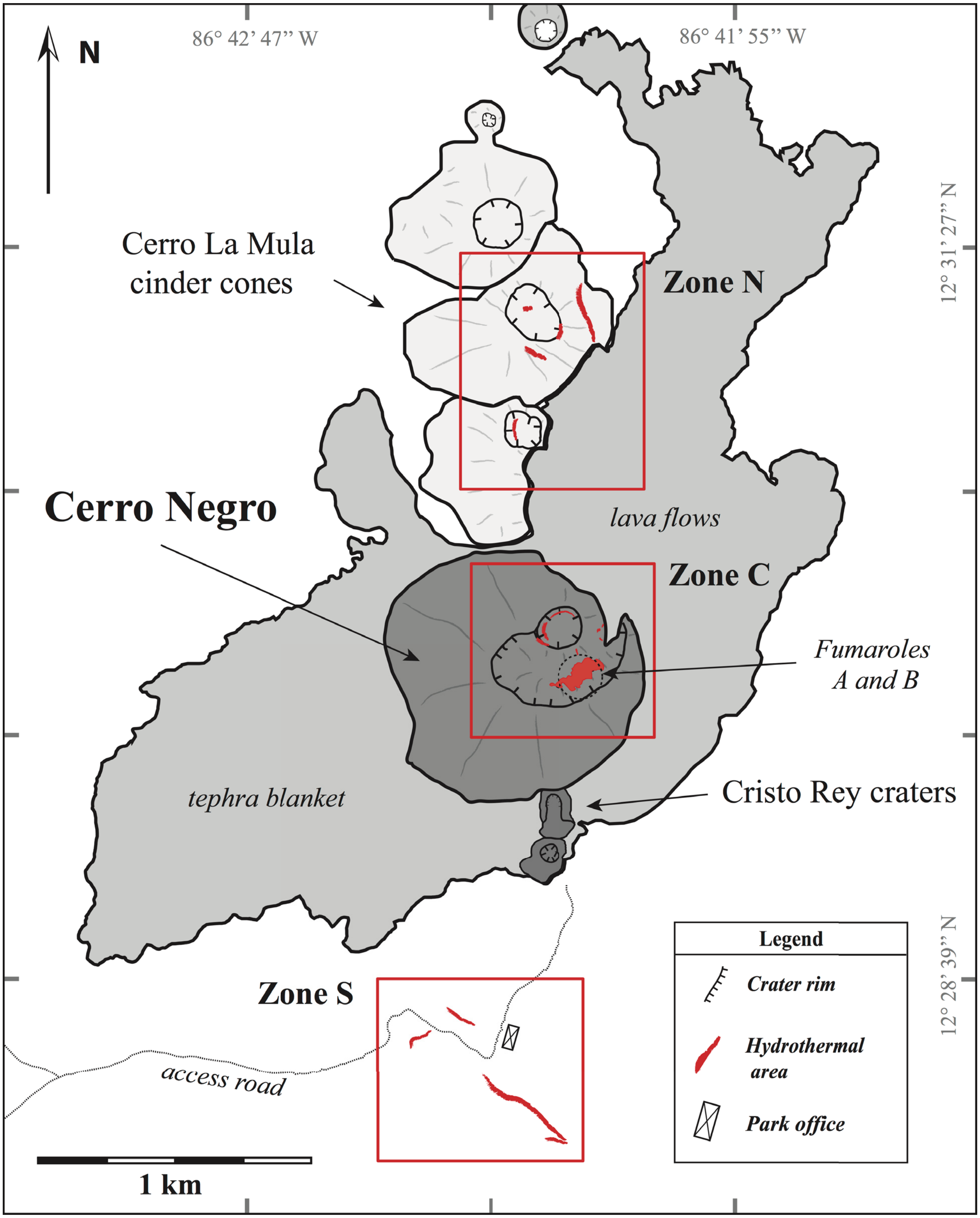
N
86° 42’ 47’’ W
86° 41’ 55’’ W
12° 31’ 27’’ N
12° 28’ 39’’ N
Cerro La Mula
cinder cones
Zone N
Cerro Negro
lava flows
Zone C
Fumaroles
A and B
Cristo Rey craters
tephra blanket
Zone S
access road
1 km
Legend
Crater rim
Hydrothermal
area
Park office

Figure 3

Histogram plots of stable carbon isotope measurements from soil gas and fumarolic samples collected in 2010, 2011, 2012 and 2013. Data have been grouped by zone and year with each individual histogram representing the number of sites, whose $\delta^{13}C$ falls within the designated range (± 0.05 to 0.5‰).

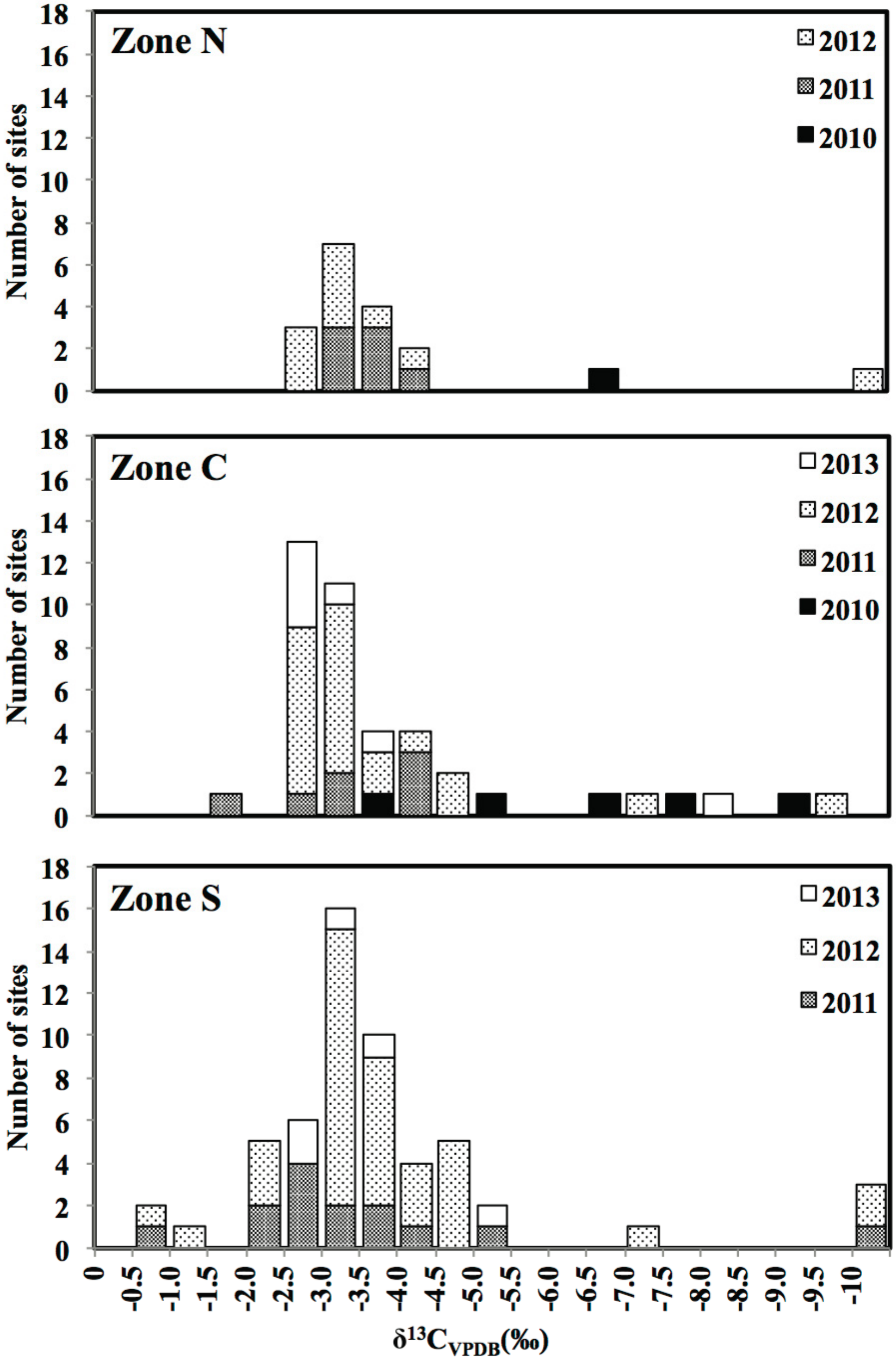
Zone N
2012
2011
2010
Zone C
2013
2012
2011
2010
Zone S
2013
2012
2011
Number of sites
0
2
4
6
8
10
12
14
16
18
0
-0.5
-1.0
-1.5
-2.0
-2.5
-3.0
-3.5
-4.0
-4.5
-5.0
-5.5
-6.0
-6.5
-7.0
-7.5
-8.0
-8.5
-9.0
-9.5
-10
$\delta^{13}C_{VPDB}$(‰)

Figure 4

Temperature (a), CO_2 concentration (b) and CO_2 flux (c) plotted against $\delta^{13}C$ for samples collected in 2010, 2011, 2012 and 2013, and grouped by zone. The largest temperature (>150°C) and CO_2 flux (>20000 g m^{-2} d^{-1}) anomalies correspond to three key sites of degassing: fumaroles A and B in zone C and a high CO_2 flux site in zone S visible in Figure 6. Magmatic/hydrothermal sites exhibit ^{13}C-enriched $\delta^{13}C$ signatures and predominantly high temperatures, CO_2 concentrations and CO_2 flux values. Background soil gas signatures characteristic of biogenic sources have ^{13}C-depleted $\delta^{13}C$ values and low temperatures, CO_2 concentrations and CO_2 fluxes. The third group of sites represents a mixing field between magmatic/hydrothermal and biogenic sources and is characterized by $\delta^{13}C$ values of ~ -20‰ and low temperatures, CO_2 concentrations and CO_2 fluxes which are nevertheless slightly higher than background soil gas values.

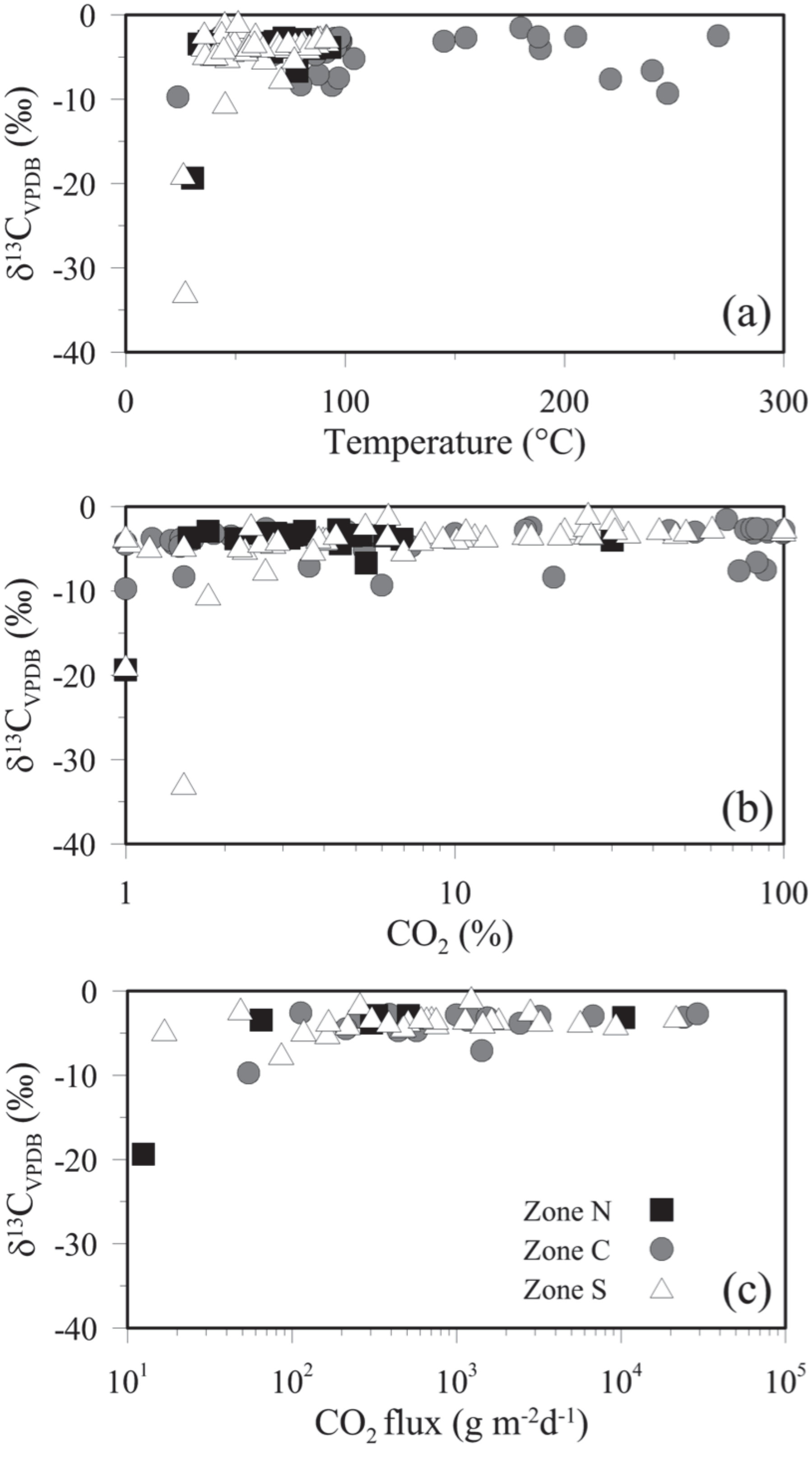
δ13CVPDB (‰)
0
-10
-20
-30
-40
(a)
0
100
200
300
Temperature (°C)
δ13CVPDB (‰)
0
-10
-20
-30
-40
(b)
1
10
100
CO2 (%)
δ13CVPDB (‰)
0
-10
-20
-30
-40
Zone N ■
Zone C ●
Zone S △
(c)
10^1
10^2
10^3
10^4
10^5
CO2 flux (g m-2d-1)

Figure 5

$\delta^{13}C$, temperature, CO_2 and hydrogen concentrations collected along a NE-SW transect across the main segment of hydrothermal activity at zone S. Measurements extend 50 m from the southwest to the northeast. The transect covers a variety of surface types from vegetated to heavily altered; as such, the grey segment represents a central part of the transect characterized by vegetation-kill. The precise location of the transect is marked on Figure 6 (lower right hand panel).

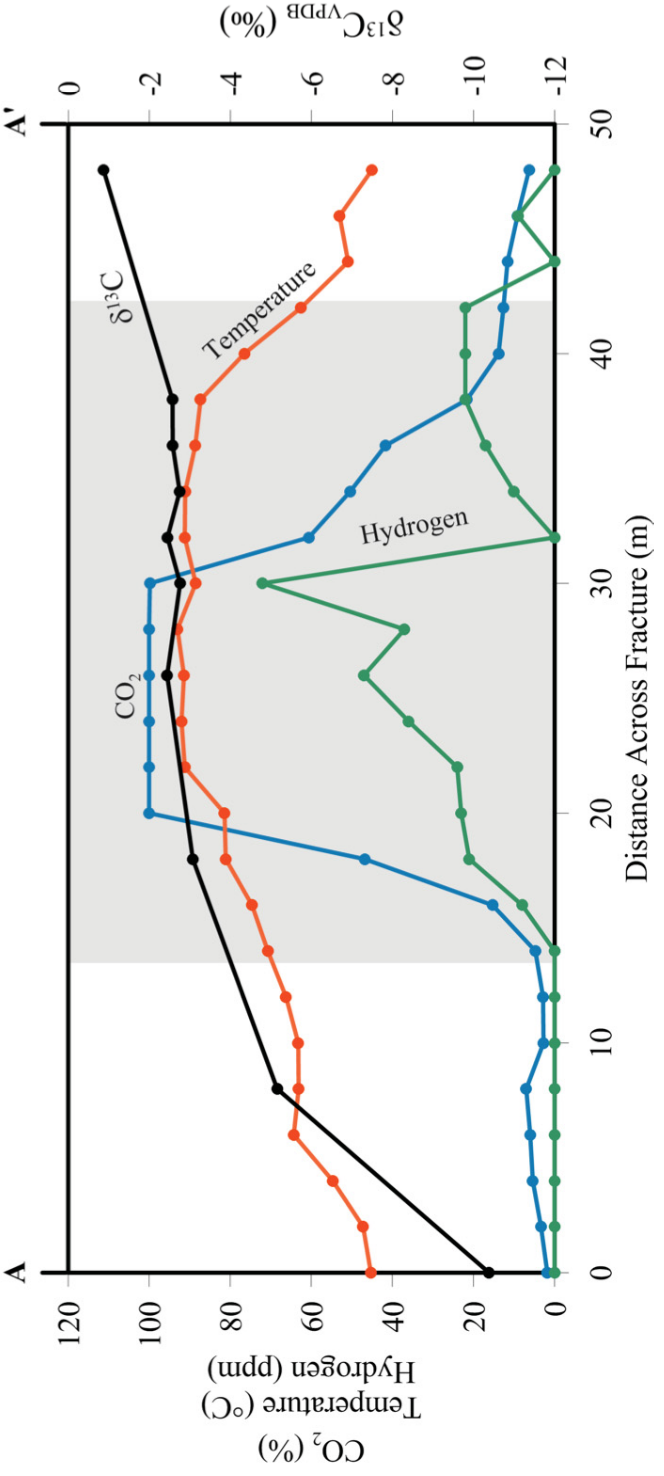
A
A'
CO$_2$ (%)
Temperature (°C)
Hydrogen (ppm)
120
100
80
60
40
20
0
δ^{13}C$_{VPDB}$ (‰)
0
-2
-4
-6
-8
-10
-12
Distance Across Fracture (m)
0
10
20
30
40
50
δ^{13}C
Temperature
CO$_2$
Hydrogen

Figure 6

CO_2 soil flux maps for zones N (a), C (b) and S (c). The left column is a series of corresponding satellite images for reference (source: Google Earth, 2013). The red dots represent locations of soil flux measurement sites in 2012. The majority of elevated flux sites are visible in the satellite photos due to chemical alteration (white areas) and vegetation kill. Contour maps are shown in the right column. Three “hot spots” of hydrothermal activity are marked in red. In zone C these represent fumaroles A and B. Areas outside the contour maps have background soil CO_2 flux below 10 g m^{-2} d^{-1} which is our measurement limit. In zone S, the black line indicated by two black arrows represents the NE-SW transect in Figure 5 (lower right hand panel).

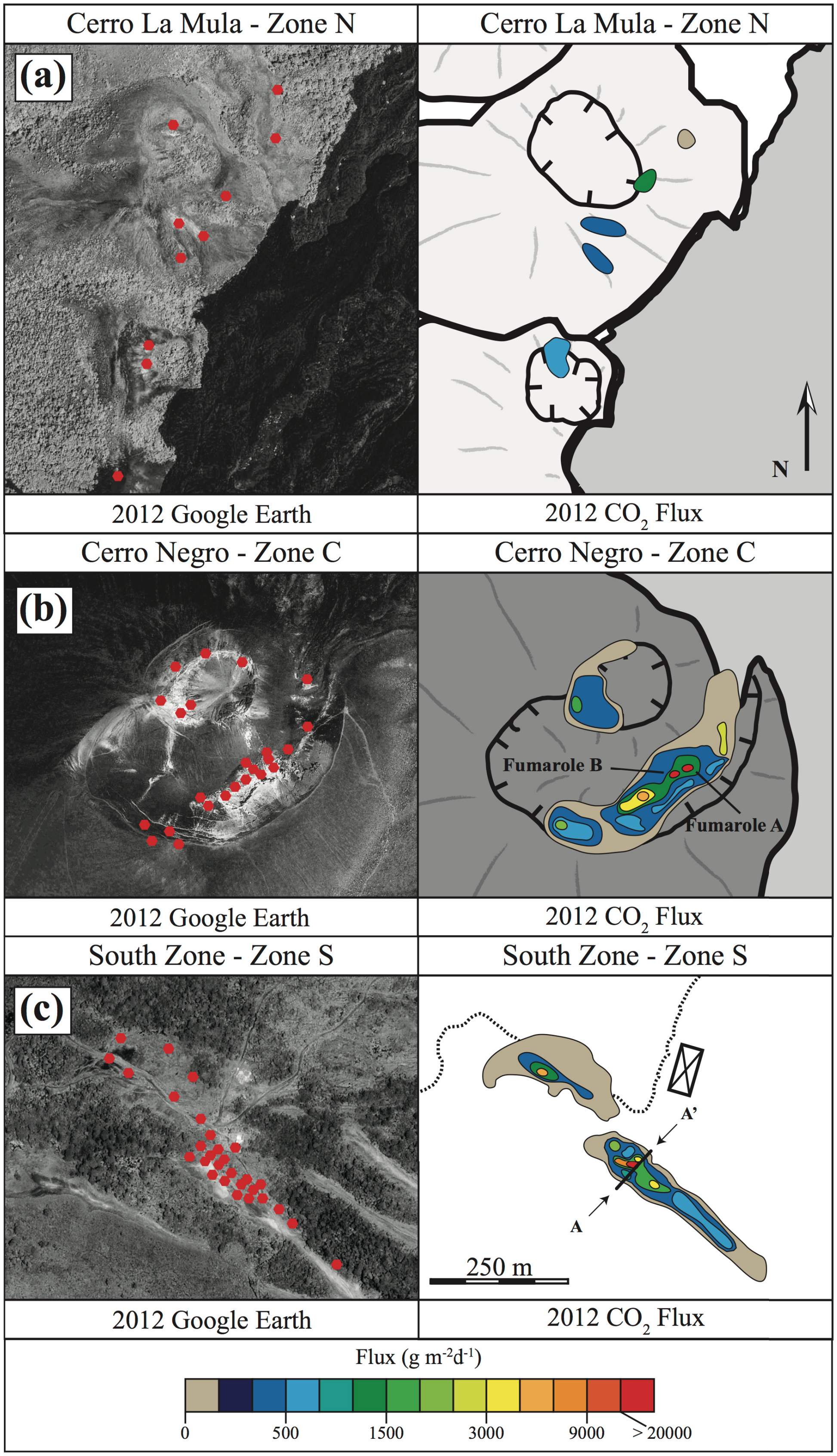
Cerro La Mula - Zone N
Cerro La Mula - Zone N
(a)
N
2012 Google Earth
2012 CO$_2$ Flux
Cerro Negro - Zone C
Cerro Negro - Zone C
(b)
Fumarole B
Fumarole A
2012 Google Earth
2012 CO$_2$ Flux
South Zone - Zone S
South Zone - Zone S
(c)
A'
A
250 m
2012 Google Earth
2012 CO$_2$ Flux
Flux (g m^{-2}d^{-1})
0
500
1500
3000
9000
> 20000

Figure 7

Plot of δ^{18}O and δD for fumaroles A and B in zone C and water well samples located 8 km from the summit of Cerro Negro. Momotombo and Mombacho fumarole values from Elkins et al. (2006). Local precipitation data from the International Atomic Energy Agency (IAEA) 2004 and World Meteorological Organization (WMO) 2004. Andesitic/arc-related water field after Giggenbach (1992).

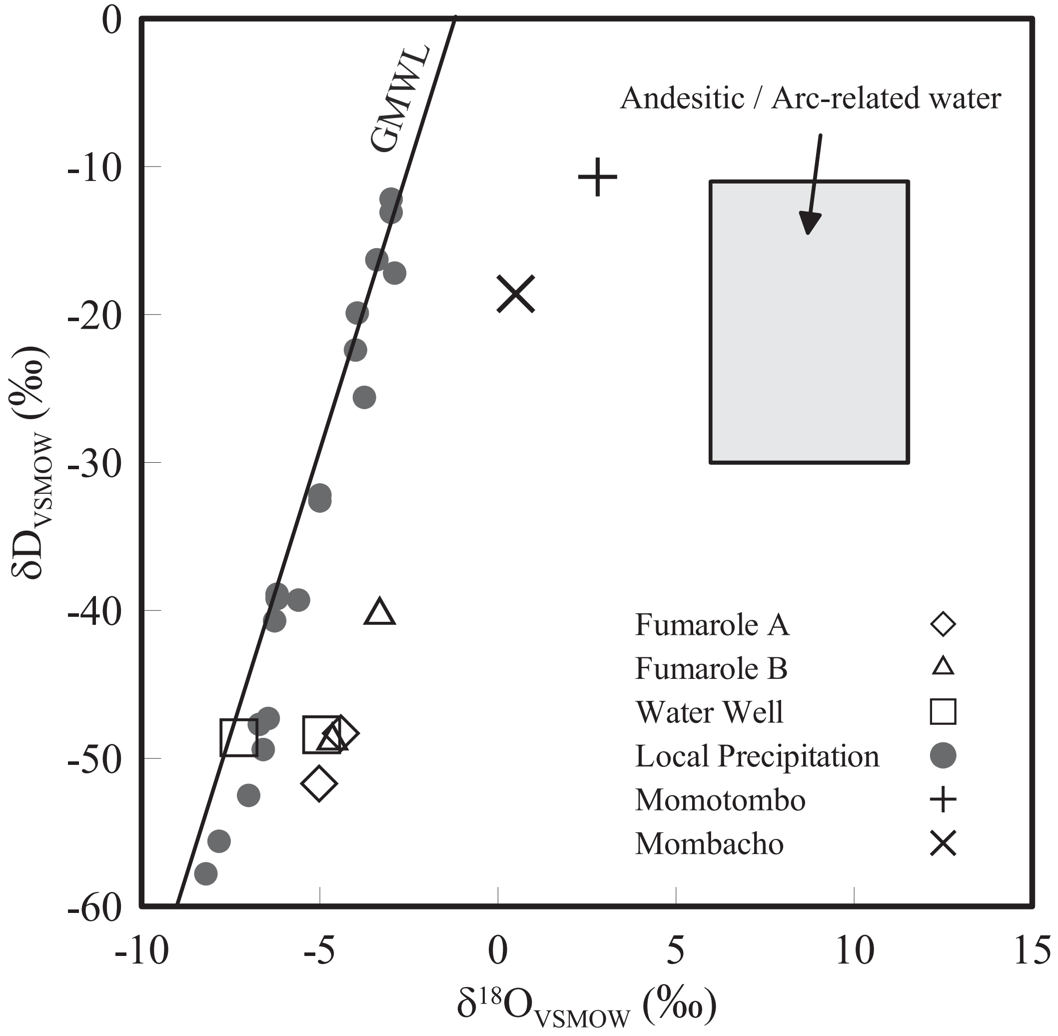
0
-10
-20
-30
-40
-50
-60
-10
-5
0
5
10
15
δD_{VSMOW} (‰)
$\delta^{18}O_{VSMOW}$ (‰)
GMWL
Andesitic / Arc-related water
Fumarole A ◇
Fumarole B △
Water Well □
Local Precipitation ●
Momotombo +
Mombacho ×

Figure 8

Plots of $\delta^{13}C$ (a), $^3He/^4He_{air\text{-}corrected}$ (b), $CO_2/^3He$ (c) for April 1992 (post eruption), December 1999, September 2010, January 2011 and 2012 and May 2013. Black arrows represent three eruptions that occurred during this time period in April 1992, May 1995 and August 1999. Grey boxes represent worldwide MORB averages for $\delta^{13}C$ (-4‰ to -9‰), $^3He/^4He$ (7-9 R_A) and $CO_2/^3He$ (4×10^9 to 26×10^9) (Shaw et al. 2003).

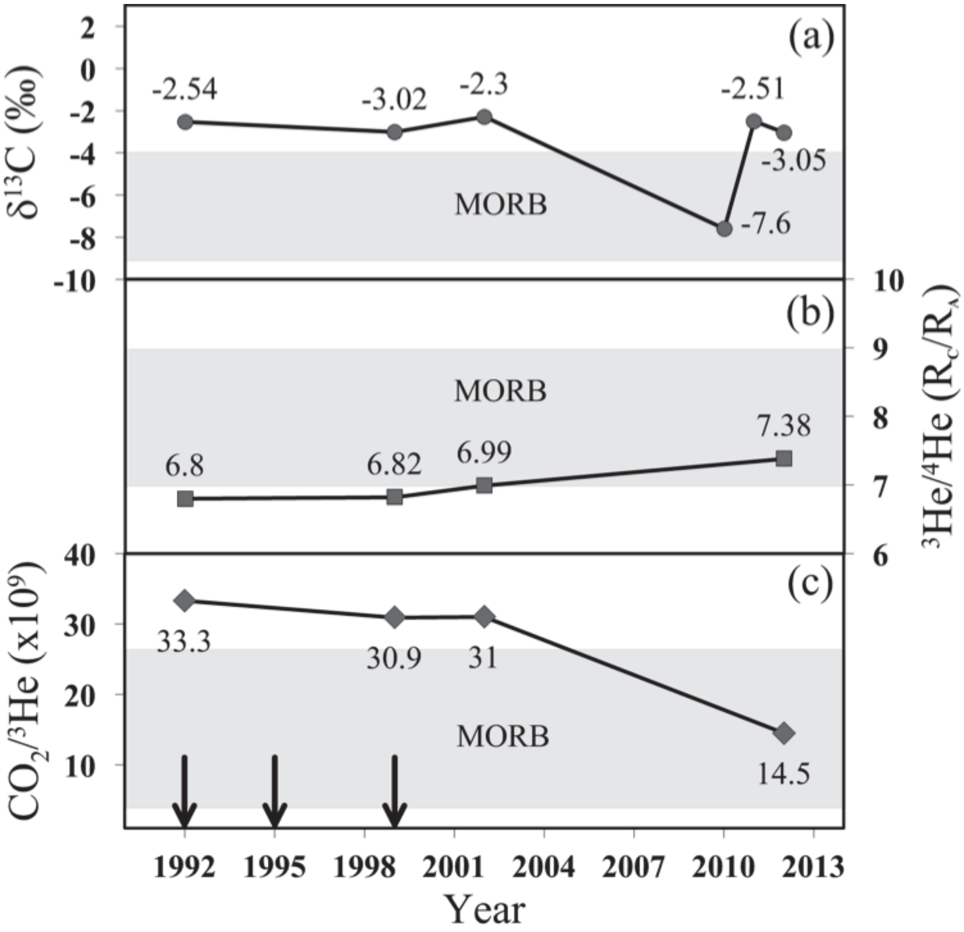
(a)
δ¹³C (‰)
2
0
-2
-4
-6
-8
-10
-2.54
-3.02
-2.3
-2.51
-3.05
-7.6
MORB
(b)
³He/⁴He (Rc/RA)
10
9
8
7
6
MORB
6.8
6.82
6.99
7.38
(c)
CO₂/³He (x10⁹)
40
30
20
10
33.3
30.9
31
14.5
MORB
1992
1995
1998
2001
2004
2007
2010
2013
Year

Figure 9

Plot of $CO_2/^3He$ vs $\delta^{13}C$ after Sano and Marty (1995). Data points in 2012 show a stronger MORB component relative to past measurements suggesting a stronger upper mantle input into the system. Solid lines represent mixing trends among the three end members represented by the grey fields. The dashed line represents a modified two-component mixing line that represents the closest approach to the data points. Given the defined end-members, the resulting gas is a predominant mixture of MORB and lithospheric/carbonate carbon, with a small component of sedimentary/organic carbon.

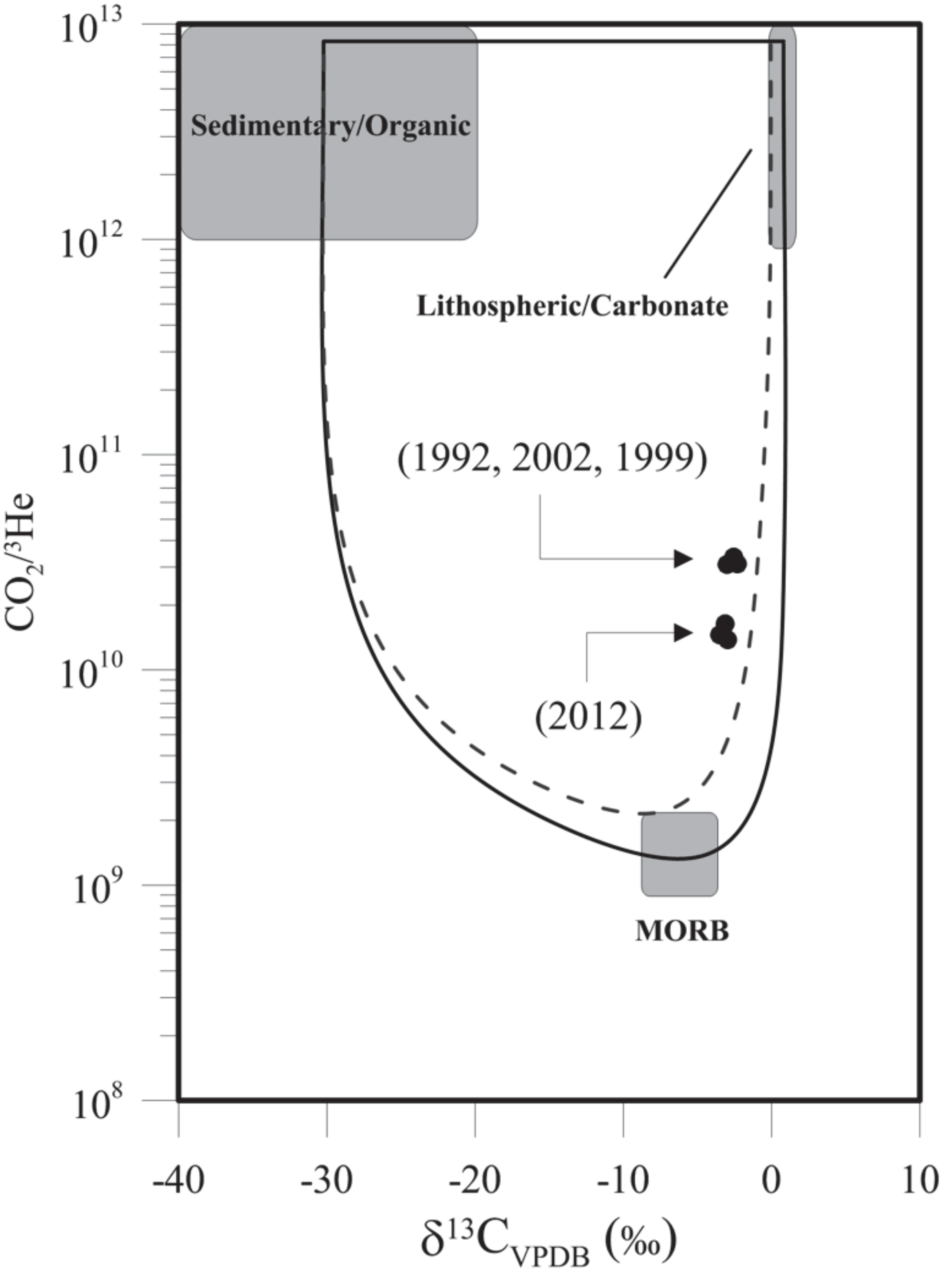

10^{13}
10^{12}
10^{11}
10^{10}
10^{9}
10^{8}
$CO_2/^3He$
Sedimentary/Organic
Lithospheric/Carbonate
(1992, 2002, 1999)
(2012)
MORB
-40
-30
-20
-10
0
10
$\delta^{13}C_{VPDB}$ (‰)

Link to Chapter 3

In Chapter 2, I highlight how small volcanic centers have deep magmatic reservoirs that enable fast ascent of magma to the surface, preserving high volatile contents, which in turn drive explosive basaltic eruptions. The identification of these conduits and magmatic reservoirs is essential because it helps us understand the likelihood of future explosive activity and provides constraints on geophysical interpretations of precursory signals. Cerro Negro and Hekla volcano in Iceland are both examples of volcanic centers with very calm repose periods and very little warning time before an eruption. It is thus essential that we can reliably identify signs of unrest prior to an eruption.

In this last chapter, I investigate the relationship between repose interval and the volatile content of Hekla magmas. Magmatic volatiles are important drivers of explosivity, so it is essential that we understand the conditions that lead to high volatile content in these magmas. I present a comprehensive study of H_2O, CO_2, S and Cl in melt inclusions from four eruptions that vary in size, composition and explosivity. I use these data to better constrain the behavior of volatiles in a range of magma compositions and to shed light upon the configuration of the plumbing network beneath Hekla. This dataset may complement future observations of seismicity and deformation indicative of changes that might signify movement of magma within reservoirs and conduits prior to an eruption.

Chapter 3

Volatile content of Hekla magmas

Gregor Lucic[1], Anne-Sophie Berg[1] and John Stix[1]

[1]Department of Earth and Planetary Sciences and GEOTOP, McGill University, 3450 University Street, Montreal, Quebec, H3A 0E8 Canada

---

Manuscript III – to be submitted

Abstract

Olivine-hosted melt inclusions from four eruptions at Hekla volcano in Iceland were analyzed for their dissolved volatile contents. Measurements of dissolved H_2O, CO_2, S and Cl contents using FTIR and electron microprobe reveal a positive correlation between the repose interval, magmatic evolution and volatile contents of magmas. H_2O is the dominant volatile species; it behaves as an incompatible element, increasing in concentration over time as a result of fractional crystallization. The full suite of H_2O contents ranges from a low of 0.80 wt. % in basaltic andesites to a maximum of 5.67 wt. % in rhyolites. In more voluminous, silicic eruptions, water contents display a range of 4 wt.% due to an overall decrease in water content in the later erupted material. Decreasing H_2O/K_2O at fixed major element compositions suggest that syn-eruptive degassing plays an important role in decreasing water content. CO_2 is present only in the most evolved eruptions; for these its concentrations are low (~20-30 ppm). The decrease in S content from basaltic andesite to rhyolite suggests that sulfide saturation is attained when the melt composition reaches basaltic andesite, resulting in the precipitation of pyrrhotite. The similarity in major element compositions of melt inclusions and matrix glasses, along with no evidence of olivine disequilibrium suggest that olivines crystalize late in the evolution of the magma chamber or even during eruption. Therefore, volatile contents in the melt inclusions represent the volatile state of the magma prior eruption or during ascent. The continued increase in water contents from basalt to rhyolite, syn-eruptive degassing and sulfide saturation suggest that the large majority, or possibly all of Hekla's melt inclusions represent volatile-undersaturated melt. Vapour saturation pressured obtained using the most volatile-rich melt inclusions suggest the presence of a magma chamber at a depth of ~7 km. This is an agreement

with geophysical observations from recent eruptions, but given the possibility of volatile-undersaturated melts this is a minimum value.

1. Introduction

The generation and evolution of water-rich silicic magmas at volcanic centers in Iceland have been a topic of great interest and debate (Bindeman et al., 2012; Hards et al., 2000; Jónasson, 2007; Kuritani et al., 2011; Lacasse et al., 2007; Martin and Sigmarsson, 2010). Spreading systems are commonly associated with H_2O-poor mafic magmas, yet in Iceland, there are voluminous eruptions of H_2O-rich silicic magmas. The origin of these magmas is thought to be a function of crustal assimilation at various storage depths, crystal fractionation, and long residence times within the thickened Icelandic crust (Schattel et al., 2014). Detailed tephrochronological and geochemical studies at Hekla volcano, Iceland's most active and productive volcanic center, have revealed that the volume of erupted material, explosivity, composition of the first erupted material and duration of the eruption are directly related to the duration of the preceding repose period (Thorarinsson, 1967; Larsen et al., 1999). In other words, the longer the repose period, the more evolved, explosive and voluminous the eruption. This is a key finding and makes this volcano an ideal natural laboratory for the study of volatile contents in both mafic and silicic magmas.

In this report, we present a detailed volatile study of four eruptions from Hekla volcano. Our aim is to address the following key questions. (1) How do volatile contents compare and contrast among large, medium and small eruptions? (2) Are the magmas volatile saturated or unsaturated prior to eruption? (3) Are large eruptions and small eruptions sourced from the same magma chamber, or is there any indication of multiple reservoirs? (4) What can H_2O-CO_2

relationships tell us about the storage depths and evolution of silicic versus mafic magmas at Hekla and in Iceland more generally?

2. Hekla volcano

Hekla's first historic eruption was recorded in 1104 AD; since that event it has erupted at least 18 times (Thorarinsson, 1967; Thorarinsson and Sigvaldason, 1972; Gronvold et al., 1983; Gudmundsson et al., 1992). In addition to these historic events, stratigraphic records reveal that Hekla's largest and most voluminous eruptions occurred in the Holocene between 1104 and > 7000 BP (Larsen and Thorarinsson, 1977). Its most recent event was a small eruption from the southwest flank in February 2000.

2.1 Evolution of magmas

Eruptive products at Hekla vary in composition from rhyolite to basalt. This range is thought to be a product of magmatic evolution at different stages (Sigmarsson et al., 1992; Sverrisdottir, 2007; Chekol et al., 2011; Portnyagin et al., 2012). (1) Initial basaltic melts rise through the crust where they evolve to basaltic andesites through fractional crystallization. (2) If these melts reside in the tholeiitic host rocks for a sufficient length of time, they evolve to dacites through a combination of fractional crystallization and crustal assimilation. If the residence time is sufficiently long, they can evolve to rhyolites. (3) Injections of basaltic andesites into these evolved chambers may produce hybrid mixtures of magma and contribute to the development of compositionally stratified magma chambers. These injections also may force the chamber into disequilibrium and trigger an eruption. (4) Less evolved compositions spend less time in the crust and may ascend with little or no assimilation and smaller amounts of fractional crystallization. The extent to which hydrothermally altered crustal rocks are assimilated is a topic of debate and is discussed below.

2.2 Estimates of magma storage

While the overall model of magmatic evolution at Hekla appears to be generally established, there is much discussion regarding the location and size of magma chambers beneath the volcano. Melt inclusion data on the saturation pressure of H_2O, obtained using the volatile-by-difference method (Devine et al., 1995), provide a minimum depth of storage at 9 km depth for the 1916 and 2000 basaltic eruptions (Moune et al., 2007). Direct measurements of H_2O in melt inclusions using Secondary Ion Mass Spectrometry (SIMS) and Fourier Transform Infrared Spectrometry (FTIR) provide a depth estimate of 5 to 6 km for the H3 and H4 silicic eruptions (Portnyagin et al., 2012).

After the 1980-81 eruption, inflationary signals suggested the presence of a magma chamber 5.5×10^7 m^3 in volume, centered at a depth of 7.7 km (Kjartansson and Gronvold, 1983). Dilatational strain data collected during the 1991 eruption suggested that magma was being erupted through a dyke, sourced from a magma chamber at 6.5 km depth with a radius of 2.5 km (Linde et al., 1993). The propagation of the dyke was initiated at 4 km depth, which could represent the roof of the magma chamber. The deflation signal during the 1991 eruption was placed at 9±6.5 km deep, with a volume of 1.45±0.60 x 10^{11} m^3 and modeled as a spherical chamber with a radius of 3.5 km (Sigmundsson et al., 1992). Ofeigsson et al. (2011) used InSAR data to identify two sources associated with the 2000 event. In the period leading up the eruption (1993-2000), they detected an inflation signal that shared a common source with the co-eruptive deflation during the event. They placed the first source at a depth of 14 to 18 km with a volume of 4 x 10^7 to 8 x 10^7 m^3. The second source produced a local inflation signal thought to be associated with the opening of the dyke. This signal had a source at 5.6 km depth, with an estimated volume of 5 x 10^6 to 6 x 10^6 m^3. Geirsson et al. (2012) used GPS data to model a horizontal ellipsoid magma chamber at a depth of 24±4 km depth, a spherical magma chamber at 24±5 km depth, or a vertical pipe-shaped chamber stretching between 10 to 21 km. In either case, the bulk of magma accumulation was interpreted to occur at deep crustal levels close to the Moho, which is situated somewhere between 20-29 km depth beneath Hekla (Allen et al., 2002). Sturkell et al. (2013) presented a review of deformational data at Hekla and concluded that the main reservoir is centered at ~10 km depth. Soosalu and Einarsson (2004) found no seismic evidence of any magma chamber in the 5-8 km depth range. Their S-wave attenuation data indicate a reservoir either shallower than 4 km or deeper than 14 km. However, the lack of hydrothermal activity argues against a reservoir shallower than 4 km (Ilyinskaya et al., 2015).

Given this large range in depth estimates obtained from geochemistry and geophysics, it remains difficult to establish a robust model for the plumbing network beneath Hekla. Modern-day monitoring covers a period in the volcano's history characterized by small eruptions of mafic compositions. In particular, we lack geophysical observations and direct measurements of volatile contents for the full range of eruptive styles and compositions from basalt to rhyolite.

This is especially significant if we consider that the magmatic network was possibly reconfigured following the 1947 eruption (Sturkell et al., 2013).

3. Sampling and analytical methods

3.1 Fieldwork

Four eruptions were sampled for volatile analysis in olivine-hosted melt inclusions. They are Holocene 3 or H3 (2,880 years BP, ^{14}C age from Dugmore et al., 1995), 1104, 1845 and 1991. These eruptions were chosen to represent a range in repose periods, compositions and volumes of erupted material. Samples were collected from exposures at five sections located at various distances and directions from Hekla (Figure 1).

The deposits of Hekla's largest and most voluminous eruption, H3, feature compositional zonation from 67.8 wt. % SiO_2 (whole rock on an anhydrous basis) at the base to 56.2 wt. % at the top (Sverrisdottir, 2007). The total volume of erupted material (lava and tephra) is estimated at 2.2 km^3 DRE (Sverrisdottir, 2007). The andesite end member was not sampled in this study, but it has been examined by others (Sverrisdottir, 2007; Portnyagin et al., 2012). The most striking feature of the deposit, best illustrated at section 1, is a change in color from white pumice fragments at the base of the deposit to reddish or pinkish pumice fragments at the top (Figures 2 and 3). A third break can be seen at section 2, where the top 15 cm of the deposit are characterized by the presence of darker pumice fragments. Based on these differences, we collected samples from three horizons: HK2013-H3-A (H3 base), HK2013-H3-B (H3 light top) and HK2011-H3-C (H3 dark top) (Figures 2 and 3).

In many respects, the 1104 eruption appears to be a smaller version of H3 (0.5 km^3 DRE from Sverrisdottir (2007)). Gradual changes in pumice color at ~20 cm, changes in grain size and the presence of a distinctive grey top suggest a zoned eruption. Whole rock data reveal that 1104 is in fact a rhyolite (Thorarinsson, 1967), recognized in Icelandic tephrochronology by its distinctive white color. At the sampled locality, the deposit is characterized by two normally graded pumice layers, the first 30 cm in thickness, overlain by a second 15 cm in thickness. Many of the pumices in the upper layer have grey banding, a feature that contributes to an overall change in color near the top of the deposit. The uppermost 5 cm of the deposit are marked by a distinct layer of grey pumice fragments interbedded with ash. Based on these distinctions, our sampling at section 3 was divided into HK2013-1104-A (1104 base), HK2013-1104-B (1104 light top) and HK2013-1104-C (1104 dark top) (Figures 2 and 3).

The 1845 eruption was sampled at section 4 (Figures 2 and 3). Similar to H3, this eruption is zoned but smaller in volume than H3 and slightly larger than 1104 (0.63 km^3 DRE from Sverrisdottir (2007). The deposit is characterized by fine lapilli at the base that grade upward into coarse lapilli. The increase in grain size is accompanied by an upward change to a darker color at 10 cm from the base which is associated with a change in whole rock composition from andesite to basaltic andesite (Thorarinsson, 1967). Samples from the 1845 package were restricted to a single horizon from the bottom 10 cm and referred to as HK2013-1845-A (or 1845).

The least evolved unit is that of the 1991 eruption, sampled on the northern flank of the volcano at section 5 (Figures 2 and 3). The deposit at this locality is 25 cm thick, reflecting the small volume of the eruption (0.15 km^3 DRE from Sverrisdottir (2007)). There is no indication of zonation in whole rock compositions from base to top, but there are distinct changes in grain size suggestive of two main eruptive pulses. This is in agreement with observations of tephra fall during the eruption (Gudmundsson et al., 1992). Whole rock compositions of the tephras and lavas plot within the basaltic andesite field (54 wt.% $SiO_{2,}$ Gudmundsson et al., 1992; Chekol et al., 2011). Samples from the 1991 eruption were collected at the base of the deposit and labeled HK2013-1991-A (or 1991).

3.2 FTIR analysis

Melt inclusions were analyzed using a Bruker Tensor 27 infrared spectrometer paired with a Bruker Hyperion 2000 microscope. Analyses were conducted with a 15x objective lens in transmission mode using a spectral resolution of 4 cm^{-1} and 256 scans for both background and sample measurements. The optical aperture was adjusted to enable three separate measurements of the same melt inclusion. With larger melt inclusions (~150 μm), it was possible to separate these points by 10 μm, but with smaller inclusions it was only possible to move the stage by 1-3 μm. In both cases, there was overlap between the sampling areas. Testing on in-house glass standards produced reproducible spectra down to an aperture diameter of 20 μm.

Peak heights for the 5200 cm^{-1} (H_2O_m), 4500 cm^{-1} (OH^-), 1630 cm^{-1} (H_2O_m), 1550 cm^{-1} and 1420 cm^{-1} ($CO_3{}^{2-}$) peaks were obtained using baselines following Newman et al. (1986), while the peak heights for the 3450 cm^{-1} ($H_2O_m + OH^-$) and 2350 cm^{-1} ($CO_{2\,m}$) peaks were obtained using a flat baseline (King et al., 2002). The size, thickness and composition of the melt inclusion determined which peaks were visible and viable. Normally, the absorbance of the 3450 cm^{-1} peak was less than 1. However, in rare instances this absorbance was between 1 and 1.5. If the top of the peak was not flattened due to saturation and the noise level was low, it was deemed usable following Newman et al. (1986). To enable low detection limits for CO_2, the entire instrument was placed in a protective shroud and purged using high purity nitrogen gas. The atmospheric CO_2 concentration within the shroud was measured at less than 50 ppm using a Green Eye CO_2 room analyzer. Using silicic and basaltic glass standards, we determined the practical detection limits for H_2O at 50 ppm, and 10 ppm for CO_2. Concentrations of CO_2 and H_2O were calculated using Beer's Law from Newman et al. (1986):

$$wt.\ \% = M*A / (\varepsilon\ d\ \rho)$$

where M is the molar mass of CO_2 or H_2O (g mol^{-1}), A is the absorption for the peak of interest, ε is the extinction coefficient for the peak (mol^{-1} cm^{-1}), d is the thickness of the wafer (cm) and ρ is the density of the glass in question (g L^{-1}). The list of extinction coefficients, their associated errors and corresponding peaks are shown in Table 1. Sample thickness was measured using the FTIR stage calibrated against a digital micrometer. The interference fringe method showed good agreement with the stage method.

Errors in the calculation of H_2O and CO_2 concentrations are associated primarily with the measurement of absorption (±2-20 %) and wafer thickness (±5 μm or ~5-15%). The error in thickness measurements is similar for all our samples, but absorption errors increase with small melt inclusions. Using replicate measurements of glass standards (M6N, M3N and PCD from Devine et al. (1995); EXP51 from Mangan and Sisson (2000)) at an aperture of 100 μm, we can reproduce absorption on the order of ±0.0001 (2σ). This places our best error estimate at ± 0.05 wt. % for H_2O and ± 5 ppm for CO_2. To obtain reliable measurements of melt inclusion glass, without any interference from the host crystal, we reduced the aperture diameter, which increases the noise of the spectra. By measuring the same melt inclusion three times we eliminated the need for smoothing, but the increased noise level is reflected in the increased error of the absorption (up to ± 20 %). In this worst-case scenario, we estimate our error at ±0.9 wt. % for H_2O and ± 15 ppm for CO_2. However, the large majority of samples have absorption errors which are much smaller, on the order of ±2-5 %. There is also an inherent error in our selection of extinction coefficients, especially when dealing with a large range in composition such as for Hekla. These were selected to represent the most accepted values (Table 1).

3.3 Electron microprobe analysis

Major elements in matrix glasses, olivines and melt inclusions, as well as S and Cl in matrix glasses and melt inclusions, were acquired using a JEOL 8900 electron microprobe at McGill University. To minimize Na loss for glasses, we used an accelerating voltage of 15 kV, a current of 2 nA and a defocused beam diameter of 15 μA. Counting times for Na were 15 s, 60 s for Cl, 120 s for S and 20 s for Si, Ti, Al, Fe, Mn, Mg, K, P. In order to improve detection limits for volatiles, we measured up to 3 points within a single melt inclusion using the accumulation method.

The practical detection limits for S and Cl were determined using repeat measurements on glass standards. Using KN9 (Stix et al., 1995) as the Cl standard and NBS620 as the S standard, we were able to define our lowest lowest reproducible concentrations as ~90 ppm for S and ~80 ppm for Cl. Repeat analyses of mineral and glass standards within a single analytical run produced an accuracy of 5% for major elements at concentrations > 1 wt.%. We used M6N, M3N, PCD and 35-1 (Devine et al., 1995) as secondary standards for major elements. Since these standards are principally characterized for different levels of H_2O, we also used them for the volatiles-by-difference method (Devine et al., 1995; Humphreys et al., 2006; Longpré et al., 2014) to compare H_2O results between the FTIR and electron microprobe (Supplementary Figure 2). Accepted values for major element, S and Cl standards are presented in Supplementary Data Table 1.

Olivine crystals were analyzed for major elements using an accelerating voltage of 20 kV, a current of 30 nA and a beam size of 5 µm. Counting times for Ca were 60 s, 40 s for Ni and 20 s for Si, Ti, Al, Fe, Mn, Mg and Cr. The olivine standard used was supplied by CM Taylor Company Supplies. For each olivine grain, three points were collected: one in the core, one close to the rim and one located between the first two and near an analyzed melt inclusion.

4. Results

4.1 Petrography and mineralogy

Tephras from all four eruptions are characterized by a mineral assemblage of plagioclase feldspar, olivine, clinopyroxene, ilmenite, magnetite, and zircon. In more evolved tephras (1104 and H3), we also observed apatite and pyrrhotite. In contrast to stratigraphic variations in crystal content observed at many other fall deposits (e.g., Hildreth and Wilson, 2007), the first erupted material for zoned eruptions is comparatively crystal rich (~10 %), while the last erupted material tends to be crystal poor (~ <1 %). Products from evolved eruptions (H3 and 1104) tend to be more crystal rich (1-10 %) than their more primitive counterparts (1-3 %) (1845 and 1991). Sulfides were observed as inclusions in olivine crystals from H3 and 1104. They are present in trace amounts in both eruptions with no clear difference in abundance between the first and last erupted material.

Olivine compositions are strongly correlated with the composition of the eruption and range from Fo_{11-13} in rhyolites, Fo_{23-26} in dacites, Fo_{43} in andesites to Fo_{59} in basaltic andesites (Figure 4). Within a single eruption, the variability is largest in H3 where the rhyolitic base has olivines of Fo_{13}, while the dacitic light and dark top have forsterite contents that range from Fo_{23} to Fo_{26}. Minor Fo zonation is observed in the olivines of H3 light and dark top (1-2 mol. %), but generally there is no obvious zonation in any of the other olivines. One olivine of Fo_{13} was found in H3 dark top, a unit where olivines of ~Fo_{25} are dominant. Olivine grains commonly contain inclusions of ilmenite, magnetite, zircon and needle-like growths of apatite. These inclusions are more common within olivines found in more evolved deposits.

Two types of melt inclusions were observed within the olivines. The first type is characterized by clear, spherical inclusions, 20-150 μm in size with occasional vapor bubbles (1-5 μm). These inclusions are restricted to rhyolites. The second type of melt inclusion is darker in color, also 20-150 μm in size, occurs as irregular fluid-like shapes and commonly contains vapor bubbles (1-10 μm). This second type of darker melt inclusions first appears in olivines from dacite deposits (H3 light top) and becomes the dominant melt inclusion type in H3 dark top, 1845 and 1991. H3 light top is the only sample where both types of melt inclusions occur together. Regardless of their visual differences, the two types are indistinguishable in terms of major elements and volatiles (see below). Any melt inclusions that possessed vapor bubbles were excluded during sample preparation and were not analyzed.

4.2 Major elements

Melt inclusions and matrix glasses were recalculated to anhydrous compositions for the purposes of comparison (Figure 5). Matrix glasses define a range in compositions from rhyolite (72.6 wt.% SiO_2) to basaltic andesite (54.8 wt. % SiO_2). The largest zoned eruption, H3, is characterized by rhyolite at the base (70.7 wt. % SiO_2) and dacite at the top (64.8 wt. % SiO_2). The change from white pumice at the base to pink pumice at the top of the deposit is associated with a change in iron content from 3.37 wt. % to 6.83 wt. % FeO*. The 1104 deposit, which appears visually zoned in the field, is characterized by rhyolitic matrix glass compositions from the base, light top and dark top. In other words, it is not chemically zoned in terms of major elements. The color change from white pumice at the base to dark pumice at the top is associated with changes in vesicularity, with the first erupted material at the base being more vesicular. The same decrease in vesicularity with stratigraphic height is observed in H3. Matrix glasses of 1845 and 1991 plot in the andesite (60.8 wt. % SiO_2) and basaltic andesite fields (54.8 wt. % SiO_2), respectively.

Olivine-hosted melt inclusions display a similar range in SiO_2 compositions (73.9 – 54.3 wt. %). The zoned nature of H3 recorded in its matrix glasses is also recorded in its melt inclusions (73.3-64.4 wt. % SiO_2). Melt inclusions from the 1104 deposit are dominated by rhyolite and show the same lack of zonation as do the matrix glasse. (73.9-70.4 wt.% SiO_2). This correlation between matrix glass and melt inclusion compositions is also observed for the 1845 and 1991 eruptions. In general, major element compositions in melt inclusions occupy a field consistent with magmatic evolution through fractional crystallization. Inflections in P_2O_5, Al_2O_3, and CaO (and MgO) mark the onset of apatite, feldspar and clinopyroxene crystallization, respectively.

A notable feature of Hekla's most evolved magmas is the variability in K_2O independent of changes in SiO_2 (Figure 5). This is most evident in melt inclusions with high SiO_2 and low MgO concentrations. In H3, we observe K_2O from 2.4 to 2.9 wt. % in H3 base and 1.9 to 2.7 wt. % in H3 dark top. For 1104, the range in K_2O is 2.4-2.9 wt. %. The larger range in K_2O for H3 is due to the wider range of magma compositions. Similar trends in K_2O and other major elements are observed in matrix glasses as well, but the magnitude of this variability is smaller (Figure 5).

One notable difference between matrix glasses and melt inclusions, most prominent for SiO_2 and K_2O, stands out. Melt inclusion data from H3 form a near-continuous array of samples between 1845 and 1104. Matrix glass data on the other hand form a gap between 66.9 to 70.8 wt. % SiO_2 and 1.97 to 2.41 wt. % K_2O.

Olivine-melt inclusion and olivine-matrix glass equilibria were examined using the following equation from Toplis (2005):

$$Kd_{OL-Melt} = \frac{X_{OL}^{Fe}}{X_{OL}^{Mg}} \bigg/ \frac{X_{Melt}^{Fe}}{X_{Melt}^{Mg}}$$

where $X^{Fe}{}_{OL}/X^{Mg}{}_{OL}$ is the ratio of Fe to Mg in olivine and $X^{Fe}{}_{Melt}/X^{Mg}{}_{Melt}$ is the ratio of Fe to Mg in the melt. The Kd ratio is typically used for melts of mafic compositions (Toplis, 2005), but studies at Hekla (Portnyagin et al., 2012) and other volcanoes (e.g., Parícutin volcano in Mexico, Elrund et al., 2010; Rowe et al., 2011) have applied it for more silicic compositions as well. Given the dependence of this ratio on complex parameters such as temperature and water content of the liquid, Toplis (2005) proposed a possible expansion of the equilibrium range of Kd values from 0.3-0.4 to 0.15-0.45 for more evolved compositions (up to 60 wt.% SiO_2). Clearly, caution is warranted here on how this parameter is applied to magmas of very different compositions. For our study, if the Kd value of a sample fell outside an expanded 0.15-0.45 range, it was removed from further consideration (Supplementary Figure 1).

A majority of the melt inclusions (45 olivines of a total of of 65) have Kd values of 0.3-0.4, suggesting they are in equilibrium with their host olivines and have experienced no post-entrapment crystallization (Toplis and Carroll, 1995). Variability in the Kd ratio increases for olivines in more silicic melt inclusions. The range is lowest in 1845 (0.29-0.33) and greatest in 1104 (0.14-0.5), the most silicic end member. Kd values of olivines versus matrix glasses show more variability. H3 dark top is dominated by olivines of Fo_{25} which have Kd values of ~0.45. One anomalous olivine from this sample has a composition of Fo_{13}, more in line with olivines from rhyolitic hosts (e.g. H3 base or 1104), and a resulting Kd of 0.9. All other olivine-matrix glass Kd values are in the 0.3-0.4 range suggesting they are in equilibrium.

4.3 Volatile elements

Melt inclusions from the four eruptions record a wide range of volatile contents. Water concentrations are highest in the first-erupted material of the most evolved eruptions, tending to decrease with stratigraphic height for these evolved eruptions and also for less evolved eruptions. The evolved eruptions are more variable in terms of major elements, H_2O, S and Cl. Lastly, melt inclusions record very little to no CO_2 for all four eruptions.

4.3.1 H_2O and CO_2

The full suite of melt inclusions from the four eruptions ranges in concentration from 0.8 to 5.67 wt.% H_2O (Figure 6). The most water-rich samples are found in H3 and 1104, and these eruptions also exhibit the largest range in water contents. The melt inclusions from 1845 and 1991 represent less evolved melts, contain less water on average than their silicic counterparts, and the range in concentrations is smaller. The deposits of 1845 and 1991 contain fever olivines, so the smaller range may partly reflect fewer analyzed samples. Overall, the increase of water correlates positively with SiO_2 and K_2O and negatively with the forsterite content of the host olivine (Figures 6 and 8).

Within the H3 and 1104 eruptions, we observe a large variability in water throughout the individual deposits and a general decrease in water with stratigraphic height. In H3, the average water concentration for the base, light top and dark top 4.57, 2.38, and 2.27 wt. %, respectively. The range of water concentrations also decreases with stratigraphic height from 3.36-5.57 wt. % at the base to 1.35-3.05 wt. % for the light top and 1.63-2.97 wt. % at the dark top. There is a single melt inclusion in H3 dark top with a water content of 4.62 wt. %, which is hosted in an olivine with a composition of Fo_{13}. Both these values clearly indicate that this crystal originated from the H3 base.

For 1104, the average water concentration for the base, light top and dark top is 4.01, 2.84, and 2.77 wt. %, respectively. In contrast to H3, the range in water concentrations in 1104 increases with stratigraphic height from 3.22-4.01 wt. % at the base to 1.04-4.82 wt. % for the light top and 1.26-5.67 wt. % for the dark top.

Samples from 1845 and 1991 were collected only from their base, hence represent the first erupted material. Their average water concentrations are 2.11 wt. % in 1845 and 1.23 wt. % in 1991. Their concentrations range from 1.12 to 3.35 wt. % in 1845, and 0.80 to 1.62 wt.% in 1991.

Our FTIR analyses for four eruptions of various compositions demonstrate that there is very little to no CO_2 preserved in the melt inclusions (Figure 7). The small amounts which were detected mark the first direct measurements of CO_2 at Hekla. Given how rare CO_2 is, we assessed its content within eruptions based on how often it was detected and in what quantities. CO_2 was measured in 7 out of 10 samples in 1104 base ranging from 9 to 38 ppm, in 5 of 13 samples in 1104 light top (5-173 ppm) and in 5 of 14 samples in 1104 dark top (8-19 ppm). No carbonate (CO_3^{2-}) was detected in any sample. The only other instances where CO_{2m} was detected was one melt inclusion in H3 light top (13 ppm), one melt inclusion in H3 dark top (15 ppm), and one melt inclusion in 1845 (29 ppm).

4.3.2 S and Cl

Sulfur concentrations in melt inclusions range from below detection limit to 820 ppm (Figure 6). Melt inclusions exhibit a notable decrease in sulfur with increasing SiO_2, K_2O, and H_2O, and show a positive correlation with FeO (Figure 9). 1991 is the most sulfur-rich eruption (715-820 ppm), followed by 1845 (270-400 ppm), and H3 light and dark top (maximum of 400 ppm). The other H3 and 1104 melt inclusions cluster at low sulfur concentrations (max. 150 ppm), many of which are below the ~90 ppm detection limit for S. Except for the zoned H3 deposit, where S varies from an average of <90 ppm at the base to 205 ppm in light top and <90 ppm in dark top, we observe no clear variability stratigraphically for S in melt inclusions.

Chlorine concentrations in melt inclusions exhibit a range of values for all four eruptions (Figure 6). 1991 and 1845 have more restricted ranges (205-530 ppm and 335-790 ppm, respectively), while H3 and 1104 show a wider range (150-1350 ppm). 1104 has consistent ranges in Cl (~ 900 ppm) and greater Cl contents (1350 ppm) than for H3, where the highest concentration is 870 ppm and the range in chlorine varies from 700 ppm in H3 base to 450 ppm in H3 dark top.

There are twelve instances in which a single crystal holds more than one melt inclusion: one instance from 1104 base, five from 1104 light top, four from 1104 dark top, and one each from H3 light top and dark top. It is difficult to assess whether the occurrence of multiple melt inclusions in 1104 is a unique feature of this eruption or simply a reflection of the quality and size of melt inclusions. We observed multiple melt inclusions in a single grain of olivine in other eruptions as well, but they were either difficult to expose simultaneously or too small for FTIR analysis. In five of the twelve cases, water concentrations differ by less than 0.8 wt.%. In six cases, the difference is ~ 0.8 wt. %. In only one case, the difference is on the order of 4.4 wt.%. In all twelve instances the change from higher to lower water concentrations is also reflected in an increase in sulfur. This negative correlation between water and sulfur is not accompanied by obvious differences in major oxides such as SiO_2, K_2O, FeO, etc.

5. Discussion

5.1 Magma evolution at Hekla

Thorarinsson (1967) discovered that the evolution of magmas from Hekla is related to the repose interval between eruptions. Major element data from this study and others (Sigmarsson et al., 1992; Sverridottir et al., 2007; Moune et al., 2007; Chekol et al., 2011; Portnyagin et al., 2012) indicate that this evolution is one principally of fractional crystallization, the extent of which is dependent on time. Hence, incompatible elements, such as K_2O, increase systematically from less evolved magmas to more evolved magmas (Figure 5). In these evolved melts there is a degree of variability of certain major elements (e.g., K_2O), which is more prevalent in melt inclusions than matrix glasses. This is suggestive of a secondary process of evolution, such as crustal assimilation, magma mixing or possibly a combination of the two (Nicholson et al., 1991; Cioni et al., 1995; de Silva and Wolff, 1995; Costa and Singer, 2002).

Crustal rocks in the southern part of Iceland are primarily metabasalts of amphibolite facies and/or pre-existing silicic intrusive rocks (Sigmarsson et al., 1992). The $^{87}Sr/^{86}Sr$ and $^{230}Th/^{232}Th$ systematics of Hekla lavas suggests that only recent dacites (e.g., 2000 pumice fall) have assimilated silicic intrusives and that older dacites and rhyolites (e.g., H3 and 1104) have evolved principally through fractional crystallization and crustal assimilation of older metabasalts (Chekol et al., 2011). Hydrothermal alteration of metabasalt host rocks (low-K greenstone and amphibolite) may alter the alkali content due to their high mobility during leaching and ion exchange (Von Damm, 1990; Hildreth and Wilson, 2007; Zelmer et al., 2008).

Hydrothermally altered crustal rocks found in the Icelandic rift zone are typically characterized by low $\delta^{18}O$ signatures (Hattori and Muehlenbachs, 1982; Sveinbjörnsdottir et al., 1986). If magmas are assimilating such rocks, the resulting compositions will be depleted in $\delta^{18}O$. The same holds true for partial melting. Hekla magmas exhibit a $\delta^{18}O$ range from 4.5 to 5.3 ‰ (Sigmarsson et al., 1992); when restricted to dacites and rhyolites, the range remains nearly identical (4.9-5.2 ‰). These values are close to those of the mantle, suggesting that either Hekla magmas have assimilated little to no crustal material or the host rock or source is not very depleted in $\delta^{18}O$. U-Th disequilibria ages from zircons in the 1158 eruptions reveal that many predate the age of the eruption by 10^3-10^5 years. The $\delta^{18}O$ composition of the zircon varies between ~1.2-5 ‰, suggesting that host rocks at Hekla vary in both age and level of $\delta^{18}O$ depletion (Bindeman et al., 2012). The most likely cause of this depletion is seawater alteration at high-temperature which produces rocks with $\delta^{18}O$ in the ~2-5 ‰ range. It is therefore possible that more hydrothermally altered crust was assimilated in Hekla's early history when the plumbing network was being established, but this no longer seems to be the dominant form of magmatic and volatile evolution.

Post-entrapment crystallization of olivine along the rims of melt inclusions along with diffusion of H could lead to variability in the major element composition and volatile contents of melt inclusions. Inspection of melt inclusion rims under optical microscope and electron back-scatter imaging do not reveal the presence of a newly crystallizing rim. Furthermore, if new rims were crystalizing, we would expect to see variability in the Fe-Mg content of the melt inclusions as well as an increase in incompatible elements such as K_2O and H_2O. Slight variability in the Kd ratio within the acceptable range (0.15-0.45) could be a result of minor post-entrapment crystallization, leading to variable K_2O. However, variable H_2O/K_2O ratios within a single eruption or even eruption sequence (e.g., 1104 dark top) suggest the presence of an additional process.

5.2 H_2O in Hekla magmas

Maximum water contents in melt inclusions increase from 1.62 wt. % for the 1991 eruption, through 3.35 wt. % for 1845, to 5.57 wt. % in H3 and 5.67 wt. % in 1104. In this respect, the maximum water content in Hekla magmas appears to be a function of magmatic evolution. The primary mechanism of magmatic evolution at Hekla is thought to be fractional crystallization; Portnyagin et al. (2012) demonstrated that the entire range of Hekla water concentrations (~0.2 to ~6 wt. % H_2O) can be accounted for by 90% of crystallization of parental mafic magmas containing 0.6 wt. % H_2O. In addition to water, potassium also behaves as an incompatible element in Hekla magmas; its increase in more evolved magmas is also suggestive of fractional crystallization. In previous studies, the H_2O/K_2O ratio for Hekla magmas, both basaltic and rhyolitic, has been stated as 2.0 (Moune et al., 2007; Portnyagin et al., 2012). However, according to our dataset, only the first erupted material of the more evolved eruption approaches this value (Figure 8). Melt inclusions from 1991, 1845 and later erupted 1104 and H3 all display lower H_2O/K_2O at fixed K_2O.

The large, silicic eruptions (e.g., H3 and 1104) show a decrease in the water contents between the first erupted and the last erupted material. The average decrease between base and light top in both H3 and 1104 is on the order of 2.2 wt. %. This decrease in water content is not restricted to melt inclusions in different olivine grains, but can be observed in multiple melt inclusions within a single olivine grain. In 1104, a single grain from the base with two melt inclusions records water contents of 4.81 and 4.35 wt. %, while a grain from 1104 dark top records water contents of 5.67 and 1.26 wt. %. As a result, the full range of water contents in H3 and 1104 is on the order of ~4 wt. %. This is a notable feature of Hekla's more evolved magmas and may result from (1) trapping melts at various stages of evolution, (2) diffusion of H through the olivine lattice, (3) syn-eruptive degassing, (4) trapping melts at different pressures, or (5) a combination of the four.

If fractional crystallization controls the amount of water within the melt, then lower water contents should be present in less evolved melts with lower K_2O contents. However, we observe a wide range in water contents with variable H_2O/K_2O ratios and no significant variability in other major elements, such as K_2O. It is therefore unlikely that melts are being trapped at various stages of fractionation within a single eruption. Gaetani et al. (2012) reported that diffusion of H from melt inclusions in olivines may occur on the order of hours or days. Given the possible long residence times and differentiation timescales on the order of thousands of years for closed-system fractionation at Hekla (Chekol et al., 2011), diffusion of H before or during eruption may have occurred. However, if H diffusion was occurring as a result of long storage times, then prior to eruption, all melt inclusions located at the same level within the magma chamber should have the same H_2O content. If melt inclusions reflect syn-eruptive degassing, then olivines crystallized during ascent and trapped pockets of melt that were degassing progressively. Unlike fractional crystallization, the change in the composition of the melt along with the Fo content of olivines should be minimal. This is consistent with our dataset. Lastly, the range in water content may reflect movement of magma within the crust and trapping of melts at different pressures or depths, but it does require that the melt is at or close to saturation before ascent. We address the saturation state of the magma in the next section.

5.3 Are magmas at Hekla volatile-saturated?

During fractional crystallization of volatile undersaturated magma, water behaves as an incompatible element, increasing its concentration in more evolved magmas. The first erupted material from H3 and 1104, with the highest H_2O contents, may represent a magma which is closest to volatile saturation at Hekla. Repose intervals for eruptions in our dataset range from 10 years for 1991, 79 years for 1845, ~250 years for 1104 and 100-500 years for H3. The repose periods for H3 and 1104 are potentially different different, as are their volumes, yet the H_2O contents of the first erupted material are similar, suggesting that the ~5.5 wt.% water represents a saturation threshold for more evolved compositions. However, water contents of ~6.2 wt. % have been reported for the H4 eruption (Portnyagin et al., 2012), with a repose interval of ~500 years. This increasing trend in water contents even for the most evolved eruptions brings into question the ultimate saturation limit of Hekla magmas.

Hartley et al. (2014) reported a large variation in the CO_2/Nb ratio (3.8-364) within melt inclusions from the neighboring 1783-1784 Laki fissure eruption. They concluded that the magmatic system was supplied by a combination of enriched and depleted primary melts. Their depleted melt inclusions remained vapor-undersaturated even at low pressures. Using the CO_2/Nb ration, Hauri et al. (2002) estimated the CO_2 concentration of the depleted mantle beneath Iceland at 140±56 ppm. These observations suggest that the carbon content of the mantle beneath Iceland and in the region of Hekla is low and variable. The low CO_2 contents of our melt inclusions and the absence of carbonate (CO_2^{3-}) are suggestive of two scenarios: (1) most of the CO_2 was lost through degassing during ascent and/or isobaric degassing, (2) the source of the magmas is CO_2 poor, or (3) both hold true.

Melt inclusions from the 1916 basaltic eruption are a good representation of the least evolved end-member erupted from Hekla. Its basaltic composition suggests that this magma underwent low degrees of fractional crystallization in the crust and is likely the closest representation of the basaltic source. Moune et al. (2007) compared the volatile evolution between the 1916 basalt and the 2000 basaltic andesite, concluding that H_2O and F were not removed from the melt prior to entrapment, but Cl and S were. Sulfur concentrations of 2200-2600 ppm in the 1916 melt inclusions demonstrate that sulfur initially behaves as an incompatible element, increasing in concentration along with H_2O and K_2O in the melt. Once the melt has evolved to the point that iron oxides, such as titanomagnetite begin to crystallize, the FeO content of the melt begins to decrease (Baker and Moretti, 2011). As a result, the system reaches sulfide saturation, and the sulfur content of the melt declines from a high of ~2700 ppm in 1916 (~47.0 wt. % SiO_2) to a high of ~900 ppm in 2000 (5.42 wt. % SiO_2). Our S dataset extends the trend established by Moune et al. (2007) from basaltic andesite compositions (e.g., 1991) to rhyolites (e.g., H3 and 1104). We observe a continuous S decrease as K_2O increases in the melt inclusions (Figures 8 and 9a). This trend correlates with decreasing FeO in the melt due to continued olivine and iron oxide crystallization. Significantly, we did observe the presence of pyrrhotite in more evolved melts (1104 and H3).

Using the SolEx model (Witham et al., 2012) for basaltic compositions at temperature of 1050°C obtained using the olivine-melt thermometer (Putirka, 2008), and oxygen fugacity at FMQ, we observe the onset of H_2O and S degassing at ~15-20 MPa. These low pressures demonstrate that the decrease in S within the melt is most likely due to sulfide saturation and not degassing.

Given the steady decrease in S caused by sulfide saturation and the continued increase of water within evolved magmas (1104, H3 and H4), we propose that only the first erupted melt inclusions from the most evolved compositions represent melts that are closest to saturation. Given our estimates of storage depths and other independent estimates of depth discussed in the next section, it is likely that the large majority and possibly all of Hekla magmas are volatile undersaturated prior to eruption. The ability of this volcanic center, located near a spreading axis, to produce silica rich magmas that may be volatile undersaturated even at 6 wt.% water is noteworthy. Therefore, depth estimates using H_2O-CO_2 vapor saturation pressures represent minimum estimates.

5.4 Magma storage depths

Using the most volatile-rich melt inclusions in more evolved compositions, we estimate minimum vapor saturation pressures of 204 MPa for H3, 203 MPa for 1104 and 80 MPa for 1845 (VolatileCalc; Newman and Lowenstern, 2002; Papale, 2006). Using a crustal density of 2,900 kg m^{-3} (Allen et al., 2002), we calculate a minimum entrapment depth of 7.2 km for H3, 7.1 km for 1104, 3 km for 1845 and 0.5-0.7 km for 1991.

The highest H_2O contents in H3 and the highest H_2O and CO_2 contents in 1104 give a similar depth estimate of ~7 km. This is a minimum value, as the magmas may be volatile-undersaturated. If they are volatile-saturated or close to saturation, then the 7 km is a robust estimate. This depth is in agreement with observations of Kjartsansson and Gronvol (1983), Linde et al. (1993), Sigmundsson et al. (1992) and Ofeigsson et al. (2011) suggesting a magma chamber within the 5-9 km depth range. Linde et al. (1993) proposed that the propagation of a dyke immediately before the 1991 was initiated at 4±1 km depth from the roof of the magma chamber centered at a depth of 6.5 km. Our estimates of storage depth for the 1845 and 1991 eruptions are minima due to their clearly volatile undersaturated nature, indicating that they are stored at depths greater than 0.7-3 km. Soosalu and Einarsson (2004) discounted the possibility of a reservoir shallow than 4 km depth based on their S-wave attenuation data. Furthermore, given the lack of hydrothermal manifestations at the surface, a substantial shallow crustal reservoir beneath Hekla seems unlikely (Ilyinskaya et al., 2015).

Observations by Geirsson et al. (2012) and a review by Sturkell et al. (2013) acknowledge the likelihood of magma movement deeper in the crust at depths >15 km. We cannot discount the possibility that more primitive magmas, such as 1845 and 1991, are stored at these depths in another magma chamber. If the minimum saturation depth for H3 base and 1104 base is calculated at ~ 7 km, then the later erupted magmas of H3 and 1104 were likely stored at greater depths within the same reservoir. The fact that samples from H3 dark top and 1104 dark top give entrapment depths of ~2.5 km, similar to 1845 and 1991, reinforces the notion that melt inclusions at Hekla may not be reliable indicators of storage depths. This implies that less evolved magmas, such as 1845 and 1991 may also reside at 7 km or deeper.

The $\delta^{18}O$ composition of Hekla magmas suggest they have undergone minimal assimilation of hydrothermally altered crust. In a recent review of silicic, water-rich magma generation in Iceland, Schattel et al. (2014) proposed that $\delta^{18}O$ may be used as a proxy for the storage depths of magmas. Reservoirs that are located in the shallow crust (~1-3 km) are more likely to assimilate oxidized (high fO_2) and hydrothermally altered low-$\delta^{18}O$ crust (-3 to +1 ‰), while reservoirs located at greater depths (~6-8 km) are less affected by assimilation of metabasalts, producing magmas with normal crustal $\delta^{18}O$ signatures (4-6 ‰) and lower states of oxidation (low fO_2).

5.5 Volatile evolution and the plumbing network beneath Hekla

Eruptive activity at Hekla displays a remarkable range in eruptive styles and products. While the prehistoric period was characterized by large, explosive eruptions of silicic magma, in recent, in historic times eruptive products have become more mafic and eruptions smaller. This change in the character of Hekla most likely reflects a periodic reconfiguration of the plumbing network. A trend towards shorter repose intervals over the last 750 years suggests that an efficient conduit has been established.

Water undersaturated basaltic melts intrude into the crust where they reside and evolve through fractional crystallization. If residence times are sufficiently long, they evolve to dacites and rhyolites. In order for this to occur, basaltic melts have to undergo ~90% crystallization. The fact that eruptive products contain at most 10% crystals suggests that a large crystal residue remains in the magma chamber or chambers. Crystal settling or mixing can occur within zoned eruptions in the form of olivines which are out of equilibrium with their host melt. However, the ultimate fate of this cumulate is unknown and may play an important role in the generation of future magmas. Olivine compositions for all four eruptions we studied represent a very narrow range in Fo contents, suggesting that the erupted olivines crystallized shortly before eruption or even during eruption as the magma ascended. Small differences in the major element compositions of the host matrix glasses and melt inclusions support this idea. Hence volatiles trapped within melt inclusions likely represent the volatile state of the magma soon before or during eruption. The most accurate representation of volatile content in the magma chamber is found within melt inclusions from the first erupted material of the more evolved eruptions. These melt inclusions are closest to volatile saturation and have undergone the least amount of syn-eruptive degassing. The lower values and greater range of water contents within the later erupted material likely reflects syn-eruptive degassing during ascent.

Due to the undersaturated nature of the melt, only the most volatile rich melt inclusions are potentially useful indicators of magma storage. According to these melt inclusions, in prehistoric times, the magma chamber may have been located at a depth of ~7 km. The undersaturated nature of Hekla's less evolved magmas prevents an accurate assessment of storage depths from these compositions. The efficient state of Hekla's plumbing network in historic times may enable the storage and ascent of magmas from deep levels. Deeper storage within a closed system, paired with the undersaturated state of the magma, is consistent with the lack of substantial surface degassing during repose periods in recent years.

6. Conclusions

Hekla volcano is a remarkable natural laboratory for the study of magmatic evolution through time. Our direct measurements of H_2O, CO_2, S and Cl in melt inclusions from four of Hekla's eruptions shed light on the relationship between repose interval, magmatic evolution, explosivity and the wide range of volatile contents seen in Icelandic magmas. Our principal conclusions are as follows:

- The entire suite of olivine-hosted melt inclusions records a wide range of H_2O contents (0.8-5.67 wt. %). Silicic magmas (H3 and 1104) have the highest dissolved water contents, followed by intermediate magmas (1845) and mafic magmas (1991) with the lowest amounts of water. The range in water contents within larger, zoned eruptions is a function syn-eruptive degassing.

- This study marks the first instance where CO_2 was detected in Hekla magmas. The only eruption with significant CO_2 is 1104 (0-170 ppm), the most evolved rhyolitic unit. In general, Hekla magmas are extremely CO_2 poor, most likely reflecting a CO_2-poor source and/or degassing prior to entrapment.

- S concentrations exhibit a decreasing trend with magmatic evolution, consistent with lower S solubility and increased sulfide precipitation.

- Melts evolve from basalt to rhyolite through fractional crystallization. Water behaves as an incompatible element and increases in more evolved compositions. The continuous trend of water increase from basalt to rhyolite along with evidence of syn-eruptive degassing suggests that the large majority of Hekla magmas are volatile undersaturated or close to saturation prior to eruption.

- The most volatile-rich samples from the first erupted material in H3 and 1104 give minimum depth estimates of ~7 km for the upper part of the magma chamber. These depths are in agreement with geophysical estimates of storage depths from recent eruptions. We cannot demonstrate or discount the possibility of magma movement and storage at greater depths (10-20 km) due to the likelihood of volatile undersaturated magmas. Depths we have obtained using volatile saturation pressures at Hekla are likely minimum estimates.

The generation of water-rich, silicic melts along spreading plate boundaries remains a topic of discussion and debate. In order to better understand the explosive potential of volcanic centers such a Hekla, our understanding of magmatic evolution and storage must improve. Despite comprehensive studies of deformation, seismicity, and magmatic and volatile evolution, the exact configuration of Hekla's plumbing network remains elusive. Recent geothermal exploration at Krafla volcano has demonstrated the difficulty in detecting reservoirs of magma in the shallow crust, and it poses the question of how many other undetected reservoirs are present beneath Icelandic volcanoes?

Acknowledgments

The authors would like to thank Karen Harp and Denis Geist for advice and assistance with sampling localities. We thank Patricia Nadeau for her help with sample collection in 2011. We are most grateful for water and CO_2 standards provided to us by Jacob Lowenstern, as well as for his discussions regarding FTIR measurements and sample preparation. Lang Shi was instrumental to our measurements with the electron microprobe, and we thank him for his help with the samples. We also thank Kim Berlo, Marc-Antoine Longpré, and Jason Coumans for their thought-provoking discussions and assistance. This research was made possible with funding to GL from GEOTOP, MAGNET and the Department of Earth and Planetary Sciences, McGill University. This study was also funded by Discovery, Accelerator, and Create grants to JS from the Natural Sciences and Engineering Research Council of Canada.

Bibliography

Allen, R. M., et al. (2002), Plume-driven plumbing and crustal formation in Iceland, Journal of Geophysical Research: Solid Earth, 107(B8), ESE 4-1-ESE 4-19, doi:10.1029/2001JB000584

Baker, D. R., and R. Moretti (2011), Modeling the Solubility of Sulfur in Magmas: A 50-Year Old Geochemical Challenge, Rev. Mineral. Geochem., 73(1), 167-213, doi:10.2138/rmg.2011.73.7

Behrens, H., N. Tamic, and F. Holtz (2004), Determination of the molar absorption coefficient for the infrared absorption band of CO2 in rhyolitic glasses, Am. Mineral., 89(2-3), 301-306

Bindeman, I., A. Gurenko, T. Carley, C. Miller, E. Martin, and O. Sigmarsson (2012), Silicic magma petrogenesis in Iceland by remelting of hydrothermally altered crust based on oxygen isotope diversity and disequilibria between zircon and magma with implications for MORB, Terra Nova, 24(3), 227-232, doi:10.1111/j.1365-3121.2012.01058.x

Chekol, T. A., K. Kobayashi, T. Yokoyama, C. Sakaguchi, and E. Nakamura (2011), Timescales of magma differentiation from basalt to andesite beneath Hekla Volcano, Iceland: Constraints from U-series disequilibria in lavas from the last quarter-millennium flows, Geochim. Cosmochim. Acta, 75(1), 256-283, doi:10.1016/j.gca.2010.10.001

Cioni, R., L. Civetta, P. Marianelli, N. Metrich, R. Santacroce, and A. Sbrana (1995), Compositional layering and syn-eruptive mixing of a periodically refilled shallow magma chamber: the AD 79 plinian eruption of Vesuvius, J. Petrol., 36(3), 739-776, doi:10.1093/petrology/36.3.739

Costa, F., and B. Singer (2002), Evolution of Holocene dacite and compositionally zoned magma, volcán San Pedro, Southern Volcanic Zone, Chile, J. Petrol., 43(8), 1571-1593, doi:10.1093/petrology/43.8.1571

Devine, J. D., J. E. Gardner, H. P. Brack, G. D. Layne, and M. J. Rutherford (1995), Comparison of microanalytical methods for estimating H2O contents of silicic volcanic glasses, Am. Mineral., 80(3-4), 319-328

Dugmore, A., et al. (1995), Radiocarbon dating tephra layers in Britain and Iceland, Radiocarbon, 37(2), 379-388

Erlund, E. J., K. V. Cashman, P. J. Wallace, L. Pioli, M. Rosi, E. Johnson, and H. D. Granados (2010), Compositional evolution of magma from Parícutin Volcano, Mexico: The tephra record, J. Volcanol. Geotherm. Res., 197(1–4), 167-187, doi: 10.1016/j.jvolgeores.2009.09.015

Gaetani, G. A., J. A. O'Leary, N. Shimizu, C. E. Bucholz, and M. Newville (2012), Rapid reequilibration of H2O and oxygen fugacity in olivine-hosted melt inclusions, Geology, 40(10), 915-918, doi:10.1130/g32992.1

Geirsson, H., P. LaFemina, T. Árnadóttir, E. Sturkell, F. Sigmundsson, M. Travis, P. Schmidt, B. Lund, S. Hreinsdóttir, and R. Bennett (2012), Volcano deformation at active plate boundaries: Deep magma accumulation at Hekla volcano and plate boundary deformation in south Iceland, J. Geophys. Res., 117(B11), doi:10.1029/2012jb009400

Gronvold, K., G. Larsen, P. Einarsson, S. Thorarinsson, and K. Saemundsson (1983), The Hekla eruption 1980–1981, Bulletin Volcanologique, 46(4), 349-363, doi:10.1007/BF02597770

Gudmundsson, A., et al. (1992), The 1991 eruption of Hekla, Iceland, Bull. Volcanol., 54(3), 238-246, doi:10.1007/BF00278391

Hards, V. L., P. D. Kempton, R. N. Thompson, and P. B. Greenwood (2000), The magmatic evolution of the Snæfell volcanic centre; an example of volcanism during incipient rifting in Iceland, J. Volcanol. Geotherm. Res., 99(1–4), 97-121, doi:http://dx.doi.org/10.1016/S0377-0273(00)00160-8

Hartley, M. E., J. Maclennan, M. Edmonds, and T. Thordarson (2014), Reconstructing the deep CO2 degassing behaviour of large basaltic fissure eruptions, Earth Planet. Sci. Lett., 393, 120-131, doi:10.1016/j.epsl.2014.02.031

Hattori, K., and K. Muehlenbachs (1982), Oxygen isotope ratios of the Icelandic crust, Journal of Geophysical Research: Solid Earth, 87(B8), 6559-6565, doi:10.1029/JB087iB08p06559

Hauri, E., K. Gronvold, N. Oskarsson, and D. McKenzie (2002), Abundance of carbon in the Icelandic mantle: constraints from melt inclusions, in American Geopgysical Union, Spring Meeting, edited by A. G. Union, p. 1, Washington D.C.

Hildreth, W., and C. J. N. Wilson (2007), Compositional zoning of the Bishop Tuff, J. Petrol., 48(5), 951-999, doi:10.1093/petrology/egm007

Humphreys, M. C. S., S. L. Kearns, and J. D. Blundy (2006), SIMS investigation of electron-beam damage to hydrous, rhyolitic glasses: Implications for melt inclusion analysis, Am. Mineral., 91(4), 667-679, doi:10.2138/am.2006.1936

Ilyinskaya, E., et al. (2015), Degassing regime of Hekla volcano 2012–2013, Geochim. Cosmochim. Acta, 159, 80-99, doi:10.1016/j.gca.2015.01.013

Jónasson, K. (2007), Silicic volcanism in Iceland: Composition and distribution within the active volcanic zones, J. Geodyn., 43(1), 101-117, doi:http://dx.doi.org/10.1016/j.jog.2006.09.004

King, P. L., T. W. Vennemann, J. R. Holloway, R. L. Hervig, J. B. Lowenstern, and J. F. Forneris (2002), Analytical techniques for volatiles: A case study using intermediate (andesitic) glasses, Am. Mineral., 87(8-9), 1077-1089, doi:0003-004X/02/0809-1077$05.00

Kjartansson, E., and K. Gronvold (1983), Location of a magma reservoir beneath Hekla Volcano, Iceland, Nature, 301(5896), 139-141, doi:10.1038/301139a0

Kuritani, T., T. Yokoyama, H. Kitagawa, K. Kobayashi, and E. Nakamura (2011), Geochemical evolution of historical lavas from Askja Volcano, Iceland: Implications for mechanisms and timescales of magmatic differentiation, Geochim. Cosmochim. Acta, 75(2), 570-587, doi:10.1016/j.gca.2010.10.009

Lacasse, C., H. Sigurdsson, S. N. Carey, H. Jóhannesson, L. E. Thomas, and N. W. Rogers (2007), Bimodal volcanism at the Katla subglacial caldera, Iceland: insight into the geochemistry and petrogenesis of rhyolitic magmas, Bull. Volcanol., 69(4), 373-399, doi:10.1007/s00445-006-0082-5

Larsen, G., A. Dugmore, and A. Newton (1999), Geochemistry of historical-age silicic tephras in Iceland, The Holocene, 9(4), 463-471, doi:10.1191/095968399669624108

Larsen, G., and S. Thorarinsson (1977), H4 and other acid Hekla tephra layers, Jökulll, 27, 28-46

Linde, A. T., K. Agustsson, I. S. Sacks, and R. Stefansson (1993), Mechanism of the 1991 eruption of Hekla from continuous borehole strain monitoring, Nature, 365(6448), 737-740, doi:10.1038/365737a0

Longpré, M.-A., J. Stix, F. Costa, E. Espinoza, and A. Muñoz (2014), Magmatic processes and associated timescales leading to the January 1835 eruption of Cosigüina volcano, Nicaragua, J. Petrol., 55(6), 1173-1201, doi:10.1093/petrology/egu022

Mandeville, C. W., J. D. Webster, M. J. Rutherford, B. E. Taylor, A. Timbal, and K. Faure (2002), Determination of molar absorptivities for infrared absorption bands of H2O in andesitic glasses, Am. Mineral., 87(7), 813-821

Mangan, M., and T. Sisson (2000), Delayed, disequilibrium degassing in rhyolite magma: decompression experiments and implications for explosive volcanism, Earth Planet. Sci. Lett., 183(3–4), 441-455, doi: 10.1016/S0012-821X(00)00299-5

Martin, E., and O. Sigmarsson (2010), Thirteen million years of silicic magma production in Iceland: Links between petrogenesis and tectonic settings, Lithos, 116(1–2), 129-144, doi:10.1016/j.lithos.2010.01.005

Moore, G., A. Chizmeshya, and P. F. McMillan (2000), Calibration of a reflectance FTIR method for determination of dissolved CO2 concentration in rhyolitic glasses, Geochim. Cosmochim. Acta, 64(20), 3571-3579, doi: 10.1016/S0016-7037(00)00447-6

Moune, S., O. Sigmarsson, T. Thordarson, and P.-J. Gauthier (2007), Recent volatile evolution in the magmatic system of Hekla volcano, Iceland, Earth Planet. Sci. Lett., 255(3-4), 373-389, doi:10.1016/j.epsl.2006.12.024

Newman, S., and J. B. Lowenstern (2002), VolatileCalc: a silicate melt–H2O–CO2 solution model written in Visual Basic for excel, Comput. Geosci., 28(5), 597-604, doi:http://dx.doi.org/10.1016/S0098-3004(01)00081-4

Newman, S., E. M. Stolper, and S. Epstein (1986), Measurement of water in rhyolitic glasses; calibration of an infrared spectroscopic technique, Am. Mineral., 71(11-12), 1527-1541

Nicholson, H., M. Condomines, J. G. Fitton, A. E. Fallick, K. Gronvold, and G. Rogers (1991), Geochemical and isotopic evidence for crustal assimilation beneath Krafla, Iceland, J. Petrol., 32(5), 1005-1020, doi:10.1093/petrology/32.5.1005

Ofeigsson, B. G., A. Hooper, F. Sigmundsson, E. Sturkell, and R. Grapenthin (2011), Deep magma storage at Hekla volcano, Iceland, revealed by InSAR time series analysis, J. Geophys. Res., 116(B5), doi:10.1029/2010jb007576

Ohlhorst, S., H. Behrens, and F. Holtz (2001), Compositional dependence of molar absorptivities of near-infrared OH- and H2O bands in rhyolitic to basaltic glasses, Chem. Geol., 174(1–3), 5-20, doi:http://dx.doi.org/10.1016/S0009-2541(00)00303-X

Papale, P., R. Moretti, and D. Barbato (2006), The compositional dependence of the saturation surface of H2O + CO2 fluids in silicate melts, Chem. Geol., 229(1–3), 78-95, doi:http://dx.doi.org/10.1016/j.chemgeo.2006.01.013

Portnyagin, M., K. Hoernle, S. Storm, N. Mironov, C. van den Bogaard, and R. Botcharnikov (2012), H2O-rich melt inclusions in fayalitic olivine from Hekla volcano: Implications for phase relationships in silicic systems and driving forces of explosive volcanism on Iceland, Earth Planet. Sci. Lett., 357-358, 337-346, doi:10.1016/j.epsl.2012.09.047

Putirka, K. D. (2008), Thermometers and Barometers for Volcanic Systems, Rev. Mineral. Geochem., 69(1), 61-120, doi:10.2138/rmg.2008.69.3

Rowe, M. C., D. W. Peate, and I. Ukstins Peate (2011), An Investigation into the nature of the magmatic plumbing system at Paricutin volcano, Mexico, J. Petrol., 52(11), 2187-2220, doi:10.1093/petrology/egr044

Schattel, N., M. Portnyagin, R. Golowin, K. Hoernle, and I. Bindeman (2014), Contrasting conditions of rift and off-rift silicic magma origin on Iceland, Geophys. Res. Lett., 41(16), 5813-5820, doi:10.1002/2014gl060780

Sigmarsson, O., M. Condomines, and S. Fourcade (1992), A detailed Th, Sr and O isotope study of Hekla: differentiation processes in an Icelandic Volcano, Contrib. Mineral. Petrol., 112(1), 20-34, doi:10.1007/BF00310953

Sigmundsson, F., P. Einarsson, and R. Bilham (1992), Magma chamber deflation recorded by the global positioning system: The Hekla 1991 Eruption, Geophys. Res. Lett., 19(14), 1483-1486, doi:10.1029/92GL01636

Silva, S. L. d., and J. A. Wolff (1995), Zoned magma chambers: the influence of magma chamber geometry on sidewall convective fractionation, J. Volcanol. Geotherm. Res., 65(1–2), 111-118, doi: 10.1016/0377-0273(94)00105-P

Soosalu, H., and P. Einarsson (2004), Seismic constraints on magma chambers at Hekla and Torfajökull volcanoes, Iceland, Bull. Volcanol., 66(3), 276-286, doi:10.1007/s00445-003-0310-1

Stix, J., G. Gauthier, and J. N. Ludden (1995), A critical look at quantitative laser-ablation ICP-MS analysis of natural and synthetic glasses, The Canadian Mineralogist, 33(2), 435-444, Stix, J., and G. D. Layne (1996), Gas saturation and evolution of volatile and light lithophile elements in the Bandelier magma chamber between two caldera-forming eruptions, Journal of Geophysical Research: Solid Earth, 101(B11), 25181-25196, doi:10.1029/96JB00815

Sturkell, E., K. Ágústsson, A. T. Linde, S. I. Sacks, P. Einarsson, F. Sigmundsson, H. Geirsson, R. Pedersen, P. C. LaFemina, and H. Ólafsson (2013), New insights into volcanic activity from strain and other deformation data for the Hekla 2000 eruption, J. Volcanol. Geotherm. Res., 256, 78-86, doi:10.1016/j.jvolgeores.2013.02.001

Sveinbjörnsdottir, A. E., M. L. Coleman, and B. W. D. Yardley (1986), Origin and history of hydrothermal fluids of the Reykjanes and Krafla geothermal fields, Iceland, Contrib. Mineral. Petrol., 94(1), 99-109, doi:10.1007/BF00371231

Sverrisdottir, G. (2007), Hybrid magma generation preceding Plinian silicic eruptions at Hekla, Iceland: evidence from mineralogy and chemistry of two zoned deposits, Geol. Mag., 144(04), 643-659, doi:10.1017/s0016756807003470

Thorarinsson, S., and G. E. Sigvaldason (1972), The Hekla Eruption of 1970, Bulletin Volcanologique, 36(2), 269-288, doi:10.1007/BF02596870

Thorarinsson, T. (1967), The eruption of Mt. Hekla 1947-1948. 1 - The eruptions of Hekla in historical times, a tephrachronological study. , Soc. Sci. Isl., 170

Toplis, M. J. (2005), The thermodynamics of iron and magnesium partitioning between olivine and liquid: criteria for assessing and predicting equilibrium in natural and experimental systems, Contrib. Mineral. Petrol., 149(1), 22-39, doi:10.1007/s00410-004-0629-4

Toplis, M. J., and M. R. Carroll (1995), An Experimental Study of the Influence of Oxygen Fugacity on Fe-Ti Oxide Stability, Phase Relations, and Mineral—Melt Equilibria in Ferro-Basaltic Systems, J. Petrol., 36(5), 1137-1170, doi:10.1093/petrology/36.5.1137

Von Damm, K. L. (1990), Seafloor hydrothermal activity: black smoker chemistry and chimneys, Annual Review of Earth and Planetary Sciences, 18(1), 173-204, doi:10.1146/annurev.ea.18.050190.001133

Witham, F., J. Blundy, S. C. Kohn, P. Lesne, J. Dixon, S. V. Churakov, and R. Botcharnikov (2012), SolEx: A model for mixed COHSCl-volatile solubilities and exsolved gas compositions in basalt, Comput. Geosci., 45, 87-97, doi:http://dx.doi.org/10.1016/j.cageo.2011.09.021

Wysoczanski, R., and K. Tani (2006), Spectroscopic FTIR imaging of water species in silicic volcanic glasses and melt inclusions: An example from the Izu-Bonin arc, J. Volcanol. Geotherm. Res., 156(3–4), 302-314, doi:http://dx.doi.org/10.1016/j.jvolgeores.2006.03.024

Yamashita, S., T. Kitamura, and M. Kusakabe (1997), Infrared spectroscopy of hydrous glasses of arc magma compositions, Geochem. J., 31(3), 169-174,

Zellmer, G., K. Rubin, K. Gronvold, and Z. Juradochichay (2008), On the recent bimodal magmatic processes and their rates in the Torfajökull–Veidivötn area, Iceland, Earth Planet. Sci. Lett., 269(3-4), 388-398, doi:10.1016/j.epsl.2008.02.026

Tables

Table 1

Table 1. FTIR extinction coefficients

Wavenumber (cm^{-1})	**E_{5200}**	**E_{4500}**	**E_{3450}**	**E_{2350}**	**E_{1630}**	**Source**
Volatile species	H_2O_m	OH	H_2O_m - OH	$CO_{2\ m}$	H_2O_m	
Rhyolite	1.61	1.73	56-100*		55	Newman et al. (1986)
				1214		Behrens et al. (2004)
Dacite	1.2	1.05				Ohlhorst et al. (2001)
			68			Yamashita et al. (1997)
					55	Wysoczanski and Tani (2006)
				1066		Moore et al. (2000)
Andesite	1.08	1.15	62			King et al. (2002)
				945	43	Mandeville et al. (2002)
Basaltic andesite	0.75	0.65				Ohlhorst et al. (2001)
			61	n/a	42	Mandeville et al. (2002)

* The E_{3450} extinction coefficient is a function of the partitioning between H_2O_m and OH. Other spectra from the same sample set, where the A_{5200} and A_{4500} peaks were visible, were used to determine the partitioning.

Table 2

Table 2. Representative matrix glass and melt inclusion data from each eruption

	1991		**1845**		**1104**						**H3**					
	HK2013-1991-A		**HK2013-1845-A**		**HK2013-1104-A**		**HK2013-1104-B**		**HK2013-1104-C**		**HK2013-H3-A**		**HK2013-H3-B**		**HK2011-H3-C**	
					base		**light top**		**dark top**		**base**		**light top**		**dark top**	
	Melt inclusion (wt. %)	*Matrix glass* (wt. %)	*Melt inclusion* (wt. %)	*Matrix glass* (wt. %)	*Melt inclusion* (wt. %)	*Matrix glass* (wt. %)	*Melt inclusion* (wt. %)	*Matrix glass* (wt. %)	*Melt inclusion* (wt. %)	*Matrix glass* (wt. %)	*Melt inclusion* (wt. %)	*Matrix glass* (wt. %)	*Melt inclusion* (wt. %)	*Matrix glass* (wt. %)	*Melt inclusion* (wt. %)	*Matrix glass* (wt. %)
SiO_2	54.0	54.8	59.6	60.8	68.6	71.9	69.5	72.6	69.4	72.6	67.6	70.7	65.7	65.7	65.7	64.8
TiO_2	2.03	1.93	0.88	0.92	0.32	0.19	0.21	0.27	0.31	0.20	0.27	0.31	0.34	0.57	0.32	0.73
Al_2O_3	15.0	15.2	16.0	15.5	13.3	13.9	12.7	14.2	13.5	14.0	13.0	13.7	13.8	15.3	13.8	15.3
FeO*	11.7	11.7	8.02	9.10	2.96	3.23	3.50	3.46	3.36	3.82	3.40	3.37	6.06	6.83	6.24	7.41
MnO	0.32	0.10	0.38	0.16	0.01	0.10	0.00	0.13	0.26	0.09	0.17	0.09	0.23	0.16	0.10	0.22
MgO	2.59	2.66	1.12	1.20	0.05	0.12	0.12	0.09	0.10	0.12	0.09	0.17	0.35	0.50	0.42	0.59
CaO	6.48	7.09	4.59	4.74	1.99	1.99	1.90	2.00	1.95	1.97	1.97	2.30	3.38	4.11	3.76	4.51
Na_2O	3.95	4.23	4.56	4.69	4.59	5.26	4.95	5.42	4.89	5.30	4.78	5.17	4.76	5.09	5.13	5.03
K_2O	1.21	1.25	1.73	1.76	2.62	2.64	2.77	2.61	2.40	2.63	2.30	2.47	2.24	1.88	2.35	1.67
P_2O_5	0.91	0.97	0.30	0.26	0.00	0.03	0.00	0.01	0.00	0.00	0.04	0.01	0.06	0.19	0.10	0.17
Total	98.5	99.9	97.3	99.1	94.5	99.4	95.7	100.8	96.2	100.7	93.7	98.3	97.0	100.3	98.0	100.5
S (ppm)	817		346		89		83		149		21		165		123	
Cl (ppm)	531		535		307		455		350		619		402		510	
H_2O_t (wt. %)	0.84		3.35		5.67		4.82		3.46		5.57		3.02		2.14	
H_2O_m (wt. %)	0.12		1.62		4.33		3.25		2.38		3.77		1.59		1.24	
OH (wt. %)	0.72		1.73		1.33		1.57		1.09		1.80		1.43		0.90	
CO_2 (ppm)	0		29		0		173		16		0		0		0	
Fo	58.8		43.0		12.2		11.7		12.1		13.1		22.8		25.1	

* Fe as FeO

Figures

Figure 1

Topographic map of Hekla volcano and surrounding area. The summit of the volcano (triangle) and sampling localities (dots) are marked for reference. The map coordinates represent the WGS1984 datum, UTM zone 27N.

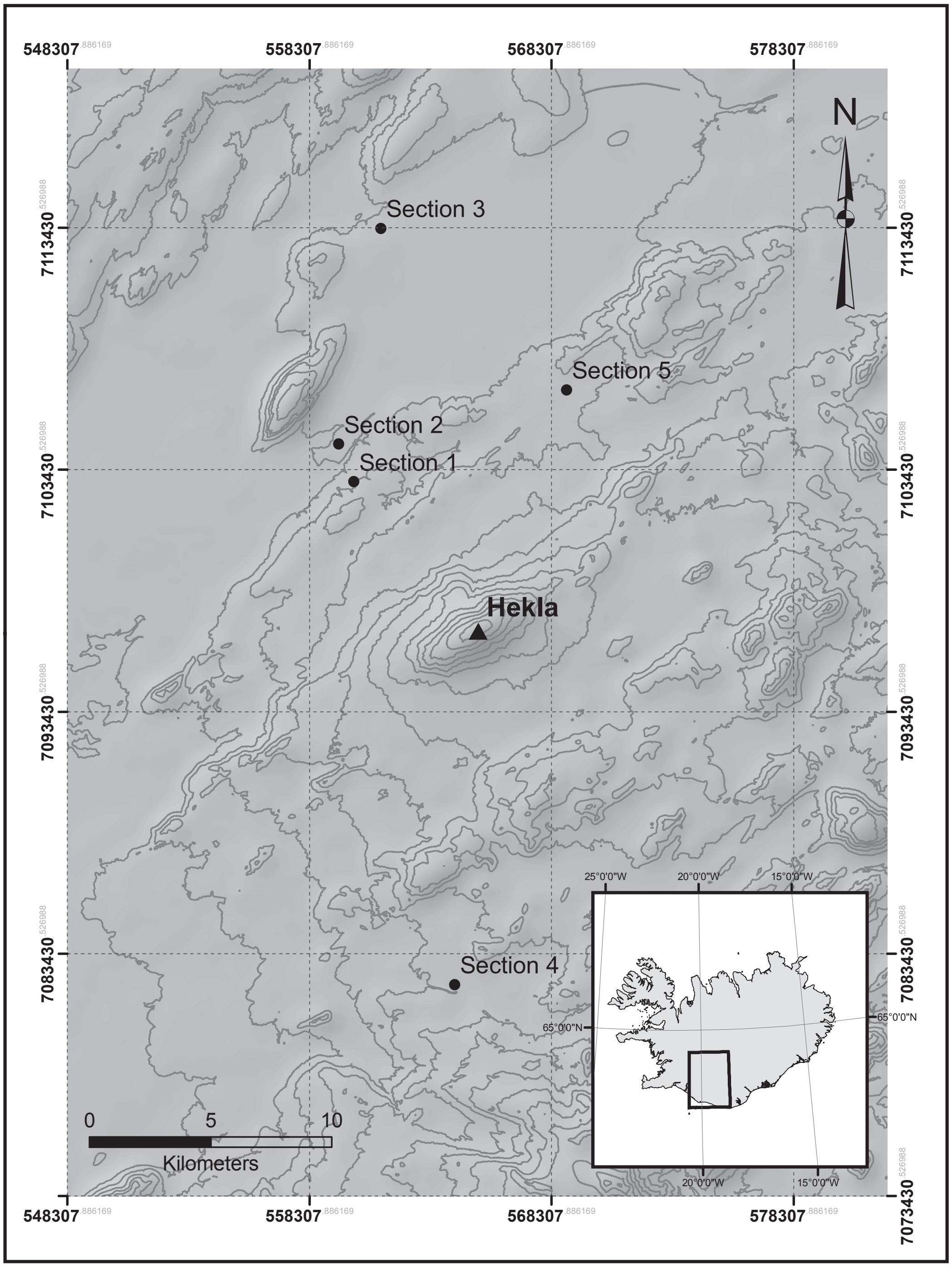
548307.886169
558307.886169
568307.886169
578307.886169
7113430.526988
7103430.526988
7093430.526988
7083430.526988
7073430.526988
N
Section 3
Section 5
Section 2
Section 1
Hekla
Section 4
0
5
10
Kilometers
25°0'0"W
20°0'0"W
15°0'0"W
65°0'0"N

Figure 2

Stratigraphic sections of sampling localities for the H3, 1104, 1845 and 1991 eruptions. Each sampling horizon is marked with a unique ID that represents the name of the volcano (HK), sampling year (e.g., 2013), eruption name (e.g., 1104) and relative horizon (A = base, B = light top, C = dark top). Datum is WGS1984, UTM zone 27N. For locations from Hekla's summit, see Figure 1.

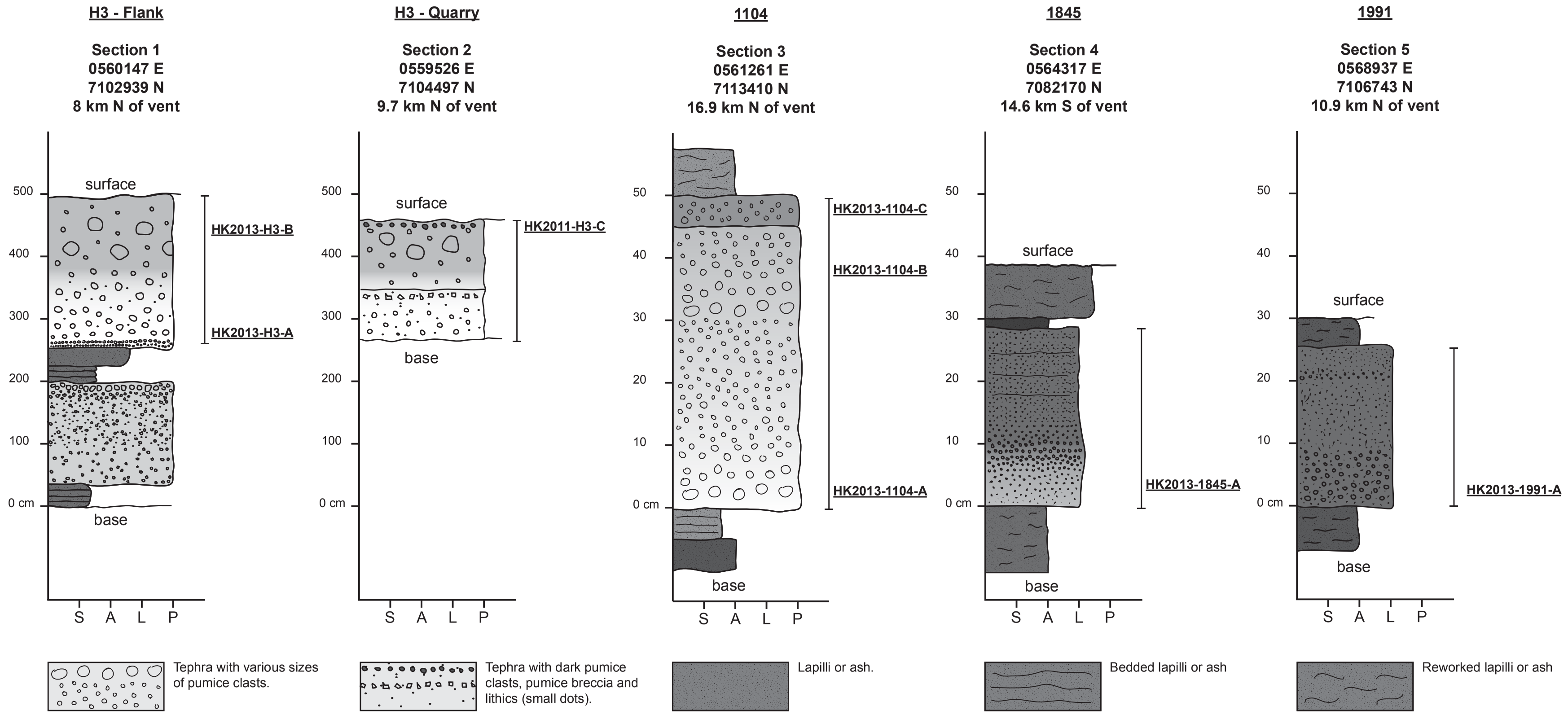
H3 - Flank
Section 1
0560147 E
7102939 N
8 km N of vent
H3 - Quarry
Section 2
0559526 E
7104497 N
9.7 km N of vent
1104
Section 3
0561261 E
7113410 N
16.9 km N of vent
1845
Section 4
0564317 E
7082170 N
14.6 km S of vent
1991
Section 5
0568937 E
7106743 N
10.9 km N of vent
500
400
300
200
100
0 cm
50
40
30
20
10
surface
base
S A L P
HK2013-H3-B
HK2013-H3-A
HK2011-H3-C
HK2013-1104-C
HK2013-1104-B
HK2013-1104-A
HK2013-1845-A
HK2013-1991-A
Tephra with various sizes of pumice clasts.
Tephra with dark pumice clasts, pumice breccia and lithics (small dots).
Lapilli or ash.
Bedded lapilli or ash
Reworked lapilli or ash

Figure 3

Field photographs of the sampling sections marked with sampling horizons. (a) At Section 1, GL is standing on top of H3 light top. Note the change in color from white pumice fragments at the base to pink pumice fragments at the top. (b) At Section 2 , JS points to a thin, ashy soil horizon, possibly a discontinuity. Note the dark horizon of pumice fragments, representative of H3 dark top. (c) At Section 3, we observe the distinct color change between the bulk of the 1104 deposit and its darker top (1104 dark top). (d) At Section 4, GL points at a change in color from light pumice fragments to dark pumice fragments within the 1845 deposit. (e) At section 5, the 1991 eruption is exposed by removing 30-40 cm of reworked material from the surface.

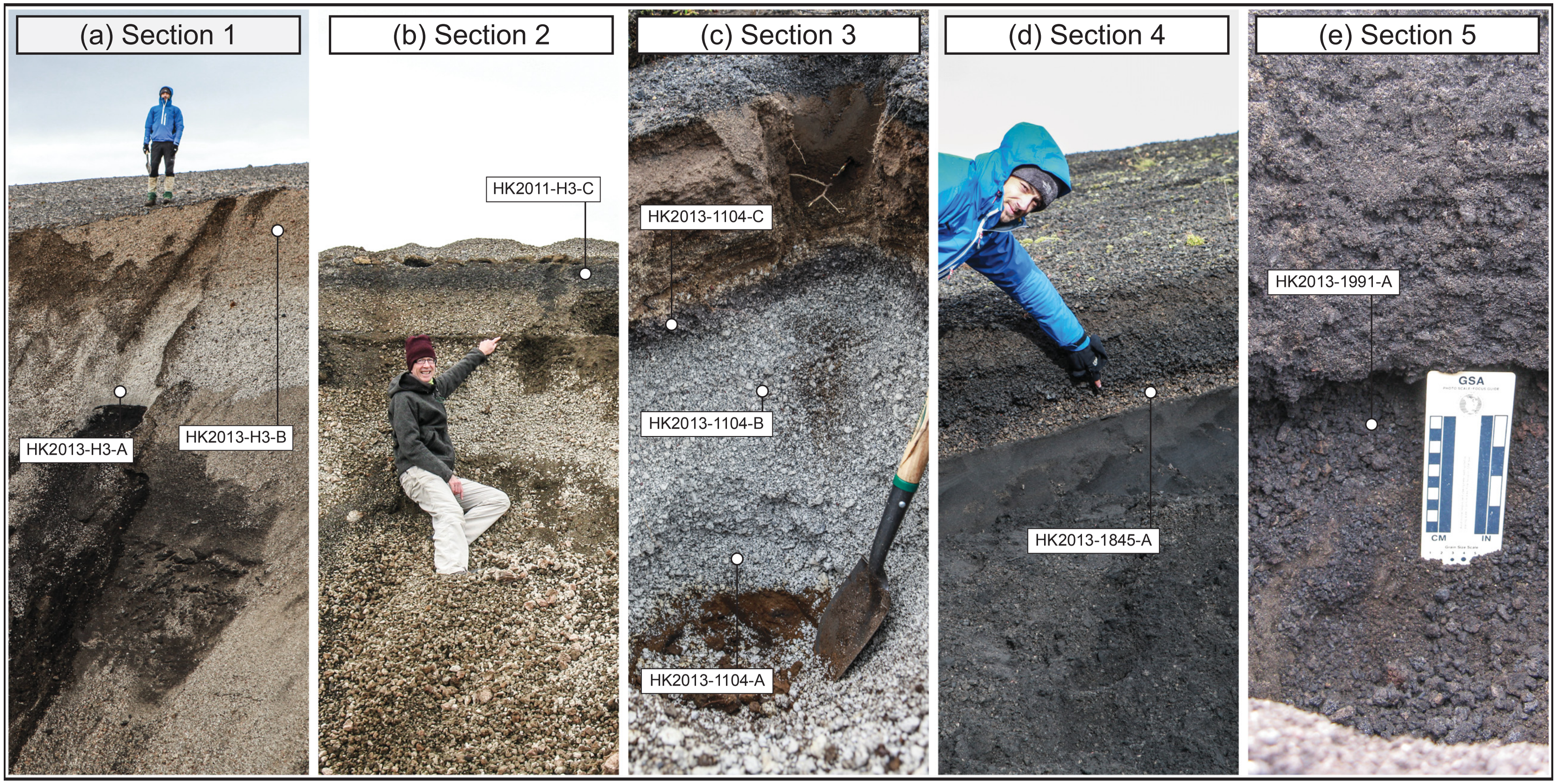
(a) Section 1
HK2013-H3-A
HK2013-H3-B
(b) Section 2
HK2011-H3-C
(c) Section 3
HK2013-1104-C
HK2013-1104-B
HK2013-1104-A
(d) Section 4
HK2013-1845-A
(e) Section 5
HK2013-1991-A
GSA
CM
IN

Figure 4

Relationship between forsterite contents of olivines plotted versus (a) SiO_2 and (b) K_2O contents of the olivine-hosted melt inclusions. Note the four distinct populations of melt inclusions that are found in basaltic andesite ($Fo_{\sim 60}$), andesite ($Fo_{\sim 42}$), dacite ($Fo_{\sim 20-25}$) and rhyolite (Fo_{11}).

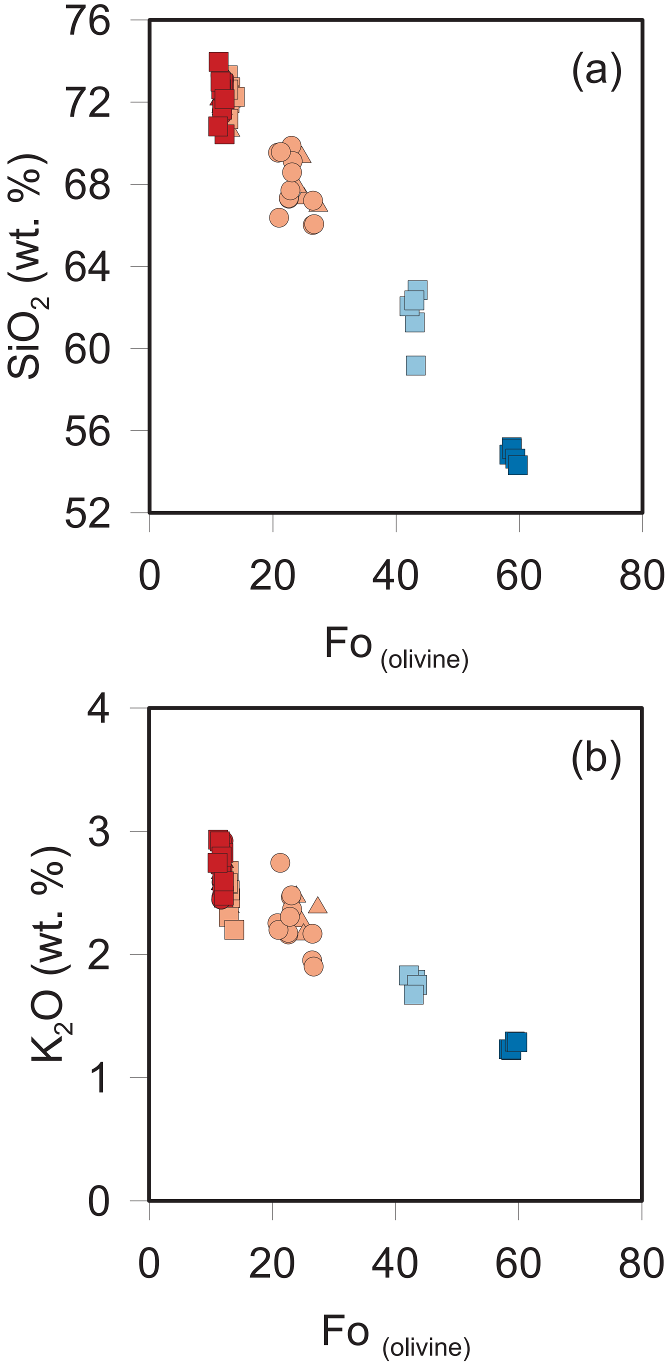
(a)
76
72
68
64
60
56
52
SiO2 (wt. %)
0
20
40
60
80
Fo (olivine)
(b)
4
3
2
1
0
K2O (wt. %)
0
20
40
60
80
Fo (olivine)

Figure 5

Select major element data for melt inclusions (large symbols) and matrix glasses (small symbols). The color coding and symbols reflect samples from different eruptions (red, orange, light blue and dark blue), and sampling horizons within the same eruption (square = base, circle = light top, triangle = dark top). These symbols and color codes are the same for other figures.

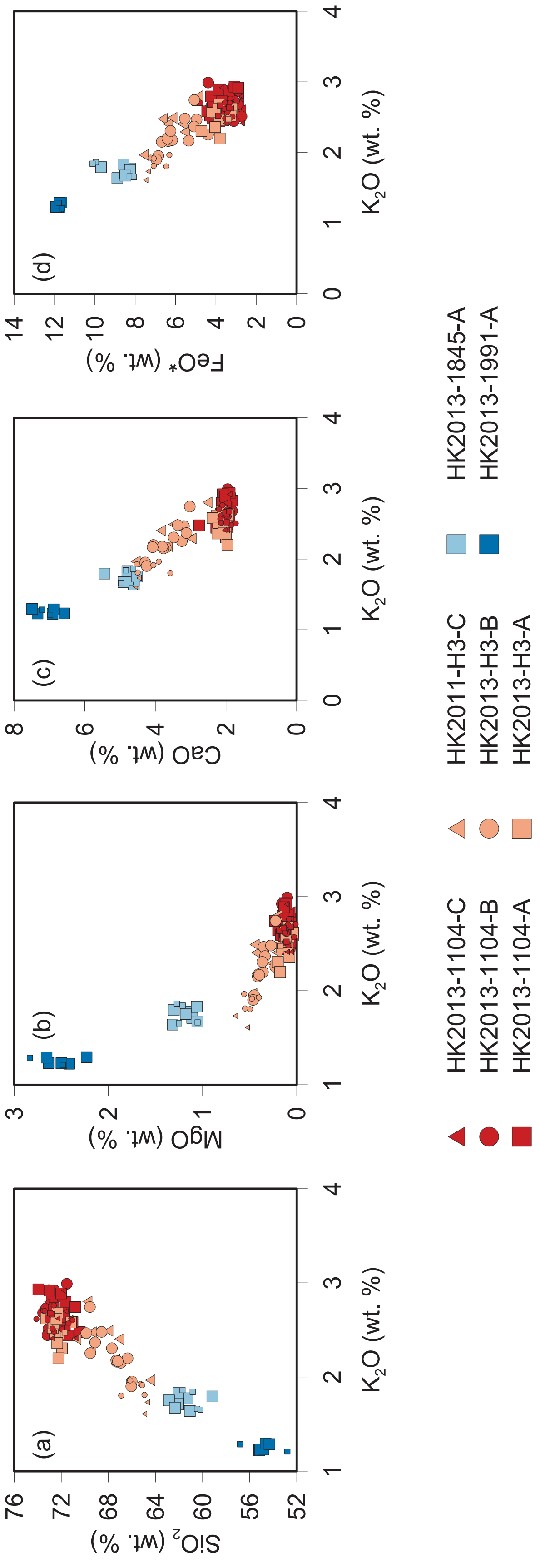
(a)
SiO$_2$ (wt. %)
76
72
68
64
60
56
52
K$_2$O (wt. %)
1
2
3
4
(b)
MgO (wt. %)
3
2
1
0
K$_2$O (wt. %)
1
2
3
4
(c)
CaO (wt. %)
8
6
4
2
0
K$_2$O (wt. %)
0
1
2
3
4
(d)
FeO* (wt. %)
14
12
10
8
6
4
2
0
K$_2$O (wt. %)
0
1
2
3
4
HK2013-1104-C
HK2013-1104-B
HK2013-1104-A
HK2011-H3-C
HK2013-H3-B
HK2013-H3-A
HK2013-1845-A
HK2013-1991-A

Figure 6

Histograms of H_2O concentrations and Fo contents of olivines plotted versus H_2O concentrations in melt inclusions. The first erupted material at the base of the stratigraphic section is located at the bottom of the figure. The range in S and Cl concentrations of each horizon are included for reference. Note the decrease in average H_2O concentrations from the first erupted to the last erupted material for the silicic eruptions.

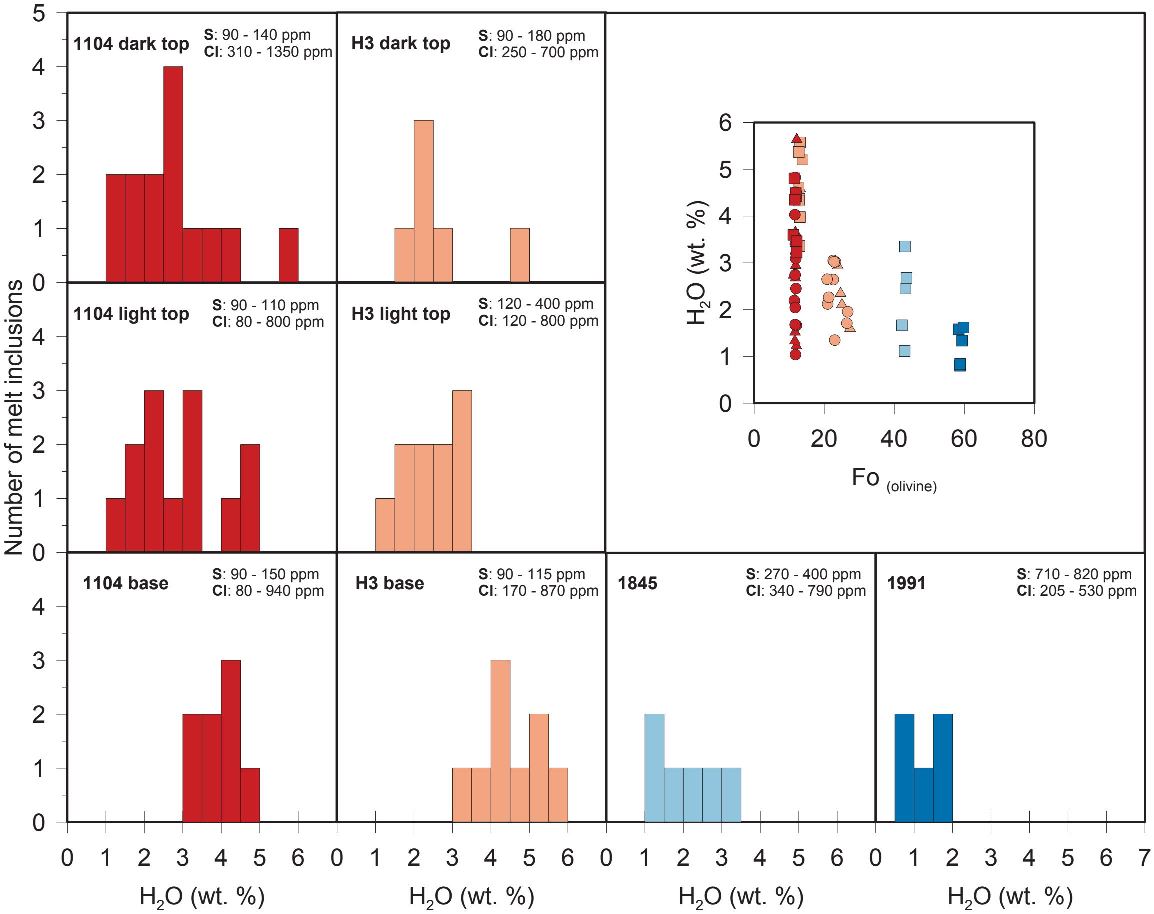
1104 dark top
S: 90 - 140 ppm
Cl: 310 - 1350 ppm
H3 dark top
S: 90 - 180 ppm
Cl: 250 - 700 ppm
1104 light top
S: 90 - 110 ppm
Cl: 80 - 800 ppm
H3 light top
S: 120 - 400 ppm
Cl: 120 - 800 ppm
1104 base
S: 90 - 150 ppm
Cl: 80 - 940 ppm
H3 base
S: 90 - 115 ppm
Cl: 170 - 870 ppm
1845
S: 270 - 400 ppm
Cl: 340 - 790 ppm
1991
S: 710 - 820 ppm
Cl: 205 - 530 ppm
Number of melt inclusions
H2O (wt. %)
Fo (olivine)
0
1
2
3
4
5
6
7
20
40
60
80

Figure 7

H_2O vs CO_2 concentrations in melt inclusions. (a) The 200, 100, 50 and 10 MPa isobars were calculated for rhyolitic melts at 1000 °C using VolatileCalc (Newman and Lowenstern, 2002). The sample with the highest water content (5.67 wt.%) and the sample with the highest CO_2 content (4.82 wt. % H_2O and 173 ppm CO_2) both give vapor saturation pressures of ~ 200 MPa. (b) Plot of K_2O vs CO_2 demonstrating the increased occurrence of CO_2 in more evolved magmas.

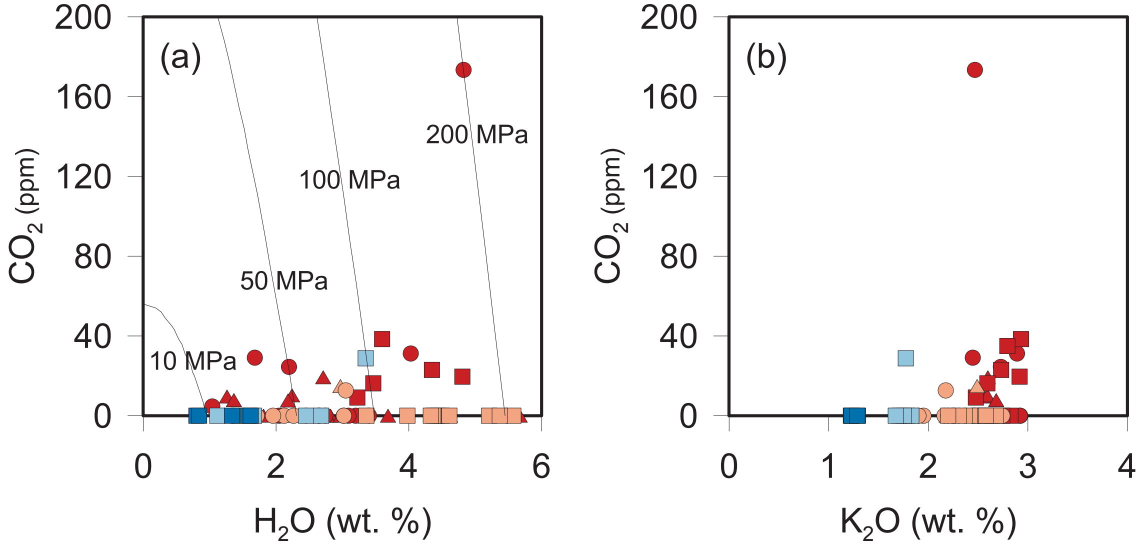
(a)
(b)
200
160
120
80
40
0
CO$_2$ (ppm)
10 MPa
50 MPa
100 MPa
200 MPa
0
2
4
6
H$_2$O (wt. %)
0
1
2
3
4
K$_2$O (wt. %)

Figure 8

The H_2O/K_2O ratio of melt inclusions from (a) first erupted material (base) and (b) later erupted material (light and dark top). The dashed line represents the previously reported ratio of ~2 from the 2000, 1916, H3 and H4 melt inclusions (Moune et al., 2007; Portnyagin et al., 2012). Note the variability in the H_2O/K_2O ratio at fixed K_2O as well as low ratios for later erupted 1104 and H3 melt inclusions, suggesting loss of water through degassing.

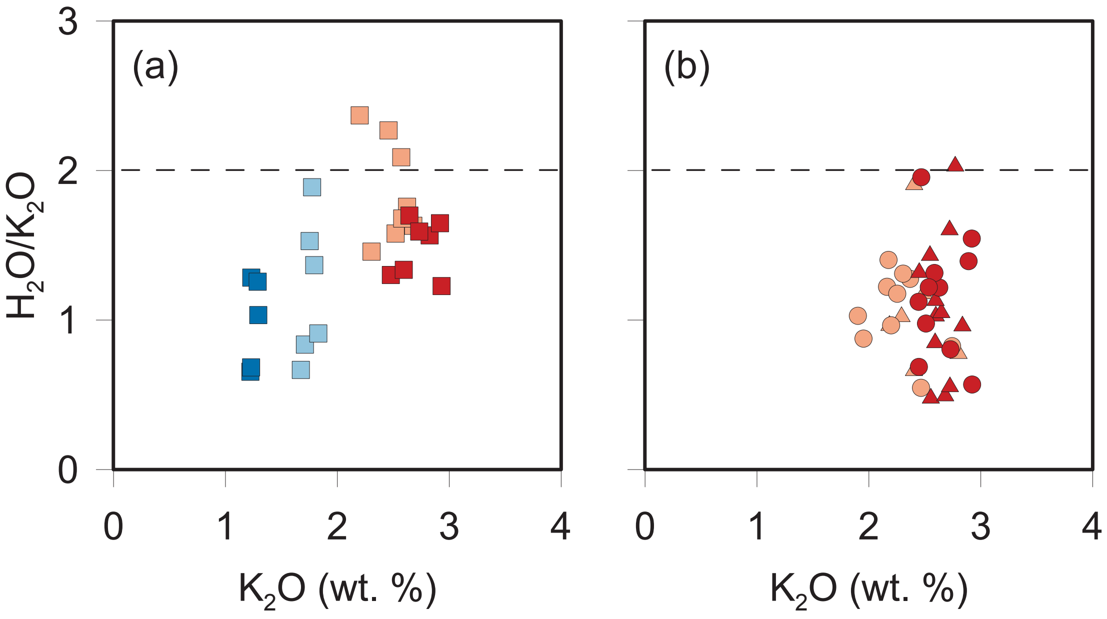
(a)
(b)
H2O/K2O
K2O (wt. %)
K2O (wt. %)
0
1
2
3
0
1
2
3
4
0
1
2
3
4

Figure 9

(a) Positive correlation between FeO* and S for melt inclusions from this study (colored symbols), and select samples from the 1916 basaltic eruption (grey diamonds) and the 2000 basaltic andesite (grey crosses) from Moune et al. (2007). (b) Early in the evolution of Hekla magmas, S behaves incompatibly and increases with K_2O. Once sulfide saturation occurs at ~0.7-0.8 wt. % K_2O, the S content decreases steadily with increasing K_2O. Many samples from the silicic eruptions are at or below the detection limits for S (~ 90 ppm).

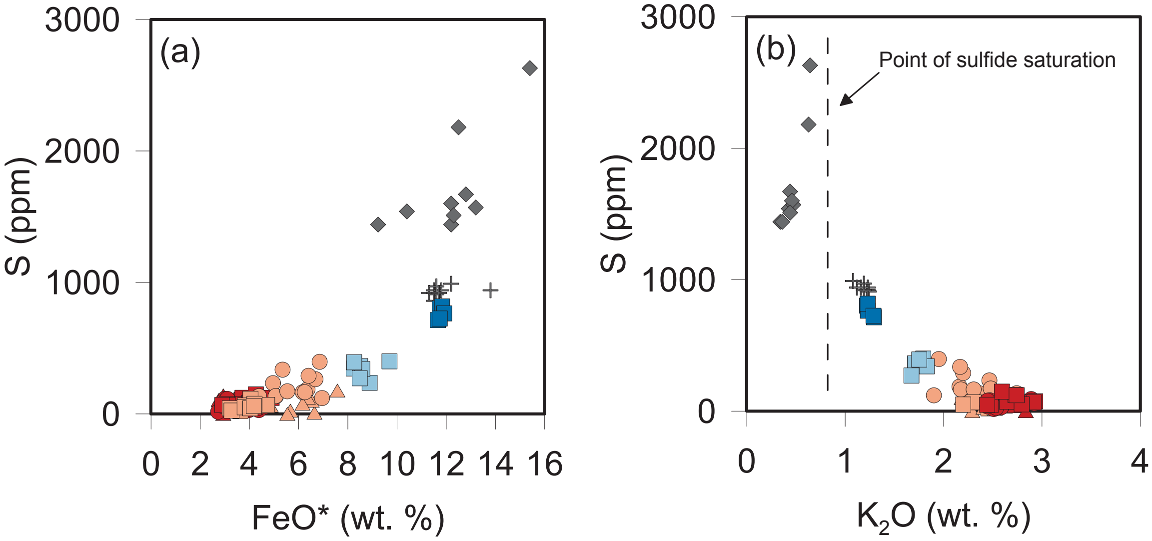
(a)
S (ppm)
3000
2000
1000
0
0 2 4 6 8 10 12 14 16
FeO* (wt. %)
(b)
Point of sulfide saturation
S (ppm)
3000
2000
1000
0
0 1 2 3 4
K_2O (wt. %)

Appendix 1

Supplementary table 1. Data on in-run glass standards for electron microprobe analysis used in this study

Standard ID	SiO_2	TiO_2	Al_2O_3	FeO*	MnO	MgO	CaO	Na_2O	K_2O	P_2O_5	Cl	SO_3	Total
35-1_1	74.2	0.00	13.6	0.70	0.21	0.07	0.38	4.60	4.03	0.06	0.01	0.01	97.86
35-1_2	75.2	0.06	14.2	0.40	0.00	0.02	0.40	4.51	4.52	0.03	0.01	0.00	99.35
35-1_3	76.3	0.00	14.4	0.67	0.11	0.03	0.43	4.52	4.30	0.08	0.00	0.00	100.91
35-1_4	75.9	0.04	14.5	0.50	0.06	0.06	0.47	4.55	4.13	0.07	0.03	0.00	100.34
35-1_5	75.6	0.16	14.1	0.17	0.04	0.00	0.62	6.12	2.70	0.01	0.02	0.00	99.47
Avg.	75.44	0.052	14.17	0.486	0.083	0.037	0.460	4.857	3.936	0.050	0.014	0.001	99.59
Accepted	74.4	0.03	13.7	0.56	low	0.47	0.47	4.25	4.21	low	0.06	low	97.70
KE12_1	70.7	0.35	7.77	8.32	0.14	0.00	0.35	7.73	4.37	0.02	0.27	0.04	100.04
KE12_2	70.3	0.34	7.64	9.18	0.19	0.00	0.49	7.35	4.26	0.00	0.23	0.05	99.98
KE12_3	70.6	0.30	7.62	8.65	0.30	0.10	0.45	7.23	4.30	0.00	0.26	0.06	99.79
KE12_4	70.6	0.38	7.67	9.10	0.27	0.00	0.38	7.28	4.20	0.00	0.33	0.03	100.13
KE12_5	71.2	0.14	7.56	7.64	0.50	0.00	0.23	7.11	4.30	0.00	0.23	0.03	98.91
KE12_6	71.2	0.47	7.60	8.38	0.32	0.00	0.33	7.17	4.23	0.00	0.28	0.06	99.96
KE12_7	71.8	0.35	7.61	7.59	0.24	0.02	0.25	6.93	4.37	0.00	0.28	0.03	99.37
Avg.	70.9	0.33	7.64	8.41	0.28	0.02	0.35	7.26	4.29	0.00	0.27	0.04	99.74
Accepted	70.3	0.33	7.62	8.36	0.26	0.02	0.35	7.28	4.27	low	0.30	0.02	98.50
KN9_1	74.7	0.07	10.5	3.33	0.21	0.00	0.04	5.26	4.56	2.16	0.31	0.00	100.99
KN9_2	74.1	0.16	10.6	4.18	0.05	0.00	0.00	5.48	4.65	0.00	0.33	0.01	99.43
KN9_3	74.2	0.22	9.89	4.77	0.12	0.00	0.34	5.57	4.45	0.01	0.32	0.00	99.82
KN9_4	74.1	0.23	10.1	3.74	0.17	0.04	0.33	5.49	4.56	0.02	0.30	0.01	99.08
KN9_5	74.8	0.25	11.1	3.84	0.20	0.02	0.06	5.53	4.34	0.01	0.30	0.02	100.33
KN9_6	74.5	0.17	11.1	3.47	0.31	0.00	0.40	5.48	4.41	0.00	0.35	0.00	100.10
KN9_7	74.9	0.08	10.8	3.39	0.14	0.00	0.08	5.53	4.42	0.02	0.30	0.00	99.54
KN9_8	74.6	0.26	10.8	2.69	0.16	0.00	0.04	5.56	4.86	0.03	0.35	0.00	99.31
KN9_9	75.3	0.11	10.4	3.61	0.02	0.01	0.07	5.48	4.39	0.01	0.29	0.02	99.55
Avg.	74.57	0.170	10.57	3.667	0.151	0.008	0.151	5.486	4.516	0.250	0.316	0.007	99.79
Accepted	74.70	0.18	10.47	3.47	0.06	0.01	0.14	5.48	4.44	0.01	0.31	low	98.96
M3N_1	70.3	0.14	13.6	1.42	0.06	0.25	1.25	3.95	4.43	0.12	0.11	0.02	95.60
M3N_2	70.9	0.39	13.1	1.55	0.00	0.20	1.10	4.05	4.69	0.04	0.11	0.01	96.17
M3N_3	70.7	0.22	13.5	1.81	0.18	0.22	1.34	4.23	4.16	0.00	0.07	0.00	96.40
M3N_4	72.3	0.46	14.1	1.22	0.12	0.27	1.32	4.07	4.17	0.05	0.05	0.01	98.07
M3N_5	71.4	0.24	12.9	1.56	0.00	0.32	1.23	4.10	4.28	0.09	0.06	0.01	96.21
M3N_6	71.2	0.30	13.1	1.83	0.07	0.23	1.36	3.95	4.13	0.00	0.12	0.00	96.28
Avg.	71.1	0.29	13.4	1.56	0.07	0.25	1.27	4.06	4.31	0.05	0.09	0.01	96.45
Accepted	71.38	0.26	13.05	1.56	0.02	0.29	1.19	4.06	4.11	low	0.08	low	95.92
M6N_1	67.7	0.37	12.7	1.45	0.00	0.21	1.36	3.64	4.15	0.06	0.06	0.00	91.71
M6N_2	67.8	0.26	12.7	1.73	0.00	0.12	1.35	3.78	4.35	0.07	0.03	0.01	92.14
M6N_3	68.7	0.19	12.3	1.83	0.09	0.38	1.35	3.82	4.22	0.03	0.09	0.02	92.92
M6N_4	67.7	0.42	12.4	1.56	0.09	0.24	1.22	3.95	3.91	0.06	0.09	0.00	91.62
M6N_5	69.1	0.21	13.0	1.66	0.00	0.28	1.17	3.93	4.25	0.12	0.07	0.00	93.78
M6N_6	69.1	0.38	13.0	1.50	0.04	0.22	1.01	3.95	3.96	0.12	0.13	0.01	93.42
M6N_7	69.1	0.38	13.0	1.50	0.00	0.22	1.01	3.80	3.96	0.12	0.13	0.01	93.18
M6N_8	68.8	0.30	12.8	1.62	0.00	0.29	1.17	3.93	4.13	0.09	0.10	0.01	93.20
M6N_9	69.3	0.18	12.8	1.36	0.14	0.17	1.12	3.96	4.01	0.10	0.12	0.00	93.23
Avg.	68.58	0.299	12.75	1.580	0.039	0.237	1.195	3.863	4.103	0.085	0.090	0.007	92.80
Accepted	69.47	0.30	12.84	1.48	0.05	0.25	1.19	4.05	4.02	low	0.07	low	93.65
M6NDP_1	68.3	0.24	12.7	1.58	0.00	0.40	1.24	3.76	4.06	0.07	0.06	0.01	92.37
M6NDP_2	70.4	0.39	7.51	9.12	0.14	0.10	0.43	7.37	4.44	0.00	0.32	0.06	100.23
M6NDP_3	67.5	0.24	13.3	1.41	0.02	0.26	1.30	4.09	3.99	0.07	0.11	0.01	92.31
M6NDP_4	69.0	0.26	13.0	1.47	0.06	0.22	1.23	4.03	3.85	0.02	0.09	0.01	93.27
Avg.	68.8	0.28	11.6	3.39	0.05	0.24	1.05	4.81	4.08	0.04	0.15	0.02	94.54
Accepted	69.47	0.30	12.84	1.48	0.05	0.25	1.19	4.05	4.02	low	0.07	low	93.65
NBS620_1	71.8	0.00	1.66	0.00	0.00	3.84	7.62	14.7	0.39	0.00	0.03	0.26	100.28
NBS620_2	72.0	0.01	1.85	0.03	0.01	3.53	7.02	14.5	0.31	0.00	0.01	0.27	99.52
NBS620_3	71.5	0.17	1.78	0.00	0.00	3.41	7.93	14.6	0.46	0.00	0.01	0.24	100.07
NBS620_4	73.3	0.00	1.97	0.07	0.00	3.61	7.33	14.7	0.46	0.02	0.03	0.29	101.73
NBS620_5	69.7	0.10	1.89	0.00	0.04	3.86	7.36	15.4	0.44	0.02	0.03	0.30	99.09
NBS620_6	73.0	0.00	1.74	0.06	0.00	3.94	6.97	15.1	0.38	0.06	0.01	0.26	101.51
NBS620_7	73.0	0.00	1.85	0.00	0.04	3.47	7.31	14.3	0.44	0.01	0.01	0.30	100.79
NBS620_8	73.4	0.01	1.73	0.00	0.00	3.90	7.00	15.4	0.29	0.00	0.00	0.26	101.98
Avg.	72.20	0.036	1.807	0.020	0.010	3.696	7.316	14.84	0.396	0.014	0.015	0.272	100.62
Accepted	72.1	0.02	1.80	0.04	low	3.69	7.11	14.4	0.41	low	low	0.28	99.82
PCD_1	76.5	0.00	12.3	1.23	0.00	0.00	0.58	3.92	4.90	0.02	0.08	0.00	99.46
PCD_2	76.9	0.05	13.2	1.09	0.00	0.04	0.58	4.11	4.76	0.02	0.10	0.01	100.87
PCD_3	77.3	0.10	12.7	1.20	0.16	0.00	0.57	4.04	4.59	0.00	0.07	0.01	100.69
PCD_4	77.2	0.07	12.4	0.66	0.22	0.02	0.49	3.75	4.74	0.00	0.05	0.01	99.58
PCD_5	76.8	0.09	12.4	0.80	0.18	0.02	0.51	4.03	4.55	0.05	0.02	0.00	99.44
Avg.	76.93	0.061	12.60	0.997	0.113	0.017	0.543	3.969	4.709	0.016	0.064	0.008	100.01
Accepted	76.40	0.07	12.44	1.02	0.03	0.02	0.53	4.21	4.68	low	0.06	low	99.40

Accepted values for KN9 from Stix et al. (1995)

Accepted values for 35-1, PCD, M3N and M6N from Devine et al. (1995)

Accepted values for KE12 from Stix and Layne (1996)

* Fe as FeO

Appendix 2

Supplementary table 2. Major element and volatile compositions (in wt. %) of olivine-hosted melt inclusions obtained by EMP

Sample ID	Inclusion ID	SiO_2	TiO_2	Al_2O_3	FeO*	MnO	MgO	CaO	Na_2O	K_2O	P_2O_5	Cl	SO_3	Total
HK2013-1991-A	1991-01-01	55.34	2.03	14.92	11.77	0.29	2.42	6.93	4.21	1.23	0.89	0.03	0.20	100.26
	1991-01-02	52.92	1.91	13.69	11.36	0.40	2.40	7.04	4.00	1.18	0.88	0.05	0.20	96.01
	1991-02-01	54.00	2.03	15.02	11.74	0.32	2.59	6.48	3.95	1.21	0.91	0.05	0.19	98.48
	1991-04-01	54.25	2.12	14.84	11.57	0.24	2.22	7.44	4.12	1.28	1.00	0.05	0.18	99.28
	1991-05-01	55.76	1.92	16.30	12.05	0.21	2.73	7.05	4.24	1.32	0.88	0.02	0.19	102.66
HK2013-1845-A	1845-01	59.61	0.88	15.99	8.02	0.38	1.12	4.59	4.56	1.73	0.30	0.05	0.08	97.29
	1845-02-01	60.91	0.99	15.40	8.83	0.13	1.19	4.96	3.68	1.63	0.24	0.07	0.09	98.11
	1845-02-02	59.91	1.04	14.94	8.14	0.18	1.21	4.22	4.06	1.50	0.24	0.07	0.05	98.54
	1845-03-01	61.60	0.95	15.16	8.43	0.22	1.10	4.75	4.86	1.70	0.36	0.05	0.09	99.25
	1845-04-01	59.05	0.92	14.85	8.17	0.16	1.01	4.56	4.19	1.74	0.40	0.03	0.08	95.16
	1845-05-01	61.47	0.91	15.00	8.08	0.16	1.15	4.42	4.50	1.71	0.27	0.05	0.10	97.82
	1845-06-01	59.83	0.89	14.66	8.14	0.10	1.01	4.71	4.68	1.61	0.24	0.05	0.07	95.97
HK2013-1104-C	1104DT-G1-01	68.63	0.32	13.29	2.96	0.01	0.05	1.99	4.59	2.62	0.00	0.03	0.02	94.50
	1104DT-G1-02	69.17	0.25	13.30	3.22	0.07	0.09	1.92	4.63	2.43	0.01	0.07	0.03	95.19
	1104DT-G2-01	68.31	0.17	12.96	2.75	0.00	0.03	1.96	4.83	2.43	0.00	0.13	0.03	93.56
	1104DT-H2-02	68.24	0.29	13.80	3.08	0.00	0.04	2.12	4.48	2.51	0.02	0.07	0.01	94.65
	1104DT-H2-04	70.04	0.21	13.28	2.74	0.13	0.08	1.98	4.96	2.62	0.00	0.08	0.01	96.11
	1104DT-H2-03	71.35	0.20	13.99	2.85	0.05	0.09	2.03	5.24	2.53	0.06	0.04	0.01	98.43
	1104DT-H1-01	69.40	0.23	13.21	2.61	0.14	0.07	1.89	4.73	2.46	0.00	0.09	0.03	94.84
	1104DT-H3-01	68.96	0.21	13.74	3.28	0.17	0.07	1.94	4.91	2.57	0.03	0.05	0.02	95.93
	1104DT-M1-01	67.80	0.44	13.18	2.76	0.31	0.06	1.87	4.73	2.66	0.01	0.04	0.00	93.83
	1104DT-M3-01	70.90	0.13	14.34	3.40	0.20	0.10	2.01	4.95	2.69	0.00	0.06	0.02	98.78
	1104DT-M4-01	68.71	0.05	13.78	3.16	0.21	0.08	1.84	4.71	2.33	0.00	0.06	0.01	94.93
	1104DT-N1-01	68.55	0.25	13.42	3.79	0.06	0.14	1.99	4.74	2.48	0.00	0.06	0.03	95.49
HK2013-1104-B	1104LT-J1-01	69.06	0.19	13.21	2.83	0.15	0.06	1.87	4.49	2.48	0.04	0.08	0.03	94.45
	1104LT-K1-01	71.85	0.20	13.70	2.68	0.12	0.12	1.90	5.20	2.47	0.00	0.06	0.00	98.29
	1104LT-K1-02	70.45	0.19	13.45	2.79	0.06	0.15	1.82	4.64	2.82	0.02	0.04	0.02	96.42
	1104LT-K2-01	68.54	0.21	13.66	3.81	0.18	0.12	2.08	4.87	2.48	0.00	0.06	0.01	96.02
	1104LT-K2-02	70.89	0.17	13.08	2.82	0.13	0.07	1.76	4.74	2.59	0.07	0.06	0.02	96.38
	1104LT-K3-01	72.24	0.27	13.45	3.07	0.10	0.09	1.94	5.07	2.41	0.02	0.06	0.01	98.72
	1104LT-K3-02	69.28	0.24	12.97	2.93	0.23	0.14	1.90	4.21	2.58	0.01	0.01	0.03	94.51
	1104LT-J3-01	69.54	0.01	13.33	4.26	0.12	0.10	1.90	5.00	2.91	0.03	0.03	0.01	97.21
	1104LT-L1-01	69.48	0.21	12.73	3.50	0.00	0.12	1.90	4.95	2.77	0.00	0.01	0.02	95.68
	1104LT-L1-2	69.98	0.23	13.57	3.55	0.14	0.06	1.94	4.83	2.39	0.01	0.04	0.02	96.75
	1104LT-L3-01	69.23	0.32	13.08	3.03	0.19	0.11	1.92	4.65	2.79	0.05	0.04	0.01	95.40
	1104LT-L4-01	69.13	0.35	12.92	3.08	0.00	0.10	1.91	4.31	2.51	0.14	0.07	0.01	94.50
	1104LT-L4-2	69.90	0.29	13.58	3.22	0.16	0.11	2.04	4.86	2.45	0.02	0.06	0.01	96.68
HK2013-1104-A	1104B-01-01	69.69	0.17	13.27	3.22	0.26	0.09	1.75	4.53	2.70	0.00	0.00	0.02	95.70
	1104B-02-01	68.44	0.19	13.01	3.20	0.08	0.06	1.79	4.54	2.48	0.05	0.04	0.02	93.88
	1104B-05-01	68.81	0.11	13.10	3.52	0.17	0.08	1.88	4.44	2.59	0.00	0.02	0.03	94.75
	1104B-05-02	69.04	0.22	13.23	2.74	0.14	0.11	1.98	4.29	2.76	0.01	0.08	0.02	94.58
	1104B-06-01	67.46	0.29	12.92	3.86	0.18	0.18	1.97	4.26	2.48	0.02	0.05	0.02	93.68
	1104B-06-02	66.59	0.22	12.84	3.94	0.16	0.14	1.97	4.42	2.60	0.02	0.07	0.01	92.95
	1104B-06-03	67.71	0.22	13.32	3.64	0.10	0.13	1.90	4.22	2.71	0.00	0.07	0.01	94.00
	1104B-07-01	66.12	0.29	13.76	3.91	0.13	0.07	2.59	4.65	2.33	0.00	0.04	0.01	93.87
	1104B-08-01	69.37	0.31	13.55	3.36	0.26	0.10	1.95	4.89	2.40	0.00	0.05	0.02	96.25
	1104B-08-02	68.05	0.40	12.91	4.02	0.21	0.16	1.80	4.23	2.45	0.05	0.03	0.04	94.32
	1104B-09-01	70.20	0.04	13.52	4.19	0.23	0.07	2.01	4.83	2.46	0.00	0.08	0.03	97.63
	1104B-09-02	67.64	0.23	13.05	4.68	0.30	0.22	1.92	4.74	2.62	0.04	0.08	0.03	95.53
	1104B-09-03	69.45	0.09	13.52	3.60	0.14	0.06	1.85	5.02	2.51	0.01	0.06	0.02	96.31
	1104B-09-04	67.55	0.13	13.52	4.21	0.09	0.13	2.17	4.73	2.46	0.01	0.09	0.01	95.08
	1104B-09-05	68.36	0.29	13.48	3.80	0.06	0.09	2.05	4.57	2.51	0.01	0.05	0.02	95.27
	1104B-10-01	65.38	0.23	13.55	3.50	0.12	0.09	2.09	4.31	2.24	0.00	0.04	0.01	91.56
HK2011-H3-C	H3DT-DD1-01	64.63	0.17	12.55	6.18	0.45	0.32	2.08	4.33	2.31	0.03	0.04	0.00	93.09
	H3DT-DD1-02	67.36	0.17	13.14	5.39	0.12	0.20	2.14	4.32	2.29	0.05	0.06	0.01	95.23
	H3DT-FF1-01	64.73	0.32	13.64	6.27	0.06	0.41	3.50	4.78	2.10	0.11	0.04	0.02	95.98
	H3DT-FF1-02	65.70	0.32	13.76	6.24	0.10	0.42	3.76	5.13	2.35	0.10	0.05	0.03	97.95
	H3DT-FF2-01	62.42	0.70	14.48	7.34	0.21	0.46	4.42	4.62	1.90	0.24	0.04	0.04	96.86
	H3DT-C1-01	66.16	0.11	13.39	5.28	0.12	0.25	2.83	4.78	2.18	0.10	0.05	0.00	95.26
	H3DT-FF2-02	63.55	0.23	13.15	5.76	0.13	0.42	3.26	4.50	2.33	0.05	0.07	0.02	93.43
HK2013-H3-B	H3LT-D1-01	65.05	0.55	14.35	6.15	0.11	0.39	3.58	4.22	2.09	0.11	0.02	0.05	96.66
	H3LT-D1-02	67.05	0.36	13.51	4.76	0.15	0.34	3.06	4.26	2.37	0.00	0.07	0.06	95.95
	H3LT-D1-03	63.92	0.47	13.94	6.38	0.32	0.40	3.60	4.14	2.05	0.17	0.04	0.06	95.48
	H3LT-E1-01	66.26	0.39	14.25	4.18	0.14	0.22	3.10	4.46	2.15	0.08	0.04	0.03	95.28
	H3LT-E2-01	65.57	0.31	14.00	4.82	0.15	0.32	2.96	4.34	2.25	0.07	0.06	0.03	94.86
	H3LT-E3-01	63.82	0.49	13.82	5.85	0.28	0.38	3.60	4.26	2.06	0.16	0.03	0.04	94.79
	H3LT-E4-01	63.24	0.42	14.08	6.10	0.11	0.34	3.87	4.79	2.10	0.12	0.07	0.07	95.28
	H3LT-E5-01	61.36	0.48	13.71	6.37	0.08	0.42	3.98	4.48	1.81	0.14	0.02	0.09	92.94
	H3LT-F1-01	65.51	0.26	12.86	4.77	0.23	0.21	2.85	4.70	2.58	0.10	0.07	0.03	94.16
	H3LT-F2-01	63.75	0.39	14.54	6.71	0.16	0.45	4.10	4.39	1.84	0.15	0.01	0.03	96.51
	H3LT-F4-01	63.17	0.54	14.22	5.03	0.21	0.37	3.83	4.31	2.04	0.17	0.04	0.08	94.00
	H3LT-EE1-01	65.68	0.34	13.85	6.06	0.23	0.35	3.38	4.76	2.24	0.06	0.04	0.04	97.01
	H3LT-EE1-02	65.44	0.39	13.34	5.29	0.23	0.26	3.21	4.76	2.37	0.07	0.03	0.04	95.43
HK2013-H3-A	H3B-01-01	67.63	0.27	12.96	3.40	0.17	0.09	1.97	4.78	2.30	0.04	0.06	0.01	93.65
	H3B-01-02	67.65	0.24	12.79	3.57	0.11	0.15	1.87	4.51	2.30	0.00	0.04	0.02	93.25
	H3B-02-01	68.23	0.16	12.88	4.47	0.21	0.19	1.90	4.54	2.19	0.00	0.06	0.02	94.83
	H3B-06-01	68.48	0.18	12.61	2.99	0.07	0.12	1.81	4.66	2.45	0.01	0.04	0.01	93.41
	H3B-06-02	68.21	0.24	12.97	3.81	0.00	0.07	2.11	4.56	2.23	0.04	0.02	0.03	94.28
	H3B-07-01	69.34	0.27	13.03	3.12	0.11	0.11	1.97	4.96	2.40	0.03	0.02	0.01	95.35
	H3B-08-01	67.99	0.15	12.90	3.59	0.14	0.09	1.99	4.59	2.52	0.00	0.05	0.02	94.01
	H3B-09-01	69.12	0.07	13.71	3.64	0.09	0.17	1.88	4.77	2.10	0.06	0.06	0.01	95.67
	H3B-10-01	67.58	0.20	12.82	3.76	0.11	0.08	1.97	4.12	2.39	0.02	0.05	0.01	93.08
	H3B-10-02	67.95	0.20	12.55	3.95	0.00	0.04	2.11	4.42	2.46	0.09	0.08	0.02	93.84
	H3B-11-01	66.17	0.21	13.18	3.89	0.08	0.11	2.21	4.68	2.40	0.01	0.04	0.01	92.97

* Fe as FeO

Appendix 3

Supplementary table 3. Major element compositions (in wt. %) of matrix glasses obtained by EMP

Sample ID	Grain ID	SiO_2	TiO_2	Al_2O_3	FeO*	MnO	MgO	CaO	Na_2O	K_2O	P_2O_5	Cl	SO_3	Total
HK2013-H3-A	H3B-GLASS-2	71.69	0.31	13.72	3.37	0.09	0.17	2.30	5.17	2.47	0.01	0.06	0.02	99.38
HK2013-H3-B	H3LT-E2-GLASS	66.90	0.57	14.47	6.45	0.22	0.50	3.57	5.35	1.80	0.19	0.07	0.05	100.13
	H3LT-GLASS-2	64.92	0.75	16.04	7.08	0.13	0.55	4.50	5.18	1.81	0.15	0.01	0.05	101.16
	H3LT-GLASS-3	65.27	0.51	15.03	7.23	0.17	0.40	4.53	5.45	1.93	0.13	0.03	0.06	100.72
	H3LT-GLASS-4	66.14	0.65	16.03	6.30	0.21	0.56	3.90	4.80	1.97	0.29	0.00	0.01	100.86
	H3LT-GLASS-6	65.12	0.39	15.06	7.08	0.08	0.48	4.05	4.66	1.92	0.19	0.04	0.04	99.08
HK2011-H3-C	H3DT-GLASS-1	64.69	0.69	15.32	7.35	0.20	0.65	4.46	5.23	1.73	0.19	0.04	0.04	100.60
	H3DT-GLASS-3	64.92	0.77	15.38	7.48	0.23	0.53	4.56	4.84	1.61	0.15	0.03	0.03	100.51
HK2013-1104-A	1104B-02-GLASS2	73.16	0.27	13.51	3.34	0.17	0.19	1.97	5.67	2.64	0.01	0.06	0.01	100.96
	1104B-05-GLASS	72.78	0.21	13.61	3.79	0.07	0.14	2.01	4.82	2.67	0.00	0.05	0.01	100.14
	1104B-GLASS-1	72.94	0.30	14.41	4.28	0.00	0.06	1.91	5.32	2.68	0.00	0.08	0.01	101.96
	1104B-GLASS-2	71.47	0.04	14.54	3.89	0.12	0.11	1.98	5.40	2.52	0.00	0.06	0.02	100.12
HK2013-1104-B	1104LT-J1-GLASS	73.16	0.35	13.29	3.50	0.06	0.12	2.00	5.79	2.61	0.00	0.05	0.01	100.92
	1104LT-K1-GLASS	71.92	0.11	13.47	3.17	0.04	0.13	1.72	5.41	2.51	0.00	0.01	0.02	98.51
	1104LT-K2-GLASS	72.61	0.28	13.36	3.53	0.00	0.09	1.85	5.37	2.48	0.03	0.05	0.00	99.64
	1104LT-K3-GLASS	71.05	0.44	13.75	3.36	0.09	0.10	1.92	5.29	2.60	0.00	0.05	0.00	98.65
	1104LT-GLASS-1	71.38	0.16	14.37	3.43	0.29	0.03	2.16	5.55	2.57	0.02	0.05	0.01	100.00
	1104LT-GLASS-2	72.63	0.19	14.75	3.28	0.00	0.08	2.10	5.18	2.76	0.01	0.03	0.02	101.03
	1104LT-GLASS-3	72.73	0.38	14.85	3.86	0.14	0.12	2.13	5.57	2.52	0.00	0.05	0.02	102.35
	1104LT-GLASS-4	73.51	0.17	14.54	3.55	0.33	0.01	2.19	5.49	2.71	0.00	0.03	0.00	102.52
	1104LT-GLASS-5	73.39	0.27	14.71	3.30	0.34	0.09	1.96	5.45	2.70	0.00	0.07	0.01	102.29
	1104LT-GLASS-6	74.11	0.30	14.90	3.59	0.05	0.12	1.98	5.15	2.62	0.00	0.08	0.01	102.89
HK2011-H3-C	1104DT-G1-GLASS	72.76	0.11	13.54	2.69	0.13	0.06	1.96	5.32	2.41	0.00	0.14	0.02	99.10
	1104DT-G2-GLASS	72.28	0.14	13.67	3.21	0.27	0.09	1.94	5.69	2.62	0.06	0.04	0.02	100.03
	1104DT-H2-GLASS	73.24	0.13	13.95	2.73	0.10	0.18	2.01	5.38	2.80	0.00	0.06	0.04	100.60
	1104DT-GLASS-2	71.62	0.21	14.76	3.53	0.00	0.12	1.93	5.07	2.70	0.06	0.06	0.00	100.02
	1104DT-GLASS-3	71.77	0.32	13.81	3.71	0.04	0.11	1.89	4.83	2.92	0.00	0.06	0.02	99.46
	1104DT-GLASS-4	70.76	0.24	13.74	3.51	0.07	0.10	2.04	5.35	2.41	0.06	0.05	0.01	98.31
	1104DT-GLASS-5	71.19	0.20	14.01	3.24	0.11	0.17	2.17	5.22	2.63	0.00	0.07	0.03	99.02
HK2013-1845-A	1845-GLASS-1	60.46	1.01	14.99	8.27	0.10	1.05	4.97	4.83	1.66	0.29	0.06	0.09	97.77
	1845-GLASS-2	60.17	0.89	15.97	8.06	0.12	1.25	4.53	4.00	1.65	0.29	0.00	0.07	97.01
	1845-GLASS-3	61.70	0.87	15.69	9.94	0.43	1.27	4.63	5.27	1.86	0.16	0.03	0.07	101.91
	1845-GLASS-4	60.83	0.92	15.25	10.11	0.00	1.21	4.84	4.64	1.84	0.31	0.00	0.08	100.02
HK2013-1991-A	1991-GLASS-2	52.78	1.96	14.55	11.62	0.12	2.48	6.98	4.01	1.21	1.06	0.05	0.12	96.92
	1991-GLASS-3	56.80	1.91	15.91	11.78	0.09	2.83	7.21	4.45	1.29	0.87	0.06	0.11	103.29

* Fe as FeO

Appendix 4

Supplementary table 4. Major element compositions (in wt. %) of olivines obtained by EMP

Sample ID	Grain ID	SiO_2	TiO_2	Al_2O_3	FeO*	MnO	MgO	CaO	Na_2O	K_2O	Cr_2O_3	NiO	Total	Fo.
HK2013-H3-A	H3B-01-OLIV1	30.7	0.05	0.02	61.5	2.11	5.21	0.25	0.00	0.00	0.01	0.00	99.8	13.1
	H3B-01-OLIV2	30.4	0.01	0.00	61.6	2.10	5.18	0.26	0.00	0.00	0.00	0.00	99.5	13.0
	H3B-01-OLIV3	30.5	0.12	0.00	61.4	2.09	5.06	0.25	0.01	0.00	0.01	0.00	99.5	12.8
	H3B-02-OLIV1	30.6	0.03	0.00	61.6	2.09	5.14	0.24	0.01	0.00	0.00	0.01	99.7	12.9
	H3B-02-OLIV2	30.8	0.02	0.00	61.6	2.13	4.98	0.26	0.00	0.00	0.00	0.01	99.7	12.6
	H3B-02-OLIV3	30.3	0.04	0.01	61.7	2.13	5.30	0.25	0.02	0.00	0.00	0.00	99.7	13.3
	H3B-06-OLIV1	30.5	0.01	0.00	61.8	2.09	5.03	0.25	0.03	0.00	0.01	0.00	99.7	12.7
	H3B-06-OLIV2	30.4	0.05	0.01	61.7	2.09	5.11	0.26	0.00	0.00	0.00	0.00	99.6	12.9
	H3B-06-OLIV3	30.6	0.04	0.01	61.7	2.11	5.11	0.25	0.01	0.00	0.01	0.01	99.9	12.9
	H3B-07-OLIV1	30.5	0.03	0.00	61.4	2.10	5.18	0.25	0.01	0.00	0.00	0.00	99.5	13.1
	H3B-07-OLIV2	30.5	0.05	0.00	61.5	2.10	5.23	0.25	0.00	0.00	0.01	0.00	99.7	13.2
	H3B-07-OLIV3	31.0	0.03	0.00	61.3	2.09	5.66	0.25	0.02	0.00	0.00	0.01	100.3	14.1
	H3B_08_OLIV1	30.4	0.02	0.00	61.5	2.17	5.11	0.24	0.02	0.00	0.00	0.00	99.5	12.9
	H3B_08_OLIV2	30.4	0.04	0.00	61.5	2.17	5.12	0.25	0.03	0.00	0.00	0.00	99.5	12.9
	H3B_08_OLIV3	31.4	0.03	0.00	61.4	2.16	5.33	0.24	0.00	0.00	0.00	0.00	100.6	13.4
	H3B_09_OLIV1	30.9	0.02	0.00	61.4	2.13	5.52	0.25	0.02	0.00	0.00	0.01	100.2	13.8
	H3B_09_OLIV2	31.1	0.02	0.00	61.4	2.12	5.45	0.24	0.00	0.00	0.00	0.00	100.3	13.6
	H3B_09_OLIV3	30.5	0.02	0.00	61.9	2.16	4.83	0.25	0.00	0.00	0.00	0.00	99.6	12.2
	H3B_10_OLIV1	30.6	0.02	0.00	61.7	2.19	5.05	0.25	0.00	0.00	0.00	0.00	99.7	12.7
	H3B_10_OLIV2	30.6	0.03	0.00	61.7	2.18	5.07	0.25	0.00	0.00	0.00	0.00	99.8	12.8
	H3B_10_OLIV3	30.8	0.02	0.00	61.5	2.15	5.30	0.26	0.02	0.00	0.00	0.00	100.0	13.3
	H3B_11_OLIV1	30.5	0.05	0.01	61.6	2.15	5.05	0.24	0.01	0.00	0.01	0.00	99.6	12.8
	H3B_11_OLIV2	30.5	0.03	0.00	61.5	2.17	5.33	0.25	0.04	0.00	0.00	0.00	99.8	13.4
	H3B_11_OLIV3	29.4	0.02	0.00	61.2	2.14	5.49	0.25	0.00	0.00	0.00	0.00	98.6	13.8
	H3B_12_OLIV1	31.6	0.21	0.00	61.2	2.11	5.36	0.24	0.00	0.00	0.00	0.00	100.7	13.5
	H3B_12_OLIV2	31.5	0.02	0.00	61.2	2.10	5.40	0.25	0.00	0.00	0.00	0.01	100.4	13.6
	H3B_12_OLIV3	31.0	0.04	0.01	61.4	2.10	4.91	0.24	0.00	0.00	0.00	0.00	99.8	12.5
HK2013-H3-B	H3LT-D1-OLIV1	31.4	0.01	0.02	57.0	1.66	9.33	0.27	0.05	0.00	0.00	0.00	99.8	22.6
	H3LT-D1-OLIV2	31.5	0.03	0.01	56.7	1.62	9.50	0.28	0.01	0.00	0.01	0.00	99.7	23.0
	H3LT-D1-OLIV3	31.3	0.02	0.02	56.2	1.59	9.94	0.29	0.02	0.00	0.00	0.01	99.4	24.0
	H3LT-E1-OLIV1	30.9	0.03	0.01	57.9	1.74	8.54	0.30	0.00	0.00	0.00	0.01	99.4	20.8
	H3LT-E1-OLIV2	30.9	0.02	0.01	57.8	1.72	8.48	0.30	0.00	0.00	0.00	0.00	99.3	20.7
	H3LT-E1-OLIV3	30.1	0.04	0.00	57.4	1.70	8.52	0.27	0.02	0.00	0.00	0.00	98.0	20.9
	H3LT-E2-OLIV1	32.0	0.02	0.00	56.9	1.65	9.64	0.30	0.03	0.00	0.00	0.00	100.6	23.2
	H3LT-E2-OLIV2	31.7	0.03	0.01	55.5	1.58	10.5	0.30	0.02	0.00	0.00	0.00	99.6	25.2
	H3LT-E3-OLIV1	31.5	0.06	0.03	57.1	1.67	9.34	0.29	0.04	0.00	0.00	0.00	100.0	22.6
	H3LT-E3-OLIV2	31.0	0.01	0.00	57.5	1.66	8.89	0.28	0.02	0.00	0.00	0.00	99.4	21.6
	H3LT-E3-OLIV3	31.0	0.02	0.01	56.8	1.63	9.94	0.29	0.03	0.00	0.01	0.00	99.7	23.8
	H3LT_E4_OLIV1	30.8	0.03	0.00	57.9	1.74	8.62	0.29	0.00	0.00	0.01	0.00	99.3	21.0
	H3LT_E4_OLIV2	31.3	0.03	0.00	57.8	1.77	8.85	0.30	0.02	0.00	0.00	0.00	100.0	21.5
	H3LT_E4_OLIV3	31.2	0.03	0.00	58.0	1.77	8.87	0.30	0.00	0.00	0.01	0.00	100.2	21.4
	H3LT_E5_OLIV1	31.6	0.02	0.00	55.0	1.53	11.1	0.27	0.07	0.00	0.00	0.00	99.6	26.5
	H3LT_E5_OLIV2	31.6	0.04	0.00	54.9	1.50	11.5	0.27	0.00	0.00	0.00	0.00	99.8	27.2
	H3LT_E5_OLIV3	32.3	0.04	0.00	54.5	1.46	11.8	0.26	0.02	0.00	0.00	0.00	100.4	27.8
	H3LT_F1_OLIV1	30.2	0.02	0.01	57.3	1.74	8.69	0.28	0.00	0.00	0.00	0.00	98.3	21.3
	H3LT_F1_OLIV2	31.2	0.04	0.01	57.4	1.71	8.67	0.30	0.01	0.00	0.00	0.00	99.3	21.2
	H3LT_F1_OLIV3	31.3	0.02	0.00	56.8	1.68	9.40	0.28	0.01	0.00	0.00	0.00	99.5	22.8
	H3LT_F1_OLIV1	31.5	0.03	0.02	55.0	1.50	11.2	0.26	0.01	0.00	0.00	0.00	99.5	26.7
	H3LT_F1_OLIV2	31.6	0.03	0.02	55.0	1.51	11.3	0.25	0.03	0.00	0.00	0.00	99.7	26.8
	H3LT_F1_OLIV3	31.9	0.04	0.00	54.6	1.48	12.1	0.27	0.00	0.00	0.00	0.01	100.5	28.4
	H3LT_F3_OLIV1	31.5	0.04	0.00	54.7	1.49	11.1	0.25	0.02	0.00	0.00	0.00	99.0	26.5
	H3LT_F3_OLIV2	30.7	0.02	0.01	54.8	1.48	11.2	0.27	0.01	0.00	0.01	0.00	98.5	26.7
	H3LT_F3_OLIV3	31.4	0.03	0.00	54.6	1.51	11.7	0.26	0.00	0.00	0.01	0.00	99.5	27.6
	H3LT_EE4_OLIV1	31.1	0.03	0.00	57.0	1.65	9.46	0.29	0.02	0.00	0.00	0.00	99.5	22.8
	H3LT_EE4_OLIV2	31.2	0.02	0.01	56.9	1.66	9.59	0.29	0.04	0.00	0.00	0.00	99.8	23.1
	H3LT_EE4_OLIV3	31.7	0.04	0.01	56.4	1.64	10.1	0.28	0.00	0.00	0.00	0.00	100.2	24.3
HK2011-H3-C	H3DT_C1_OLIV1	31.3	0.03	0.00	56.0	1.59	10.3	0.30	0.01	0.00	0.00	0.00	99.5	24.7
	H3DT_C1_OLIV2	31.4	0.01	0.01	56.6	1.60	10.1	0.30	0.02	0.00	0.00	0.00	100.0	24.1
	H3DT_C1_OLIV3	31.3	0.03	0.02	56.4	1.64	10.0	0.29	0.03	0.00	0.01	0.00	99.8	24.0
	H3DT_DD1_OLIV1	30.5	0.04	0.00	61.5	2.11	5.19	0.26	0.00	0.00	0.00	0.00	99.6	13.1
	H3DT_DD1_OLIV2	30.5	0.03	0.00	61.6	2.13	5.15	0.26	0.00	0.00	0.00	0.01	99.6	13.0
	H3DT_DD1_OLIV3	30.3	0.01	0.00	61.4	2.09	5.23	0.27	0.01	0.00	0.00	0.00	99.3	13.2
	H3DT_FF1_OLIV1	31.3	0.05	0.00	56.1	1.61	10.5	0.30	0.03	0.00	0.00	0.00	99.9	25.1
	H3DT_FF1_OLIV2	30.9	0.02	0.00	57.1	1.67	9.49	0.30	0.00	0.00	0.00	0.00	99.4	22.9
	H3DT_FF1_OLIV3	31.6	0.04	0.01	55.1	1.56	11.6	0.28	0.01	0.00	0.00	0.00	100.2	27.4
	H3DT_FF2_OLIV1	31.2	0.04	0.00	56.6	1.66	9.96	0.29	0.00	0.00	0.00	0.00	99.7	23.9
	H3DT_FF2_OLIV2	31.3	0.04	0.00	56.2	1.64	10.4	0.28	0.00	0.00	0.01	0.01	99.9	24.9

Appendix 4 – continued

HK2013-1104-A	1104B-01-OLIV1	30.6	0.04	0.00	62.1	2.16	4.77	0.28	0.02	0.00	0.00	0.00	100.0	12.0
	1104B-01-OLIV2	30.5	0.01	0.00	61.9	2.19	4.63	0.29	0.01	0.00	0.00	0.00	99.5	11.8
	1104B-01-OLIV3	30.2	0.04	0.00	62.0	2.17	4.64	0.30	0.00	0.00	0.00	0.00	99.3	11.8
	1104B-02-OLIV1	30.6	0.01	0.01	61.9	2.17	4.69	0.29	0.00	0.00	0.01	0.00	99.7	11.9
	1104B-02-OLIV2	30.3	0.03	0.03	61.8	2.18	4.73	0.29	0.04	0.00	0.01	0.00	99.4	12.0
	1104B-02-OLIV3	30.4	0.04	0.00	61.9	2.15	4.72	0.30	0.02	0.00	0.00	0.00	99.5	12.0
	1104B-04-OLIV1	28.5	0.04	0.00	61.7	2.19	4.36	0.28	0.01	0.00	0.00	0.01	97.0	11.2
	1104B-05-OLIV1	30.2	0.03	0.00	62.3	2.20	4.59	0.28	0.01	0.00	0.00	0.00	99.7	11.6
	1104B-05-OLIV2	30.3	0.03	0.00	62.1	2.19	4.52	0.28	0.02	0.00	0.00	0.00	99.4	11.5
	1104B-05-OLIV3	30.3	0.04	0.00	61.9	2.18	4.79	0.29	0.00	0.00	0.00	0.00	99.5	12.1
	1104DT_06_OLIV1	30.1	0.02	0.00	62.2	2.29	4.65	0.29	0.00	0.00	0.02	0.02	99.6	11.8
	1104DT_06_OLIV2	30.2	0.04	0.00	62.2	2.26	4.76	0.31	0.02	0.00	0.01	0.00	99.8	12.0
	1104DT_06_OLIV3	30.3	0.02	0.00	62.5	2.22	4.32	0.30	0.00	0.00	0.00	0.00	99.6	11.0
	1104DT_07_OLIV1	30.5	0.04	0.00	61.7	2.22	4.78	0.30	0.00	0.00	0.01	0.00	99.5	12.1
	1104DT_07_OLIV2	30.4	0.04	0.00	62.0	2.20	4.61	0.30	0.02	0.00	0.00	0.00	99.6	11.7
	1104DT_07_OLIV3	30.5	0.02	0.02	62.1	2.23	4.45	0.30	0.00	0.00	0.00	0.00	99.7	11.3
	1104DT_08_OLIV1	30.5	0.03	0.00	62.2	2.22	4.82	0.29	0.03	0.00	0.00	0.00	100.1	12.1
	1104DT_08_OLIV2	29.7	0.01	0.00	62.2	2.25	4.72	0.30	0.05	0.00	0.01	0.00	99.2	11.9
	1104DT_08_OLIV3	30.8	0.02	0.00	62.1	2.22	4.81	0.28	0.01	0.00	0.01	0.00	100.2	12.1
	1104DT_09_OLIV1	28.5	0.03	0.20	62.2	2.22	4.35	0.30	0.02	0.00	0.00	0.00	97.7	11.1
	1104DT_09_OLIV2	29.9	0.04	0.00	62.4	2.29	4.59	0.29	0.01	0.00	0.02	0.00	99.6	11.6
	1104DT_09_OLIV3	30.4	0.03	0.00	62.2	2.23	4.57	0.29	0.03	0.00	0.02	0.00	99.7	11.6
HK2013-1104-B	1104LT-J1-OLIV1	30.3	0.04	0.00	62.0	2.22	4.72	0.29	0.01	0.00	0.00	0.00	99.6	11.9
	1104LT-J1-OLIV2	30.6	0.04	0.00	62.0	2.18	4.84	0.29	0.01	0.00	0.00	0.00	100.0	12.2
	1104LT-J1-OLIV3	30.2	0.03	0.00	62.0	2.22	4.53	0.31	0.01	0.00	0.00	0.01	99.4	11.5
	1104LT-K1-OLIV1	31.0	0.03	0.00	61.9	2.18	4.76	0.30	0.02	0.00	0.00	0.00	100.2	12.1
	1104LT-K1-OLIV2	30.4	0.03	0.01	62.2	2.20	4.73	0.29	0.03	0.00	0.00	0.01	100.0	11.9
	1104LT-K1-OLIV3	29.9	0.03	0.00	62.2	2.20	4.57	0.30	0.03	0.00	0.00	0.00	99.2	11.6
	1104LT-K2-OLIV1	30.1	0.10	0.00	62.3	2.19	4.65	0.29	0.02	0.00	0.00	0.01	99.7	11.7
	1104LT-K2-OLIV2	30.2	0.02	0.00	62.3	2.19	4.57	0.30	0.02	0.00	0.00	0.00	99.7	11.6
	1104LT-K2-OLIV3	30.9	0.03	0.01	62.2	2.21	4.65	0.30	0.02	0.00	0.00	0.01	100.3	11.8
	1104LT-K3-OLIV1	30.9	0.03	0.00	61.9	2.22	4.59	0.28	0.00	0.00	0.00	0.00	99.9	11.7
	1104LT-K3-OLIV2	30.7	0.03	0.00	62.1	2.16	4.52	0.29	0.03	0.00	0.00	0.01	99.8	11.5
	1104LT-K3-OLIV3	30.8	0.05	0.02	61.8	2.21	4.49	0.29	0.03	0.00	0.00	0.00	99.7	11.5
	1104LT_J2_OLIV1	30.2	0.03	0.00	62.2	2.24	4.57	0.29	0.00	0.00	0.00	0.00	99.5	11.6
	1104LT_J2_OLIV2	30.2	0.00	0.00	62.3	2.23	4.42	0.29	0.01	0.00	0.00	0.00	99.5	11.2
	1104LT_J2_OLIV3	29.6	0.04	0.00	62.1	2.23	4.43	0.31	0.04	0.00	0.01	0.00	98.7	11.3
	1104LT_J3_OLIV1	30.0	0.03	0.01	62.2	2.25	4.54	0.29	0.05	0.00	0.00	0.00	99.5	11.5
	1104LT_J3_OLIV2	30.3	0.01	0.00	62.3	2.28	4.60	0.29	0.02	0.00	0.00	0.00	99.8	11.6
	1104LT_J3_OLIV3	30.6	0.03	0.00	62.2	2.24	4.74	0.30	0.04	0.00	0.00	0.00	100.1	12.0
	1104LT_JL1_OLIV1	30.5	0.05	0.00	62.4	2.21	4.65	0.29	0.02	0.00	0.00	0.00	100.2	11.7
	1104LT_JL1_OLIV2	30.4	0.02	0.01	62.7	2.23	4.62	0.29	0.01	0.00	0.00	0.00	100.2	11.6
	1104LT_JL1_OLIV3	30.1	0.03	0.00	62.3	2.19	4.47	0.29	0.06	0.00	0.00	0.00	99.4	11.3
	1104LT_L2_OLIV1	30.3	0.03	0.00	62.2	2.21	4.64	0.30	0.05	0.00	0.00	0.00	99.8	11.7
	1104LT_L2_OLIV2	30.4	0.01	0.00	62.3	2.25	4.67	0.29	0.03	0.00	0.00	0.01	99.9	11.8
	1104LT_L2_OLIV3	31.0	0.03	0.00	62.1	2.22	4.63	0.29	0.00	0.00	0.00	0.00	100.2	11.7
	1104LT_L3_OLIV1	30.4	0.03	0.00	62.7	2.21	4.71	0.28	0.00	0.00	0.00	0.00	100.3	11.8
	1104LT_L3_OLIV2	30.4	0.04	0.00	62.7	2.29	4.61	0.28	0.05	0.00	0.00	0.00	100.4	11.6
	1104LT_L3_OLIV3	31.3	0.01	0.00	62.5	2.27	4.78	0.28	0.07	0.00	0.00	0.00	101.2	12.0
	1104LT_L4_OLIV1	30.1	0.04	0.00	62.2	2.24	4.70	0.30	0.03	0.00	0.00	0.00	99.7	11.9
	1104LT_L4_OLIV2	30.6	0.03	0.00	62.3	2.26	4.63	0.27	0.03	0.00	0.00	0.00	100.2	11.7
	1104LT_L4_OLIV3	30.7	0.04	0.00	62.3	2.21	4.72	0.29	0.02	0.00	0.01	0.00	100.3	11.9
HK2011-H3-C	1104DT-G1-OLIV1	30.8	0.02	0.00	62.2	2.23	4.82	0.29	0.00	0.00	0.00	0.01	100.3	12.2
	1104DT-G1-OLIV2	30.9	0.03	0.00	62.0	2.18	4.76	0.30	0.03	0.00	0.00	0.00	100.1	12.0
	1104DT-G1-OLIV3	31.2	0.03	0.00	61.9	2.17	4.89	0.28	0.02	0.00	0.01	0.00	100.6	12.3
	1104DT-G2-OLIV1	30.3	0.04	0.00	62.0	2.19	4.57	0.29	0.01	0.00	0.00	0.01	99.5	11.6
	1104DT-G2-OLIV2	29.9	0.05	0.00	62.1	2.18	4.49	0.30	0.00	0.00	0.00	0.00	99.0	11.4
	1104DT-G2-OLIV3	30.6	0.04	0.01	61.9	2.14	4.87	0.29	0.01	0.00	0.00	0.00	99.8	12.3
	1104DT-H1-OLIV1	30.3	0.05	0.00	62.2	2.18	4.65	0.28	0.01	0.00	0.00	0.01	99.7	11.8
	1104DT-H1-OLIV2	30.4	0.03	0.00	61.8	2.17	4.56	0.28	0.02	0.00	0.00	0.01	99.2	11.6
	1104DT-H1-OLIV3	30.9	0.02	0.00	61.3	2.15	4.48	0.28	0.00	0.00	0.00	0.01	99.2	11.5
	1104DT-H2-OLIV1	30.7	0.02	0.01	61.9	2.21	4.65	0.29	0.00	0.00	0.00	0.01	99.8	11.8
	1104DT-H2-OLIV2	30.5	0.03	0.00	61.8	2.14	4.68	0.28	0.02	0.00	0.00	0.00	99.4	11.9
	1104DT-H2-OLIV3	30.5	0.03	0.00	61.4	2.16	4.73	0.30	0.01	0.00	0.00	0.00	99.1	12.1
	1104DT_H3_OLIV1	30.3	0.03	0.00	62.4	2.26	4.66	0.30	0.05	0.00	0.00	0.00	99.9	11.8
	1104DT_H3_OLIV2	29.6	0.04	0.00	62.5	2.26	4.62	0.30	0.01	0.00	0.00	0.00	99.4	11.6
	1104DT_H3_OLIV3	30.5	0.04	0.00	62.4	2.25	4.40	0.29	0.04	0.00	0.00	0.01	99.9	11.2
	1104DT_M1_OLIV1	30.2	0.04	0.00	61.9	2.25	4.42	0.29	0.01	0.00	0.00	0.00	99.2	11.3
	1104DT_M1_OLIV2	30.2	0.02	0.00	62.1	2.26	4.59	0.29	0.00	0.00	0.00	0.00	99.5	11.6
	1104DT_M1_OLIV3	30.2	0.06	0.01	62.3	2.22	4.61	0.29	0.00	0.00	0.00	0.00	99.7	11.7
	1104DT_M3_OLIV1	30.3	0.04	0.00	62.5	2.22	4.63	0.31	0.01	0.00	0.00	0.00	100.0	11.7
	1104DT_M3_OLIV2	30.9	0.01	0.00	62.5	2.23	4.77	0.29	0.01	0.00	0.00	0.01	100.7	12.0
	1104DT_M3_OLIV3	31.2	0.37	0.01	61.9	2.16	5.02	0.28	0.00	0.00	0.00	0.00	100.9	12.6
	1104DT_M4_OLIV1	30.1	0.01	0.00	62.1	2.21	4.79	0.29	0.02	0.00	0.01	0.00	99.6	12.1
	1104DT_M4_OLIV2	30.2	0.05	0.00	62.0	2.19	4.89	0.31	0.00	0.00	0.00	0.00	99.6	12.3
	1104DT_M4_OLIV3	30.9	0.04	0.01	62.1	2.22	4.97	0.29	0.02	0.00	0.00	0.00	100.6	12.5
	1104DT_N1_OLIV1	30.4	0.02	0.00	62.3	2.29	4.69	0.29	0.01	0.00	0.00	0.00	99.9	11.8
	1104DT_N1_OLIV2	30.6	0.02	0.00	62.4	2.24	4.72	0.28	0.00	0.00	0.00	0.00	100.2	11.9
	1104DT_N1_OLIV3	30.5	0.05	0.00	61.9	2.18	4.41	0.29	0.02	0.00	0.00	0.00	99.3	11.3

Appendix 4 – continued

HK2013-1845-A	1845_02_OLIV1	33.2	0.03	0.02	45.6	1.14	19.4	0.24	0.00	0.00	0.01	0.00	99.6	43.1
	1845_02_OLIV2	32.3	0.03	0.01	45.6	1.18	18.6	0.25	0.01	0.00	0.00	0.00	97.9	42.1
	1845_01_OLIV1	33.2	0.02	0.00	45.8	1.21	19.4	0.26	0.04	0.00	0.00	0.00	100.0	43.0
	1845_01_OLIV2	33.5	0.01	0.00	45.2	1.19	20.5	0.24	0.00	0.00	0.00	0.00	100.7	44.7
	1845_01_OLIV3	34.4	0.02	0.03	45.3	1.20	19.3	0.25	0.00	0.00	0.01	0.00	100.5	43.2
	1845_04_OLIV1	33.4	0.04	0.02	45.7	1.24	18.7	0.25	0.02	0.00	0.01	0.00	99.3	42.2
	1845_04_OLIV2	33.2	0.04	0.02	45.6	1.20	19.4	0.25	0.03	0.00	0.00	0.00	99.7	43.1
	1845_04_OLIV3	33.3	0.02	0.00	45.3	1.18	19.7	0.25	0.02	0.00	0.00	0.00	99.8	43.6
	1845_05_OLIV1	33.7	0.04	0.00	45.9	1.19	19.8	0.24	0.03	0.00	0.00	0.00	101.0	43.5
	1845_05_OLIV2	33.1	0.01	0.01	45.8	1.19	19.8	0.24	0.00	0.00	0.01	0.00	100.1	43.5
	1845_05_OLIV3	32.2	0.02	0.01	45.9	1.19	19.3	0.24	0.02	0.00	0.00	0.00	98.9	42.8
	1845_06_OLIV1	33.3	0.02	0.00	45.8	1.19	19.3	0.25	0.00	0.00	0.01	0.00	99.9	43.0
	1845_06_OLIV2	32.7	0.03	0.00	45.7	1.19	19.6	0.24	0.01	0.00	0.00	0.01	99.5	43.3
	1845_06_OLIV3	33.4	0.03	0.01	45.5	1.19	20.5	0.25	0.01	0.00	0.00	0.01	100.9	44.6
HK2013-1991-A	1991_01_OLIV1	34.9	0.03	0.02	35.5	0.78	28.4	0.24	0.02	0.00	0.00	0.00	100.0	58.8
	1991_01_OLIV2	35.3	0.04	0.01	35.5	0.78	28.4	0.25	0.00	0.00	0.03	0.01	100.3	58.8
	1991_01_OLIV3	35.5	0.12	0.00	35.4	0.78	28.2	0.23	0.01	0.00	0.02	0.00	100.2	58.7
	1991_02_OLIV1	35.0	0.03	0.02	35.5	0.77	27.9	0.21	0.01	0.00	0.00	0.00	99.4	58.4
	1991_02_OLIV2	34.9	0.04	0.02	35.3	0.80	28.8	0.23	0.02	0.00	0.01	0.00	100.1	59.2
	1991_02_OLIV3	36.6	0.01	0.00	35.3	0.79	30.6	0.22	0.01	0.00	0.00	0.00	103.5	60.7
	1991_04_OLIV1	34.4	0.03	0.01	35.3	0.77	28.9	0.29	0.01	0.00	0.00	0.00	99.7	59.4
	1991_04_OLIV2	34.9	0.01	0.00	35.5	0.77	28.9	0.24	0.00	0.00	0.01	0.00	100.3	59.2
	1991_04_OLIV3	35.4	0.03	0.00	35.5	0.78	28.2	0.22	0.01	0.00	0.00	0.00	100.2	58.7
	1991_05_OLIV1	35.4	0.02	0.00	35.6	0.78	29.7	0.22	0.03	0.00	0.01	0.00	101.8	59.8
	1991_05_OLIV2	36.1	0.02	0.01	35.5	0.76	30.6	0.22	0.00	0.00	0.00	0.00	103.2	60.5
	1991_05_OLIV3	35.2	0.03	0.01	35.0	0.77	30.0	0.23	0.03	0.00	0.00	0.00	101.3	60.4

* Fe as FeO

Appendix 5

Supplementary table 5. H_2O (in wt. %) and CO_2 (in ppm) volatile contents of melt inclusions obtained by FTIR. Calculated Kd ratios after Toplis (2005)

Sample ID	Inclusion ID	H_2O_t	H_2O_m	OH	CO_2	Kd (O-Mi)
HK2013-1991-A	1991-01	0.80	0.31	0.49	0	0.25
	1991-02	0.84	0.53	1.05	0	0.28
	1991-03	1.58	0.12	0.72	0	0.26
	1991-04	1.34	0.47	0.87	0	0.23
	1991-05	1.62	0.62	1.00	0	0.27
HK2013-1845-A	1845-01	3.35	1.62	1.73	29	0.32
	1845-02	2.45	1.00	1.45	0	0.31
	1845-03	1.43	0.69	0.74	0	
	1845-04	1.67	0.92	0.75	0	0.30
	1845-05	2.68	1.76	0.92	0	0.33
	1845-06	1.12	0.65	0.46	0	0.29
HK2013-1104-A	1104-01	4.42	2.71	1.71	0	0.36
	1104-02	4.49	3.20	1.29	0	0.26
	1104-04	3.60	2.56	1.04	38	0.58
	1104-05-A	4.35	2.98	1.36	23	0.32
	1104-05-B	4.81	3.45	1.35	20	0.52
	1104-06				35	0.46
	1104-07	3.22	2.24	0.99	9	0.23
	1104-08	3.46	2.38	1.09	16	0.50
	1104-09-C				0	0.66
	1104-10	3.74	2.65	1.09	14	
HK2013-1104-B	1104-J1-01	3.20	2.32	0.88	0	0.27
	1104-K1-01	1.66	0.80	0.86	0	0.70
	1104-K1-02	2.45	1.60	0.85	0	0.59
	1104-K2-01	3.40	2.49	0.91	0	0.40
	1104-K3-01	2.74	1.81	0.93	0	0.37
	1104-K3-02	2.19	1.07	1.12	24	0.63
	1104-L1-01	4.82	3.25	1.57	173	0.24
	1104-L1-02	4.03	2.77	1.26	31	0.45
	1104-L2-01	2.04	1.15	0.89	0	
	1104-L2-03	1.04	0.61	0.43	5	
	1104-L3-01	4.51	2.76	1.75	0	0.46
	1104-L4-01	3.09	1.31	0.55	0	0.43
	1104-L4-02	1.68	1.05	0.63	29	0.26
HK2013-1104-C	1104-G1-01	5.67	4.33	1.33	0	0.23
	1104-G1-02	1.26	0.39	0.87	10	0.37
	1104-G2-01	2.24	1.30	0.94	10	0.14
	1104-H1-01	2.71	1.86	0.85	19	0.36
	1104-H2-01	2.82	1.87	0.95	0	0.15
	1104-H2-02	4.41	3.36	1.05	0	0.38
	1104-H3-01	3.69	2.70	0.99	0	0.20
	1104-H3-02	1.36	0.89	0.47	8	0.27
	1104-M1-01	2.77	1.55	1.22	0	0.31
	1104-M2-01	2.18	1.23	0.95	8	
	1104-M2-02	1.81	1.10	0.71	0	
	1104-M3-01	1.55	0.52	1.04	0	0.37
	1104-M4-01	3.27	1.83	1.44	0	0.32
	1104-N1-01	2.98	1.80	1.18	0	0.49
HK2013-H3-A	H3-01	5.57	3.77	1.80	0	0.31
	H2-03	3.36	2.49	0.87	0	0.50
	H3-06	4.61	3.43	1.17	0	0.47
	H3-07	3.98	3.00	0.97	0	0.40
	H3-08	4.37	3.24	1.13	0	0.28
	H3-09	5.21	3.14	2.06	0	0.51
	H3-10	5.37	3.76	1.61	0	0.25
	H3-11	4.33	2.93	1.40	0	0.32
	H3-12	4.30	2.86	1.44	0	
HK2013-H3-B	H3-D1-01	2.64	1.39	1.25	0	0.38
	H3-D1-02					
	H3-D1-02-02	1.35	0.70	0.64	0	0.42
	H3-E1-01	2.65	1.61	1.04	0	0.35
	H3-E2-01	3.02	1.54	1.48	0	0.39
	H3-E3-01	3.05	1.72	1.33	13	0.39
	H3-E4-01	2.12	1.18	0.94	0	0.37
	H3-E5-01	1.71	0.95	0.75	0	0.32
	H3-EE-01	3.02	1.59	1.43	0	0.35
	H3-EE-01-02					0.29
	H3-F1-01	2.26	1.39	0.88	0	0.29
	H3-F2-01	1.96	1.11	0.85	0	0.32
	H3-F4-01					0.36
HK2011-H3-C	H3-B1-01	2.22	1.37	0.85	0	
	H3-C1-01	2.38	1.29	1.09	0	0.26
	H3-DD1-01	4.62	2.75	1.87	0	0.43
	H3-FF1-01	2.14	1.24	0.90	0	0.34
	H3-FF1-02	1.63	0.84	0.79	0	0.32
	H3-FF2-01	2.97	1.53	1.44	15	0.41

Appendix 6

Supplementary table 6. Peak heights from FTIR spectra, calculated glass density after Nichols (2005) and thickness measurements by FTIR stage

Sample ID	Inclusion ID	Peak heights					Density	Thickness	Extinction Coefficients				
		A_{5200}	A_{4500}	A_{3450}	A_{2350}	A_{1630}	gL^{-1}	μm	E_{5200}	E_{4500}	E_{3450}	E_{2350}	E_{1630}
HK2013-H3-A	H3-01	0.0384	0.0253	0.944	0.0000	0.506	2421	47	1.61	1.73	71.4	1214	55
	H2-03	0.0345	0.0130	0.526	0.0000	0.180	2434	64	1.61	1.73	71.4	1214	55
	H3-06	0.0565	0.0208	0.909	0.0000	0.745	2426	76	1.61	1.73	71.4	1214	55
	H3-07	0.0574	0.0200	0.988	0.0000	0.562	2414	89	1.61	1.73	71.4	1214	55
	H3-08	0.0291	0.0110	1.149	0.0000	0.630	2421	42	1.61	1.73	71.4	1214	55
	H3-09	0.0330	0.0234	0.948	0.0000	0.547	2420	49	1.61	1.73	71.4	1214	55
	H3-10	0.0303	0.0140	0.614	0.0000	0.354	2427	37	1.61	1.73	71.4	1214	55
	H3-11	0.0370	0.0189	1.073	0.0000	0.684	2435	58	1.61	1.73	71.4	1214	55
	H3-12	0.0344	0.0186	0.526	0.0000	0.326	2422	56	1.61	1.73	71.4	1214	55
HK2013-H3-B	H3-D1-01	0.0194	0.0000	1.124	0.0000	0.479	2499	45	1.2	1.05	68	1066	55
	H3-D1-02	0.0000	0.0000	0.416	0.0000	0.197	2460	45	1.2	1.05	68	1066	55
	H3-D1-02-02	0.0000	0.0000	0.575	0.0000	0.243	2504	45	1.2	1.05	68	1066	55
	H3-E1-01	0.0212	0.0049	0.932	0.0000	0.460	2455	38	1.2	1.05	68	1066	55
	H3-E2-01	0.0220	0.0135	1.135	0.0000	0.467	2465	40	1.2	1.05	68	1066	55
	H3-E3-01	0.0194	0.0055	0.975	0.0026	0.446	2496	34	1.2	1.05	68	1066	55
	H3-E4-01	0.0000	0.0000	0.610	0.0000	0.274	2507	30	1.2	1.05	68	1066	55
	H3-E5-01	0.0000	0.0000	0.444	0.0185	0.200	2519	27	1.2	1.05	68	1066	55
	H3-EE-01	0.0000	0.0000	0.688	0.0000	0.293	2492	24	1.2	1.05	68	1066	55
	H3-EE01-02	0.0000	0.0000	0.067	0.0000	0.013	2477	24	1.2	1.05	68	1066	55
	H3-F1-01	0.0000	0.0000	0.807	0.0000	0.400	2461	38	1.2	1.05	68	1066	55
	H3-F2-01	0.0000	0.0000	0.565	0.0172	0.259	2517	30	1.2	1.05	68	1066	55
	H3-F4-01	0.0000	0.0000	0.214	0.0000	0.091	2489	44	1.2	1.05	68	1066	55
HK2011-H3-C	H3-B1-01	0.0279	0.0127	1.068	0.0000	0.537	2452	52	1.2	1.05	68	1066	55
	H3-C1-01	0.0000	0.0000	0.589	0.0000	0.259	2466	27	1.2	1.05	68	1066	55
	H3-DD1-01	0.0000	0.0000	0.932	0.0000	0.449	2475	22	1.2	1.05	68	1066	55
	H3-FF1-01	0.0000	0.0000	0.827	0.0000	0.387	2500	41	1.2	1.05	68	1066	55
	H3-FF1-02	0.0000	0.0000	0.631	0.0000	0.265	2502	41	1.2	1.05	68	1066	55
	H3-FF2-01	0.0140	0.0034	0.665	0.0021	0.277	2542	23	1.2	1.05	68	1066	55
HK2013-1104-A	1104-01	0.0304	0.0207	0.948	0.0000	0.520	2410	52	1.61	1.73	71	1214	55
	1104-02	0.0299	0.0129	1.436	0.0000	0.688	2412	43	1.61	1.73	71	1214	55
	1104-04	0.0254	0.0111	1.269	0.0118	0.627	2402	46	1.61	1.73	71	1214	55
	1104-05-A	0.0372	0.0183	1.213	0.0088	0.650	2416	58	1.61	1.73	71	1214	55
	1104-05-B	0.0428	0.0180	1.191	0.0075	0.649	2406	58	1.61	1.73	71	1214	55
	1104-06	0.0325	0.0346	0.598	0.0087	0.320	2428	37	1.61	1.73	71	1214	55
	1104-07	0.0247	0.0117	1.233	0.0031	0.627	2442	51	1.61	1.73	71	1214	55
	1104-08	0.0469	0.0230	1.581	0.0099	0.834	2429	91	1.61	1.73	71	1214	55
	1104-09-C	0.0000	0.0000	0.703	0.0000	0.302	2444	60	1.61	1.73	71	1214	55
	1104-10	0.0379	0.0168	1.471	0.0062	0.817	2428	66	1.61	1.73	71	1214	55
HK2013-1104-B	1104-J1-01	0.0397	0.0063	1.281	0.0000	0.720	2405	42	1.61	1.73	71	1214	55
	1104-K1-01	0.0000	0.0000	0.696	0.0000	0.259	2404	44	1.61	1.73	71	1214	55
	1104-K1-02	0.0000	0.0000	1.027	0.0000	0.520	2405	44	1.61	1.73	71	1214	55
	1104-K2-01	0.0232	0.0092	1.160	0.0000	0.566	2430	43	1.61	1.73	71	1214	55
	1104-K3-01	0.0000	0.0000	0.742	0.0000	0.380	2409	29	1.61	1.73	71	1214	55
	1104-K3-02	0.0000	0.0000	0.593	0.0046	0.225	2407	29	1.61	1.73	71	1214	55
	1104-L1-01	0.0271	0.0141	1.135	0.0447	0.549	2419	39	1.61	1.73	71	1214	55
	1104-L1-02	0.0231	0.0113	1.182	0.0080	0.523	2419	39	1.61	1.73	71	1214	55
	1104-L2-01	0.0000	0.0000	0.763	0.0000	0.333	2507	38	1.61	1.73	71	1214	55
	1104-L2-03	0.0049	0.0038	0.231	0.0012	0.077	2413	38	1.61	1.73	71	1214	55
	1104-L3-01	0.0211	0.0114	1.059	0.0000	0.503	2411	25	1.61	1.73	71	1214	55
	1104-L4-01	0.0348	0.0146	1.286	0.0000	0.703	2417	73	1.61	1.73	71	1214	55
	1104-L4-02	0.0166	0.0106	1.194	0.0141	0.486	2429	73	1.61	1.73	71	1214	55
HK2013-1104-C	1104-G1-01	0.0552	0.0182	0.962	0.0000	0.490	2413	59	1.61	1.73	71	1214	55
	1104-G1-02	0.0000	0.0000	0.635	0.0034	0.152	2414	53	1.61	1.73	71	1214	55
	1104-G2-01	0.0328	0.0253	1.650	0.0079	0.800	2407	117	1.61	1.73	71	1214	55
	1104-H1-01	0.0222	0.0110	0.991	0.0071	0.457	2403	56	1.61	1.73	71	1214	55
	1104-H2-01	0.0000	0.0000	1.110	0.0000	0.570	2407	42	1.61	1.73	71	1214	55
	1104-H2-02	0.0300	0.0101	1.211	0.0000	0.589	2410	42	1.61	1.73	71	1214	55
	1104-H3-01	0.0355	0.0140	1.092	0.0000	0.537	2418	61	1.61	1.73	71	1214	55
	1104-H3-02	0.0118	0.0067	0.740	0.0032	0.216	2423	61	1.61	1.73	71	1214	55
	1104-M1-01	0.0275	0.0134	0.830	0.0000	0.360	2413	32	1.61	1.73	71	1214	55
	1104-M2-01	0.0094	0.0078	0.462	0.0018	0.167	2418	35	1.61	1.73	71	1214	55
	1104-M2-02	0.0000	0.0000	0.609	0.0000	0.287	2418	35	1.61	1.73	71	1214	55
	1104-M3-01	0.0000	0.0096	0.756	0.0000	0.195	2418	51	1.61	1.73	71	1214	55
	1104-M4-01	0.0000	0.0000	0.631	0.0000	0.274	2412	20	1.61	1.73	71	1214	55
	1104-N1-01	0.0164	0.0000	0.846	0.0000	0.395	2427	30	1.61	1.73	71	1214	55
HK2013-1845-A	1845-01	0.0075	0.0013	0.691	0.0037	0.232	2578	23	1.08	1.15	62	945	43
	1845-02	0.0076	0.0117	1.001	0.0000	0.352	2592	49	1.08	1.15	62	945	43
	1845-03	0.0000	0.0000	0.835	0.0000	0.279	2579	66	1.08	1.15	62	945	43
	1845-04	0.0000	0.0000	0.777	0.0000	0.298	2579	53	1.08	1.15	62	945	43
	1845-05	0.0136	0.0076	1.197	0.0000	0.454	2569	50	1.08	1.15	62	945	43
	1845-06	0.0091	0.0069	1.167	0.0000	0.494	2578	90	1.08	1.15	62	945	43
HK2013-1991-A	1991-01	0.0000	0.0000	0.586	0.0000	0.155	2717	80	0.75	0.65	61	1	42
	1991-02	0.0000	0.0000	0.546	0.0000	0.127	2723	38	0.75	0.65	61	1	42
	1991-03	0.0000	0.0000	0.362	0.0000	0.037	2721	47	0.75	0.65	61	1	42
	1991-04	0.0000	0.0000	0.245	0.0000	0.059	2724	20	0.75	0.65	61	1	42
	1991-05	0.0000	0.0000	0.239	0.0000	0.063	2721	16	0.75	0.65	61	1	42

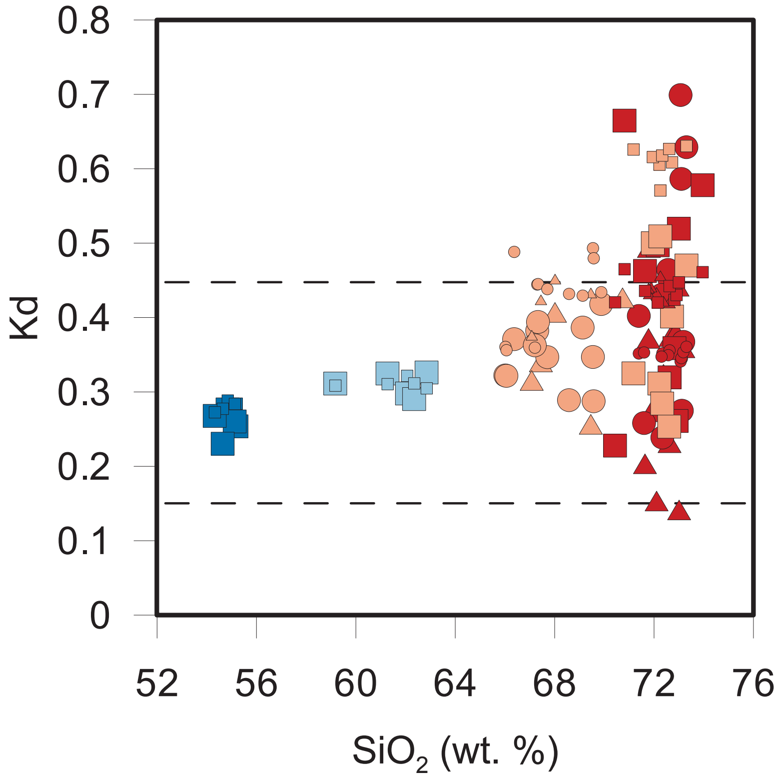

Supplementary Figure 1

The distribution of Kd ratios between olivine and melt inclusions (large symbols) and between olivine and matrix glasses (small symbols) for all four eruptions. The dashed lines represent the acceptable 0.15-0.45 range defined by Toplis (2005).

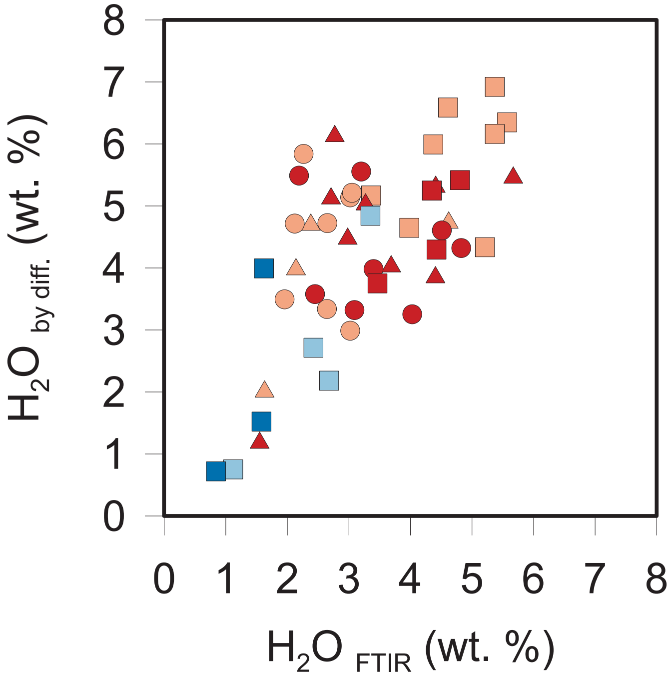

Supplementary Figure 2

Comparison of water concentrations calculated using the by-difference method and using Beer's Law (FTIR).

General conclusions

1. Main findings

My main findings are as follows:

- The Picarro^{TM} cavity ring-down spectrometer (CRDS) can be used to provide precise and accurate, same-day analyses of stable carbon isotopes in the field. This method may be used to identify and characterize active and diffuse CO_2 anomalies associated with volcanic centers and fault systems.

- Carbon dioxide in soil gases at Long Valley caldera is a mixture of atmospheric, biogenic and magmatic-hydrothermal sources of carbon. Magmatic signatures are strongest along faults and fractures situated along the southern margin of the resurgent dome. This region of the caldera represents a highly permeable zone that provides efficient conduits for the transport of fluids and gases. It formed due to an interplay between regional deformation and asymmetric caldera resurgence.

- Magmatic degassing and manifestations of hydrothermal activity at Cerro Negro volcano are strongly influenced by near surface fractures, as well as a deep conduit that formed as a result of regional extension. This network of faults and fractures has changed its permeability over time, with a systematic migration of volcanic and hydrothermal activity with time from north to south. Mantle-like $^{3}He/^{4}He$ ratios of fumarolic gases suggest that the main conduit transports magmatic gases from great depth to the surface with minimal crustal interaction.

- There has been little variation in the stable carbon isotope signatures of soil gases both in space and time over a 20-year period, reinforcing the notion that soil gases at Cerro Negro are supplied by a near-constant source of volatile-rich magmas at depth. Despite the volcano being overdue for eruption, there is currently no evidence to suggests the arrival of new magma at shallow depth.

- Volatile contents in olivine-hosted melt inclusions from four eruptions at Hekla volcano reveal a positive correlation between repose interval, magmatic evolution, explosivity and volatile content. Evolved magmas that have resided in the crust for long periods of time have evolved through a combination of fractional crystallization and assimilation, leading to a progressive increase in water content due to its incompatible nature.

- Larger, silicic eruptions of Hekla have higher H_2O and CO_2 contents in the early erupted material. This suggests that the magma chamber is zoned in terms of its volatile contents with the most volatile-rich magma located at or near the top. Melt inclusions from the early erupted material, with the highest H_2O and CO_2 contents, most likely represent volatile-saturated magmas. These magmas yield a vapor saturation pressure equivalent to melt storage at ~7 km depth. Overall, the low CO_2 and variable H_2O contents of melt inclusions make estimating magma storage at deeper levels problematic.

2. Contributions to knowledge

My study of three volcanic centers has revealed a remarkable degree of similarity among them despite differences in their sizes and ranges of volcanic activity. Studies of volcanic degassing and soil gases at Long Valley caldera and Cerro Negro volcano revealed a close relationship between regional structure and the volcanic edifice. At both study areas, regional deformation exerts an important control on degassing-related permeability and magmatic conduits. This may lead to a migration of eruptive activity or simply introduce variability in the distribution of zones where magmatic gases are reaching the surface. The development of a field-portable spectrometer is an important step towards characterizing changes in the isotopic compositions of magmatic gases in near-real time, as well as identifying areas where they might be reaching the surface. Our understanding of volcanic degassing and magmatic volatiles is important for monitoring purposes at volcanoes such as Cerro Negro and Hekla. Both of these volcanic centers exhibit very little or no warning time prior to eruption. Changes in the stable isotope composition of magmatic gases may increase these warning times by identifying the arrival of new, volatile-rich magma. In this respect, it is important that we understand the evolution of volatiles within a magma chamber. At Hekla, I have demonstrated that dissolved volatile contents magmas exhibit a positive correlation with repose period. Despite uncertainties in the configuration of the plumbing network beneath Hekla, this relationship can be used to predict the explosive potential of future eruptions. In the end, the work presented in this thesis sheds light on the application of magmatic volatiles as tracers of volcanic activity at three different volcanoes. Each study provides insight into the behavior of volatiles at the surface and at depth.

3. Topics for further research

Quantifying the flux of magmatic volatiles from the mantle to the atmosphere remains a challenge and a topic of debate. Contributions from diffuse zones of degassing along fault lines, zones which are not associated with volcanic activity, remain an important target for future soil gas studies. Recent advances in portable spectrometers and remotely operated vehicles (ROVs) are opening interesting avenues of research. The deployment of spectrometers that measure the isotopic composition of volcanic plumes and soil gases in real-time remains an important goal for volcano monitoring and early warning systems.

Our appreciation of the size and distribution of magma reservoirs at depth depends on our understanding of past and present day volatile contents in magmas. Our estimates of the depths at which magmas reside depend upon our ability to recognize melts that are volatile saturated and those that are volatile undersaturated, and also quantifying degassing of volatiles from melt inclusions. This is especially important for volcanic centers such as Hekla that exhibit a large range of volatile contents in a wide range of magma compositions.